UNIVERSITY OF OKLAHOMA

GRADUATE COLLEGE

COLLECTIVE BEHAVIORS OF QUANTUM EMITTERS COUPLED TO A STRUCTURED PHOTONIC ENVIRONMENT

A DISSERTATION

SUBMITTED TO THE GRADUATE FACULTY

in partial fullfillment of the requirements for the

Degree of

DOCTOR OF PHILOSOPHY

By

JUGAL TALUKDAR
Norman, Oklahoma
2023

COLLECTIVE BEHAVIORS OF QUANTUM EMITTERS COUPLED TO A STRUCTURED PHOTONIC ENVIRONMENT

A DISSERTATION APPROVED FOR THE
HOMER L. DODGE DEPARTMENT OF PHYSICS AND ASTRONOMY

BY THE COMMITTEE CONSISTING OF

Dr. Doerte Blume, Chair

Dr. Kieran Mullen

Dr. Arne Schwettmann

Dr. Bruno Uchoa

Dr. Jonathan Kujawa

Dedicated to my grandmother and my parents

Acknowledgements

I would like to begin by expressing my sincere gratitude to my advisor Prof. Doerte Blume. As my doctoral advisor, she has dedicated a significant amount of time and effort to support and guide me in my academic endeavors. She taught me approaches to tackle physics problems, such as asking targeted scientific questions, and integrating numerical calculations and pen-paper calculations along with visual representations to address key aspects of the problem in a systematic manner. Whenever I faced challenges in making progress, she consistently had uplifting interactions with me that motivated me. I am forever in debt for the influence she had in my personal and professional growth. The financial support, including research assistantships and travel grants, has enabled me to develop my skills and present my research at numerous events such as the Boulder Summer School, APS DAMOP, APS March Meeting, ITAMP Winter School, and Minerva-Gentner Symposium, which helped me to learn new physics and to build valuable connections. Additionally, I appreciate her constructive feedback on all my research talks and posters, which has helped me to improve my presentation skills. If I have the ambition to succeed as a researcher, it is largely due to the platform that she selflessly provided me with. Furthermore, I appreciate her assistance in helping me acquire leadership experiences through GPSI and the AMO/CM physics faculty hiring committee. Finally, I would like to thank her for granting me the opportunity to explore research projects that align with my interests in the field of quantum optics, and for the incredible support that followed.

I would like to express my deep gratitude to the members of my thesis advisory committee (TAC): Dr. Kieran Mullen, Dr. Bruno Uchoa, Dr. Arne Schwettmann, Dr. Jonathan Kujawa, and Dr. Kam Wai Chan (former member). Their willingness to dedicate their time amidst their busy schedules to serve on my committee is something I am incredibly thankful for. I appreciate their prompt responses to my emails, timely completion of official paperwork, and the invaluable feedback they provided during the annual evaluation meet-

ings. In particular, I would like to extend my heartfelt thanks to Kieran and Arne for their guidances during some of the challenging phases of my life as a graduate student. Kieran also served as my instructor for four fundamental physics courses, and I am truly grateful for the knowledge I gained from those classes.

I am extremely grateful to our former group members Qingze, Jianwen, and Su-Ju, for their suggestions, support and maintaining a jovial atmosphere. I would like to express my special gratitude to Qingze for his assistance in various aspects of my research work and engaging in insightful discussions. Through our interactions, I gained extensive knowledge about programming in C and learnt approaches to tackle physics problems numerically. I am grateful to our group members Kevin, Dave, Aidan, Bala, and Xylo, who are not just my colleagues but also dear friends. I am thankful for the support provided by all of them. I would like to extend my sincere gratitude to Kevin for introducing me to the fascinating world of the Python programming language. Our numerous physics discussions have truly broadened my perspective on both my own research and his research in unique ways.

I would like to thank my friends, both on and off campus, who have stood by me during difficult times. In particular, the sincere support I have received from Shashi, Gaurav, Geo, Veena, Bhupalee, and Hadi has had a profoundly positive impact on me. I am incredibly grateful to the cricket group "Sooner Strikers" for making every weekend memorable. Despite the exhaustion from seven hours of cricket under the scorching summer sun in Norman, those moments were rewarding and fulfilling. I eagerly wait for the arrival of cricket weekend because it leaves a refreshing impact on me. I will miss all the tactical discussions and spirited arguments we engaged in, all driven by our shared passion for playing cricket.

During this journey, Prerona (Jun), my partner in life has consistently supported me with love and care. She has constantly motivated me to aspire for grand dreams while maintaining a realistic perspective. I express deep gratitude to my parents for their incredible love, care,

and encouragement, well throughout my life. They worked hard to ensure that I received an excellent education, something they themselves were unable to obtain. I will never forget their tireless dedication, which elevated my standard of living from studying by the dim light of a kerosene lamp in my primary school days to solving algebra and geometry problems under the illumination of electric bulbs in my middle school days.

Lastly, I would like to acknowledge the financial support I received from the NSF through Grant PHY-1806259 and PHY-2110158, and from Homer L. Dodge department of physics and astronomy through graduate teaching assistantships.

Table of Contents

Abstract ix

List of Figures xxvii

1 Introduction 1

2 Background on quantized light-emitter interaction 8
2.1 Emitter-photon interaction: From quantum Rabi to Jaynes-Cummings Hamiltonian . 9
2.2 Structured photonic environment . . . 13
2.3 One-excitation manifold . . . 16
2.3.1 Single-emitter properties: $N_e = 1$ . . . 19
2.3.2 Multi-emitter properties: $N_e \gg 1$ . . . 26
2.4 Two-excitation manifold . . . 27
2.5 Dissipative processes in a cavity array . . . 31
2.6 Experimental realization: Circuit QED platforms . . . 32

3 Undamped Rabi oscillations due to polaron-emitter hybrid states in non-linear photonic wave guide coupled to emitters 34
3.1 Undamped Rabi oscillations due to polaron-emitter hybrid states in non-linear photonic wave guide coupled to emitters . . . 35

4 Two emitters coupled to a bath with Kerr-like non-linearity: Exponential decay, fractional populations, and Rabi oscillations 46
4.1 Introduction . . . 47
4.2 System Hamiltonian and theoretical techniques . . . 50
4.2.1 System Hamiltonian . . . 50
4.2.2 Mode structure of the bath Hamiltonian . . . 55
4.2.3 Solving the Schrödinger equation . . . 57
4.2.4 Adiabatic elimination of single-photon states . . . 60
4.2.5 Markov approximation for $\hat{H}^{\mathrm{adia},0}$ . . . 65
4.3 Stationary solution . . . 69
4.3.1 Overview . . . 69
4.3.2 Near the bottom of the band: Two-state model . . . 72
4.4 Dynamics . . . 77
4.5 Conclusion . . . 83

5 Photon-induced droplet-like bound states in one-dimensional qubit array 85
5.1 Introduction . . . 86
5.2 Derivation of Effective Qubit Hamiltonian . . . 88
5.2.1 Total Hamiltonian $\hat{H}$ . . . 88
5.2.2 Effective spin Hamiltonian $\hat{H}_{\mathrm{spin}}$ . . . 91
5.3 Stationary Solutions . . . 96
5.4 Dynamics . . . 106
5.5 Conclusion . . . 111
5.6 Acknowledgement . . . 112

6 Conclusions and outlook **113**

A Single-emitter dynamics **118**

B Details on adiabatic elimination **120**

C Derivation of $\hat{H}_{\text{spin}}$ **123**

D Technical details: Numerical calculations **128**
D.1 Size of the Hilbert space 128
D.2 Exact diagonalization to evaluate time-dependence 134

E Technical details: Analytical calculations **141**
E.1 Evaluation of lattice sums: Contour integral 141
E.2 Two-photon bound state energy and wavefunction 145
E.3 Two-photon scattering state wavefunction 152

References **155**

Abstract

The study of a quantum system coupled to an environment plays an indispensable role in expanding our understanding of quantum mechanics. It has a broad impact, encompassing fundamental inquiries in quantum physics as well as applications in quantum technologies. The primary focus of our work is on a "big" quantum system that consists of two distinct subsystems, one characterized by spin degrees of freedom and the other by bosonic degrees of freedom. Our research falls in the realm of quantum optics, where the bosonic degrees of freedom which constitute the "environment" are realized by photons in cavities. The spin degrees of freedom are realized by two-level quantum emitters that represent the "system" under study.

The collective radiative behaviors of the emitters coupled to a single mode cavity are described frequently by the Dicke model, which treats a subset of the full Hilbert space. Motivated by recent experimental developments in quantum optics and circuit quantum electrodynamics (QED) platforms, we replaced the single-mode cavity by a one-dimensional array of coupled cavities with Kerr-like non-linearity. The presence of the Kerr-like non-linearity gives rise to a nontrivial mode structure of the bath that supports two-photon bound states. Working in the weak emitter-photon coupling regime, we investigated collective behaviors exhibited by a group of quantum emitters in the two-excitation manifold.

We developed a theoretical atom-optical framework that treats the emitter-photon coupled system fully quantum mechanically. We covered a wide range of theoretical approaches in our study, starting from the Schrödinger equation and extending to the Markov approximation, which is critical also for quantum master equation treatment. By using the theoretical atom-optical framework, we sought to identify the radiative pathways and effective interactions of the emitters coupled to the structured photonic environment.

For two excited emitters with transition energy in resonance with the two-photon bound state band, the radiative properties were studied. It was found that when the emitters are in

resonance with the band edge and are well-separated, undamped Rabi oscillations occur; Rabi oscillations do not exist without the Kerr-like nonlinearity. A photonic polaron-like state that forms as a result of all-to-all interaction in the center-of-mass momentum space of the two-photon bound states was identified.

For an emitter array with a large number of emitters, operating within the band gap regime, an effective spin Hamiltonian was derived. Interestingly, a reversal in the hierarchy of interaction energy scales was observed. This led to the discovery of a series of novel correlated bound states that exhibit droplet-like characteristics.

The findings of our atom-optical theory provide a guide for future experimental and theoretical studies of spin-boson coupled systems. The parameter regimes considered in this thesis can be applied to several circuit QED experimental platforms and the predictions can be tested with state-of-the-art technology.

List of Figures

1.1 Illustration of a closed quantum system, which includes two parts: subsystem A, represented by a red filled square, and subsystem B, represented by a blue filled square. We employ a different "labeling" scheme, where subsystem A is labeled as the "system," while subsystem B is labelled as the "environment." It implies that we can treat the "system" as an open quantum system. In our study, a group of emitters takes on the role of the system, while the photonic degrees of freedom constitute the environment. 1

1.2 Illustration of effective interactions among a group of emitters (red filled squares) mediated by a photonic bath (blue filled rectangle). In the absence of emitter-photon coupling (illustrated on the left), the emitters do not interact with one another. However, upon introducing the emitter-photon coupling (illustrated on the right), effective interactions arise among the emitters mediated by the shared photonic environment. 3

2.1 Illustration of the system being investigated: A collection of quantum emitters coupled to a structured photonic environment. The structured photonic environment consists of an array of N cavities arranged in a circular ring, where each cavity is represented by a blue box. The ring configuration enforces periodic boundary conditions, meaning that the first cavity ($n = 1$) is positioned adjacent to the last cavity ($n = N$). The green lines labeled with J depict the photon hopping strength between neighboring cavities, which are separated by a distance denoted by a. Within each cavity, there exists an on-site interaction denoted by U, which characterizes the effective interaction between photons in the same cavity. The quantum emitters are shown as two two-level systems with energy levels $|g\rangle$ and $|e\rangle$, possessing an energy separation of $\hbar\omega_e$. These emitters are coupled to the cavities labeled as n_i and n_j such that $|n_i - n_j| = x/a$, with a coupling strength denoted by g. 15

2.2 Single-photon energy spectrum as a function of the scaled momentum ka/π. The energy shown here is shifted in such a way that the $k = 0$ single-photon state has zero energy. 17

2.3 Eigenenergy of the Hamiltonian $\hat{H}_1$ for $N_e = 1$, $g/J = 0.02$, $\delta_1/J = 0$, and $N = 1001$ as a function of the eigenstate index. The energy is measured with respect to the bottom of the single-photon band, i.e., $E_{0,1}$. Inset: Blow-up of the lower part of the energy spectrum. 19

2.4 The emitter and photonic components in the emitter-photon bound states for $g/J = 0.02$. (a) Emitter component b_e is shown as a function of δ_1/J. (b) The photonic component b_k as a function of the scaled single-photon momentum ka/π for various δ_1/J. The solid black, dotted blue, dashed red, dash dotted green, and solid magenta lines are obtained for $\delta_1/J = 0.01$, 0.005, 0, -0.005, and -0.01, respectively. 21

2.5 Energy of the emitter-photon bound state as a function of $\delta_1/J = 0$ for $g/J = 0.02$. Here, the energy is measured with respect to the lowest energy $E_{0,1}$ of the single-photon band. 22

2.6 Radiation dynamics for the initial state $|\psi_1(0)\rangle = |e, \text{vac}\rangle$ for $g/J = 0.02$. The dotted black, dash-dotted green, solid red, and dashed blue shows the population $|d_e(t)|^2$ for $\delta_1/J = 0.2$, 0.005, 0, and -0.02 respectively. . . . 23

2.7 Square of the absolute value of the projection of the initial state $|\psi_1(0)\rangle$ onto the energy eigenstates $|\phi_E\rangle$ of the Hamiltonian $\hat{H}_1$ as a function of the eigenenergy E, measured relative to the bottom $E_{0,1}$ of the single-photon band, for $N_e = 1$ and $g/J = 0.02$. The energy detuning δ_1/J is set to (a) $\delta_1/J = 0.2$, (b) $\delta_1/J = 0.005$, (c) $\delta_1/J = 0$, and (d) $\delta_1/J = -0.02$. The red square corresponds to the largest value of $|\langle\phi_E|\psi_1(0)\rangle|^2$. 24

2.8 The band structures of our system in the two-excitation manifold for $\hbar\omega_c/J = 20$ and $\hbar\omega_e/J = 17.6$. (a) The solid black line shows the total energy of an excited emitter and a single photon as a function of the scaled single-photon momentum ka/π. This energy is obtained by adding $\hbar\omega_e$ to the single-photon energy given in Eq. (2.30). (b) The eigen spectrum of the two-photon system is shown as a function of the scaled center-of-mass momentum Ka/π. The solid blue line shows the energy of the two-photon bound state, $E_{K,b}$, which is given by Eq. (2.46), considering $U/J = -4$. The gray shaded area represents the two-photon scattering continuum. Both in (a) and (b), the dashed red line corresponds to the energy $2\hbar\omega_e$ associated with two excited emitters. 28

2.9 The dependence of the binding energy E_{binding}/J of a two-photon bound state on the scaled center-of-mass momentum Ka/π for different values of U/J. The solid black, the dashed red, and the dotted blue lines are obtained for $U/J = -0.6$, -1, and -2, respectively. 29

2.10 The photonic fraction $\sum_k |b_k|^2$ of the emitter-photon bound state as a function of δ_1/J for $g/J = 0.02$ and $N_e = 1$. 32

3.1 (a) Schematic of the Hamiltonian $\hat{H}$. The cavity array and two-level emitters (2LE) are shown; the role of the different energy terms is illustrated. (b) Illustration of the Hilbert space structure of $\hat{H}$ (left), $\hat{H}^{\text{adia}}$ (middle), and $\hat{H}^{\text{2-st.}}$ (right). The matrix element $M_b(k,n,K)$ is defined in Ref. [127]. . . 38

3.2 $|c_{ee}(t)|^2$ as a function of $Jt/\hbar$ for the initial state $|e,e,\text{vac}\rangle$, $U/J = -1$, $g/J = 1/50$, and $\delta/J = 0.0431$ (left) and $\delta/J = 0.0011$ (right). Top, middle, and bottom rows are for $x/a = 0$, 5, and 10, respectively. Black solid, red dotted, blue dashed, and green dash-dash-dotted lines are obtained using $\hat{H}$, $\hat{H}^{\text{adia}}$, $\hat{H}^{\text{adia}}$ with $G_{K,K'} = 0$, and $\hat{H}^{\text{adia}}$ with $G_{K,K'} = \Delta_e = 0$, respectively. . 39

3.3 Static results ($U/J = -1$, $g/J = 1/50$, and $\delta/J = 0.0011$). (a) Black solid, red dotted, and magenta dash-dotted lines show the eigen energies corresponding to hybridized states of $\hat{H}$, $\hat{H}^{\text{adia}}$, and $\hat{H}^{\text{2-st.}}$, respectively, as a function of x/a. The gray dashed line shows $(E - E_{0,b})/J = 0$. (b) The black solid line shows $E_{K,b}$ as functions of Ka/π (main panel) and the state index (inset). The red circles show the eigen energies supported by $\hat{H}_b^{\text{adia}}$ (index 1 corresponds to the polaron state). (c) The squares, circles, and triangles show the dimensionless quantities $\text{Re}(G_{K^{(0)},K^{(0)}}(x))/10$, $\text{Re}(F_{K^{(0)},b}(x))$, and $\text{Im}(F_{K^{(0)},b}(x))$ as a function of x/a for $K^{(0)}a/\pi = 0.0152$. 41

3.4 State composition of hybridized polaron-emitter states ($U/J = -1$, $g/J = 1/50$, and $\delta/J = 0.0011$). (a) Projection of $|e,e,\text{vac}\rangle$ onto Ψ_+ (upper three lines) and Ψ_- (lower three lines) as a function of x/a. Black solid, red dotted, and magenta dash-dotted lines are obtained using $\hat{H}$, $\hat{H}^{\text{adia}}$, and $\hat{H}^{\text{2-st.}}$, respectively. (b)/(c) Projection of Ψ_+ and Ψ_- onto $|g,g,K\rangle$ as a function of Ka/π for $x/a = 10$. The line styles are the same as in (a); black solid and red dotted lines are nearly indistinguishable on the scale shown. 43

4.1 Illustration of system under study. (a) Schematic of system Hamiltonian. Each blue box represents a cavity. The tunnel-coupling between neighboring cavities, which are separated by a, is shown by the lines labeled by J. The onsite interaction U characterizes the effective photon-photon interaction; the U-term of the Hamiltonian $\hat{H}$, Eq. (4.2), only plays a role for $N_{\text{exc}} \geq 2$. Two two-level emitters with energy levels $|g\rangle_j$ and $|e\rangle_j$ ($j = 1$ or 2) are coupled to cavities n_1 and n_2 (n_1 and n_2 are fixed, $n_1 - n_2 = x/a$) with strength g. The black line illustrates a two-photon bound state that is supported by the cavity array. The physics explored in this paper occurs in the regime where the size of the two-photon bound state is comparable to the emitter separation x. (b) Illustration of the system-bath Hamiltonian $\hat{H}_{\text{sb}}$, Eq. (4.4), in the emitter Hilbert space. Going from $|e\rangle_1|e\rangle_2|\text{vac}\rangle$ to $|g\rangle_1|g\rangle_2|K\rangle$ requires two single-photon processes of strength g. (c) Illustration of the effective Hamiltonian $\hat{H}^{\text{adia}}$, Eq. (4.28), in the emitter Hilbert space. The adiabatic elimination introduces an effective two-photon coupling between states $|e\rangle_1|e\rangle_2|\text{vac}\rangle$ and $|g\rangle_1|g\rangle_2|K\rangle$. This work monitors the change of the population of the state $|e\rangle_1|e\rangle_2|\text{vac}\rangle$ with time. 52

4.2 Two-photon eigen spectrum as a function of the scaled center-of-mass wave number Ka/π. Note that the energy is shifted such that the bottom of the two-photon bound state band sits at zero. (a) The gray-shaded energy band corresponds to the two-photon scattering continuum, Eq. (4.9). The thick blue solid line shows the energy $E_{K,b}$ of the two-photon bound state for $U/J = -1$. While the gray band and thick blue solid line appear to coincide for $K = 0$ on the scale shown, we note that the bottom of the two-photon scattering continuum at $K = 0$ lies $(-4+\sqrt{17})J \approx 0.123J$ above the $K = 0$ two-photon bound state energy. This separation is sufficiently large for the two-photon scattering continuum to play a negligible role in the system dynamics considered in this paper. The thin dashed line shows the energy of the state $|e,e,\text{vac}\rangle$ for $\delta/J = 0.0431$. (b) Blow-up of (a), focusing on the region around the bottom of the band. The blue solid and blue dashed lines are the same as in (a). The horizontal green solid and magenta dotted lines show the energy of the state $|e,e,\text{vac}\rangle$ for $\delta/J = 0.0011$ and 0.0001, respectively. The labels "(A)", "(B)", and "(C)" refer to the three scenarios introduced in the second to last paragraph of Sec. 4.2.1. 54

4.3 Contour plots of the effective dimensionless interactions $\vec{F}_{K,b}(n_1,n_2)$ between the states $|e,e,\text{vac}\rangle$ and $\hat{P}^{\dagger}_{K,b}|g,g,\text{vac}\rangle$ as functions of Ka/π and x/a for $\delta/J = 0.0011$; to obtain the actual interaction strength, $\vec{F}_{K,b}(n_1,n_2)$ needs to be multiplied by $g^2/(N^{1/2}J)$. (a) $\text{Re}[\vec{F}_{K,b}(n_1,n_2)]$ for $U/J = -1$. (b) $\text{Im}[\vec{F}_{K,b}(n_1,n_2)]$ for $U/J = -1$. (c) $\text{Re}[\vec{F}_{K,b}(n_1,n_2)]$ for $U/J = -5/2$. (d) $\text{Im}[\vec{F}_{K,b}(n_1,n_2)]$ for $U/J = -5/2$. The color scheme for each of the four panels is different. 63

4.4 Contour plots of the real part of the effective dimensionless interactions $\underline{G}_{K,K'}(n_1,n_2)$ between the states $|g,g,K\rangle$ and $|g,g,K'\rangle$ as functions of Ka/π and $K'a/\pi$ for $\delta/J = 0.0011$; to obtain the actual interaction strength, $\underline{G}_{K,K'}(n_1,n_2)$ needs to be multiplied by $g^2/(NJ)$. (a) Re$[\underline{G}_{K,K'}(n_1,n_2)]$ for $U/J = -1$ and $x/a = 0$. (b) Re$[\underline{G}_{K,K'}(n_1,n_2)]$ for $U/J = -5/2$ and $x/a = 0$. (c) Re$[\underline{G}_{K,K'}(n_1,n_2)]$ for $U/J = -1$ and $x/a = 10$. (d) Re$[\underline{G}_{K,K'}(n_1,n_2)]$ for $U/J = -5/2$ and $x/a = 10$. The color schemes for $U/J = -1$ [(a) and (c)] are the same; similarly, the color schemes for $U/J = -5/2$ [(b) and (d)] are the same. 64

4.5 Lines show the dimensionless decay constant $\Gamma_{\text{bath}}\hbar J^3/g^4$, obtained within the Markov approximation [Eq. (4.31)]. (a) The black solid, red dashed, blue dotted, and magenta dash-dotted lines show $\Gamma_{\text{bath}}\hbar J^3/g^4$ as a function of U/J for $\delta/J = 0.0431$ and $x/a = 0$, 2, 4, and 6, respectively. (b) The black solid, blue dotted, and magenta dash-dotted lines show $\Gamma_{\text{bath}}\hbar J^3/g^4$ as a function of δ/J for $U/J = -1$ and $x/a = 0$, 4, and 6, respectively. For comparison, the open black circles show the decay constant extracted from the dynamics for the full Hamiltonian $\hat{H}$ for $x/a = 0$ and $g/J = 1/50$; the Markov approximation results (solid line) capture the decay constant extracted from the full decay dynamics quite well. Note that the Markov approximation breaks down when δ/J approaches zero (left portion of the panel) and when δ/J approaches the two-photon scattering continuum (right portion of the panel). 67

4.6 Energy of the two lowest eigen states as a function of δ/J for $U/J=-1$ and $g/J=1/50$. (a) The black solid and red dashed lines show the energy for $\hat{H}^{\text{adia},1}$ and $\hat{H}^{\text{adia},0}$, respectively, for $x=0$. For comparison, the open circles show the eigen energies for $\hat{H}$ (using a basis that excludes the two-photon scattering states). The energies for $\hat{H}$ and $\hat{H}^{\text{adia},1}$ agree very well. (b) The black solid and black dotted lines show the energies of $\hat{H}^{\text{adia},1}$ for $x/a=0$ and $x/a=5$, respectively. A clear separation dependence can be seen. In both panels, the lower state corresponds to a hybridized bound state with appreciable $|e,e,\text{vac}\rangle$ and $|g,g,\text{pol}\rangle$ contributions (see Sec. 4.3.2 for details). 70

4.7 Visualization of eigen spectrum of $\hat{H}^{\text{adia},1}$ as a function of the detuning δ/J for $U/J=-1$, $g/J=1/50$, and $x=0$. The density of states $\rho_E(E)$ of the continuum portion of the energy spectrum, which is dominated by states that have no or extremely small emitter admixtures, is shown in color (the legend is shown on the right; arbitrary units are used). The lowest hybridized bound state (black solid line) is well separated from the energy continuum. The second lowest state (black dashed line) is separated by a small gap from the continuum for negative δ/J and part of the continuum for positive δ/J. . 71

4.8 Contour plots of the effective dimensionless interaction $F_{K^{(0)},b}(n_1,n_2)$ between the states $|e,e,\mathrm{vac}\rangle$ and $\hat{P}^{\dagger}_{K^{(0)},b}|g,g,\mathrm{vac}\rangle$ and the effective dimensionless interaction $G_{K^{(0)},K^{(0)}}(n_1,n_2)$ between the states $|g,g,K^{(0)}\rangle$ and $|g,g,K^{(0)}\rangle$ as functions of δ/J and U/J; to obtain the actual interaction strengths, $F_{K^{(0)},b}(n_1,n_2)$ and $G_{K^{(0)},K^{(0)}}(n_1,n_2)$ need to be multiplied by $g^2/(N^{1/2}J)$ and $g^2/(NJ)$, respectively. (a) $\mathrm{Re}[F_{K^{(0)},b}(n_1,n_2)]$ for $x/a=0$. (b) $\mathrm{Re}[F_{K^{(0)},b}(n_1,n_2)]$ for $x/a=10$. (c) $\mathrm{Re}[G_{K^{(0)},K^{(0)}}(n_1,n_2)]$ for $x/a=0$. (d) $\mathrm{Re}[G_{K^{(0)},K^{(0)}}(n_1,n_2)]$ for $x/a=10$. The color schemes for $\mathrm{Re}[F_{K^{(0)},b}(n_1,n_2)]$ are different for the two separations. The color schemes for $\mathrm{Re}[G_{K^{(0)},K^{(0)}}(n_1,n_2)]$, in contrast, are the same for the two separations. 74

4.9 Energy of the hybridized states as a function of U/J for $g/J=1/50$, $\delta/J=0.0011$, and $x/a=10$. The black circles and red lines are obtained using the full Hamiltonian $\hat{H}$ and the two-state Hamiltonian $\hat{H}^{\text{2-st.}}$, respectively. The agreement is very good for the parameter regime considered. 76

4.10 Projection of the initial state $|e,e,\mathrm{vac}\rangle$ onto the energy eigen states ϕ_E of $\hat{H}$ for $U/J=-1$ and $g/J=1/50$. The square of the absolute value of the overlap onto scattering states and bound states is shown by black circles and red squares, respectively, for (a) $\delta/J=0.0431$ and $x/a=0$, (b) $\delta/J=0.0431$ and $x/a=10$, (c) $\delta/J=0.0011$ and $x/a=0$, and (d) $\delta/J=0.0011$ and $x/a=10$. 78

4.11 Radiation dynamics for the initial state $|e,e,\text{vac}\rangle$, $U/J=-1$, and $g/J=1/50$. The lines show the population $P_{ee}(t)$ for various x/a and δ/J. The value of x/a increases from the top row to the bottom row ($x/a=0$, 5, and 10 for the first, second, and third row, respectively). The value of δ/J decreases from the left most to the right most column ($\delta/J=0.0431$, 0.0011, and 0.0001 for the first, second, and third column, respectively). In all panels, the solid, dotted, and dashed lines show $P_{ee}(t)$ obtained by propagating the initial state $|e,e,\text{vac}\rangle$ under the Hamiltonian $\hat{H}$, $\hat{H}^{\text{adia,1}}$, and $\hat{H}^{\text{adia,0}}$, respectively. The data shown in panels (a)-(f) are also shown in Ref. [60]. 80

4.12 Contour plot of the populations $|c_{K,b}(t)|^2$ of the two-photon bound states $|g,g,K\rangle$ as functions of the dimensionless center-of-mass wave number Ka/π and the dimensionless time $Jt/\hbar$ for $U/J=-1$ and $g/J=1/50$. (a) $\delta/J=0.0431$ and $x/a=0$. (b) $\delta/J=0.0011$ and $x/a=0$. (c) $\delta/J=0.0431$ and $x/a=10$. (d) $\delta/J=0.0011$ and $x/a=10$. The color scheme and range of the vertical axis are adjusted in each panel for ease of viewing. 81

4.13 Population $P_{ee}(t)=|c_{ee}(t)|^2$ as a function of time for $U/J=-1$, $g/J=1/50$, $\delta/J=0.0011$, and $x/a=5$. The black solid line shows $P_{ee}(t)$ obtained by propagating the initial state $|e,e,\text{vac}\rangle$ under the Hamiltonian $\hat{H}$. The red dashed and blue dash-dotted lines show $P_{ee}(t)$ obtained using Eqs. (4.51) and (4.54), respectively. 82

5.1 Schematic of the set up. The jth qubit is coupled with strength g to the n_jth cavity of a one-dimensional cavity array (blue boxes) with lattice spacing a. The cavities are tunnel-coupled to nearest neighbors with strength J (blue lines between two neighboring blue boxes). For more than one photonic excitation, there exists an onsite interaction U between photons. As a result of the onsite interaction, the cavity array (bath) supports two-photon bound states. One of these is shown by the black line above the cavity array. The distance between two neighboring qubits is denoted by x. In the schematic, x is equal to a; values of $x/a = 0$ and 2 are also discussed in this work. The top-left rectangular box illustrates a qubit, i.e., a two-level system with a transition energy $\hbar\omega_e$ between the ground state $|g\rangle$ and the excited state $|e\rangle$. 89

5.2 Schematic of the energy bands for the one- and two-excitation manifolds for fixed ω_c, ω_e, and U. This work focuses on the band gap regime, i.e., negative detunings δ. Adiabatic elimination of the gray single-photon and green two-photon bound state bands introduces the effective interactions W and Y (see Fig. 5.3 for an illustration of these interactions), respectively, between qubit groups. The two-photon scattering continuum is far off-resonant and does not play a role. Explicit expressions for the energy bands can be found, e.g., in Ref. [125]. 91

5.3 Schematic of constrained single-qubit hopping interaction W and pair hopping interaction Y entering into $\hat{H}_{\text{spin}}$. (a) The term $W_{jl}\hat{\sigma}_i^+\hat{\sigma}_j^+\hat{\sigma}_i^-\hat{\sigma}_l^-$ (here illustrated assuming $i \neq j \neq l$) describes the annihilation of an excitation at the lth qubit and the creation of an excitation at the jth qubit (solid blue arrow). This corresponds to the hopping of an excitation with strength W_{jl}, with the excitation at the ith qubit acting as a "spectator", i.e., the single-qubit hopping is only allowed if qubit i is excited. (b) The term $Y_{ij,lh}\hat{\sigma}_i^+\hat{\sigma}_j^+\hat{\sigma}_l^-\hat{\sigma}_h^-$ (here illustrated assuming $i \neq j \neq l \neq h$) describes the annihilation of excitations at qubits l and h, and the creation of excitations at qubits i and j (solid purple arrows). This corresponds to the hopping of a pair of excitations with strength $Y_{ij,lh}$. The open blue and open purple arrows show selected additional constrained hopping and pair hopping interactions, respectively. 93

5.4 The red solid and blue dashed lines show the dimensionless on-site hopping energy $W(0)/J$ (left axis) and length L_0/a (right axis) as a function of the detuning δ/J for $g/J = 1/50$ and $U/J = -1$. 95

5.5 Contour plot of the effective dimensionless interaction $Y_{ij,lh}J^3/g^4$ for $U/J = -1$, $\delta/J = -1/50$, $N_e = 60$, and $x/a = 1$. The x- and y-axis are labeled by the index pairs (i, j) and (l, h); the plot includes all (i, j) and (l, h) pairs with $|j-i| \leq 9$ and $|h-l| \leq 9$. In each block, the separation (i.e., $j-i$ and $h-l$) between the two qubit excitations is fixed while the "center-of-mass coordinates" [i.e., $(i+j)/2$ and $(l+h)/2$] are changing. As an example, the blue rectangle corresponds to a block with $|j-i| = 2$ and $|h-l| = 3$. Values of $(x, y) = (100, 150)$, e.g., correspond to $(i, j) = (41, 43)$ and $(l, h) = (33, 36)$. 97

5.6 Eigenenergy, measured with respect to $E_{0,b}$, for $N_e = 60$, $g/J = 1/50$, $U/J = -1$, $\delta/J = -1/50$, and $x/a = 1$ as a function of the state index. The black filled circles, red open squares, and blue open circles show the energy for $\hat{H}_{\text{spin}}$, $\hat{H}_{\text{single}}$, and $\hat{\tilde{H}}_{\text{single}}$, respectively. Inset: Blow-up of the lower part of the energy spectrum. 99

5.7 Energy of droplet-like states, measured with respect to $E_{0,b}$, for $N_e = 60$, $g/J = 1/50$, $U/J = -1$, and $x/a = 1$ as a function of (a) the excitation number n for $\delta/J = -1/50$ and (b) the detuning δ/J for $n = 1$. The black filled circles, green open triangles, red open squares, and blue open circles show the energies for $\hat{H}_{\text{spin}}$, $\hat{H}_{\text{single}}$, the variational wavefunction given in Eqs. (5.18)-(5.20), and for the perturbative calculation ($\hat{H}_{\text{pair}}$ is treated in first-order perturbation theory), respectively. In (a), the red and black symbols are nearly indistinguishable. In (b), all four calculations yield, on the scale shown, nearly indistinguishable energies except when $|\delta/J|$ is extremely small. The arrow in (b) marks the detuning used in (a). 101

5.8 Pair correlation function $P_{\text{pair}}(\alpha)$ for the ground state as a function of the separation α between two excited qubits for $N_e = 60$, $g/J = 1/50$, $U/J = -1$, $x/a = 1$, and (a) $\delta/J = -1/50$ and (b) $\delta/J = -3/20$. The black solid, blue dotted, and red dashed lines are for $\hat{H}_{\text{full}}$, $\hat{H}_{\text{spin}}$, and $\hat{H}_{\text{single}}$, respectively. The inset in (a) replots the blue dotted line and additionally shows the variational results by green open circles. 102

5.9 Contour plots of the expansion coefficients $c_{ij}^{(n)}$ as functions of R and r for $N_e = 60$, $g/J = 1/50$, $U/J = -1$, $\delta/J = -1/50$, and $x/a = 1$. The coefficients are obtained by diagonalizing the effective Hamiltonian $\hat{H}_{\text{spin}}$. (a), (b), (c), and (d) are for n=1 (droplet-like ground state), 2 (droplet-like first excited state), 3 (droplet-like second excited state), and 4 (droplet-like third excited state), respectively. 104

5.10 Square of the absolute value of the projection of the initial state $|\psi(0)\rangle$ onto the energy eigenstates $|\phi_E\rangle$ of $\hat{H}_{\text{spin}}$ as a function of the eigenenergy E, measured relative to the bottom $E_{0,b}$ of the two-photon bound state band, for $N_e = 60$, $g/J = 1/50$, $U/J = -1$, $\delta/J = -1/50$, and $x/a = 1$. (a) The initial state is $|\psi(0)\rangle = |\text{PS}\rangle$. (b) The initial state is $|\psi(0)\rangle = |\text{FS}\rangle$. The red square and blue triangle correspond to the two largest values of $|\langle\phi_E|\text{FS}\rangle|^2$. 107

5.11 Pair correlation function $P_{\text{pair}}(\alpha,t)$ for $\hat{H}_{\text{spin}}$ as a function of time for three different separations α for $N_e = 60$, $g/J = 1/50$, $U/J = -1$, $\delta/J = -1/50$, and $x/a = 1$. The solid black, red dashed, and blue dotted lines show $P_{\text{pair}}(\alpha,t)$ for $\alpha = 1$, 6, and 21, respectively. The initial state $|\psi(0)\rangle$ is equal to (a) $|\text{PS}\rangle$ and (b) $|\text{FS}\rangle$. 108

5.12 Snapshots of $P_{\text{corr}}(i,j,t)$ for $\hat{H}_{\text{spin}}$ for $N_e = 60$, $g/J = 1/50$, $U/J = -1$, $\delta/J = -1/50$, and $x/a = 1$ as functions of i and j for the initial state $|\psi(0)\rangle = |\text{FS}\rangle$. (a)-(h) correspond to $Jt/\hbar = 0$, 960, 2220, 3080, 4440, 5220, 6540, and 7500, respectively. As discussed in the main text in the context of Fig. 5.9, the coefficients $c_{i,j}^{(n)}$ are only defined for $i < j$; to plot $P_{\text{corr}}(i,j,t)$, we artificially set $c_{i,j}^{(n)} = c_{j,i}^{(n)}$ for $i > j$ and $c_{i,j}^{(n)} = 0$ for $i = j$ for ease of readibility. 109

C.1 Approximations made to obtain the effective spin Hamiltonian $\hat{H}_{\text{spin}}$ (right column) from the total Hamiltonian $\hat{H}$ (left column). The schematic considers $N_e = 4$ as an example and shows only a subset of the basis kets. The red and black horizontal lines show a subset of basis kets. The blue, pink, purple, green, and dark red lines represent interactions. As a result of the adiabatic elimination of the single-photon states $|eggg, k\rangle$, the interactions 1 and 2 give rise to the interaction W between the states $|eegg, \text{vac}\rangle$ and $|egeg, \text{vac}\rangle$ (solid pink line), the interactions 1 and 3 give rise to the interaction F between the states $|eegg, \text{vac}\rangle$ and $|gggg, K_1\rangle$ (solid purple line), the interactions 2 and 3 give rise to the interaction F between the states $|egeg, \text{vac}\rangle$ and $|gggg, K_1\rangle$ (dotted purple line), the interactions 1 and 4 give rise to the interaction F between the states $|eegg, \text{vac}\rangle$ and $|gggg, K_2\rangle$ (dashed purple line), the interactions 2 and 4 give rise to the interaction F between the states $|egeg, \text{vac}\rangle$ and $|gggg, K_2\rangle$ (dash-dotted purple line), and the interactions 3 and 4 give rise to the interaction G between the states $|gggg, K_1\rangle$ and $|gggg, K_2\rangle$ (green line). As a result of setting G to zero and adiabatically eliminating the two-photon bound states $|gggg, K\rangle$, the interactions F (e.g., solid and dotted lines, and dashed and dash-dotted lines) give rise to the interaction Y between the states $|eegg\rangle$ and $|egeg\rangle$ (solid dark red line). The down shifts of the red basis states in the middle and right columns represent the Stark shifts that are due to the adiabatic eliminations. 127

D.1 Memory required to store a Hamiltonian with matrix elements treated as complex double precision variables as a function of the size of the cavity array N for two emitters, i.e., $N_e = 2$. The unit used for the memory is Giga Bytes (GB). (a) The Hamiltonian is the full Hamiltonian. (b) The Hamiltonian is obtained excluding the two-photon scattering states. . . . 130

D.2 Memory required to store a Hamiltonian with matrix elements treated as complex double precision variables for an emitter array with $N_e = 80$ emitters as a function of the size of the cavity array N. The Hamiltonian considered is obtained by excluding the two-photon scattering states. The unit used for the memory is Giga Bytes (GB). 131

D.3 Pair correlation function $P_{\text{pair}}(\alpha)$ for the ground state of $\hat{H}_{\text{spin}}$ (given in Eq. (5.8)) as a function of the separation α between two excited qubits for $g/J = 0.02$, $U/J = -1$, $x/a = 1$, and $\delta/J = -0.02$. The blue dash-dotted, green dashed, red dotted, and black solid lines are for $N_e = 10$, $N_e = 20$, $N_e = 40$, and $N_e = 60$, respectively. The inset replots the black solid line and additionally shows the results for $N_e = 80$ by magenta solid circles. . 132

D.4 Coupling matrix element $M_b(k,n,K)$ between a single-photon state with momentum k and a two-photon bound state with center-of-mass momentum K as a function of the size of the cavity array N. (a) $\text{Re}[M_b(k,n,K)]$ for $n = 2$, $U/J = -0.7$, $ka = 0.01$, and $Ka = 0.001$. (a) $\text{Im}[M_b(k,n,K)]$ for $n = 2$, $U/J = -0.7$, $ka = 0.01$, and $Ka = 0.001$. 137

D.5 The population $P_{ee}(t)$ of the state $|ee, \text{vac}\rangle$ as a function of time for $g/J = 0.02$, $U/J = -1.0$, $\delta/J = 0.0431$, $x/a = 0$, and $N = 9001$. 139

D.6 Schematic of two emitters coupled to the same site of an array of cavities under periodic boundary condition. The blue boxes represent cavities in the array. In the left figure, the emitters are in excited states denoted by solid red filled circles inside the purple oval, and there are no two-photon bound states present in the cavity array. On the right, the diagram shows the emission of the resonant two-photon bound state $\left|\Psi_{K_0,b}\right\rangle$ into the cavity array, with the emitters in their ground states shown by the solid black filled circles inside the purple oval. The resonant two-photon bound state travels with the group velocity $v_{K_0,b}$ from the site of emission (where both emitters are coupled to the same site) and returns to the same site, as indicated by the circular solid magenta arrow. 140

E.1 The solid line shows the scaled dimensionless effective interaction $\frac{Y_{ij,lh}J^3}{g^4}$ between the emitter states $\hat{\sigma}_i^+\hat{\sigma}_j^+\left|gg\cdots g\right\rangle$ and $\hat{\sigma}_l^+\hat{\sigma}_h^+\left|gg\cdots g\right\rangle$ as a function of the size of the cavity array N for $N_e = 10$, $U/J = -0.7$, $\delta/J = -0.02$, $x/a = 1$, $(i,j) = (1,4)$, and $(l,h) = (1,8)$. 144

Chapter 1

Introduction

In quantum mechanics, physical systems are categorized into two types: closed and open quantum systems [1, 2]. A closed quantum system is isolated and does not interact or exchange energy, particles, and information with its surrounding environment [3, 4]. On the other hand, an open quantum system does interact with its environment. When an open quantum system is considered together with its entire surrounding environment, it falls into the category of a closed quantum system. A closed quantum system can be

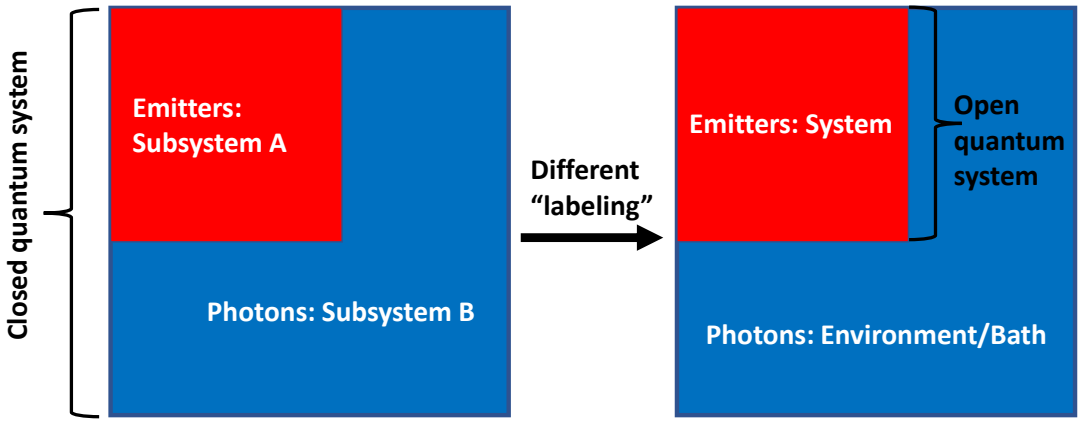

Figure 1.1: Illustration of a closed quantum system, which includes two parts: subsystem A, represented by a red filled square, and subsystem B, represented by a blue filled square. We employ a different "labeling" scheme, where subsystem A is labeled as the "system," while subsystem B is labelled as the "environment." It implies that we can treat the "system" as an open quantum system. In our study, a group of emitters takes on the role of the system, while the photonic degrees of freedom constitute the environment.

divided into subsystems based on the nature (boson, spin, etc.) and the number of degrees of freedom each subsystem possesses [5]. Therefore, we can select one of the subsystems

as the "system" under study, while considering the rest as its surrounding "environment". Typically, an environment possesses an abundance of degrees of freedom, resulting in a multitude of available states. The availability of large number of states within the bath provides numerous pathways for the system to dissipate various entities such as information, energy, and particles. Figure 1.1 illustrates the system-environment labeling schematically. Under the new scheme, the "system" under study can be treated as an open quantum system.

A truly perfect closed quantum system does not exist in reality because there will always be a larger environment that can be taken into account, with which the system is interacting. Therefore, it is absolutely necessary to study the system-environment coupling in order to gain insight into the characteristics of the system. The study of the interaction between a system and its environment plays a crucial role in our understanding of quantum physics [6, 7, 8, 9]. This interaction is essential for addressing fundamental questions in various fields, including quantum thermodynamics [10, 11, 12, 13], quantum optics [14, 15, 16], condensed matter physics [17, 18, 19, 20], and quantum information science [21, 22, 23]. The phenomena like decoherence [24, 25, 26] and thermalization [27, 28, 29], depends on how the system under investigation interacts with its surrounding environment. It is also important to consider system-environment coupling when assessing the advantages and limitations of quantum technologies. For example, the schemes for quantum error correction can be described within the framework of an open quantum system in quantum computing platforms [30, 31, 32, 33]. This framework incorporates noise models that account for the interactions between the qubits and the environment [34, 35]. The performance of platforms studying quantum metrology is also influenced by the system-bath interaction [36, 37, 38, 39, 40, 41]. In order to enhance measurement precision, for instance, in the context of opto-mechanical systems, it is crucial to carefully consider and study how the mechanical degrees of freedom couple to the optical field [42, 43].

In our research, we focus on a "big" quantum system that contains spin and bosonic

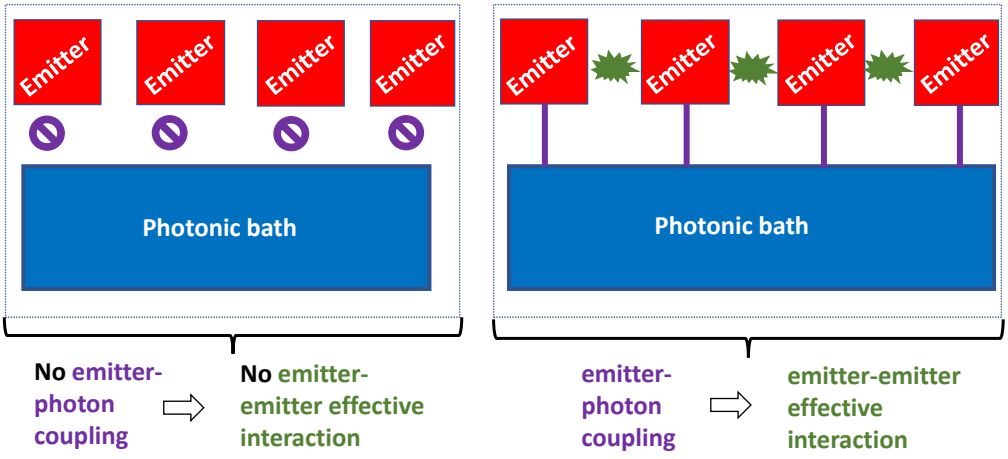

Figure 1.2: Illustration of effective interactions among a group of emitters (red filled squares) mediated by a photonic bath (blue filled rectangle). In the absence of emitter-photon coupling (illustrated on the left), the emitters do not interact with one another. However, upon introducing the emitter-photon coupling (illustrated on the right), effective interactions arise among the emitters mediated by the shared photonic environment.

degrees of freedom. The spin degrees of freedom represent the system being investigated, while the bosonic degrees of freedom represent the environment. Our work falls in the realm of quantum optics, where the bosonic degrees of freedom correspond to photons in cavities and the spin degrees of freedom correspond to a group of non-interacting two-level quantum emitters. While the quantum emitters do not possess inherent interactions among themselves, their interaction with the shared photonic bath leads to the emergence of an effective interaction between them. Figure 1.2 provides a schematic representation of how a collection of emitters can exhibit effective interactions mediated by the photonic environment. By modifying the mode structure of the photonic bath, it is possible to tune the strength of the effective interaction between the emitters. In essence, the collective behaviors of the emitters relies heavily on the specific band structure of the photonic bath. An example of collective radiative behavior is the burst of photon emission from a group of emitters

coupled to a common bath. In this case, the collective photon emission is significantly more intense than the independent emission from individual emitters. This phenomenon of non-equilibrium collective radiation is known as superradiance, which has been a prominent topic of research in the field of quantum optics for the past few decades [45, 46, 47, 48]. Conversely, subradiance is the opposite phenomenon, where the emission of photons from a group of emitters is suppressed compared to the case of independent emitters [49, 50, 51].

Typically, the collective behavior of the emitters in terms of radiation is described using models such as the Dicke model, which involves a group of two-level emitters coupled to a single-mode cavity [44]. Recent experimental advancements in quantum optics and circuit QED platforms have made it possible to engineer intriguing photonic environments [52, 53, 54, 55, 56, 57, 58]. For instance, experimental realizations of the Bose-Hubbard model for photons have been achieved using superconducting circuits [59]. These engineered environments offer exciting opportunities to manipulate the interaction between light and matter, laying the groundwork for studying the collective behavior of emitters coupled to a photonic bath. In our work, we extend the concept of a photonic bath to a one-dimensional photonic waveguide, where strong confinement in the transverse directions restricts the propagation of photons to one dimension. The low-dimension and directionality of the photonic waveguide results in intricate effective interactions among the collection of emitters that leads to interesting correlated dynamics [14, 15, 50, 114, 115, 116, 117, 118, 119, 120, 121].

More specifically, we consider a one-dimensional array of coupled cavities that exhibits Kerr-like non-linearity as the photonic bath. The photonic bath is described by the one-dimensional Bose-Hubbard Hamiltonian for photons. The Kerr-like nonlinearity in the cavity array gives rise to a nontrivial mode structure in the bath, supporting two-photon bound states. The emitters are either coupled to the same cavity or distributed among different cavities. By considering the weak coupling between the emitters and the photons,

we investigate the emitter-photon system within the two-excitation manifold.

The Hilbert space associated with the "big" emitter-photon system is exceedingly large in size. Consequently, employing a full quantum mechanical treatment to study the emitter-photon coupled system poses a formidable challenge. To address this, various theoretical and numerical methods, such as perturbative treatments, have been utilized to investigate systems with a large number of degrees of freedom [97, 105, 145, 146, 147, 148, 149, 150, 151, 152]. In this thesis, we present a comprehensive atom-optical theoretical framework that treats both the emitter system and the photonic bath fully quantum mechanically. As the group of emitters and the coupled cavity array constitute a closed quantum system, we analyze their time-dependent and time-independent properties by employing the Schrödinger equation. To mitigate the computational cost, we simplify the problem by truncating the Hilbert space that involves neglecting the two-photon scattering states. In the regime of weak emitter-photon coupling, the influence of the two-photon scattering states on the dynamics is negligible. Consequently, calculations performed within the reduced Hilbert space are essentially equivalent to those conducted in the full Hilbert space. Additionally, we employ an effective non-hermitian Hamiltonian framework, a suitable method commonly used to investigate open quantum systems. This approach is well-suited for our study due to the large number of photonic degrees of freedom involved and the weak coupling between the emitter and cavity array. By utilizing this framework, we gain deeper insights into the effective interactions among the emitter degrees of freedom, while taking into account the simplifications introduced by the Born-Markov approximation. This also builds the foundation to employ a quantum master equation formalism [3, 4].

The core of this thesis revolves around the role played by the number of emitters and two frequency regimes relative to the band of two-photon bound states: the "inside band" and the "band gap" physics. In the inside band regime, we explore the radiative behavior of two emitters [60, 61]. The physics behind remarkable undamped Rabi oscillation observed

in this scenario bears close resemblance to impurity models discussed in the context of condensed matter physics [62]. On the other hand, in the band gap regime, we uncover an effective spin Hamiltonian governing the effective interactions between emitters in an emitter array [63]. The band gap regime provides a foundation for studying the quantum simulation of spin-$1/2$ systems in the context of cavity QED and circuit QED platforms. It is worth mentioning that quantum simulation of spin systems is important for expanding our understanding of correlated matter [64, 65, 66, 67, 68]. The theoretical findings presented in this thesis serve as a valuable guide for future experimental and theoretical investigations of emitter-photon coupled systems.

The remainder of this thesis is organized as follows. The focus of this dissertation is to examine the physics of a collection of qubits or emitters coupled to a structured photonic environment that has Kerr-like nonlinearity. In Chapter 2, the interactions between emitters and photons are reviewed to gain insight into the static and dynamic properties of the system. In order to establish a basis for the two-excitation manifold physics, the emitter-photon coupled system is discussed in the one-excitation manifold. In order to explore the potential ways of implementing our system in an experimental setting, we provide a brief summary of the dissipative processes in the emitter-photon coupled system.

Chapter 3 contains the manuscript that has been published in Physical Review A [J. Talukdar and D. Blume, "Undamped Rabi oscillations due to polaron-emitter hybrid states in non-linear photonic wave guide coupled to emitters," Physical Review A, 106(1), 013722, 2022]. In this work, we identified a set of physical parameters which leads to undamped Rabi oscillations that are facilitated by the coupled cavity system. The oscillatory nature of dynamics deviates from the typical exponential decay and fractional population behavior. I proposed the idea of this work and developed, in discussion with D. Blume, the project. I performed all the calculations and made all the figures. D. Blume wrote the first draft of the manuscript.

Chapter 4 contains the manuscript that has been published in Physical Review A [J. Talukdar and D. Blume, "Two emitters coupled to a bath with Kerr-like non-linearity: Exponential decay, fractional populations, and Rabi oscillations," Physical Review A, 105(6), 063501, (2022)]. The role of Kerr-like non linearity in the static and dynamic characteristics of two emitters coupled to the cavity array is thoroughly examined and discussed in this study. In this work, I developed all the numerical and analytical tools, performed all the calculations and made all the figures. I created a comprehensive report that included key results and details of the calculations, while D. Blume wrote the first draft of the manuscript.

Chapter 5 contains the manuscript that has been under review in Physical Review A [J. Talukdar and D. Blume, "Photon-induced droplet-like bound states in one-dimensional qubit array"]. The focus of this research is on the effective spin Hamiltonian derived in terms of the degrees of freedom of the qubit array and explores novel correlated bound states that are supported by the array. Inspired by my undergraduate research, I collaborated with D. Blume to develop this project. I performed all the calculations, made all the figures, and wrote the first draft of the manuscript.

Chapter 7 concludes and provides an outlook of this thesis. We summarize and connect the results discussed in Chapters 3–5 and give an overview of the possibility of further extension to our work.

Lastly, this thesis includes five supplementary chapters in the form of appendices, which specifically address the technical aspects of our research. Appendices A to C consist of the appendices related to the manuscripts discussed in Chapters 3 to 5. Appendix D focuses on the technical aspects of the numerical calculations performed, providing an overview of the matrix diagonalization of the emitter-photon coupled Hamiltonian and the memory requirements. Appendix E delves into the details of the analytical calculations, presenting step-by-step calculations for certain integrals and discussing the calculation of the energy and wave function of a two-photon bound states using the Lippmann-Schwinger equation.

Chapter 2

Background on quantized light-emitter interaction

This chapter provides an analysis of the interaction between light and matter, specifically in the context of cavity QED [69, 70, 71, 72]. The theoretical framework that has been developed for the interaction between light and matter in atomic-optical systems can also be applied to circuit QED systems such as superconducting qubits, josephson junctions, and coupled resonator waveguide [53, 55, 57, 58, 73].

The primary focus of our work is on a two-level system that serves as a quantum emitter. The Hamiltonian that describes this system is given by:

$$H_{\mathrm{TLS}} = \frac{\hbar\omega_e}{2}\left(\hat{\sigma}^z + \hat{I}\right), \tag{2.1}$$

where ω_e represents the frequency at which the emitter transitions between its ground state $|g\rangle$ and excited state $|e\rangle$. The operators $\hat{\sigma}^z$ and $\hat{I}$ are the Pauli matrix and identity operator, respectively. In terms of the states of the emitter, $\hat{\sigma}^z$ can be written as $|e\rangle\langle e| - |g\rangle\langle g|$ and $\hat{I}$ as $|e\rangle\langle e| + |g\rangle\langle g|$. In our work we consider single mode cavities. The Hamiltonian for a single mode cavity is given by

$$\hat{H}_{\mathrm{cav}} = \hbar\omega_c \hat{a}^\dagger \hat{a}, \tag{2.2}$$

where ω_c is the mode frequency of the cavity, and $\hat{a}$ and $\hat{a}^\dagger$ are the photonic annihilation and creation operator, respectively. Prior to discussing the time-independent and time-dependent characteristics of a collection of emitters interacting with a structured photonic environment, we introduce the interaction of light with matter in the context of an emitter coupled to a single-mode cavity.

2.1 Emitter-photon interaction: From quantum Rabi to Jaynes-Cummings Hamiltonian

The light-matter interaction for an emitter coupled a single-mode cavity involves the interaction between the dipole moment of the two-level system and the quantized cavity field [69, 70, 71, 72]. The emitter-photon interaction in the Schrödinger picture is given by

$$\hat{H}_{\text{int}} = -\hat{\vec{d}}.\hat{\vec{E}}(\vec{r}), \tag{2.3}$$

where $\hat{\vec{d}}$ and $\hat{\vec{E}}(\vec{r})$ correspond to the dipole moment operator of the two-level system and the electric field operator, respectively. Equation (2.3) describes the interaction between light and matter under the dipole approximation, which assumes that the spatial variation of the electromagnetic field over the emitter is negligible. Thus, the cavity field that appears in Eq. (2.3) has a position dependence evaluated at the position $\vec{r}$ of the emitter. The dipole operator for the emitter is defined as

$$\hat{\vec{d}} = \vec{d}_{eg}(\hat{\sigma}^{+} + \hat{\sigma}^{-}), \tag{2.4}$$

where $\vec{d}_{eg} = \langle e|\,\vec{d}\,|g\rangle$ is the dipole moment element, and $\hat{\sigma}^{+} = |e\rangle\langle g|$, and $\hat{\sigma}^{-} = |g\rangle\langle e|$ are the emitter raising and lowering operator, respectively. The cavity field can be written as [72]

$$\hat{\vec{E}}(\vec{r}) = \sqrt{\frac{\hbar\omega_c}{2\varepsilon_0}}\left(\vec{\beta}(\vec{r})\hat{a} + \vec{\beta}^{*}(\vec{r})\hat{a}^{\dagger}\right), \tag{2.5}$$

where $\vec{\beta}(\vec{r})$ is the spatial profile of the cavity field. The normalization condition

$$\int d^3\vec{r}|\vec{\beta}(\vec{r})|^2 = 1 \tag{2.6}$$

implies that we can define a cavity volume V, and using the approximation where the spatial mode is uniform across the cavity, we get

$$\vec{\beta}(\vec{r}) = \frac{1}{\sqrt{V}}\vec{\varepsilon}, \tag{2.7}$$

where $\vec{\varepsilon}$ is the polarization of the field mode at the position of the emitter in the cavity. Plugging Eq. (2.7) into Eq. (2.5), we get

$$\hat{\vec{E}} = \sqrt{\frac{\hbar\omega_c}{2\varepsilon_0 V}}\left(\hat{a}+\hat{a}^\dagger\right)\vec{\varepsilon}. \tag{2.8}$$

On substituting the expressions for $\hat{\vec{d}}$ and $\hat{\vec{E}}$ from Eqs. (2.4) and (2.8), into Eq. (2.3), we obtain the emitter-photon interaction Hamiltonian that reads

$$\hat{H}_{\text{int}} = g\left(\hat{a}^\dagger\hat{\sigma}^- + \hat{a}\hat{\sigma}^+ + \hat{a}^\dagger\hat{\sigma}^+ + \hat{a}\hat{\sigma}^-\right), \tag{2.9}$$

where g is the coupling constant that is defined as

$$g = -\sqrt{\frac{\hbar\omega_c}{2\varepsilon_0 V}}\vec{d}_{eg}.\vec{\varepsilon}. \tag{2.10}$$

Equation (2.9) is the quantum Rabi Hamiltonian [74, 75, 76], which describes the emitter-field interaction.

In order to understand the conserved quantities related to the interaction between an emitter and a single-mode cavity, as described by the emitter-photon interaction Hamiltonian $\hat{H}_{\text{int}}$, we need to introduce two operators. The first is the total excitation number operator $\hat{N}_{\text{ex}}^{(1)}$, which can be expressed as [76]:

$$\hat{N}_{\text{ex}}^{(1)} = \hat{\sigma}^+\hat{\sigma}^- + \hat{a}^\dagger\hat{a}. \tag{2.11}$$

The second operator is the parity operator $\hat{P}$, which is given by [76]:

$$\hat{P} = -\sigma_z(-1)^{\hat{a}^\dagger\hat{a}}. \tag{2.12}$$

Our analysis reveals that when considering the Hamiltonian described in Eq. (2.9), the commutator of $\hat{H}_{\text{int}}$ and $\hat{N}_{\text{ex}}^{(1)}$ is non-zero, i.e., $[\hat{H}_{\text{int}}, \hat{N}_{\text{ex}}^{(1)}] \neq 0$. It implies that $\hat{H}_{\text{int}}$ does not conserve the total number of excitations. However, the parity of the system remains conserved due to the fact that the commutator of $\hat{H}_{\text{int}}$ and $\hat{P}$ is zero, i.e., $[\hat{H}_{\text{int}}, \hat{P}] = 0$, and $\hat{H}_{\text{int}}$ does not have an explicit time dependence [76].

In our work, we focus on a specific scenario characterized by significantly higher energies associated with both the single-mode cavity and the emitter compared to the strength of the emitter-photon coupling. In other words, we consider the case where the values of g are much smaller than $\hbar\omega_e$ and $\hbar\omega_c$, i.e., $g \ll \hbar\omega_e, \hbar\omega_c$. This particular condition is commonly referred to as the weak coupling regime [71, 72]. This regime enables us to make the rotating wave approximation to Eq. (2.9). In order to understand the details of the rotating wave approximation [71, 72], we move to the interaction picture. In this picture, the emitter-field coupling term in the quantum Rabi Hamiltonian can be obtained from the following transformation

$$\hat{H}_{\text{int, I}}(t) = \hat{U}^{\dagger}(t)\hat{H}_{\text{int}}\hat{U}(t), \tag{2.13}$$

where

$$\hat{U}(t) = \exp\left[\imath\frac{\hat{H}_{\text{TLS}} + \hat{H}_{\text{cav}}}{\hbar}t\right]. \tag{2.14}$$

In the interaction picture, the emitter and the photonic operators can be written as

$$\hat{U}^{\dagger}(t)\hat{a}\hat{U}(t) = \exp(-\imath\omega_c t)\hat{a}, \tag{2.15}$$

$$\hat{U}^{\dagger}(t)\hat{a}^{\dagger}\hat{U}(t) = \exp(\imath\omega_c t)\hat{a}^{\dagger}, \tag{2.16}$$

$$\hat{U}^{\dagger}(t)\hat{\sigma}^{-}\hat{U}(t) = \exp(-\imath\omega_e t)\hat{\sigma}^{-}, \tag{2.17}$$

and

$$\hat{U}^{\dagger}(t)\hat{\sigma}^{+}\hat{U}(t) = \exp(\imath\omega_e t)\hat{\sigma}^{+}. \tag{2.18}$$

On inserting Eq. (2.9) into Eq. (2.13) and then using the results from Eqs. (2.15)-(2.18), we obtain

$$\begin{aligned}\hat{H}_{\text{int, I}}(t) = g\left[\exp\left(\imath(\omega_c - \omega_e)t\right)\hat{a}^{\dagger}\hat{\sigma}^{-} + \exp\left(-\imath(\omega_c - \omega_e)t\right)\hat{a}\hat{\sigma}^{+}\right] + \\ g\left[\exp\left(\imath(\omega_c + \omega_e)t\right)\hat{a}^{\dagger}\hat{\sigma}^{+} + \exp\left(-\imath(\omega_c + \omega_e)t\right)\hat{a}\hat{\sigma}^{-}\right].\end{aligned} \tag{2.19}$$

We make the assumption that the emitter is almost in resonance with the cavity mode, which means that $\omega_e \approx \omega_c$. When studying the time evolution of the system in the interaction

picture, we encounter the integral $\exp\left[-\frac{\imath}{\hbar}\int \hat{H}_{\text{int, I}}(t')dt'\right]$. Upon examining the expression for $\hat{H}_{\text{int, I}}(t)$, we observe that contributions from the term $g[\exp(\imath(\omega_c+\omega_e)t)\,\hat{a}^\dagger\hat{\sigma}^+ + \exp(-\imath(\omega_c+\omega_e)t)\,\hat{a}\hat{\sigma}^-]$ cancel out over time due to its rapid oscillations at the frequency $(\omega_c+\omega_e)$ with a very small amplitude. However, the term $g[\exp(\imath(\omega_c-\omega_e)t)\,\hat{a}^\dagger\hat{\sigma}^- + \exp(-\imath(\omega_c-\omega_e)t)\,\hat{a}\hat{\sigma}^+]$ exhibits much slower oscillations, thereby making it the dominant contribution to the time-dependent wavefunction in the interaction picture. Consequently, in the weak coupling regime, we can neglect the term with dependence on $(\omega_c+\omega_e)$ in Eq. (2.19). This leads to

$$\hat{H}_{\text{int, I}}(t) \approx g\left[\exp(\imath(\omega_c-\omega_e)t)\,\hat{a}^\dagger\hat{\sigma}^- + \exp(-\imath(\omega_c-\omega_e)t)\,\hat{a}\hat{\sigma}^+\right]. \tag{2.20}$$

On switching back to the Schrödinger picture, under the rotating wave approximation, the quantum Rabi Hamiltonian reduces to the Jaynes-Cummings Hamiltonian [72, 76]:

$$\hat{H}_{\text{int}} = g(\hat{a}^\dagger\hat{\sigma}^- + \hat{a}\hat{\sigma}^+). \tag{2.21}$$

We can generalize the formalism we have developed to study an emitter coupled to a cavity to N_e emitters in the presence of an array of N single-mode cavities [60, 61, 63, 105, 106]. The Hamiltonian describing the array of N single-mode cavities, denoted by $\hat{H}_{\text{cavity-array}}$, can be expressed as:

$$\hat{H}_{\text{cavity-array}} = \hbar\omega_c \sum_{n=1}^{N} \hat{a}_n^\dagger \hat{a}_n, \tag{2.22}$$

where $\hat{a}_n^\dagger$ represents the creation operator for photons at the n^{th} cavity, while $\hat{a}_n$ denotes the annihilation operator for photons at the n^{th} cavity. The emitter-photon interaction Hamiltonian $\hat{H}_{\text{int}}$ given in Eq. (2.21) is also extended to include N_e emitters in the presence of an array of N cavities. The Hamiltonian in this case is denoted by $\hat{H}_{\text{emitter-photon}}$ and can be expressed as:

$$\hat{H}_{\text{emitter-photon}} = g\sum_{i=1}^{N_e}(\hat{a}_{n_i}^\dagger\hat{\sigma}_{n_i}^- + \hat{a}_{n_i}\hat{\sigma}_{n_i}^+), \tag{2.23}$$

where n_i denotes the position of the i^{th} emitter in the cavity array. In the same spirit, we

generalize the bare emitter Hamiltonian $\hat{H}_{\text{TLS}}$ given in Eq. (2.1) to the case with N_e emitters

$$H_{\text{emitter}} = \frac{\hbar\omega_e}{2}\sum_{j=1}^{N_e}\left(\hat{\sigma}_j^z + \hat{I}_j\right). \tag{2.24}$$

This thesis will focus on three scenarios, namely, when the number of emitters is one ($N_e = 1$), when it is two ($N_e = 2$), and when it is much greater than one ($N_e \gg 1$), all within the one- and two-excitation manifolds.

For N_e emitters and N cavities, we can define a generalized operator for the total number of excitations $\hat{N}_{\text{ex}}$ as [60, 61, 63]

$$\hat{N}_{\text{ex}} = \sum_{i=1}^{N_e}\hat{\sigma}_i^+\hat{\sigma}_i^- + \sum_{n=1}^{N}\hat{a}_n^\dagger\hat{a}_n. \tag{2.25}$$

Similar to the case where a two-level system is coupled to a cavity, we find that the total number of excitations is conserved for the case of multiple emitters coupled to an array of cavities in the weak coupling limit since $[\hat{H}_{\text{emitter-photon}}, \hat{N}_{\text{ex}}] = 0$ [60, 61, 63]. Thus, we can work in different excitation number manifold separately as they are decoupled. The upcoming section provides an overview of the structured photonic environment.

2.2 Structured photonic environment

The study of bath engineering is a highly fascinating topic when it comes to investigating light-matter interaction [77, 78]. It allows for the manipulation of important properties like band structure of a given environment, thus providing control over the entities coupled to the bath. Specifically, in the realm of photonic bath, it is possible to modify the dispersion relation so that it deviates from a linear or quadratic form and instead takes on a cosine form [105, 106]. In this thesis, a structured or non-trivial photonic environment refers to a scenario where the dispersion relation does not follow a linear or quadratic form. An array of coupled cavities belongs to the classification of structured photonic environments. Our research involves the presence of a Kerr-like non-linearity in the structured photonic

environment, which results in a more complex mode structure for the photonic environment. The structured photonic environment in our research can be represented using the Bose-Hubbard Hamiltonian for photons [59, 60, 61, 63, 106]. This Hamiltonian can be written as:

$$\hat{H}_{\text{photon}} = \hbar\omega_c \sum_{n=1}^{N} \hat{a}_n^\dagger \hat{a}_n - J \sum_{n=1}^{N} \left(\hat{a}_n^\dagger \hat{a}_{n+1} + \hat{a}_{n+1}^\dagger \hat{a}_n \right) + \frac{U}{2} \sum_{n=1}^{N} \hat{a}_n^\dagger \hat{a}_n^\dagger \hat{a}_n \hat{a}_n, \tag{2.26}$$

where U is the onsite interaction between two photons, J is the photon hopping amplitude between two nearest neighboring cavities, N is the number of cavities, and n corresponds to the position index of the cavities in the array. The first term in Eq. (2.26) represents the energy related to the single-mode characteristic of the cavities (as shown in Eq. (2.22)). The second term corresponds to the phenomenon of photon hopping between adjacent sites within the cavity array, where a photon is created at site n and annihilated at site $n+1$, and vice versa. This hopping process, as described by the second term, results in the coupling between neighboring cavities in the array, hence the term "coupled" cavity array. The third term accounts for the interaction between two photons that occur at the same site.

In our study, we adopt periodic boundary conditions. Figure 2.1 illustrates a ring of N cavities, which is equivalent to an array of cavities subject to periodic boundary conditions. The periodic boundary condition plays a crucial role when considering the second term in Eq. (2.26), as it accounts for the hopping between the last cavity and the first cavity, which are positioned adjacent to each other due to the periodic boundary conditions. In terms of the photonic operators, $\hat{a}_{N+1}^\dagger$ and $\hat{a}_{N+1}$ can be regarded as being equivalent to $\hat{a}_1^\dagger$ and $\hat{a}_1$, respectively, in a ring of cavities.

The key feature of our work is the presence of Kerr-like non-linearity in the structured photonic environment that appears in the form of the on-site interaction U in the Bose-Hubbard Hamiltonian [60, 61, 63, 106]. Without this on-site interaction, the remaining components of Eq. (2.26) represent the tight-binding Hamiltonian [105]. The tight-binding Hamiltonian solely accounts for the hopping of photons within the cavity array and does

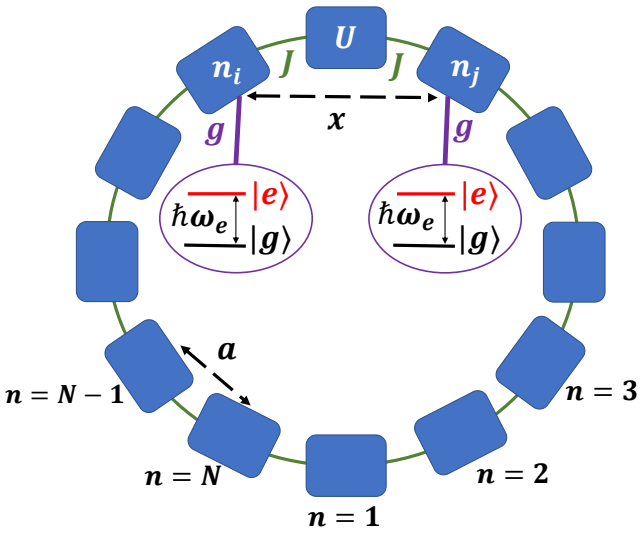

Figure 2.1: Illustration of the system being investigated: A collection of quantum emitters coupled to a structured photonic environment. The structured photonic environment consists of an array of N cavities arranged in a circular ring, where each cavity is represented by a blue box. The ring configuration enforces periodic boundary conditions, meaning that the first cavity ($n = 1$) is positioned adjacent to the last cavity ($n = N$). The green lines labeled with J depict the photon hopping strength between neighboring cavities, which are separated by a distance denoted by a. Within each cavity, there exists an on-site interaction denoted by U, which characterizes the effective interaction between photons in the same cavity. The quantum emitters are shown as two two-level systems with energy levels $|g\rangle$ and $|e\rangle$, possessing an energy separation of $\hbar\omega_e$. These emitters are coupled to the cavities labeled as n_i and n_j such that $|n_i - n_j| = x/a$, with a coupling strength denoted by g.

not consider any interaction between photons. On the other hand, the Bose-Hubbard Hamiltonian considers both the hopping of photons in the cavity array and the interaction between two photons when they occupy the same site. The sign of U determines the type of photon-photon interaction, with positive U leading to repulsive interactions and

negative U to attractive ones [125]. In our work, we consider attractive onsite photon-photon interaction, i.e., $U < 0$ [60, 61, 63]. The impact of the Kerr-like non-linearity is apparent when considering two or more than two photons in the emitter-photon system. We can express the U-dependent term as $\frac{U}{2}\sum_{n=1}^{N}\hat{\eta}_n\,(\hat{\eta}_n - 1)$, where $\hat{\eta}_n = \hat{a}_n^{\dagger}\hat{a}_n$ is the photon number operator at site n in the cavity array. Although we focus on the two-excitation manifold, the single-photon excitation manifold is also essential in determining the properties of the system. Hence, we begin with a discussion of the one-excitation manifold.

2.3 One-excitation manifold

In the one-excitation manifold, as the name suggests, the total number of emitter and photonic excitations is one, i.e., $\langle \hat{N}_{ex} \rangle = 1$. In this manifold, U (onsite interaction term) plays no role in the Hamiltonian that describes the structured photonic environment. In the reduced Hilbert space of one-excitation, the photonic bath Hamiltonian $\hat{H}^{(1)}_{\text{photon}}$ can be written in the single-photon momentum basis $|k\rangle$ as

$$\hat{H}^{(1)}_{\text{photon}} = \sum_{k} E_{k,1}\hat{a}_k^{\dagger}\hat{a}_k, \tag{2.27}$$

where $\hat{a}_k^{\dagger}$ is related to $|k\rangle$ as $\hat{a}_k^{\dagger}|\text{vac}\rangle = |k\rangle$. The photonic operators $\hat{a}_k$ and $\hat{a}_k^{\dagger}$ in the momentum space are related to the operators $\hat{a}_n$ and $\hat{a}_n^{\dagger}$, respectively, in the position space through a discrete Fourier transformation [105, 106]:

$$\hat{a}_k = \frac{1}{\sqrt{N}}\sum_{n=1}^{N}\exp(\imath kna)\hat{a}_n. \tag{2.28}$$

and

$$\hat{a}_k^{\dagger} = \frac{1}{\sqrt{N}}\sum_{n=1}^{N}\exp(-\imath kna)\hat{a}_n^{\dagger}, \tag{2.29}$$

where a denotes the cavity array spacing and N denotes the number of cavities in the array. The energy of a single-photon $E_{k,1}$ with momentum k appears in Eq. (2.27) and it is given by [105]

$$E_{k,1} = \hbar\omega_c - 2J\cos(ka). \tag{2.30}$$

Figure 2.2 shows the single photon energy as a function of the momentum k. We see that the energy is shifted in such a way that the zero of the energy is at $k = 0$. The single photon band has a width of $4J$. Since we are working in a discretized space, the single-photon momentum k also takes discretized values k_j that read

$$k_j = -\pi/a + \frac{2\pi}{Na}(j-1), \tag{2.31}$$

where $j = 1, 2, 3, \cdots, N$. In our discussion, we drop the subscript j in describing the single-photon momentum. An important point worth mentioning is that $\sum_k$ refers to $\sum_{k=-\pi/a}^{\pi/a}$, i.e., a sum over the first Brillouin zone.

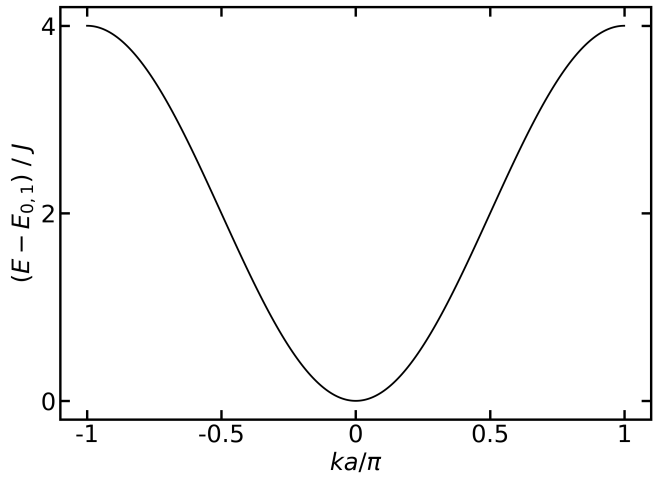

Figure 2.2: Single-photon energy spectrum as a function of the scaled momentum ka/π. The energy shown here is shifted in such a way that the $k = 0$ single-photon state has zero energy.

Using the momentum space representation of the photonic modes from Eqs. (2.28)-(2.29), the emitter-photon Hamiltonian given in Eq. (2.23) can expressed as

$$\hat{H}_{\text{emitter-photon}} = \frac{g}{\sqrt{N}} \sum_{j=1}^{N_e} \sum_{k} \left[\exp\left(\imath k n_j a\right) \hat{a}_k^\dagger \hat{\sigma}_{n_j}^- + \exp\left(-\imath k n_j a\right) \hat{a}_k \hat{\sigma}_{n_j}^+ \right]. \tag{2.32}$$

Thus, in the one-excitation manifold, the total Hamiltonian denoted by $\hat{H}_1$ is defined as

$$\hat{H}_1 = \hat{H}_{\text{emitter}} + \hat{H}^{(1)}_{\text{photon}} + \hat{H}_{\text{emitter-photon}}. \tag{2.33}$$

Plugging the expressions for $\hat{H}_{\text{emitter}}$, $\hat{H}^{(1)}_{\text{photon}}$, and $\hat{H}_{\text{emitter-photon}}$ from Eqs. (2.24), (2.27), and (2.32), respectively, into Eq. (2.33), we obtain

$$\hat{H}_1 = \frac{\hbar\omega_e}{2}\sum_{j=1}^{N_e}\left(\hat{\sigma}^z_j + I_j\right) + \sum_k E_{k,1}\hat{a}^\dagger_k\hat{a}_k + \\ \frac{g}{\sqrt{N}}\sum_{j=1}^{N_e}\sum_k\left[\exp\left(\imath k n_j a\right)\hat{a}^\dagger_k\hat{\sigma}^-_{n_j} + \exp\left(-\imath k n_j a\right)\hat{a}_k\hat{\sigma}^+_{n_j}\right]. \tag{2.34}$$

We solve the time-dependent Schrödinger equation

$$\imath\hbar\frac{d}{dt}\left|\psi_1(t)\right\rangle = \hat{H}_1\left|\psi_1(t)\right\rangle, \tag{2.35}$$

using the following wavefunction ansatz

$$\left|\psi_1(t)\right\rangle = \exp(-\imath\omega_e t)\left[\sum_{j=1}^{N_e} d_j(t)\sigma^+_j\left|g,\cdots,g,\text{vac}\right\rangle + \sum_k c_k(t)\hat{a}^\dagger_k\left|g,\cdots,g,\text{vac}\right\rangle\right]. \tag{2.36}$$

The ansatz in Eq. (2.36) is expressed in the single excitation basis elements: $\sigma^+_j\left|g,\cdots,g,\text{vac}\right\rangle$, i.e, an emitter at site j is excited and no photons are present, and $\hat{a}^\dagger_k\left|g,\cdots,g,\text{vac}\right\rangle$, i.e., all the emitters are in the ground state and there is one photon with momentum k. We solve for the coefficients $d_j(t)$ and $c_k(t)$ that govern the dynamics of the system. On substituting Eq. (2.36) into Eq. (2.35) and using the expression in Eq. (2.34), we get the following set of coupled differential equations

$$\imath\hbar\dot{d}_j(t) = \frac{g}{\sqrt{N}}\sum_k\exp\left(\imath k n_j a\right)c_k(t) \tag{2.37}$$

and

$$\imath\hbar\dot{c}_k(t) = \left[2J - \delta_1 - 2J\cos\left(ka\right)\right]c_k(t) + \frac{g}{\sqrt{N}}\sum_{j=1}^{N_e}\exp\left(-\imath k n_j a\right)d_j(t). \tag{2.38}$$

The energy parameter δ_1 is defined as

$$\delta_1 = \hbar\omega_e - (\hbar\omega_c - 2J), \tag{2.39}$$

which is the energy detuning of the emitter from the bottom of the single-photon energy band. The following two sections discuss the physics of the single-excitation manifold, with a focus on the number of emitters N_e and the energy detuning δ_1.

2.3.1 Single-emitter properties: $N_e = 1$

We investigate the behavior of the single-emitter system in the weak coupling regime, considering various values of energy detuning δ_1, by analyzing its time-independent as well as time-dependent characteristics. We diagonalize the Hamiltonian $\hat{H}_1$ given in Eq. (2.34)

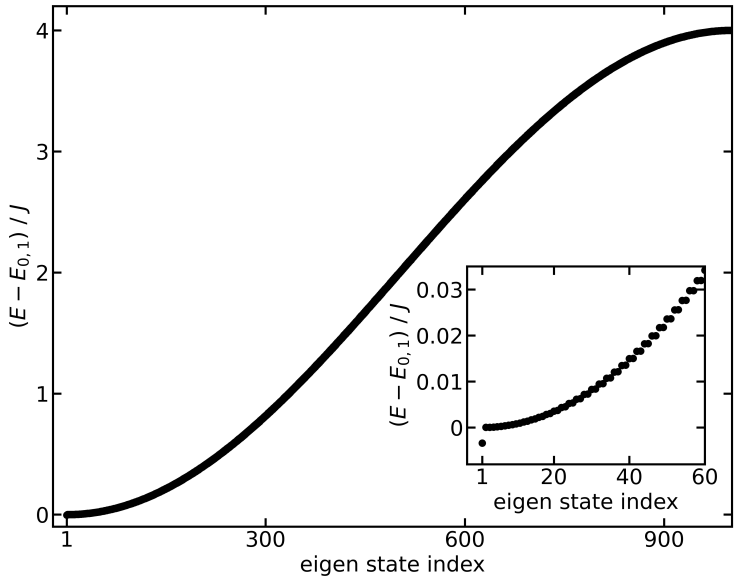

Figure 2.3: Eigenenergy of the Hamiltonian $\hat{H}_1$ for $N_e = 1$, $g/J = 0.02$, $\delta_1/J = 0$, and $N = 1001$ as a function of the eigenstate index. The energy is measured with respect to the bottom of the single-photon band, i.e., $E_{0,1}$. Inset: Blow-up of the lower part of the energy spectrum.

for $N_e = 1$ in the basis $|e, \text{vac}\rangle$ and $\hat{a}_k^\dagger |g, \text{vac}\rangle$, and obtain the eigenenergy and eigenstates. Due to the presence of the $\hat{H}_{\text{emitter-photon}}$ piece in the total Hamiltonian $\hat{H}_1$ given in Eq. (2.34), hybridization occurs between the emitter and photonic degrees of freedom and this leads

to the formation of intricate emitter-photon dressed states [105]. Figure 2.3 shows the eigenenergy of $\hat{H}_1$ as a function of eigenstate index for $g/J = 0.02$ and $\delta_1/J = 0$. Amongst these dressed states, there is an emitter-photon bound state that lies isolated below the continuum of eigenstates. A blow up of the energy spectrum is shown in the inset of Fig. 2.3, where one can see the state that lies below the bottom of a continuum of eigenstates.

We can express the wavefunction of the emitter-photon bound state as

$$|\psi_{\text{bound}}\rangle = b_e|e,\text{vac}\rangle + \sum_k b_k \hat{a}_k^\dagger |g,\text{vac}\rangle \tag{2.40}$$

where b_e is the coefficient of the emitter component $|e,\text{vac}\rangle$ and the b_k are the coefficients of the photonic components $\hat{a}_k^\dagger|g,\text{vac}\rangle$. We find that b_e and the b_k are real numbers. Figure 2.4 illustrates the dependence of b_e and b_k on the detuning δ_1/J for $g/J = 0.02$. In Fig. 2.4(a), b_e is shown as a function of δ_1/J. We see that as b_e is negative and that the magnitude of b_e increases with decreasing δ_1/J. It implies that the contribution of the emitter components $|b_e|^2$ in the emitter-photon bound state increases as δ_1/J becomes increasingly negative. In Fig. 2.4(b), the photonic component b_k is plotted as a function of the scaled single-photon momentum ka/π for $\delta_1/J = 0.01$ (solid black line), $\delta_1/J = 0.005$ (dotted blue line), $\delta_1/J = 0$ (dashed red line), $\delta_1/J = -0.005$ (dash dotted green line), and $\delta_1/J = -0.01$ (solid magenta line). We see that the distribution of b_k exhibits a peak at $k = 0$ with a decaying tail as the magnitude of k increases for all cases. Furthermore, as the value of δ_1/J becomes more negative, the peak value of b_k at $k = 0$ decreases, and the overall distribution becomes much broader in k. Specifically, the distribution of b_k exhibits the highest peak with a rapidly decaying tail for $\delta_1/J = 0.01$ (solid black line) and the smallest peak with a broader tail for $\delta_1/J = -0.01$ (solid magenta line). Overall, the distribution of b_k with respect to k closely resembles a Lorentzian distribution.

It is important to note that the emitter-photon bound state does not exist for all values of δ_1/J. It emerges only when the emitter energy lies around the band edge of the single-photon band. Figure 2.5 shows the energy of the bound state as a function of δ_1/J. As the

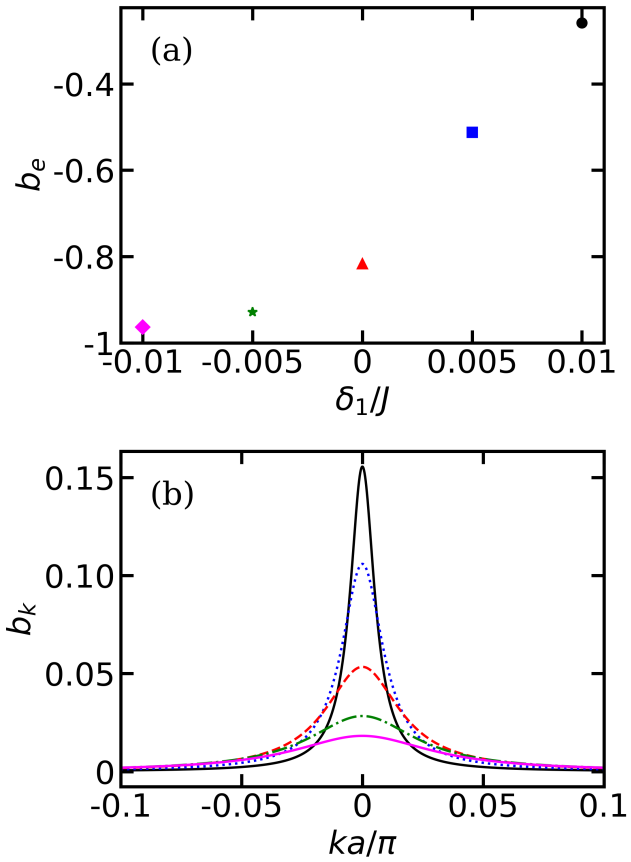

Figure 2.4: The emitter and photonic components in the emitter-photon bound states for $g/J = 0.02$. (a) Emitter component b_e is shown as a function of δ_1/J. (b) The photonic component b_k as a function of the scaled single-photon momentum ka/π for various δ_1/J. The solid black, dotted blue, dashed red, dash dotted green, and solid magenta lines are obtained for $\delta_1/J = 0.01, 0.005, 0, -0.005$, and -0.01, respectively.

δ_1/J decreases, the energy of the emitter-photon bound state decreases, i.e., it becomes energetically more separated from the continuum of emitter-photon eigenstates [105]. The continuum of emitter-photon eigenstates is primarily composed of photonic degrees of freedom. The energy and state properties of these states are similar to those of single-photon states of the non-interacting system, which leads to their radiative nature [105]. However,

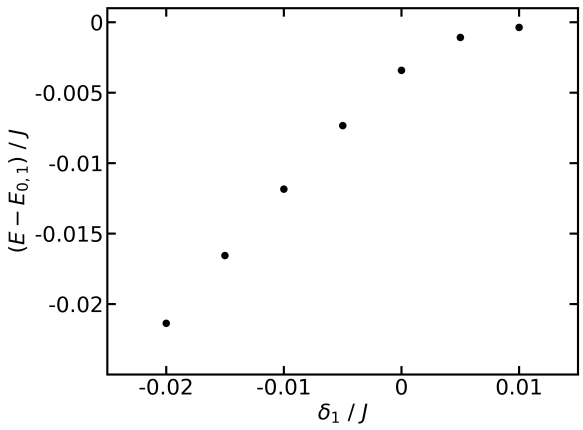

Figure 2.5: Energy of the emitter-photon bound state as a function of $\delta_1/J = 0$ for $g/J = 0.02$. Here, the energy is measured with respect to the lowest energy $E_{0,1}$ of the single-photon band.

the emitter-photon bound state exhibits a significant presence of the emitter component, rendering it non-radiative in nature [105].

To probe the emitter-photon bound states, it is crucial to examine the time-independent properties of the emitter-photon coupled system. For $N_e = 1$, the time-dependent wavefunction ansatz given in Eq. (2.36) takes the form

$$|\psi_1(t)\rangle = \exp(-\imath\omega_e t)\left[d_e(t)\,|e,\mathrm{vac}\rangle + \sum_k c_k(t)\hat{a}_k^\dagger\,|g,\mathrm{vac}\rangle\right]. \tag{2.41}$$

The system is initialized in the state $|e,\mathrm{vac}\rangle$, in which the emitter is in the excited state and there are no photons present. Figure 2.6 shows the population $|d_e(t)|^2$ of the state $|e,\mathrm{vac}\rangle$ as a function of time for $\delta_1/J = 0.2$ (dotted black line), $\delta_1/J = 0.005$ (dash-dotted green line), $\delta_1/J = 0$ (solid red line), and $\delta_1/J = -0.02$ (dashed blue line). It is obtained by propagating the initial state $|\psi_1(0)\rangle = |e,\mathrm{vac}\rangle$ under the Hamiltonian $\hat{H}_1$ for $N_e = 1$. The dotted black line corresponds to the case where the emitter transition energy is in resonance with the energy of a single-photon state with momentum k away from the bottom of the single-photon band. Exponential decay of the population can be seen in this case [168].

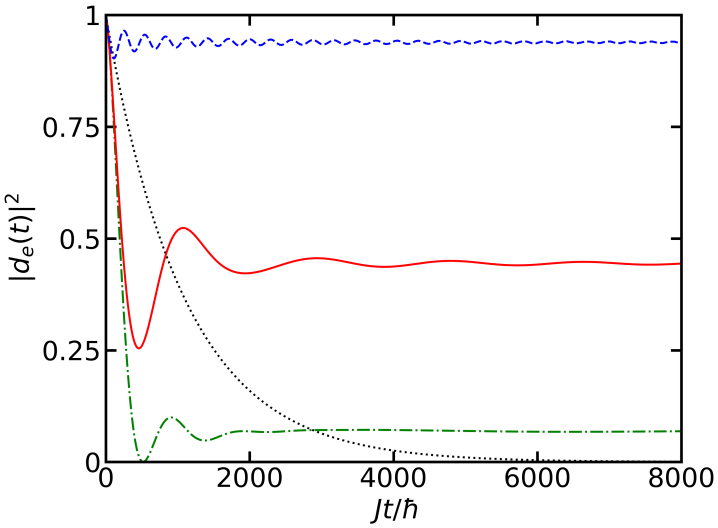

Figure 2.6: Radiation dynamics for the initial state $|\psi_1(0)\rangle = |e, \text{vac}\rangle$ for $g/J = 0.02$. The dotted black, dash-dotted green, solid red, and dashed blue shows the population $|d_e(t)|^2$ for $\delta_1/J = 0.2$, 0.005, 0, and -0.02 respectively.

Conversely, the cases where the emitter transition energies are in proximity to the band edge of the single-photon band, are shown by the dash-dotted green, solid red, and dashed blue lines. We see that the population of the $|e, \text{vac}\rangle$ does not show exponential decay and instead attains a constant value in the long time limit for $\delta_1/J = 0.005$, 0, and -0.02. More precisely, the behavior of $|d_e(t)|^2$ is characterized by a rapid initial decline, followed by damped oscillations, ultimately reaching a steady non-zero value. This pattern, where $|d_e(t)|^2$ maintains a constant non-zero value in the long-time limit, can be attributed to the hybridization of the emitter and photonic degrees of freedom [105, 107, 167].

We know that the initial state that we have considered, i.e, $|e, \text{vac}\rangle$ is not an eigenstate of the total Hamiltonian in Eq. (2.34). The initial state $|e, \text{vac}\rangle$ can be written as a linear combination of the non-radiative emitter-photon bound and radiative continuum of eigenstates. Figure 2.7 shows the decomposition of the initial state into the energy eigenstates $|\phi_E\rangle$ of the total Hamiltonian $\hat{H}_1$ for $g/J = 0.02$. In Fig. 2.7(a), square of the absolute

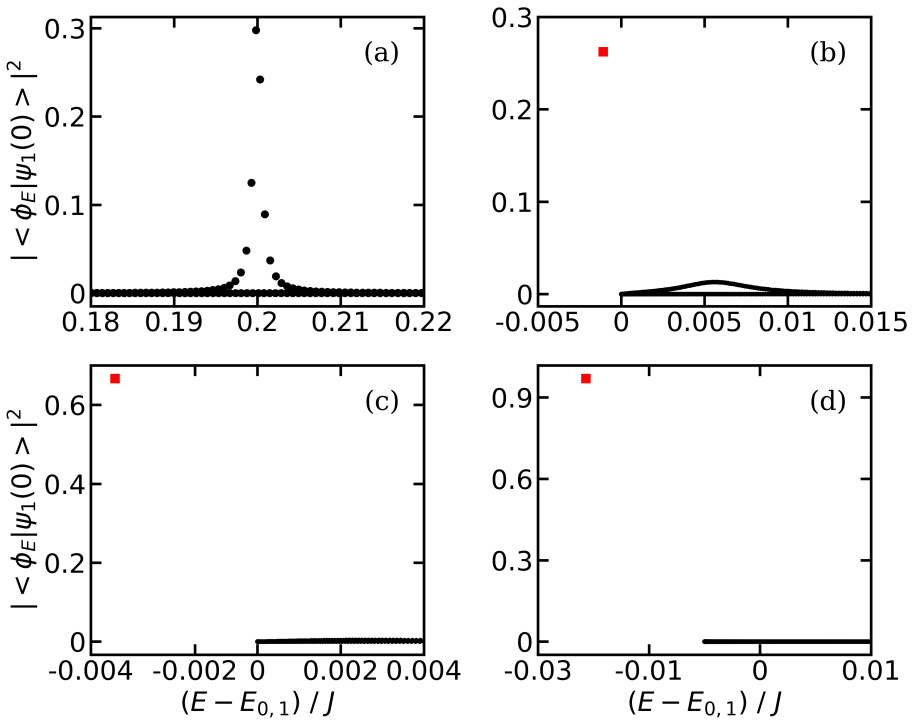

Figure 2.7: Square of the absolute value of the projection of the initial state $|\psi_1(0)\rangle$ onto the energy eigenstates $|\phi_E\rangle$ of the Hamiltonian $\hat{H}_1$ as a function of the eigenenergy E, measured relative to the bottom $E_{0,1}$ of the single-photon band, for $N_e = 1$ and $g/J = 0.02$. The energy detuning δ_1/J is set to (a) $\delta_1/J = 0.2$, (b) $\delta_1/J = 0.005$, (c) $\delta_1/J = 0$, and (d) $\delta_1/J = -0.02$. The red square corresponds to the largest value of $|\langle\phi_E|\psi_1(0)\rangle|^2$.

value of the projection of $|\psi_1(0)\rangle$ onto the energy eigenstates $|\phi_E\rangle$ of the Hamiltonian $\hat{H}_1$ is shown as a function of the shifted eigenenergy $E - E_{0,1}$ for $\delta_1/J = 0.2$. We can see that the emitter-photon eigenstates that lie inside the continuum of the interacting system dominate the contribution to the initial state. The dominating eigenstates are radiative in nature as they have negligible emitter component. This leads to complete decay of the population in $|e, \text{vac}\rangle$ to the photonic bath. Figure 2.7(b)-(d), show $|\langle\phi_E|\psi_1(0)\rangle|^2$ as a function of eigenenergy E of the Hamiltonian $\hat{H}_1$, measured relative to the bottom $E_{0,1}$ of the single-photon band, for $\delta_1/J = 0.005$, $\delta_1/J = 0$, and $\delta_1/J = -0.02$, respectively. We

see that the emitter-photon bound states (solid red square) dominates over the radiative emitter-photon eigenstates (solid black circle). Thus, radiative continuum of eigenstates can not dictate the dynamics for these cases and this leads to the population dynamics with non-exponential behavior [107, 167]. Furthermore, we see that the maximum value of $|\langle\phi_E|\psi_1(0)\rangle|^2$, which represents the contribution of the emitter-photon bound state, is larger in Fig. 2.7(d) compared to Fig. 2.7(c), and it is even greater than in Fig. 2.7(b). Thus, the contribution of the emitter-photon bound state towards the initial state $|e,\text{vac}\rangle$ increases as the value of the detuning δ_1/J decreases. It implies that the amount of population that will decay into the bath will decrease with decreasing δ_1/J.

During the time evolution of the system, intricate interference of the dressed states results in oscillatory behavior in the emitter population, with the oscillation frequency determined roughly by the energy difference between the two dominant emitter-photon dressed states. The amplitude of the oscillations in Fig. 2.6 decreases over time because the energy in the radiative dressed state component is lost into the photonic environment. Thus, the population in $|e,\text{vac}\rangle$ attains a constant value in the long time limit. This characteristics of the population dynamics is referred to as finite population trapping [107, 167]. Since the energy in the emitter-photon hybridized bound state that lies below the interacting radiative continuum does not decay into the photonic environment, finite population trapping is observed. This is also called fractional population behavior that is commonly observed near the band edge of the single-photon band [107, 167].

When the detuning parameter δ_1/J is negative, i.e., when the energy of the emitter is in the band gap region below the single-photon energy band, we observe that the population of the state $|e,\text{vac}\rangle$ does not exhibit any signs of decay or a significant fractional population. For example, in Fig. 2.6, the population $|d_e(t)|^2$ for $\delta_1/J = -0.02$ (blue dashed line) mostly stays in the state $|e,\text{vac}\rangle$. Only 10% of the population decays into the photonic bath. This can be explained by the fact that as δ_1/J becomes increasingly negative, the overlap between

the state $|e, \text{vac}\rangle$ and the emitter-photon bound state approaches 100%, causing minimal changes in the population over time. For example, in Fig. 2.7(d), we see that the emitter-photon bound state contributes approximately 97% to the initial state $|e, \text{vac}\rangle$ for $g/J = 0.02$ and $\delta_1/J = -0.02$. Moreover, the emitter-photon bound state contains negligible photonic fraction, i.e., it has dominant emitter component for $g/J = 0.02$ and $\delta_1/J = -0.02$.

In the next section, we increase the number of emitters to a value much greater than one ($N_e \gg 1$) and derive an effective spin Hamiltonian in the band gap regime ($\delta_1/J < 0$) by operating within the single excitation manifold.

2.3.2 Multi-emitter properties: $N_e \gg 1$

When working in the bandgap regime where $\delta_1/J < 0$, we observe that the influence of the single-photon modes is small: the photon mode occupations remain relatively unchanged over time, particularly when the emitter-photon coupling strength g/J is weak ($g/J \ll 1$). In this regime, we can adiabatically eliminate the single-photon states [174]. The necessary conditions for the applicability of this approximation can be summarized as follows: $g/J \ll 1$, $\delta_1/J < 0$, and $|\delta_1| > g$ [106, 174]. The adiabatic elimination of the single-photon modes starts by setting the right-hand side of Eq. (2.38) to zero. As a result, we obtain

$$c_k(t) = -\frac{g}{\sqrt{N}} \sum_{l=1}^{N_e} \frac{\exp(\imath k a n_l)}{2J - \delta_1 - 2J\cos(ka)} d_l(t) \tag{2.42}$$

Plugging the expression of $c_k(t)$ into Eq. (2.37), we obtain

$$\imath\hbar \dot{d}_j(t) = \sum_{l=1}^{N_e} W_{jl} d_l(t), \tag{2.43}$$

where $W_{jl} = -\frac{g^2}{N} \sum_k \frac{\exp\left(\imath k a \left(n_j - n_l\right)\right)}{2J - \delta_1 - 2J\cos(ka)}$. The evaluation of the sum is discussed in Appendix E. To write Eq. (2.43) in matrix form, we introduce the vector $\vec{d}$ through $\vec{d} = (d_1, d_2, \cdots, d_{N_e})^T$. The W-terms are then collected in the matrix $\mathbb{W}$ with elements $\mathbb{W}_{jl} = W_{jl}$. Consequently, Eq. (2.43) can be written as:

$$\imath\hbar \dot{\vec{d}} = \mathbb{W}\vec{d}. \tag{2.44}$$

Considering the basis of single excitations, denoted by $\left|g,\cdots,e_j,\cdots,g\right\rangle$, we compare Eq. (2.44) with the time-dependent Schrödinger equation for the effective Hamiltonian $\hat{H}_{\text{eff}}^{(1)}$, where the matrix form of the operator $\hat{H}_{\text{eff}}^{(1)}$ is equivalent to $\mathbb{W}$. In operator form, the effective Hamiltonian $\hat{H}_{\text{eff}}^{(1)}$ can be expressed as:

$$\hat{H}_{\text{eff}}^{(1)} = \sum_{i=1}^{N_e}\sum_{j=1}^{N_e} W_{ij}\hat{\sigma}_i^{+}\hat{\sigma}_j^{-}. \tag{2.45}$$

The effective spin Hamiltonian $\hat{H}_{\text{eff}}^{(1)}$ lives in the Hilbert space that is spanned by the emitter degrees of freedom (the photonic degrees of freedom have been removed) [174]. As we transition into the two-excitation manifold, the effective Hamiltonian $\hat{H}_{\text{eff}}^{(1)}$ undergoes modifications which is explained in Chapter 5. Furthermore, the presence of the Kerr-like non-linearity introduces a new kind of pair-pair interaction in the two-excitation manifold.

2.4 Two-excitation manifold

When considering a system with two excitations, the combined number of emitter and photonic excitations is two, i.e., $\langle\hat{N}_{\text{ex}}\rangle = 2$. There are three possible combinations of the emitter and photonic degrees of freedom in this scenario. Firstly, two of the emitters can be in excited states with no photons present in the environment. Secondly, one of the emitters can be excited while there is a photon in the environment. Lastly, there can be two photons in the environment with all emitters in their ground state. The energy associated with the second scenario can be calculated by adding the energy of an excited emitter to the energy of a single photon $E_{k,1}$ (given in Eq. (2.30)). Figure 2.8(a) depicts the total energy of an excited emitter and a single photon as a function of the scaled momentum ka/π for the single-photon state for $\hbar\omega_c/J = 20$ and $\hbar\omega_e/J = 17.6$. The black line in Fig. 2.8(a) is essentially equivalent to Fig. 2.2 if we account for the overall energy shifts.

When we move to the two-excitation manifold, the energy spectrum of the structured photonic environment becomes more intricate. The eigenstates of $\hat{H}_{\text{photon}}$ in this manifold

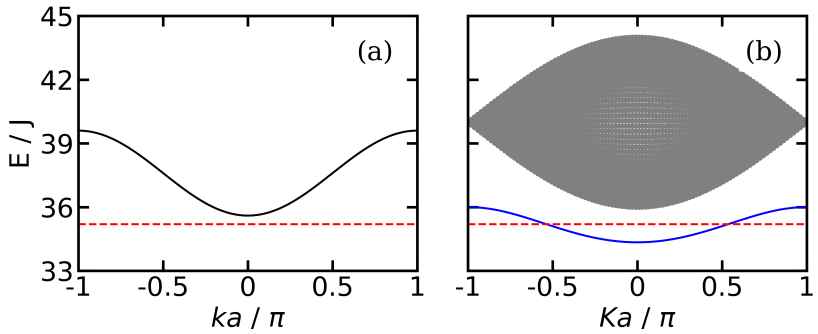

Figure 2.8: The band structures of our system in the two-excitation manifold for $\hbar\omega_c/J = 20$ and $\hbar\omega_e/J = 17.6$. (a) The solid black line shows the total energy of an excited emitter and a single photon as a function of the scaled single-photon momentum ka/π. This energy is obtained by adding $\hbar\omega_e$ to the single-photon energy given in Eq. (2.30). (b) The eigen spectrum of the two-photon system is shown as a function of the scaled center-of-mass momentum Ka/π. The solid blue line shows the energy of the two-photon bound state, $E_{K,b}$, which is given by Eq. (2.46), considering $U/J = -4$. The gray shaded area represents the two-photon scattering continuum. Both in (a) and (b), the dashed red line corresponds to the energy $2\hbar\omega_e$ associated with two excited emitters.

can be divided into two categories: photon-photon scattering states and two-photon bound states. A photon-photon scattering state is not bound and can occupy any available space in the cavity array. It differs from two non-interacting photons because its wavefunction experiences a phaseshift due to the interaction U (see Appendix E). The scattering states form a continuum, with the highest and lowest points determined by the minimum and maximum energy of two non-interacting photons, while keeping the center-of-mass momentum K constant. The gray shaded region in Fig. 2.8(b) corresponds to the scattering continuum of two photons for $\hbar\omega_c/J = 20$. The width of the continuum is due to the possibility of multiple relative momenta k between two photons for a fixed value of center-of-mass momentum K.

The energy of the two-photon bound state with center-of-mass momentum K lie below

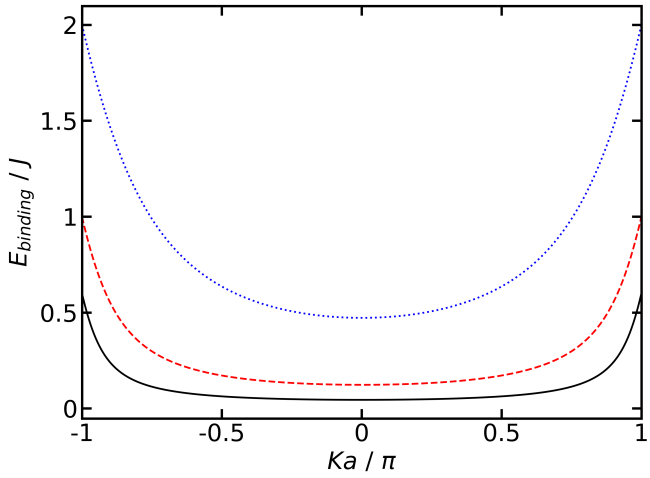

Figure 2.9: The dependence of the binding energy E_{binding}/J of a two-photon bound state on the scaled center-of-mass momentum Ka/π for different values of U/J. The solid black, the dashed red, and the dotted blue lines are obtained for $U/J = -0.6$, -1, and -2, respectively.

the two-photon scattering continuum for $U/J < 0$ and it is given by

$$E_{K,b} = 2\hbar\omega_c - \sqrt{U^2 + 16J^2\cos^2(Ka/2)}. \tag{2.46}$$

The solid blue line in Fig. 2.8(b) shows the energy of a two-photon bound state as a function of the scaled center-of-mass momentum Ka/π for $\hbar\omega_c/J = 20$ and $U/J = -4$. A two-photon bound state has a wavefunction that decays exponentially as the separation between the two photons increases in the cavity array.

The binding energy, denoted by E_{binding}, for a two-photon bound state with a fixed center-of-mass momentum K, is defined as the absolute difference between the energy of the bound state and the minimum energy of two non-interacting photons with the same center-of-mass momentum K. Mathematically, it can be expressed as (for details see Appendix E):

$$E_{\text{binding}} = |4J\cos(Ka/2) - \sqrt{U^2 + 16J^2\cos^2(Ka/2)}|. \tag{2.47}$$

Figure 2.9 illustrates how the binding energy E_{binding} varies with the center-of-mass momentum K for different values of U/J. The dotted blue line corresponds to $U/J = -0.6$, the

dashed red line represents $U/J = -1$, and the solid black line corresponds to $U/J = -2$. A consistent trend is observed in all cases. The two-photon bound state exhibits the lowest binding energy when the center-of-mass momentum is zero, while the state with a center-of-mass momentum of $\pm\pi/a$ displays the largest binding energy. For a fixed value of U, as the magnitude of center-of-mass momentum K increases, the binding energy also increases. Consequently, the wavefunction of the two-photon bound state becomes more localized, being broadest at $K = 0$ and narrowest at $Ka = \pi$. Additionally, we observe that as the U becomes more negative, for a given K, the binding energy increases, resulting in a two-photon bound state that occupies fewer cavity sites.

In our work, we capitalize on the non-trivial mode structure of the photonic bath by strategically choosing the energy of the two excited quantum emitters [60, 61, 63]. We ensure that the energy is either in resonance or off-resonance (in the bandgap below) with the two-photon bound states. Figure 2.8 provides an illustration of such parameter combinations. Specifically, we consider the values $U/J = -4$, $\hbar\omega_c/J = 20$, and $\hbar\omega_e/J = 17.6$, which satisfy the resonance condition mentioned earlier. In Fig. 2.8(b), we observe that the energy of two excited emitters (dashed red line), is in resonance with the band corresponding to the two-photon bound state (solid blue line). However, it is off-resonant with respect to the two-photon scattering continuum depicted by the gray shaded region. Additionally, Figure 2.8(a) demonstrates that in the two-excitation manifold, the single-photon modes are off-resonant as the energy associated with two excited emitters (dashed red line) lies below the total energy of the excited emitter and single-photon band (solid black line). In Chapters 3–5, we provide a comprehensive analysis of both time-dependent and time-independent characteristics of a collection of quantum emitters coupled to a structured photonic environment featuring onsite photon-photon interaction U in the two-excitation manifold.

2.5 Dissipative processes in a cavity array

In order to understand how our system could be realized experimentally, it is necessary to examine the dissipative processes that arise from both the emitter and the structured photonic environment. The emitters plus cavity array system contains two types of dissipative processes [105, 106]. The first is associated with the inherent lifetime T_0 of the excited state, of each emitter. The second relates to the cavity dissipation, which involves the loss of a photon from a cavity at a rate $\hbar^{-1}\kappa$. In other words, $\hbar\kappa^{-1}$ is the lifetime of a photon in a cavity. In our work, the energy of an excited emitter is set such that the energy of two excited emitters is in resonance with the two-photon bound state band [60, 61] or lies in the band gap region below the two-photon bound state band [63]. In both cases, the energy of an excited emitter is off-resonant with respect to the single-photon band where δ_1/J is always negative. Thus, single-photon radiative pathways are essentially suppressed. However, the emitter-photon coupled system supports an emitter-photon bound state in the one-excitation manifold with non-zero single-photon components. In the single-excitation manifold, the photonic component of the emitter-photon bound state combines with the life time of a single-photon to yield the timescale T_c [105, 106]. We assume that κ is smaller than the energy scales of the emitter-photon coupled system, i.e, $\kappa \ll |\delta_1|, g, J$. Under this approximation, the time scale T_c is given by $T_c^{-1} = \kappa\sum_k |b_k|^2$ [105, 106], where b_k is the coefficient of the photonic components in the emitter-photon bound state (see Eq. (2.40)). The total rate of dissipation for an excited emitter is given by $\Gamma_d \approx T_0^{-1} + T_c^{-1}$, which sets a limit on the characteristic time scale to observe crucial physical properties of the emitter-photon coupled system. Figure 2.10 shows the dependence of the photonic fraction $\sum_k |b_k|^2$ on δ_1/J for $g/J = 0.02$. We see that as the detuning δ_1/J becomes increasingly negative, the population of the photonic components in the emitter-photon bound state decreases. For the cases considered in Chapters 3–5, the photonic fraction $\sum_k |b_k|^2$ is less than 1.5% for $g/J = 0.02$ and δ_1/J ranging from -0.04 to -0.1365 [60, 61, 63]. Thus, the

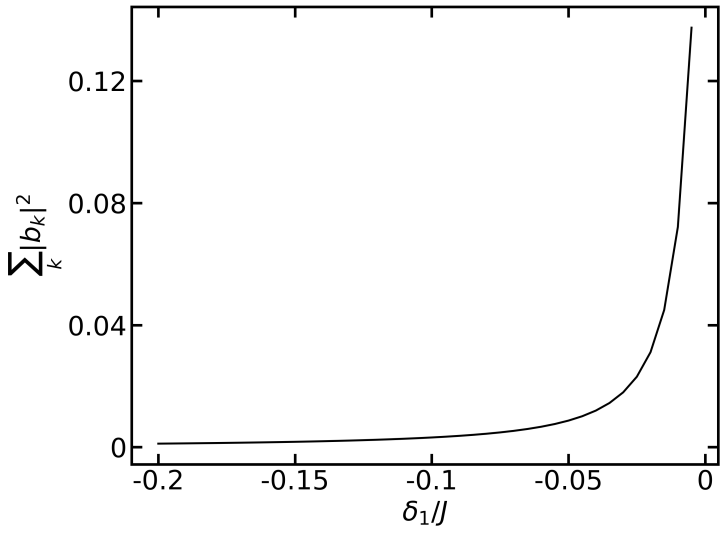

Figure 2.10: The photonic fraction $\sum_k |b_k|^2$ of the emitter-photon bound state as a function of δ_1/J for $g/J = 0.02$ and $N_e = 1$.

rate of single-photon loss is significantly reduced as we work in the two-excitation manifold. This implies that the time scale T_c that is associated with the cavity dissipation process increases compared to the case, where the transition energy of an emitter is in resonance with the single-photon band. This is crucial for the experimental implementation of the emitter-photon coupled system.

2.6 Experimental realization: Circuit QED platforms

The atom-optical framework investigated theoretically in this study can be implemented in the most up-to-date experimental setups [52, 53, 54, 55, 56, 57, 58]. However, there are limitations to the time scale of experiments due to dissipative processes. In our research, we were able to observe both radiative and non-radiative phenomena over a time scale of approximately $10^4 J/\hbar$ [60, 61, 63]. To achieve this time scale in experiments, the photon decay rate κ must be taken into account. For instance, in order to achieve a time scale of

$10^4 J/\hbar$, κ/J should be on the order of 10^{-2} or less.

From the experimental perspectives, we will briefly discuss recent advancements in light-matter interaction experiments utilizing the circuit QED platform. Circuit QED offers various benefits over cavity QED experimental setups, including much higher cooperativity and the ability to produce different Hamiltonian geometries due to advances in fabrication techniques, resulting in significant advancements in bath engineering [73].

To implement our system experimentally, we require quantum emitters, cavities, emitter-cavity coupling, and non-linearities within the cavity. These essential elements can be provided by superconducting circuits [79]. In the field of circuit QED, the quantization of oscillations in superconducting circuits effectively represents the role of photons. Superconducting circuits operate in the microwave frequency range, hence terminologies such as microwave cavities and microwave photons are commonly used. In the circuit QED setup, a superconducting qubit serves as a two-level system, and the microwave cavities are realized through transmission line resonators [73, 79]. The presence of Kerr-like non-linearity originates from the nonlinear behavior associated with Josephson junctions within the superconducting circuits [59].

The coupling between superconducting qubits and the array of resonators, in the absence of onsite photon-photon interaction, has been investigated experimentally, leading to the exploration of qubit-photon bound states [55, 57, 58]. Furthermore, experimental work has also been conducted on a relatively shorter array of microwave cavities (with $N = 3$) to study the effects of onsite photon-photon interaction [56]. Recent advancements have demonstrated the realization of the Bose-Hubbard model for photons in the regime where $|U|/J \gg 1$ [59]. However, our work focuses on the regime, where $|U|/J \approx 1$. It is anticipated that further experimental progress will be made regarding the exploration of the case, where the strength of the photon hopping amplitude J and the photon-photon onsite interaction U are comparable, i.e., $|U| \approx J$.

Chapter 3

Undamped Rabi oscillations due to polaron-emitter hybrid states in non-linear photonic wave guide coupled to emitters

by J. Talukdar[1, 2] and D. Blume[1, 2]

[1]Homer L. Dodge Department of Physics and Astronomy, The University of Oklahoma,
440 W. Brooks Street, Norman, Oklahoma 73019, USA

[2]Center for Quantum Research and Technology, The University of Oklahoma,
440 W. Brooks Street, Norman, Oklahoma 73019, USA

The collective dynamics of two non-interacting two-level emitters, which are coupled to a structured wave guide that supports two-photon bound states, is investigated. Tuning the energy of the two emitters such that they are in resonance with the two-photon bound state energy band, we identify parameter regimes where the system displays fractional populations and essentially undamped Rabi oscillations. The Rabi oscillations, which have no analog in the single-emitter dynamics, are attributed to the existence of a collective polaron-like photonic state that is induced by the emitter-photon coupling. The full dynamics is reproduced by a two-state model, in which the photonic polaron interacts with the state $|e,e,\text{vac}\rangle$ (two emitters in their excited state and empty wave guide) through a Rabi coupling frequency that depends on the emitter separation. Our work demonstrates that emitter-photon coupling can lead to an all-to-all momentum space interaction between two-photon bound states and tunable non-Markovian dynamics, opening up a new direction for emitter arrays coupled to a waveguide.

3.1 Undamped Rabi oscillations due to polaron-emitter hybrid states in non-linear photonic wave guide coupled to emitters

Multi-level emitters coupled to a radiation field in a periodic structure are essential for delivering on the promises surrounding the second quantum revolution. Ongoing research is exploring a variety of platforms, including nano-photonic lattices [80, 81, 82, 83, 84], plasmonic wave guides [85], and superconducting resonator arrays [86, 87] coupled to atoms [88, 89, 90], quantum dots [182], quantum solid-state defects [92, 93], or superconducting qubits [47, 94, 95, 96, 57]. Applications range from quantum information processing to quantum networking to quantum simulations [97, 98, 99, 100, 101, 102, 175]. Recent experimental milestones include the heralded creation of a single collective excitation in a chain of atoms coupled to a waveguide [103] and the demonstration of photon (anti-) bunching for weak atom-photon coupling by taking advantage of dissipation [104]. Emitters coupled to a wave guide also constitute a promising platform with which to study fundamental questions associated with open quantum systems, with the emitters playing the role of the system and the wave guide or electromagnetic modes playing the role of the bath [105, 106, 107, 108, 109, 110].

Building on the tremendous successes of cavity quantum electrodynamics (QED), wave guide QED plays a key role in a plethora of quantum technologies [59, 111]. The coupling of one or more excited multi-level emitters to a continuum of electromagnetic modes leads, in most cases, to irreversible correlated radiation dynamics [44, 112]. Quite generally, the strong transverse confinement in a waveguide speeds up the radiation dynamics compared to the free case [113]. Moreover, the directionality of a one-dimensional waveguide facilitates the build-up of correlations (or anti-correlations) between emitters that are separated by distances larger than the natural wave length of the wave guide leading to superradiance, subradiance, and entanglement generation [114, 14, 115, 116, 117, 118, 119, 15, 120, 50, 121]. The emergence of these characteristics can be explained in terms of constructive

and destructive interferences. This work predicts long-lived oscillatory radiation dynamics for a generic waveguide QED set-up that can be realized experimentally with existing state-of-the-art technology. The oscillatory radiation dynamics is distinct from the typically observed irreversible correlated radiation dynamics.

We consider a structured or non-trivial bath, namely a wave guide with non-linearity that supports a band of two-photon bound states (or more generally, a band of bound bath quantum pairs) [106]. Working in the quantum regime, where the system contains just two excitations, the influence of the non-trivial mode structure of the bath on the radiation dynamics is investigated within a full quantum mechanical framework. Non-Markovian dynamics is observed. Rather counterintuitively, a regime is identified where the radiation dynamics is described nearly perfectly by a two-state Rabi model. An analytical framework that elucidates the underlying physical mechanism is developed. It is shown that two emitters separated by multiple lattice sites are, in certain parameter regimes, glued together and coupled to a wave guide with all-to-all momentum space interactions. It is as if the band of two-photon bound states was feeling a localized (in real space) impurity that leads to the formation of a photonic polaron-like state with which the two-emitter unit interacts, creating hybridized symmetric and anti-symmetric states that exchange population, undergoing essentially undamped Rabi oscillations.

Figure 3.1(a) illustrates the set-up. The total Hamiltonian $\hat{H}$ consists of the system, tight-binding bath or wave guide, and system-bath Hamiltonians $\hat{H}_s$, $\hat{H}_b$, and $\hat{H}_{sb}$ [106],

$$\hat{H}_s = \frac{\hbar\omega_e}{2}\sum_{j=1}^{N_e}(\hat{\sigma}_j^z + \hat{I}_j), \tag{3.1}$$

$$\hat{H}_b = \hbar\omega_c\sum_{n=1}^{N}\hat{a}_n^\dagger\hat{a}_n - J\sum_{n=1}^{N}\left(\hat{a}_n^\dagger\hat{a}_{n+1} + \hat{a}_{n+1}^\dagger\hat{a}_n\right) + \frac{U}{2}\sum_{n=1}^{N}\hat{a}_n^\dagger\hat{a}_n^\dagger\hat{a}_n\hat{a}_n, \tag{3.2}$$

and

$$\hat{H}_{sb} = g\sum_{j=1}^{N_e}\left(\hat{a}_{n_j}\hat{\sigma}_j^+ + \hat{a}_{n_j}^\dagger\hat{\sigma}_j^-\right), \tag{3.3}$$

where $\hbar\omega_e$, $\hbar\omega_c$, J, and U denote the energy difference of the excited and ground state of the emitter, the photon energy in the middle of the single-photon band, the hopping energy, and the engineered or intrinsic onsite energy, respectively. Since the coupling energy g is small compared to $|U|$ and J, counterrotating terms are not included in $\hat{H}_{sb}$; throughout, positive g and J and negative U are considered (positive U yield the same results). The emitter operators $\hat{\sigma}_j^z = |e\rangle_j\langle e| - |g\rangle_j\langle g|$, $\hat{I}_j = |e\rangle_j\langle e| + |g\rangle_j\langle g|$, $\hat{\sigma}_j^+ = |e\rangle_j\langle g|$, and $\hat{\sigma}_j^- = |g\rangle_j\langle e|$ act on the jth emitter located at lattice site n_j with ground and excited states $|g\rangle_j$ and $|e\rangle_j$. The bath operators $\hat{a}_{n_j}^\dagger$ and $\hat{a}_{n_j}$ create and destroy a photon at lattice site n_j ($j = 1, \cdots, N_e$ and $n_j \in 1, \cdots, N$). Throughout, we consider $N_e = 2$ emitters with separation x, $x = n_1 - n_2$, and large number of lattice sites N. The bath Hamiltonian $\hat{H}_b$ supports, due to the Kerr-like nonlinearity U, a band of two-photon bound states, one bound state with energy $E_{K,b}$ for each two-photon center-of-mass wave vector K [123, 124, 125, 126]. Throughout, the emitter energy is tuned such that $2\hbar\omega_e$ is equal to $E_{K^{(0)},b}$ at the uncoupled resonance wave vector $K^{(0)}$. Since we are interested in the two-excitation subspace with $K^{(0)}a$ close to zero, the detuning δ is measured from the bottom of the two-photon bound state band, $\delta = 2\hbar\omega_e - 2\hbar\omega_c + \sqrt{U^2 + 16J^2}$.

To describe the time evolution of the initial state $|e, e, \text{vac}\rangle$, we expand the time-dependent wave packet $|\Psi(t)\rangle$ as [106]

$$\begin{aligned} |\Psi(t)\rangle = \quad & \exp(-2\imath\omega_e t)\Big[c_{ee}|e,e,\text{vac}\rangle + \sum_K c_{K,b}|g,g,K\rangle \\ & + \sum_k c_{1k}|e,g,k\rangle + \sum_k c_{2k}|g,e,k\rangle\Big], \end{aligned} \tag{3.4}$$

where $c_{ee}(t)$, $c_{K,b}(t)$, $c_{1k}(t)$, and $c_{2k}(t)$ denote expansion coefficients, and $|k\rangle = \hat{a}_k^\dagger|\text{vac}\rangle$ and $|K\rangle = \hat{P}_{K,b}^\dagger|\text{vac}\rangle$ single-photon states with wave vector k and photon-pair states with center-of-mass wave vector K, respectively. The operators $\hat{a}_k^\dagger$ and $\hat{a}_n^\dagger$ are related via a Fourier transform. Our ansatz does not account for the two-photon scattering continuum since it plays a negligible role for the parameter combinations considered in this paper [122].

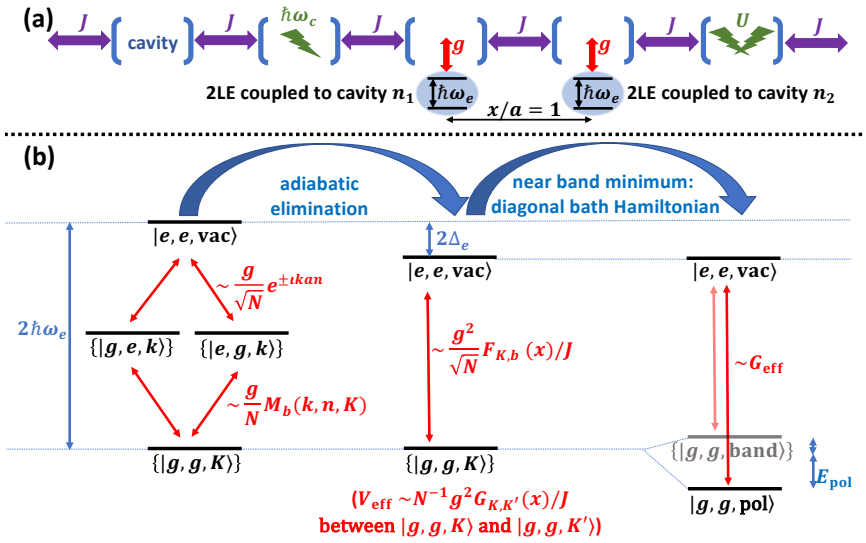

Figure 3.1: (a) Schematic of the Hamiltonian $\hat{H}$. The cavity array and two-level emitters (2LE) are shown; the role of the different energy terms is illustrated. (b) Illustration of the Hilbert space structure of $\hat{H}$ (left), $\hat{H}^{\text{adia}}$ (middle), and $\hat{H}^{\text{2-st.}}$ (right). The matrix element $M_b(k,n,K)$ is defined in Ref. [127].

The solid lines in the left column of Fig. 3.2 show the population $|c_{ee}(t)|^2$ of the state $|e,e,\text{vac}\rangle$ as a function of time for $U/J = -1$, $g/J = 1/50$, $\delta/J = 0.0431$, and $x/a = 0$, 5, and 10, obtained by propagating the ansatz given in Eq. (3.4) using $\hat{H}$. For this detuning, $|c_{ee}(t)|^2$ decreases approximately exponentially. This is the Markovian regime, discussed in Ref. [106], where propagation with the adiabatic Hamiltonian $\hat{H}^{\text{adia}}$ yields quite accurate results (dotted, dashed, and dash-dash-dotted lines show results for three different variants of $\hat{H}^{\text{adia}}$). The adiabatic Hamiltonian $\hat{H}^{\text{adia}}$, which lives in a reduced Hilbert space that excludes

the single-photon states $|e,g,k\rangle$ and $|g,e,k\rangle$, is introduced below [middle of Fig. 3.1(b)]. The inset of Fig. 3.2(c) for $x/a = 10$ shows that the short-time behavior of $|c_{ee}(t)|^2$ deviates from a pure exponential decay. This is due to the fact that the dynamics is, for $x/a \gg 1$, seeded by the creation of two uncorrelated photons. For larger times, the fall-off is, as for smaller separations, again governed by correlated two-photon dynamics.

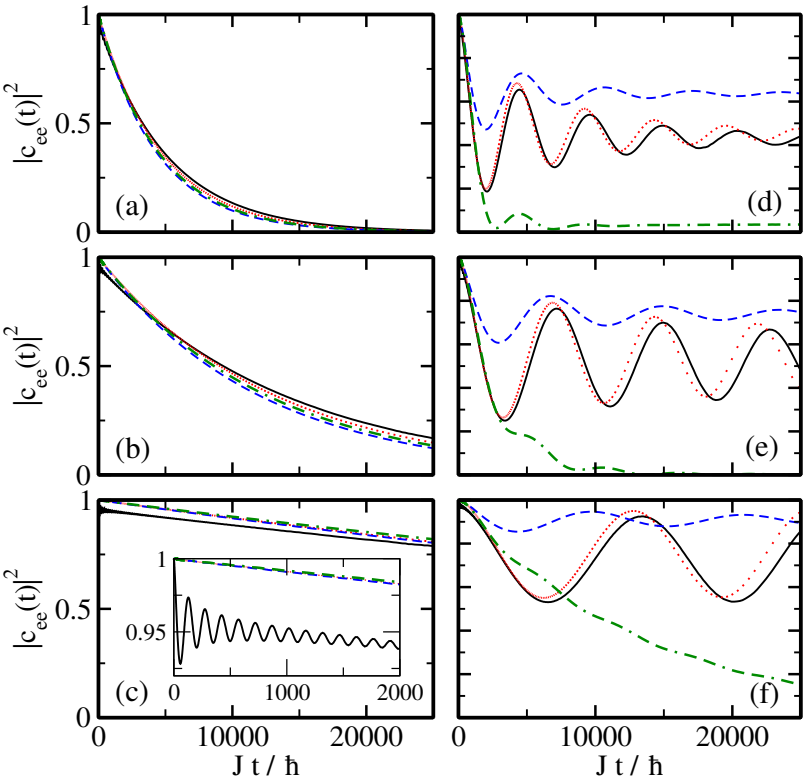

Figure 3.2: $|c_{ee}(t)|^2$ as a function of $Jt/\hbar$ for the initial state $|e,e,\text{vac}\rangle$, $U/J = -1$, $g/J = 1/50$, and $\delta/J = 0.0431$ (left) and $\delta/J = 0.0011$ (right). Top, middle, and bottom rows are for $x/a = 0$, 5, and 10, respectively. Black solid, red dotted, blue dashed, and green dash-dash-dotted lines are obtained using $\hat{H}$, $\hat{H}^{\text{adia}}$, $\hat{H}^{\text{adia}}$ with $G_{K,K'} = 0$, and $\hat{H}^{\text{adia}}$ with $G_{K,K'} = \Delta_e = 0$, respectively.

When the emitter energy is set such that δ is very small ($K^{(0)}a \approx 0$), the radiation dynamics changes drastically. The right column of Fig. 3.2 shows an example for $\delta/J = 0.0011$. For $x = 0$ [Fig. 3.2(d)], the propagation under $\hat{H}$ (solid line) yields damped oscillatory be-

havior. In the long-time limit, the system is characterized by fractional populations. This is analogous to the single-emitter case [107, 108], where the emitter frequency is in resonance with the single-photon scattering band. As the separation increases [Figs. 3.2(e)-3.2(f) show results for $x/a = 5$ and 10, respectively], the dynamics for the Hamiltonian $\hat{H}$ (solid lines) are characterized by slower oscillations and weaker damping. For $x/a = 10$, the oscillations resemble nearly perfect two-state Rabi oscillations. Even though the emitters are coupled to a bath, dephasing is essentially absent for large separations. These undamped Rabi oscillations have no analog in the single-emitter system [107, 108].

The oscillation frequencies in Figs. 3.2(d)-3.2(f) correspond to the energy difference between the two energy eigen states of $\hat{H}$ that have the largest overlap with $|e,e,\mathrm{vac}\rangle$ [solid lines in Fig. 3.3(a)]; we label these states Ψ_+ and Ψ_-. For $x/a \gtrsim 5$, $\Psi_\pm$ have an energy that is smaller than $E_{K=0,b}$, i.e., both states are bound with respect to the $g = 0$ two-photon bound state band [solid line in Fig. 3.3(b)]. For $x/a \lesssim 5$, the energy of Ψ_+ remains below the bottom of the two-photon band while that of Ψ_- lies in the continuum. The quantity $|\langle e,e,\mathrm{vac}|\Psi_+\rangle|^2$ increases from about 0.66 to 0.99 as x/a increases from 0 to 20 [upper solid line in Fig. 3.4(a)]; $|\langle e,e,\mathrm{vac}|\Psi_-\rangle|^2$, in contrast, is comparatively small for $x/a \lesssim 4$, increases for $x/a = 5$ to 7, and then slowly decreases as x/a increases further [lower solid line in Fig. 3.4(a)].

To understand the emergence of the bound states and their dependence on x, we adiabatically eliminate the states $|e,g,k\rangle$ and $|g,e,k\rangle$, i.e., we assume that the change of the expansion coefficients $c_{1k}(t)$ and $c_{2k}(t)$ in Eq. (3.4) with time can be neglected [106]. This introduces a Stark shift $2\Delta_e$ as well as effective all-to-all momentum space interactions, proportional to $N^{-1}g^2G_{K,K'}(x)/J$, between two-photon bound states with wave vectors K and K'. The structures of $\hat{H}$ and the Hamiltonian $\hat{H}^{\mathrm{adia}}$ after adiabatic elimination are sketched, respectively, in the left and middle diagrams of Fig. 3.1(b). For the larger δ considered in Fig. 3.2 (left column), the $2\Delta_e$ and $G_{K,K'}(x)$ terms have negligible effects on

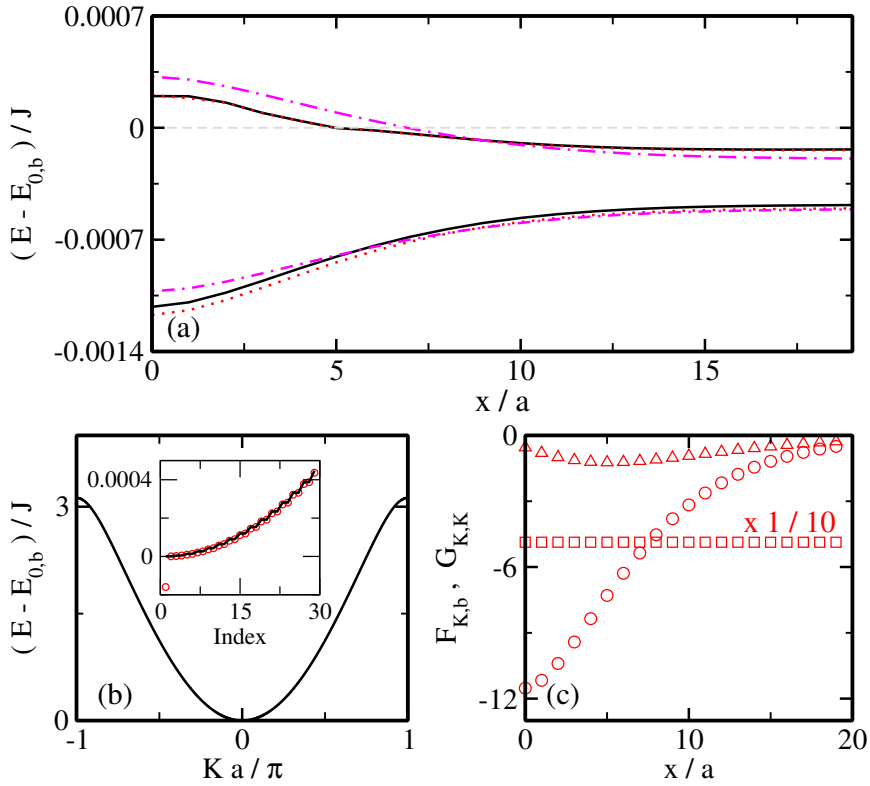

Figure 3.3: Static results ($U/J=-1$, $g/J=1/50$, and $\delta/J=0.0011$). (a) Black solid, red dotted, and magenta dash-dotted lines show the eigen energies corresponding to hybridized states of $\hat{H}$, $\hat{H}^{\text{adia}}$, and $\hat{H}^{\text{2-st.}}$, respectively, as a function of x/a. The gray dashed line shows $(E-E_{0,b})/J=0$. (b) The black solid line shows $E_{K,b}$ as functions of Ka/π (main panel) and the state index (inset). The red circles show the eigen energies supported by $\hat{H}_b^{\text{adia}}$ (index 1 corresponds to the polaron state). (c) The squares, circles, and triangles show the dimensionless quantities $\text{Re}(G_{K^{(0)},K^{(0)}}(x))/10$, $\text{Re}(F_{K^{(0)},b}(x))$, and $\text{Im}(F_{K^{(0)},b}(x))$ as a function of x/a for $K^{(0)}a/\pi=0.0152$.

the radiation dynamics [the dotted, dashed, and dash-dash-dotted lines in Figs. 3.2(a)-3.2(c) agree well]; as a consequence, Ref. [106] set them to zero in their reduced Hilbert space description. For the smaller δ (right column of Fig. 3.2), in contrast, both terms have a non-negligible effect on the dynamics as evidenced by the fact that the dotted, dashed, and dash-dash-dotted lines in Figs. 3.2(d)-3.2(f) disagree.

The adiabatic Hamiltonian $\hat{H}^{\text{adia}}$ contains the system, bath, and system-bath Hamiltonians $\hat{H}_s^{\text{adia}}$, $\hat{H}_b^{\text{adia}}$, and $\hat{H}_{sb}^{\text{adia}}$,

$$\hat{H}_s^{\text{adia}} = 2\Delta_e |e,e,\text{vac}\rangle\langle e,e,\text{vac}|, \tag{3.5}$$

$$\begin{aligned}\hat{H}_b^{\text{adia}} &= \sum_K E_{K,b}|g,g,K\rangle\langle g,g,K| \\ &\quad + \sum_{K,K'} \frac{g^2}{JN} G_{K,K'}(x)|g,g,K\rangle\langle g,g,K'|,\end{aligned} \tag{3.6}$$

and

$$\hat{H}_{sb}^{\text{adia}} = \sum_K \frac{g^2}{J\sqrt{N}} F_{K,b}(x)|g,g,K\rangle\langle e,e,\text{vac}| + h.c. \tag{3.7}$$

The analytical expressions for the effective interactions $g^2N^{-1/2}F_{K,b}(x)/J$ and $g^2N^{-1}G_{K,K'}(x)/J$ are lengthy and not reproduced here [106, 61]. The dotted lines in Figs. 3.2, 3.3(a), and 3.4(a) show the results obtained by propagating the initial state $|e,e,\text{vac}\rangle$ with $\hat{H}^{\text{adia}}$. The dotted lines agree quite well with the full calculation (solid lines) for all detunings and separations considered, suggesting that the reduced Hilbert space model captures the key physics. Thus, we use it to develop physical intuition.

To start with, we analyze the $K \approx K' \approx K^{(0)} \approx 0$ portion of $\hat{H}_b^{\text{adia}}$, which should govern the radiation dynamics when $|\delta/J|$ approaches zero. In this regime, the imaginary part of $G_{K,K'}(x)$ is vanishingly small and the real part, shown for $\delta/J = 0.0011$ by the squares in Fig. 3.3(c), is negative and nearly independent of x. If we replace $E_{K,b}$ by $E_{0,b}$ (i.e., use a flat band) and $G_{K,K'}(x)$ by $G_{K^{(0)},K^{(0)}}(x)$, then the eigen energies of the bath Hamiltonian are $E_{0,b} - (N-1)g^2N^{-1}G_{K^{(0)},K^{(0)}}(x)/J$ (one-fold degenerate) and $E_{0,b} + g^2N^{-1}G_{K^{(0)},K^{(0)}}(x)/J$ [$(N-1)$-fold degenerate]. The eigen state of the one-fold degenerate bound state reads $N^{-1/2}\sum_K |K\rangle$, i.e., it has polaron character. While the flat band model overestimates the binding energy of the polaron by a fair bit, it shows that the attractive all-to-all interactions $g^2N^{-1}G_{K,K'}(x)/J$ are responsible for the fact that the band of bound photon pairs splits into

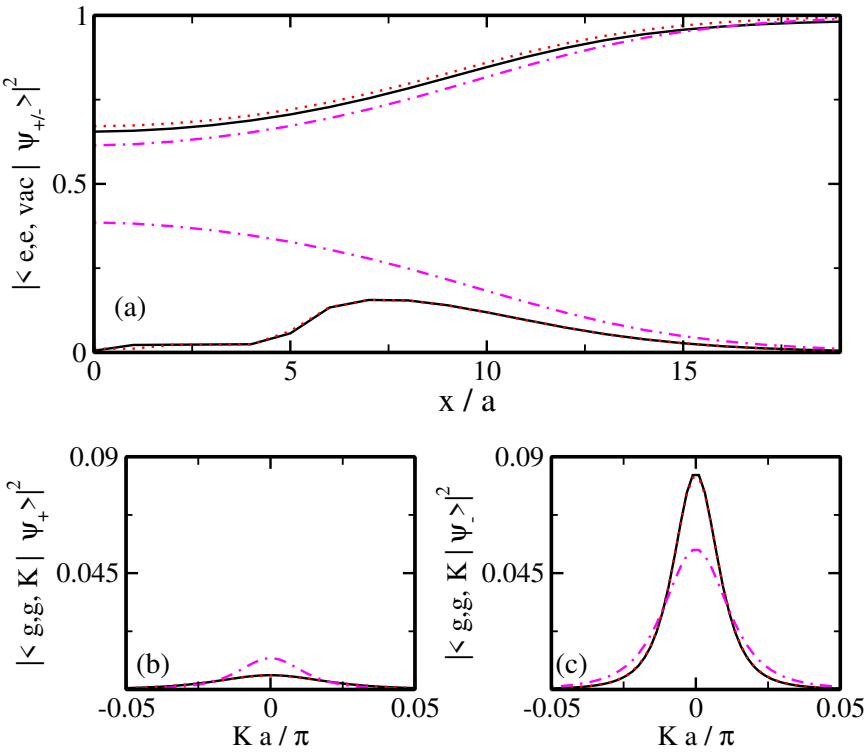

Figure 3.4: State composition of hybridized polaron-emitter states ($U/J = -1$, $g/J = 1/50$, and $\delta/J = 0.0011$). (a) Projection of $|e,e,\mathrm{vac}\rangle$ onto Ψ_+ (upper three lines) and Ψ_- (lower three lines) as a function of x/a. Black solid, red dotted, and magenta dash-dotted lines are obtained using $\hat{H}$, $\hat{H}^{\mathrm{adia}}$, and $\hat{H}^{\text{2-st.}}$, respectively. (b)/(c) Projection of Ψ_+ and Ψ_- onto $|g,g,K\rangle$ as a function of Ka/π for $x/a = 10$. The line styles are the same as in (a); black solid and red dotted lines are nearly indistinguishable on the scale shown.

a collective polaron-like bound state and a band that is slightly shifted upward compared to the $G_{K,K'}(x) = 0$ case. This interpretation continues to hold when a more accurate treatment is employed. The band curvature can be thought of as introducing a wave vector cutoff $(L_{\mathrm{eff}})^{-1}$. Taylor-expanding $E_{K,b}$ up to order $(Ka)^2$, making the ansatz $|\mathrm{pol}\rangle = \sum_K d_K |K\rangle$ with $d_K = 2N^{-1/2}(L_{\mathrm{eff}}^{-1}a/2)^{3/2}/[(Ka)^2 + (L_{\mathrm{eff}}^{-1}a/2)^2]$, and treating L_{eff} as a variational parameter, the energy E_{pol} of the polaron $|\mathrm{pol}\rangle$ can be found analytically. For the parameters considered in Fig. 3.3(b), the analytical result is in excellent agreement with the lowest eigen energy of $\hat{H}_b^{\mathrm{adia}}$, which is shown in Fig. 3.3(b) by the circle for state index 1.

Since $G_{K^{(0)},K^{(0)}}(x)$ is, for fixed δ/J and U/J, approximately independent of x, the separation dependence displayed in Figs. 3.2(d)-3.2(f) must enter through $F_{K^{(0)},b}(x)$. Figure 3.3(c) shows that $\mathrm{Re}(F_{K^{(0)},b}(x))$ (circles) has a strong x dependence and is much larger, in magnitude, than $\mathrm{Im}(F_{K^{(0)},b}(x))$ (triangles). Rewriting $\hat{H}^{\mathrm{adia}}$ in the basis in which $\hat{H}_b^{\mathrm{adia}}$ is diagonal, we find that the state $|e,e,\mathrm{vac}\rangle$ couples comparatively strongly to the state $|g,g,\mathrm{pol}\rangle$ and comparatively weakly to all other bath states. The dynamics in the $|\delta/J| \to 0$ limit is thus approximately described by the two-state Hamiltonian $\hat{H}^{\text{2-st.}}$,

$$\hat{H}^{\text{2-st.}} = \hat{H}_s^{\mathrm{adia}} + E_{\mathrm{pol}}|g,g,\mathrm{pol}\rangle\langle g,g,\mathrm{pol}| + (G_{\mathrm{eff}}|g,g,\mathrm{pol}\rangle\langle e,e,\mathrm{vac}| + h.c.). \tag{3.8}$$

Using our variational expression for $|g,g,\mathrm{pol}\rangle$, we find

$$G_{\mathrm{eff}} = \frac{g^3(U^2+16J^2)^{1/4}}{2J^{5/2}} F_{K^{(0)},b}(x)|G_{K^{(0)},K^{(0)}}(x)|^{1/2}. \tag{3.9}$$

The eigen energies of the hybridized polaron-emitter states Ψ_+ and Ψ_- supported by Eq. (4.45) for $U/J=-1$, $g/J=1/50$, and $\delta/J=0.0011$ [dash-dotted lines in Figs. 3.3(a)] agree reasonably well with those of $\hat{H}$ when x/a is large. State Ψ_+ is symmetric (the coefficients of $|e,e,\mathrm{vac}\rangle$ and $|g,g,\mathrm{pol}\rangle$ are both positive) while Ψ_- is anti-symmetric (the coefficients have opposite signs). The two-state description deteriorates with decreasing separation; the state composition of the more weakly bound state Ψ_-, which has a smaller overlap with the emitter state $|e,e,\mathrm{vac}\rangle$ [lower three lines in Fig. 3.4(a); Fig. 3.4(c)] than the more deeply bound state Ψ_+ [upper three lines in Fig. 3.4(a); Fig. 3.4(b)], deviates notably from that obtained by diagonalizing $\hat{H}$. In fact, for $x/a \lesssim 5$, the first excited state of $\hat{H}$ is no longer a simple superposition of $|e,e,\mathrm{vac}\rangle$ and $|g,g,\mathrm{pol}\rangle$ but instead contains multiple nearly degenerate energy eigen states with energy close to $E_{K=0,b}$. In the dynamics, this results in dephasing, thereby explaining the damping observed in Figs. 3.2(d)-3.2(e).

In summary, our analysis shows that the essentially undamped Rabi oscillations are associated with population exchange between two hybridized polaron-emitter states. These

states are distinct from previously predicted hybridized states [105, 128, 129, 130, 131, 132]. For the parameters considered in this paper, the more weakly-bound hybridized state merges into the continuum for $x/a \lesssim 5$, making the emergence of long-lived Rabi oscillations an intriguing emitter separation-dependent long-range phenomenon. When the emitters are close together, the radiation dynamics, starting with $|e,e,\text{vac}\rangle$ at $t = 0$, leads to quasi-stationary fractional populations. When the emitters are spaced further apart, regular revivals are observed. We emphasize the crucial role of the Stark shift $2\Delta_e$ and the attractive all-to-all momentum space interactions. Neglecting these terms yields the dash-dotted lines in Figs. 3.2(d)-3.2(f). Setting $2\Delta_e$ to the correct value but using $G_{K,K'}(x) = 0$ yields the dashed lines.

Our work illustrates that the structure of the bath Hamiltonian with Kerr-like non-linearity can be modified non-trivially—introducing attractive all-to-all momentum space interactions—through the coupling to two two-level emitters, resulting in qualitatively new radiation dynamics. Continuing to work in the two-excitation manifold, extension to arrays of regularly spaced emitters where neighboring emitters have a fixed separation (simple emitter lattice) or alternating separations (emitter superlattice) offers the prospect of establishing non-trivial bath-induced correlations between separated emitter pairs. Taking an alternative viewpoint, this work points toward utilizing emitters to create bath Hamiltonian with unique characteristics, including challenging-to-generate all-to-all interactions. Our analysis assumes that losses from the wave guide can be neglected. Over the time scales considered, this should be justified for several state-of-the-art experiments.

Acknowledgement: Support by the National Science Foundation through grant number PHY-1806259 is gratefully acknowledged. This work used the OU Supercomputing Center for Education and Research (OSCER) at the University of Oklahoma (OU). A discussion with Kieran Mullen on impurities in solid state systems is gratefully acknowledged.

Chapter 4

Two emitters coupled to a bath with Kerr-like non-linearity: Exponential decay, fractional populations, and Rabi oscillations

by J. Talukdar[1, 2] and D. Blume[1, 2]

[1]Homer L. Dodge Department of Physics and Astronomy, The University of Oklahoma,
440 W. Brooks Street, Norman, Oklahoma 73019, USA

[2]Center for Quantum Research and Technology, The University of Oklahoma,
440 W. Brooks Street, Norman, Oklahoma 73019, USA

We consider two non-interacting two-level emitters that are coupled weakly to a one-dimensional non-linear wave guide. Due to the Kerr-like non-linearity, the wave guide considered supports—in addition to the scattering continuum—a two-body bound state. As such, the wave guide models a bath with non-trivial mode structure. Solving the time-dependent Schrödinger equation, the radiation dynamics of the two emitters, initially prepared in their excited states, is presented. Changing the emitter frequency such that the two-emitter energy is in resonance with one of the two-body bound states, radiation dynamics ranging from exponential decay to fractional populations to Rabi oscillations is observed. Along with the detuning, the dependence on the separation of the two emitters is investigated. Approximate reduced Hilbert space formulations, which result in effective emitter-separation and momentum dependent interactions, elucidate the underlying physical mechanisms and provide an avenue to showcase the features that would be absent if the one-dimensional wave guide did not contain a non-linearity. Our theoretical findings apply to a number of experimental platforms and the predictions can be tested with state-of-the-art technology. In addition, the weak-coupling Schrödinger equation based results provide

critical guidance for the development of master equation approaches.

4.1 Introduction

Since it is hard to fully isolate quantum systems in realistic experimental settings, the quantum mechanical treatment of a system coupled to a bath is important from a practical point of view [7]. Taking a somewhat philosophical viewpoint, one may furthermore argue that truly isolated quantum systems never exist since any quantum system is part of a larger universe, i.e., embedded into an environment [3]. In addition, any measurement on the system involves, according to measurement theory, interactions between the system and the environment or bath [133, 134, 135].

The fact that systems are interacting with or can be made to interact with the environment that they are embedded into provides a wealth of opportunities. For example, bath engineering can be used to control the dynamics of the system, thereby providing an alternative approach to the preparation of pre-specified target states [136, 137, 138, 139, 140, 141, 142, 143, 144]. The idea is quite simple. As an example, imagine two non-interacting few-level emitters that are both coupled to a bath. Even though the emitters are not interacting, the action of the bath on the emitters can be interpreted as an effective interaction between the emitters. The effective emitter-emitter interaction can be adjusted, by modifying the mode structure of the bath, such that the emitters are driven into a quasi-stationary state.

In most cases, the full quantum mechanical treatment of the dynamics of the entire system, i.e., the system and the environment, is extremely challenging due to the tremendously large Hilbert space. To make progress, a range of approaches has been pursued [145]. In the weak-coupling limit, perturbative and master equation approaches have been developed [105, 97]. The strong-coupling limit can in some cases also be tackled perturbatively [146, 147, 148, 149, 150, 151, 152]. The present work does not make any of these approximations and instead analyzes the dynamics of the emitter-

waveguide system using the time-dependent Schrödinger equation, working—as, e.g., Refs. [153, 154, 155, 156, 157, 158, 106]—with the essentially full Hilbert space; the Hilbert space truncation made (i.e., dropping of two-photon scattering states) leaves the dynamics essentially unchanged for the parameter combinations investigated. To make the calculations feasible, we restrict ourselves to a one-dimensional bath with a non-trivial but still relatively simple mode structure. Losses to the "outside world" are neglected entirely, i.e., the emitter-bath system is treated as a closed system (the wave guide is assumed to be lossless).

For concreteness, our work focuses on a photonic lattice with lattice spacing a, nearest neighbor tunneling J, and on-site interaction U [106, 60]. The two two-level emitters are assumed to be located at or coupled to specific lattice sites [see Fig. 4.1(a)]. When both emitters are coupled to the same lattice site, the spacing x vanishes; when both emitters are coupled to adjacent lattice sites, x is equal to a; and so on. This model Hamiltonian was introduced in Ref. [106]. While our work builds on the theory framework introduced in Ref. [106], the emphasis of our study is distinct. Specifically, our work complements Ref. [106] in that we focus on the physics near the bottom or the top of the band as opposed to on the physics in the middle of the band, i.e., we consider a different range of detuning δ/J, where δ/J is defined with respect to the bottom of the two-photon bound state band for negative U and with respect to the top of the two-photon bound state band for positive U [159],

$$\delta = 2\hbar\omega_e - 2\hbar\omega_c - \mathrm{sign}(U)\sqrt{U^2+16J^2}. \tag{4.1}$$

Here, $\hbar\omega_e$ is the transition energy of the emitter and $2\hbar\omega_c + \mathrm{sign}(U)\sqrt{U^2+16J^2}$ the bottom of the band for negative U and the top of the band for positive U ($\hbar\omega_c$ is the energy in the middle of the single-photon energy band; see Fig. 4.2 for an illustration). We initialize the emitters in their excited state $|e\rangle_1|e\rangle_2$ and the waveguide in the vacuum state $|\mathrm{vac}\rangle$ at time $t = 0$. Working in the subspace of two excitations, we study the radiation

dynamics. Throughout, we refer to the bath as photon bath. We emphasize, however, that the formalism applies also to a phonon bath and baths consisting of other quasi-particles. The Hamiltonian considered conserves the total number of excitations (see, e.g., Refs. [153, 154, 106, 160, 105]), which is defined as the sum of the number of emitter excitations and the number of photons. Key objectives of our work are to unravel the dependence of the radiation dynamics on the emitter separation x and the detuning δ.

Our main results can be summarized as follows: (i) The radiation dynamics depends strongly on the emitter separation, detuning, and strength of the non-linearity. (ii) Focusing on parameter combinations where the single-photon contributions can be eliminated adiabatically (this implies moderate x/a, not too large $|U|/J$, and detuning δ such that the system is on resonance with the two-photon band or just slightly off-resonance), we observe radiation dynamics ranging from exponential decay to fractional population to Rabi oscillations. (iii) As discussed in Ref. [106], the Markov approximation provides a faithful description of the exponential decay of the initial state; our semi-analytic expression for the decay constant is compared with that for a single emitter case where the emitter energy is in resonance with the single-photon energy band, excluding the region near the band edge. (iv) When the onsite interaction is negative and the detuning is chosen such that the energy of the two emitters is in the band but close to the bottom of the band (the actual value of δ/J depends on the separation x and the coupling strength g/J), the emitters do not decay to the ground state but instead approach a steady state that is characterized by fractional populations. Some of the time-dependent characteristics can be explained in terms of effective photon-pair–photon-pair interactions. (v) Detuning extremely close to the bottom of the band [as in (iv), the actual value of δ/J depends on the separation x and the coupling strength g/J] leads to weakly-damped or essentially undamped Rabi oscillations, which display a notable separation dependence and can be explained in terms of two bound hybridized photonic polaron–excited emitter states. An analytical two-state

model that provides a semi-quantitative description of the Rabi oscillations is derived. We note in passing that our results in support of the conclusions summarized under (iii) form the basis for developing master equation formulations.

The remainder of this article is organized as follows. Section 4.2 introduces the model Hamiltonian and the approaches used to solving the time-dependent and time-independent Schrödinger equation. Sections 4.3 and 4.4 present our time-independent and time-dependent results. Last, Sec. 4.5 provides a summary and outlook. Appendix A reviews single-emitter results from the literature while Appendix B contains technical details related to the adiabatic elimination.

4.2 System Hamiltonian and theoretical techniques

Sections 4.2.1 and 4.2.2 introduce the full system Hamiltonian and the bath Hamiltonian, respectively. Our approach for solving the full Schrödinger equation is summarized in Sec. 4.2.3. The adiabatic elimination of the single-photon states is discussed in Sec. 4.2.4. Building on the reduced Hilbert space Hamiltonian that results after the adiabatic elimination, Sec. 4.2.5 discusses the Markov approximation.

4.2.1 System Hamiltonian

The total Hamiltonian $\hat{H}$ is given by [106, 60]

$$\hat{H} = \hat{H}_{\mathrm{s}} + \hat{H}_{\mathrm{b}} + \hat{H}_{\mathrm{sb}}, \tag{4.2}$$

where $\hat{H}_{\mathrm{s}}$ denotes the system Hamiltonian, $\hat{H}_{\mathrm{b}}$ the bath Hamiltonian, and $\hat{H}_{\mathrm{sb}}$ the system-bath coupling [see Fig. 4.1(a) for a schematic]. We consider a system consisting of N_e two-level emitters with energy separation $\hbar\omega_e$ between the ground state $|g\rangle_j$ and the excited state $|e\rangle_j$ of the jth emitter. Specifically, $\hat{H}_{\mathrm{s}}$ is given by

$$\hat{H}_{\mathrm{s}} = \frac{\hbar\omega_e}{2} \sum_{j=1}^{N_e} (\hat{\sigma}_j^z + \hat{I}_j), \tag{4.3}$$

where $\hat{\sigma}_j^z = |e\rangle_j\langle e| - |g\rangle_j\langle g|$ and $\hat{I}_j = |g\rangle_j\langle g| + |e\rangle_j\langle e|$. The inclusion of the identity $\sum_{j=1}^{N_e}\hat{I}_j$ in Eq. (4.3) introduces an energy shift such that the energy of the state with N_e emitters in their excited state and the bath in the vacuum state is equal to $N_e\hbar\omega_e$. The energy shift due to the identity introduces an overall phase in the time-dependent wave packet but does not impact the population dynamics. The jth emitter is coupled to the n_jth lattice site of the wave guide, i.e., the emitters do not move during the dynamics.

Triggered by the system-bath Hamiltonain $\hat{H}_{\rm sb}$ with coupling strength g, the emitters can change their state from $|e\rangle_j$ to $|g\rangle_j$ and from $|g\rangle_j$ to $|e\rangle_j$,

$$\hat{H}_{\rm sb} = g\sum_{j=1}^{N_e}\left(\hat{a}_{n_j}\hat{\sigma}_j^+ + \hat{a}_{n_j}^\dagger\hat{\sigma}_j^-\right). \tag{4.4}$$

Here, $\hat{\sigma}_j^+$ and $\hat{\sigma}_j^-$ denote raising and lowering operators of the jth emitter, $\hat{\sigma}_j^+ = |e\rangle_j\langle g|$ and $\hat{\sigma}_j^- = |g\rangle_j\langle e|$. The operators $\hat{a}_{n_j}^\dagger$ and $\hat{a}_{n_j}$, respectively, create and destroy a photon at lattice site n_j, where the label n_j takes values from 1 to N with N denoting the number of lattice sites or cavities of the wave guide. We are interested in the regime where the dynamics is independent of N (large N limit). Since the system-bath Hamiltonian does not include any counterrotating terms, the treatment is restricted to the weak-coupling regime where $|g|$ is small compared to the other energy scales of the system [72].

The Hamiltonian $\hat{H}_{\rm b}$ is taken to be a one-dimensional array of tunnel coupled cavities in the tight-binding limit. It is characterized by the "photon energy" $\hbar\omega_c$ (the middle of the single-photon energy band has energy $\hbar\omega_c$), the tunneling energy J, and the onsite interaction energy U:

$$\begin{aligned}\hat{H}_{\rm b} = \quad & \hbar\omega_c\sum_{n=1}^{N}\hat{a}_n^\dagger\hat{a}_n - J\sum_{n=1}^{N}\left(\hat{a}_n^\dagger\hat{a}_{n+1} + \hat{a}_{n+1}^\dagger\hat{a}_n\right)\\ & + \frac{U}{2}\sum_{n=1}^{N}\hat{a}_n^\dagger\hat{a}_n^\dagger\hat{a}_n\hat{a}_n.\end{aligned} \tag{4.5}$$

In Eq. (4.5), the photons are assumed to interact, due to the presence of a Kerr-like medium, either effectively repulsively ($U > 0$) or effectively attractively ($U < 0$). A positive U gives

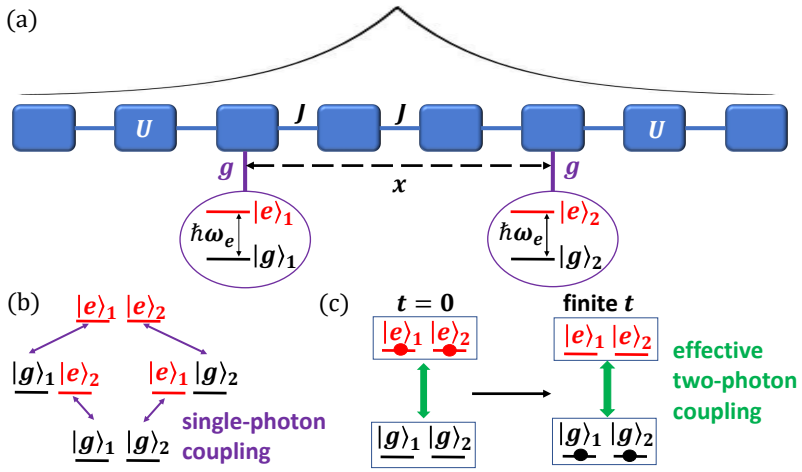

Figure 4.1: Illustration of system under study. (a) Schematic of system Hamiltonian. Each blue box represents a cavity. The tunnel-coupling between neighboring cavities, which are separated by a, is shown by the lines labeled by J. The onsite interaction U characterizes the effective photon-photon interaction; the U-term of the Hamiltonian $\hat{H}$, Eq. (4.2), only plays a role for $N_{\text{exc}} \geq 2$. Two two-level emitters with energy levels $|g\rangle_j$ and $|e\rangle_j$ ($j = 1$ or 2) are coupled to cavities n_1 and n_2 (n_1 and n_2 are fixed, $n_1 - n_2 = x/a$) with strength g. The black line illustrates a two-photon bound state that is supported by the cavity array. The physics explored in this paper occurs in the regime where the size of the two-photon bound state is comparable to the emitter separation x. (b) Illustration of the system-bath Hamiltonian $\hat{H}_{\text{sb}}$, Eq. (4.4), in the emitter Hilbert space. Going from $|e\rangle_1|e\rangle_2|\text{vac}\rangle$ to $|g\rangle_1|g\rangle_2|K\rangle$ requires two single-photon processes of strength g. (c) Illustration of the effective Hamiltonian $\hat{H}^{\text{adia}}$, Eq. (4.28), in the emitter Hilbert space. The adiabatic elimination introduces an effective two-photon coupling between states $|e\rangle_1|e\rangle_2|\text{vac}\rangle$ and $|g\rangle_1|g\rangle_2|K\rangle$. This work monitors the change of the population of the state $|e\rangle_1|e\rangle_2|\text{vac}\rangle$ with time.

rise to a two-photon bound state with center-of-mass wave vector K that lies above the two-photon continuum while a negative U gives rise to a two-photon bound state with center-of-mass wave vector K that lies below the two-photon scattering continuum [123, 124, 125, 126].

The bath Hamiltonian considered here has been chosen for several reasons: (i) The eigen energies and eigen states of $\hat{H}_{\rm b}$ are known analytically (see below) [125]. (ii) Despite its simplicity, the Hamiltonian $\hat{H}_{\rm b}$ supports a non-trivial mode structure, namely the above-mentioned two-photon bound state [123, 124, 125, 126]. (iii) It was predicted in Ref. [106] that the emission dynamics of $\hat{H}$ displays, for certain parameter combinations, sub-radiance and super-correlations. These intriguing findings motivate our quest to map out constructive and destructive interferences, with the goal of identifying the dominant emission pathways. Throughout, we are interested in situations where the initial $t = 0$ state contains two excitations in the emitter Hilbert space (i.e., $|\Psi(0)\rangle = |e\rangle_1|e\rangle_2|{\rm vac}\rangle$) and where the dynamics is driven, at least in part, by the non-trivial mode structure of the bath, i.e., by the existence of the two-photon bound states supported by $\hat{H}_{\rm b}$. For brevity, we adopt the notation $|e\rangle_1|e\rangle_2|{\rm vac}\rangle = |e,e,{\rm vac}\rangle$, etc. The next section discusses selected properties of $\hat{H}_{\rm b}$.

The Hamiltonian $\hat{H}$ has four independent energy scales: δ, g, J, and U. Throughout, J, $\hbar/J$, and a are used as energy unit, time unit, and length unit, respectively. To reduce the parameter space, we analyze the system properties for fixed g/J as functions of δ/J and x/a. The dependence on U/J is explored a bit; most calculations presented, however, are for $U/J = -1$. Throughout, we work in the weak coupling regime, i.e., we use $g/J = 1/50$. Section 4.5 comments briefly on the dependence of the system properties on g/J. As illustrated in Fig. 4.2, the detuning δ is set such that the energy $2\hbar\omega_e$ of the initial state is, for $g = 0$, (A) in resonance with a two-photon bound state with Ka/π not too close to 0 and not too close to ± 1 [see the horizontal dashed line in Fig. 4.2(b) as an example]; (B) in resonance with a two-photon bound state with Ka/π a bit larger than 0 [see the horizontal solid line in Fig. 4.2(b) as an example]; and (C) in resonance with the two-photon bound state extremely close to the bottom of the band [$K^{(0)}a/\pi \approx 4.5 \times 10^{-3}$; see the horizontal dotted line in Fig. 4.2(b) as an example].

We note that single-photon losses are not included in our treatment. This is justified

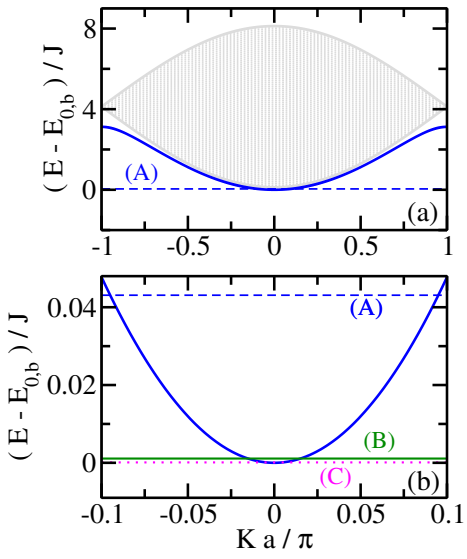

Figure 4.2: Two-photon eigen spectrum as a function of the scaled center-of-mass wave number Ka/π. Note that the energy is shifted such that the bottom of the two-photon bound state band sits at zero. (a) The gray-shaded energy band corresponds to the two-photon scattering continuum, Eq. (4.9). The thick blue solid line shows the energy $E_{K,b}$ of the two-photon bound state for $U/J = -1$. While the gray band and thick blue solid line appear to coincide for $K = 0$ on the scale shown, we note that the bottom of the two-photon scattering continuum at $K = 0$ lies $(-4+\sqrt{17})J \approx 0.123J$ above the $K = 0$ two-photon bound state energy. This separation is sufficiently large for the two-photon scattering continuum to play a negligible role in the system dynamics considered in this paper. The thin dashed line shows the energy of the state $|e,e,\text{vac}\rangle$ for $\delta/J = 0.0431$. (b) Blow-up of (a), focusing on the region around the bottom of the band. The blue solid and blue dashed lines are the same as in (a). The horizontal green solid and magenta dotted lines show the energy of the state $|e,e,\text{vac}\rangle$ for $\delta/J = 0.0011$ and 0.0001, respectively. The labels "(A)", "(B)", and "(C)" refer to the three scenarios introduced in the second to last paragraph of Sec. 4.2.1.

if the dynamics governed by $\hat{H}$ is notably faster than the dynamics associated with the single-photon losses. Using the parameters of Fig. 4.11 as an example, this implies that the single-photon loss rate is assumed to be smaller than $\approx 10^{-4}J/\hbar$.

4.2.2 Mode structure of the bath Hamiltonian

Since the Hamiltonian $\hat{H}_{\mathrm{b}}$ commutes with the photon number operator $\hat{N}$ [123, 124, 125],

$$\hat{N} = \sum_{n=1}^{N} \hat{a}_n^\dagger \hat{a}_n, \tag{4.6}$$

$\hat{H}_{\mathrm{b}}$ is block-diagonal in the number of photons. In what follows, we discuss the eigen spectrum of $\hat{H}_{\mathrm{b}}$ in the one- and two-photon subspaces.

We start with the single-photon subspace. The single-photon energy E_k reads [161]

$$E_k = \hbar\omega_c - 2J\cos(ka), \tag{4.7}$$

where the single-photon wave number k ($ka/\pi \in [-1,1]$) is a good quantum number. The single-photon eigen states with energy E_k are denoted by $|\psi_k\rangle$. Equation (4.7) shows that E_k is equal to $\hbar\omega_c$ for $ka/\pi = \pm 1/2$ (this is the middle of the band), equal to $\hbar\omega_c - 2J$ for $ka/\pi = 0$ (this is the bottom of the band), and equal to $\hbar\omega_c + 2J$ for $ka/\pi = \pm 1$. For later reference, we note that the single-photon group velocity v_k is given by

$$v_k = \frac{2Ja}{\hbar}\sin(ka). \tag{4.8}$$

This shows that a single photon travels, "on average," two lattice sites per characteristic time $\hbar/J$ for $ka/\pi = \pm 1/2$ and not at all for $ka = 0$ and $ka/\pi = \pm 1$. According to this classical average-speed-picture, two individually launched photons may not interfere with each other if the photon's wave number is close to zero or $\pm\pi/a$, or if the emitters are separated by many lattice sites.

We now turn to the two-photon subspace, which is spanned by scattering states $|\psi_{K,q}\rangle$ with energy $E_{K,q}$ and bound states $|\psi_{K,b}\rangle$ with energy $E_{K,b}$ [123, 124, 125, 126]. The center-of-mass wave number K is a good quantum number. The gray band in Fig. 4.2(a) shows the two-photon scattering energy $E_{K,q}$ [123, 124, 125],

$$E_{K,q} = 2\hbar\omega_c - 4J\cos\left(\frac{Ka}{2}\right)\cos(qa), \tag{4.9}$$

as a function of K ($Ka/\pi \in [-1,1]$). The energy continuum arises from the fact that the relative wave number q can take a range of values that depends on K (e.g., $qa/\pi \in [-1,1]$ for $K = 0$ and $qa/\pi = 0$ for $Ka/\pi = \pm 1$). The middle of the scattering continuum lies at $2\hbar\omega_c$, and the scattering continuum has a width of $8J$ for $Ka/\pi = 0$ and a width of 0 for $Ka/\pi = \pm 1$. While the two-photon scattering energies $E_{K,q}$ are independent of U, the associated scattering states depend on U.

In addition, the Hamiltonian $\hat{H}_{\mathrm{b}}$ supports one two-photon bound state with energy $E_{K,b}$ for each K [123, 124, 125, 126],

$$E_{K,b} = 2\hbar\omega_c + \mathrm{sign}(U)\left[U^2 + 16J^2\cos^2\left(\frac{Ka}{2}\right)\right]^{1/2}. \tag{4.10}$$

For negative U/J, the bound state lies below the scattering continuum (see the thick blue solid line in Fig. 4.2 for $U/J = -1$). In this case, the binding energy for a given K is defined as the energy difference between the lower edge of the scattering continuum ($E_{K,q}$ with $q = 0$) and the bound state energy $E_{K,b}$. The situation for positive U/J is similar, except that the bound state lies above the scattering continuum. The binding energy increases with increasing $|U|/J$; correspondingly, the two-photon bound state wave function becomes more localized. We note that two-photon bound states [162] and repulsively bound atom pairs in optical lattices [163] have been observed experimentally.

The horizontal lines in Fig. 4.2(b) show the energy of the state $|e\rangle_1|e\rangle_2|\mathrm{vac}\rangle$ for three different values of δ/J: $\delta/J = 0.0431$ (dashed line) corresponds to scenario (A), $\delta/J = 0.0011$ (solid line) corresponds to scenario (B), and $\delta/J = 0.0001$ (dotted line) corresponds to scenario (C). The crossings between the energy of the initial state and the energy $E_{K,b}$ of the two-photon bound state define the uncoupled (i.e., $g = 0$) resonance wave numbers $\pm K^{(0)}$ [106], where $K^{(0)}$ is defined to be positive. For finite coupling strength g, the value of the resonance wave vector shifts from $K^{(0)}$ to $K^{(*)}$ (see Appendix B for details).

In scenario (A), radiation is emitted predominantly, via intermediate single-photon states, into two-photon bound states with wave numbers $\approx \pm K^{(*)}$, leading to exponential

decay [106]. Since the group velocity $v_{K,b}$ [125],

$$v_{K,b} = \frac{1}{\hbar}\frac{\partial E_{K,b}}{\partial K}, \tag{4.11}$$

of the two-photon bound state depends on K ($v_{K,b}$ is zero for $Ka/\pi = 0$ and ± 1 and finite for all other Ka), the decay constant shows a distinct dependence on the resonance wave number or, equivalently, on the detuning δ/J [106]. In scenario (B), the near-flatness of the band implies that the initial energy is nearly equal to that of several two-photon bound states with $|Ka/\pi| \ll 1$. This leads, as shown in Sec. 4.4, to fractional populations. In scenario (C), the two-photon bound state band splits into a band and an emitter-photon coupling induced polaron-like bound state that hybridizes with the state $|e,e,\mathrm{vac}\rangle$ upon inclusion of the coupling between the polaron-like bound state and the state $|e,e,\mathrm{vac}\rangle$, leading to essentially undamped Rabi oscillations that are reproduced very well by a two-state model. Selected results for scenarios (B) and (C) are discussed in Ref. [60].

4.2.3 Solving the Schrödinger equation

Since $\hat{H}$ commutes with the excitation operator $\hat{N}_{\mathrm{exc}}$ [153, 154, 106, 160, 105],

$$\hat{N}_{\mathrm{exc}} = \hat{N} + \sum_{j=1}^{N_e} \hat{\sigma}_j^+ \hat{\sigma}_j^-, \tag{4.12}$$

the number of excitations N_{exc} (eigenvalue of $\hat{N}_{\mathrm{exc}}$) is conserved. Correspondingly, the time evolution of an initial state with $N_{\mathrm{exc}} = 2$ under the Hamiltonian $\hat{H}$, Eq. (4.2), can be expanded in terms of the states $|e,e,\mathrm{vac}\rangle$, $\hat{a}_n^\dagger|e,g,\mathrm{vac}\rangle$, $\hat{a}_n^\dagger|g,e,\mathrm{vac}\rangle$, and $\hat{a}_n^\dagger\hat{a}_{n'}^\dagger|g,g,\mathrm{vac}\rangle$, where n and n' take the values $1,\cdots,N$. Alternatively, the time-dependent state $|\Psi(t)\rangle$ can

be expanded using the zero-, one-, and two-photon eigen states of $\hat{H}_{\rm b}$ [106],

$$\begin{aligned}|\Psi(t)\rangle = \quad & \exp(-2\imath\omega_e t)[c_{ee}(t)|e,e,\text{vac}\rangle + \\ & \sum_k c_{1k}(t)\hat{a}_k^\dagger|e,g,\text{vac}\rangle + \\ & \sum_k c_{2k}(t)\hat{a}_k^\dagger|g,e,\text{vac}\rangle + \\ & \sum_K c_{K,b}(t)\hat{P}_{K,b}^\dagger|g,g,\text{vac}\rangle + \\ & \sum_{K,q} c_{K,q}(t)\hat{P}_{K,q}^\dagger|g,g,\text{vac}\rangle],\end{aligned} \tag{4.13}$$

where $|\psi_k\rangle = \hat{a}_k^\dagger|\text{vac}\rangle$, $|\psi_{K,b}\rangle = \hat{P}_{K,b}^\dagger|\text{vac}\rangle$, and $|\psi_{K,q}\rangle = \hat{P}_{K,q}^\dagger|\text{vac}\rangle$. The operators $\hat{a}_n^\dagger$ and $\hat{a}_k^\dagger$ are related via a Fourier transform in the standard way,

$$\hat{a}_k^\dagger = \frac{1}{\sqrt{N}}\sum_{n=1}^{N}\exp(\imath kan)\hat{a}_n^\dagger. \tag{4.14}$$

Inserting Eq. (4.13) into the time-dependent Schrödinger equation

$$\imath\hbar\frac{\partial\Psi(t)}{\partial t} = \hat{H}\Psi(t) \tag{4.15}$$

and projecting onto the basis states, we obtain a set of first-order differential equations for the time-dependent expansion coefficients [106],

$$\imath\hbar\dot{c}_{ee}(t) = \frac{g}{\sqrt{N}}\sum_{\alpha=1,2}\sum_k \exp\big(\imath kan_\beta\big)c_{\alpha k}(t), \tag{4.16}$$

$$\begin{aligned}\imath\hbar\dot{c}_{\alpha k}(t) = \Delta_k c_{\alpha k}(t) + \frac{g}{\sqrt{N}}\exp\big(-\imath kan_\beta\big)c_{ee}(t) + \frac{g}{N}\sum_K M_b(k,n_\alpha,K)c_{K,b}(t) + \\ \frac{g}{N}\sum_{K,q} M_q(k,n_\alpha,K)c_{K,q}(t),\end{aligned} \tag{4.17}$$

$$\imath\hbar\dot{c}_{K,b}(t) = \Delta_{K,b}c_{K,b}(t) + \frac{g}{N}\sum_{\alpha=1,2}\sum_k [M_b(k,n_\alpha,K)]^* c_{\alpha k}(t), \tag{4.18}$$

and

$$\imath\hbar\dot{c}_{K,q}(t) = \Delta_{K,q}c_{K,q}(t) + \frac{g}{N}\sum_{\alpha=1,2}\sum_k [M_q(k,n_\alpha,K)]^* c_{\alpha k}(t). \tag{4.19}$$

For $N_{\text{exc}} = 2$ (recall, this is the focus of our work), Eqs. (4.16)-(4.19) are equivalent to the time-dependent Schrödinger equation. The quantities Δ_k, $\Delta_{K,b}$, and $\Delta_{K,q}$ denote energy detunings:

$$\Delta_k = E_k - \hbar\omega_e, \tag{4.20}$$

$$\Delta_{K,b} = E_{K,b} - 2\hbar\omega_e, \tag{4.21}$$

and

$$\Delta_{K,q} = E_{K,q} - 2\hbar\omega_e. \tag{4.22}$$

In Eq. (4.17), α takes the values 1 or 2. The value of β depends on α: $\beta = 2$ for $\alpha = 1$ and $\beta = 1$ for $\alpha = 2$ in Eqs. (4.16)-(4.17). The matrix elements $M_b(k,n,K)$ and $M_q(k,n,K)$ measure the contribution of a photon with wave number k to the two-photon bound state and to the two-photon scattering state, respectively, after acting with $\hat{a}_n$ on the two-photon state,

$$M_b(k,n,K) = N\langle\psi_k|\hat{a}_n|\psi_{K,b}\rangle \tag{4.23}$$

and

$$M_q(k,n,K) = N\langle\psi_k|\hat{a}_n|\psi_{K,q}\rangle. \tag{4.24}$$

The matrix element $M_b(k,n,K)$ reads [106]

$$M_b(k,n,K) = \sqrt{2}\sum_m \exp\left[\imath m\left(k - \frac{K}{2}\right)a + \imath n(K-k)a\right]\psi_{K,b}(m)], \tag{4.25}$$

where $\psi_{K,b}(m) = \langle r = ma|\psi_{K,b}\rangle$ with $|r\rangle$ denoting the relative distance between the two photons; $M_q(k,n,K)$ is obtained by replacing the subscript b in Eq. (4.25) by q. The matrix elements $M_b(k,n,K)$ and $M_q(k,n,K)$ are defined such that their values for a given k, n, and K [and q for $M_q(k,n,K)$] are independent of N; they differ by a factor N from those defined in Ref. [106].

We solve the coupled differential equations by discretizing the wave numbers k, K, and q. For N lattice sites and $N_{\mathrm{exc}} = 2$ excitations, we have $N^2 + (N_e + 1)N + 1$ expansion coefficients. If the scattering continuum can be neglected, the computational complexity reduces dramatically since the number of coupled equations reduces from order N^2 to order N. For the parameters considered in this work, we found—by performing calculations for $N \leq 300$—that the scattering continuum plays a negligible role. This is consistent with the findings of Ref. [106]. Thus, the results presented are calculated using N up to 9001, excluding the scattering continuum from the Hilbert space.

Two numerical approaches are used. First, we use the Runge-Kutta algorithm [164] with adjustable time step to propagate the coefficients for a given initial state at $t = 0$ to time t. Second, we express the Hamiltonian $\hat{H}$ in terms of the uncoupled $g = 0$ basis states using the matrix elements defined above. Determining the finite g eigen states through diagonalization, we project the initial state onto the eigen states of $\hat{H}$. Since the exact diagonalization approach is numerically more stable, the results presented in this paper are obtained using that approach.

The eigen spectrum of $\hat{H}$ provides complementary clues for understanding the emitter dynamics. For finite g, eigen states with hybridized character that contain photon and emitter contributions can exist [60]; for certain parameter combinations, these strongly-mixed states have energies that lie "outside" the two-photon bound state band. These states are discussed in more detail in Sec. 4.3. Hybridized light-matter states play a critical role in many other related contexts [165, 108, 167, 166].

4.2.4 Adiabatic elimination of single-photon states

This section discusses the construction of a reduced dimensionality Hamiltonian that "lives" in the Hilbert space spanned by the states $|g, g, \mathrm{vac}\rangle$, $\hat{P}^\dagger_{K,b}|g, g, \mathrm{vac}\rangle$, and $\hat{P}^\dagger_{K,q}|g, g, \mathrm{vac}\rangle$. The basis states $\hat{a}^\dagger_k|e, g, \mathrm{vac}\rangle$ and $\hat{a}^\dagger_k|g, e, \mathrm{vac}\rangle$ are removed and accounted for approximately

through effective interactions in the reduced dimensionality Hilbert space [see Figs. 4.1(b) and 4.1(c)]. The construction of the reduced dimensionality Hamiltonian is based on the adiabatic elimination of $c_{1k}(t)$ and $c_{2k}(t)$ from the coupled equations [106, 169]. The approximation requires that the change of $c_{1k}(t)$ and $c_{2k}(t)$ with time in Eqs. (4.16)-(4.19) can be neglected.

Even though the adiabatic elimination approach removes $c_{1k}(t)$ and $c_{2k}(t)$ from the coupled equations, we emphasize that the single-photon states play an important role even in the regime where the differential equations after adiabatic elimination provide a faithful description of the dynamics. This can be seen by inspecting Eqs. (4.16)-(4.19). If we start, e.g., with $c_{ee}(0) = 1$, then the evolution of the initial state for $t = 0^+$ is driven by the change of $\dot{c}_{\alpha k}(t)$; this follows since the $c_{ee}(t)$-coefficient appears on the right hand side of Eq. (4.17) but not on the right hand side of Eqs. (4.18) and (4.19). The key point of the adiabatic elimination is that the single-photon states serve as intermediate states—population goes into and out of these states at roughly equal rates such that the majority of the population is in the basis states with two emitter excitations and zero emitter excitations. The adiabatic elimination breaks down when g becomes too large (the actual value of g/J depends on the values of δ/J, U/J, and x/a).

Carrying out the adiabatic elimination and neglecting the effective coupling matrix elements $H_{K,K',q}(n_1,n_2)$ and $J_{K,K',q,q'}(n_1,n_2)$ that involve the two-photon scattering continuum (see Appendix B), Eqs. (4.16)-(4.19) reduce to a set of differential equations that can be written in terms of the effective adiabatic Hamiltonian $\hat{H}^{\rm adia}$. In matrix form, we find [106]

$$\imath\hbar\frac{\partial}{\partial t}\begin{pmatrix} c_{ee}(t) \\ \vec{c}_{K,b}(t) \end{pmatrix} = \underline{H}^{\rm adia}\begin{pmatrix} c_{ee}(t) \\ \vec{c}_{K,b}(t) \end{pmatrix}, \tag{4.26}$$

where

$$\vec{c}_{K,b}(t) = (c_{K_1,b}(t),\cdots,c_{K_N,b}(t))^T, \tag{4.27}$$

$$\underline{H}^{\text{adia}} = \begin{pmatrix} 2\Delta_e & 0 \\ 0 & \underline{\Delta}_{K,b} \end{pmatrix} + \frac{g^2}{J} \begin{pmatrix} 0 & N^{-1/2}(\vec{F}_{K,b}(n_1,n_2))^T \\ N^{-1/2}[\vec{F}_{K,b}(n_1,n_2)]^* & N^{-1}\underline{G}_{K,K'}(n_1,n_2) \end{pmatrix}, \tag{4.28}$$

and

$$\vec{F}_{K,b}(n_1,n_2) = (F_{K_1,b}(n_1,n_2),\cdots,F_{K_N,b}(n_1,n_2))^T. \tag{4.29}$$

The definition of the vector $\vec{F}_{K,b}(n_1,n_2)$ is given in Eq. (B.4). The matrices $\underline{\Delta}_{K,b}$ and $\underline{G}_{K,K'}(n_1,n_2)$ have dimension $N\times N$: $\underline{\Delta}_{K,b}$ is diagonal with $\Delta_{K_1,b},\cdots,\Delta_{K_N,b}$ on the diagonal and the elements of $\underline{G}_{K,K'}(n_1,n_2)$ are given by $G_{K_l,K_{l'}}(n_1,n_2)$ [Eq. (B.6)], with l and l' taking the values $1,\cdots,N$. The second term on the right hand side of Eq. (4.28) represents effective interactions that arise due to the elimination of the single-photon states. The element $F_{K_l,b}(n_1,n_2)$ represents an effective interaction between the state $|e,e,\text{vac}\rangle$ and the two-photon bound state with center-of-mass wave number K_l while the element $G_{K_l,K_{l'}}(n_1,n_2)$ represents an effective interaction between the two-photon bound state with wave number K_l and the two-photon bound state with wave number $K_{l'}$. We note that $F_{K_l}(n_1,n_2)$ and $G_{K_l,K'_{l'}}(n_1,n_2)$ are independent of g and, in general, complex.

Figure 4.3 shows $\vec{F}_{K,b}(n_1,n_2)$ as functions of Ka/π and x/a for $\delta/J = 0.0011$ and two different U/J, namely $U/J=-1$ (top row) and $U/J=-5/2$ (bottom row). The real and imaginary parts of $\vec{F}_{K,b}(n_1,n_2)$ are shown in the left and right columns, respectively. We note that the system properties only depend on the emitter separation x/a and not independently on the actual emitter positions n_1 and n_2; to make Fig. 4.3, the separation is—to aid with the visualization—treated as a continuous as opposed to a discrete variable. The magnitude of the real part of the effective interactions is larger for $U/J=-1$ (weakly-bound state) than for $U/J=-5/2$ (more strongly-bound state). The characteristics common to both U/J values considered in Fig. 4.3 are: First, the real part of the effective interactions is most negative near $Ka/\pi = x/a = 0$, even though the resonance wave vector $K^{(0)}$ differs in the two cases

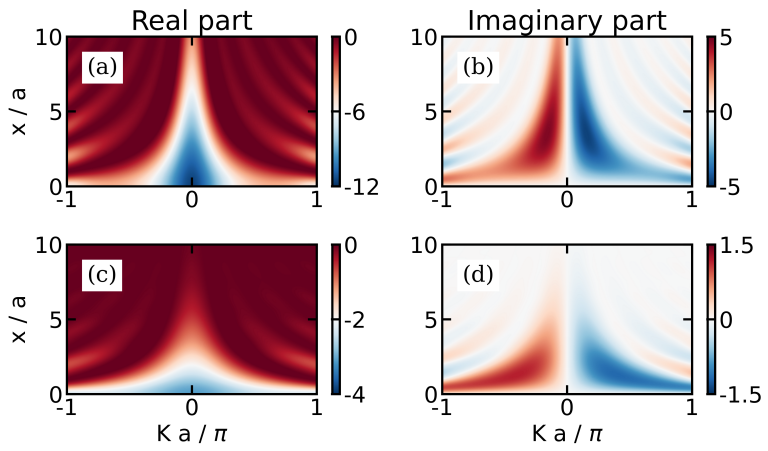

Figure 4.3: Contour plots of the effective dimensionless interactions $\vec{F}_{K,b}(n_1,n_2)$ between the states $|e,e,\mathrm{vac}\rangle$ and $\hat{P}^{\dagger}_{K,b}|g,g,\mathrm{vac}\rangle$ as functions of Ka/π and x/a for $\delta/J = 0.0011$; to obtain the actual interaction strength, $\vec{F}_{K,b}(n_1,n_2)$ needs to be multiplied by $g^2/(N^{1/2}J)$. (a) $\mathrm{Re}[\vec{F}_{K,b}(n_1,n_2)]$ for $U/J = -1$. (b) $\mathrm{Im}[\vec{F}_{K,b}(n_1,n_2)]$ for $U/J = -1$. (c) $\mathrm{Re}[\vec{F}_{K,b}(n_1,n_2)]$ for $U/J = -5/2$. (d) $\mathrm{Im}[\vec{F}_{K,b}(n_1,n_2)]$ for $U/J = -5/2$. The color scheme for each of the four panels is different.

$[K^{(0)}a/\pi = 0.0152$ for Figs. 4.3(a)/(b) and $K^{(0)}a/\pi = 0.0162$ for Figs. 4.3(c)/(d)]. Second, the real part of the effective interactions displays a larger K dependence for $x/a = 0$ than for $x/a > 0$. Third, for fixed Ka/π, the real part of the effective interactions is characterized by an overall fall-off that sits on top of small amplitude oscillations. Fourth, the magnitude of the imaginary part of the effective interactions is very small for $Ka/\pi \approx 0$. The separation and wave vector dependencies of $\vec{F}_{K,b}(n_1,n_2)$ have, as shown in the later sections, a strong impact on the system dynamics.

Section 4.4 shows that the effective interactions $\underline{G}_{K,K'}(n_1,n_2)$ play a non-negligible role for scenarios (B) and (C), corresponding to the horizontal solid and dotted lines in Fig. 4.2(b). The effective interactions $\underline{G}_{K,K'}(n_1,n_2)$ between two two-photon bound states, one with K and the other with K', depend—for fixed U/J and δ/J—on Ka, $K'a$, and x/a. Figure 4.4

shows the real part of $\underline{G}_{K,K'}(n_1,n_2)$ for $\delta/J = 0.0011$ for two different separations, namely, $x = 0$ (top row) and $x/a = 10$ (bottom row). The left and right columns are for $U/J = -1$ and $U/J = -5/2$, respectively. The key characteristics are: (i) The oscillatory structure of the real part of $\underline{G}_{K,K'}(n_1,n_2)$ increases with increasing separation. (ii) For the onsite interaction and detuning considered, the real part of $\underline{G}_{K,K'}(n_1,n_2)$ is negative; the most negative values are found for $K = K' = 0$ for $x/a = 0$ and $x/a = 10$. We note that the imaginary part of $\underline{G}_{K,K'}(n_1,n_2)$ (not shown) is zero for $K = K'$.

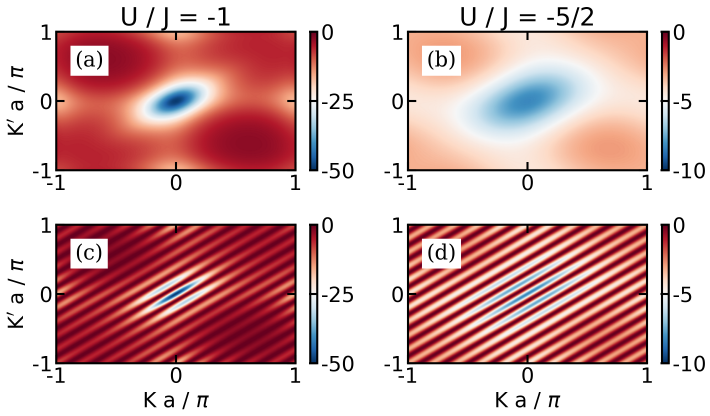

Figure 4.4: Contour plots of the real part of the effective dimensionless interactions $\underline{G}_{K,K'}(n_1,n_2)$ between the states $|g,g,K\rangle$ and $|g,g,K'\rangle$ as functions of Ka/π and $K'a/\pi$ for $\delta/J = 0.0011$; to obtain the actual interaction strength, $\underline{G}_{K,K'}(n_1,n_2)$ needs to be multiplied by $g^2/(NJ)$. (a) $\mathrm{Re}[\underline{G}_{K,K'}(n_1,n_2)]$ for $U/J = -1$ and $x/a = 0$. (b) $\mathrm{Re}[\underline{G}_{K,K'}(n_1,n_2)]$ for $U/J = -5/2$ and $x/a = 0$. (c) $\mathrm{Re}[\underline{G}_{K,K'}(n_1,n_2)]$ for $U/J = -1$ and $x/a = 10$. (d) $\mathrm{Re}[\underline{G}_{K,K'}(n_1,n_2)]$ for $U/J = -5/2$ and $x/a = 10$. The color schemes for $U/J = -1$ [(a) and (c)] are the same; similarly, the color schemes for $U/J = -5/2$ [(b) and (d)] are the same.

Since $\hat{H}^{\mathrm{adia}}$ is hermitian [this can be seen readily by inspecting $\underline{G}_{K,K'}(n_1,n_2)$], the population is normalized at all times, i.e., $|c_{ee}(t)|^2 + \sum_K |c_{K,b}(t)|^2 = 1$, and the eigen energies of $\hat{H}^{\mathrm{adia}}$ are real. The validity of the approximations (adiabatic elimination and dropping of scattering states) can thus be assessed in two complementary ways, namely by comparing

the time evolution of, e.g., the initial state $|e,e,\mathrm{vac}\rangle$ under $\hat{H}$ and $\hat{H}^{\mathrm{adia}}$ and by comparing the eigen spectra of $\hat{H}$ and $\hat{H}^{\mathrm{adia}}$. Reference [106] constructed a master equation, using Eq. (4.28) with $G_{K_l,K_{l'}}(n_1,n_2)=0$ as a starting point. We denote $\hat{H}^{\mathrm{adia}}$ with $G_{K_l,K_{l'}}(n_1,n_2)=0$ and $\neq 0$ by $\hat{H}^{\mathrm{adia},0}$ and $\hat{H}^{\mathrm{adia},1}$, respectively. Section 4.4 shows that $\hat{H}^{\mathrm{adia},1}$ significantly expands the applicability regime of the reduced dimensionality Hamiltonian compared to $\hat{H}^{\mathrm{adia},0}$ in certain parameter regimes.

4.2.5 Markov approximation for $\hat{H}^{\mathbf{adia},0}$

For scenario (A), the population of the initial state $|e,e,\mathrm{vac}\rangle$ decays approximately exponentially for x/a not too large. As shown in Ref. [106], the decay constant can be determined analytically in this regime using the Markov approximation. Appendix B shows that $\tilde{c}_{ee}(t)$, where $\tilde{c}_{ee}(t)$ denotes the expansion coefficient for the state that rotates with $2\Delta_e$, falls off exponentially according to

$$\tilde{c}_{ee}(t)=\exp\left(-\Gamma_{\mathrm{bath}}t\right), \tag{4.30}$$

where Γ_{bath} is given by

$$\Gamma_{\mathrm{bath}}=\frac{g^4 a}{J^3\hbar}|F_{K^{(*)},b}(n_1,n_2)|^2\rho(K^{(*)}). \tag{4.31}$$

Here, $K^{(*)}$ is defined through

$$E_{K^{(*)},b}=2\hbar\omega_e+2\Delta_e, \tag{4.32}$$

with the "Stark shift" $2\Delta_e$ [106],

$$2\Delta_e=-\frac{2}{N}\sum_k\frac{g^2}{\Delta_k}, \tag{4.33}$$

quantifying the shift of the state $|e,e,\mathrm{vac}\rangle$ due to the "renormalization" by the single-photon states. Correspondingly, the decoupled ($g=0$) resonance wave number $K^{(0)}$ gets shifted to $K^{(*)}$ for finite g/J; the use of $K^{(*)}$ in place of $K^{(0)}$, as done in Ref. [106], provides an

improved description. The density of states $\rho(K^{(*)})$ at the resonance wave vector can be written as

$$\rho(K^{(*)}) = J\left(\hbar v_{K^{(*)},b}\right)^{-1}. \tag{4.34}$$

When $|g/J|$ is not much smaller than 1, the adiabatic elimination and, correspondingly, the concept of a resonant wave number looses its meaning. The importance of the Stark shift $2\Delta_e$ increases as $K^{(0)}a$ and, correspondingly, the detuning δ/J approach zero.

Figures 4.5(a) and 4.5(b) show the decay constant $\Gamma_{\text{bath}}\hbar J^3/g^4$ as a function of the onsite interaction U/J and the detuning δ/J, respectively, for various separations ($x/a = 0$ to 6). It can be seen that the radiation dynamics is characterized by a larger dimensionless decay constant (faster decay) for $x/a = 0$ (solid line) than for $x/a = 6$ (dash-dotted line). This makes sense intuitively since a larger separation is associated with a smaller, in magnitude, effective interaction $F_{K^{(*)},b}(n_1,n_2)$. The dependence on U/J [see Fig. 4.5(a)] can also be understood readily intuitively. As $|U/J|$ increases, the two-photon bound state becomes more localized and the coupling to the state $|e,e,\text{vac}\rangle$ decreases. The Markov approximation results shown in Fig. 4.5(a) agree quite well with the decay constants extracted from full numerical calculations (not shown).

The dependence of the dimensionless decay constant, calculated within the Markov approximation, on the detuning is non-monotonic [see Fig. 4.5(b)]. The increase of $\Gamma_{\text{bath}}\hbar J^3/g^4$ as the dimensionless detuning δ/J, for fixed x/a, approaches zero [left part of Fig. 4.5(b)] is unphysical. This increase is due to the break-down of the Markov approximation in the vicinity of the bottom of the band, where the density of states of two-photon bound states is large and diverges as $\delta/J \to 0$. The open circles in Fig. 4.5(b) show the decay constant for $x/a = 0$, extracted from calculations for the full Hamiltonian $\hat{H}$. While the agreement with the Markov approximation results is quite good, we note that the full dynamics displays non-exponential characteristics for small δ/J that get "averaged" when fitting to an exponential. The Markov approximation also breaks down when δ/J becomes too large

[right part of Fig. 4.5(b)]. The reason for this break-down is that the adiabatic elimination is not valid when $2\hbar\omega_e$ is close to the two-photon scattering continuum.

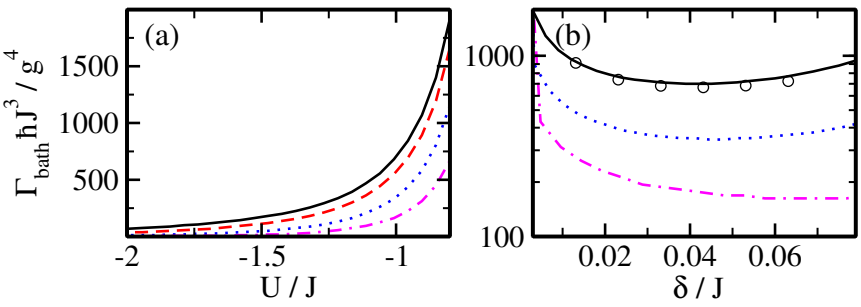

Figure 4.5: Lines show the dimensionless decay constant $\Gamma_{\text{bath}}\hbar J^3/g^4$, obtained within the Markov approximation [Eq. (4.31)]. (a) The black solid, red dashed, blue dotted, and magenta dash-dotted lines show $\Gamma_{\text{bath}}\hbar J^3/g^4$ as a function of U/J for $\delta/J = 0.0431$ and $x/a = 0$, 2, 4, and 6, respectively. (b) The black solid, blue dotted, and magenta dash-dotted lines show $\Gamma_{\text{bath}}\hbar J^3/g^4$ as a function of δ/J for $U/J = -1$ and $x/a = 0$, 4, and 6, respectively. For comparison, the open black circles show the decay constant extracted from the dynamics for the full Hamiltonian $\hat{H}$ for $x/a = 0$ and $g/J = 1/50$; the Markov approximation results (solid line) capture the decay constant extracted from the full decay dynamics quite well. Note that the Markov approximation breaks down when δ/J approaches zero (left portion of the panel) and when δ/J approaches the two-photon scattering continuum (right portion of the panel).

To recapitulate, we arrived at Eq. (4.30) by making four distinct approximations: adiabatically eliminating $c_{1k}(t)$ and $c_{2k}(t)$, neglecting the two-photon scattering continuum, neglecting $\underline{G}_{K,K'}(n_1,n_2)$, and making the Markov approximation. It is useful to compare the results obtained for the two-emitter case with non-linear bath to those for a single emitter [$\hat{H}$ in Eq. (4.2) with $N_e = 1$ and $U = 0$ with initial state $|e,\text{vac}\rangle$]. Appendix A shows that the decay constant Γ_{single} for the single-emitter system evaluates within the Markov

approximation to

$$\Gamma_{\text{single}} = \frac{g^2 a}{\hbar J} \rho_{\text{single}}(k^{(0)}), \tag{4.35}$$

where

$$\rho_{\text{single}}(k^{(0)}) = J \left(\hbar v_{k^{(0)}}\right)^{-1}, \tag{4.36}$$

with $k^{(0)}$ denoting the single-photon resonance wave vector.

Comparison of Eqs. (4.31) and (4.35) indicates that the two-emitter dynamics, in the regime where $|c_{ee}(t)|^2$—starting in the state $|e,e,\text{vac}\rangle$—falls off exponentially, is the same as that for the single emitter system, provided (i) the dimensionless densities of states $a\rho(K^{(*)})$ and $a\rho_{\text{single}}(k^{(0)})$ take the same value and (ii) the coupling constant g_{single} of the single emitter system is set to

$$g_{\text{single}} = \frac{g^2}{J} |F_{K^{(*)},b}(n_1, n_2)|; \tag{4.37}$$

the quantities on the right hand side are understood to be those characterizing the two-emitter system. To match the densities of states, we consider $K^{(*)}a$ and $k^{(0)}a$ values that are sufficiently large for the Markov approximation to hold but sufficiently small for $\Delta_{K,b}$ and E_k to be well approximated by their Taylor-expanded expressions up to order $(Ka)^2$ and $(ka)^2$, respectively. Comparing the slopes of the quadratic terms, we find that the dimensionless densities of states match if the tunneling coupling strength J_{single} of the single emitter system is set to

$$J_{\text{single}} = 2J \left[\left(\frac{U}{J}\right)^2 + 16 \cos^2 \left(\frac{K^{(*)} a}{2} \right) \right]^{-1/2}; \tag{4.38}$$

the quantities on the right hand side are, again, understood to be those characterizing the two-emitter system.

The meaning of Eqs. (4.37) and (4.38) is as follows. Say we have a coupled two-emitter–cavity system in the Markovian regime. For a given U/J, g/J, δ/J, and x/a, this implies

that the exponential decay of the population is characterized by Γ_{bath}. Imagine now that we want to design a coupled single-emitter–cavity system such that the exponential decay of $|d_e(t)|^2$, see Eq. (B.1), is characterized by $\Gamma_{\text{single}} = \Gamma_{\text{bath}}$. This goal is accomplished if the tunneling coupling strength J_{single} and coupling strength g_{single} of the single-emitter–cavity system are chosen according to Eqs. (4.37) and (4.38).

Using that $|F_{K^{(*)},b}(n_1,n_2)|$ is—for the parameters considered in this paper (see Fig. 4.3 for two examples)—of the order of 1 to 10, Eq. (4.37) shows that the two-emitter dynamics considered is slower than the single-emitter dynamics would be if the single emitter was in resonance with the single-photon band. Importantly, if the two-emitter energy is in resonance with the two-photon bound state band, then the single-emitter energy is not in resonance with the single-photon band (at least not for the parameters considered in this work). We note that appreciable single-emitter dynamics is observed for large x/a for certain parameter combinations (see Sec. 4.4 for details).

4.3 Stationary solution

This section discusses the stationary solutions of the coupled emitter-cavity system under study. Section 4.3.1 provides an overview for different detunings while Sec. 4.3.2 focuses on the physics near the bottom of the band.

4.3.1 Overview

To assess the reliability of the different approximations, we compare the energy spectrum obtained by diagonalizing $\hat{H}^{\text{adia,0}}$, $\hat{H}^{\text{adia,1}}$, and $\hat{H}$ (using a basis that excludes the two-photon scattering states) for $U/J = -1$ for various δ/J. Figure 4.6(a) shows the lowest two eigen energies for $x/a = 0$. The zero of the energy axis corresponds to the bottom of the $g = 0$ two-photon energy band. The eigen energies of the full Hamiltonian (open circles) are reproduced much better by $\hat{H}^{\text{adia,1}}$ (black solid lines) than by $\hat{H}^{\text{adia,0}}$ (red dashed lines).

Specifically, neglecting the effective interactions $\underline{G}_{K,K'}(n_1,n_2)$ leads to a weakening of the binding of the lowest energy state, especially for positive δ/J. The lowest energy state is a hybridized bound state that contains contributions from the state $|e,e,\text{vac}\rangle$ and two-photon bound states. The hybridized state is clearly separated from the energy continuum. The character of the lowest energy eigen state is elucidated in the next section.

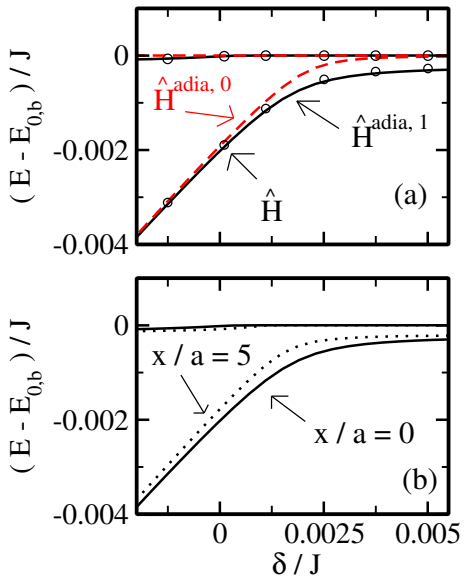

Figure 4.6: Energy of the two lowest eigen states as a function of δ/J for $U/J=-1$ and $g/J=1/50$. (a) The black solid and red dashed lines show the energy for $\hat{H}^{\text{adia},1}$ and $\hat{H}^{\text{adia},0}$, respectively, for $x=0$. For comparison, the open circles show the eigen energies for $\hat{H}$ (using a basis that excludes the two-photon scattering states). The energies for $\hat{H}$ and $\hat{H}^{\text{adia},1}$ agree very well. (b) The black solid and black dotted lines show the energies of $\hat{H}^{\text{adia},1}$ for $x/a=0$ and $x/a=5$, respectively. A clear separation dependence can be seen. In both panels, the lower state corresponds to a hybridized bound state with appreciable $|e,e,\text{vac}\rangle$ and $|g,g,\text{pol}\rangle$ contributions (see Sec. 4.3.2 for details).

The density of states $\rho_E(E)$ (number of states per unit energy interval) of the energy continuum, which reduces to the two-photon bound state band for $g=0$, is shown by the color map in Fig. 4.7 for the same parameters as those used in Fig. 4.6(a). The density of

states is large near the bottom of the energy band and decreases as one moves away from the bottom of the band. While the coupling constant g has a profound effect on the two lowest eigen states (black solid and dashed lines in Fig. 4.7), the density of states depends comparatively weakly on g.

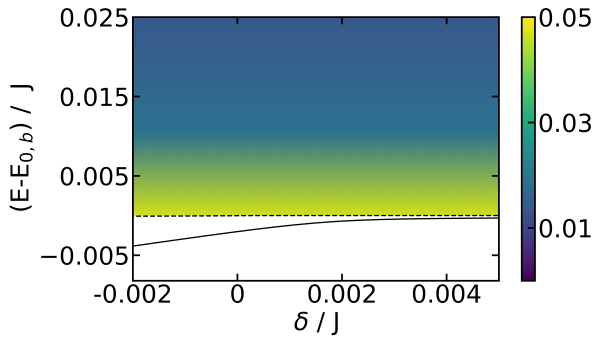

Figure 4.7: Visualization of eigen spectrum of $\hat{H}^{\text{adia},1}$ as a function of the detuning δ/J for $U/J = -1$, $g/J = 1/50$, and $x = 0$. The density of states $\rho_E(E)$ of the continuum portion of the energy spectrum, which is dominated by states that have no or extremely small emitter admixtures, is shown in color (the legend is shown on the right; arbitrary units are used). The lowest hybridized bound state (black solid line) is well separated from the energy continuum. The second lowest state (black dashed line) is separated by a small gap from the continuum for negative δ/J and part of the continuum for positive δ/J.

To elucidate the dependence on the separation for $U/J = -1$, we work with $\hat{H}^{\text{adia},1}$. Figure 4.6(b) shows the two lowest eigen energies as a function of δ/J for $x/a = 0$ (solid line) and $x/a = 5$ (dotted line). The binding energy of the lowest hybridized bound state decreases with increasing x/a. This might be expected naively since a larger emitter separation is associated with reduced interactions. Interestingly, the second lowest energy state has a somewhat lower energy for $x/a = 5$ than for $x/a = 0$; this can be seen most clearly in Fig. 4.6(b) for negative detuning but also holds true for positive δ/J. An analysis of the corresponding eigen state reveals that the second lowest state for $x/a = 5$ has bound

state character not only for negative but also for positive detuning. For $x/a = 0$, in contrast, the second lowest state merges into the continuum when the detuning is positive. The emergence of a second bound state with increasing separation is somewhat counterintuitive. We checked that the full Hamiltonian $\hat{H}$ also supports a second bound state, i.e., we checked that its appearance is not an artefact of the adiabatic approximation. To gain additional insights, the next section discusses a two-state model that captures key aspects of the two hybridized bound states that exist for $U/J = -1$, small detuning, and sufficiently large x/a.

4.3.2 Near the bottom of the band: Two-state model

An important conclusion of the previous section is that the adiabatic Hamiltonian $\hat{H}^{\text{adia,1}}$ captures the key features of the bound states supported by the full Hamiltonian $\hat{H}$. Using $\hat{H}^{\text{adia,1}}$, we now review the physical picture that was introduced in Ref. [60]. Since the effective interactions $\underline{G}_{K,K'}(n_1,n_2)$ cannot be neglected near the bottom of the band (see the previous section), the bath Hamiltonian contains off-diagonals in the $\{|g,g,K\rangle, |e,e,\text{vac}\rangle\}$ basis. To proceed, we change the basis. We continue to use $|g,g\rangle$ and $|e,e\rangle$ with energy 0 and $2\Delta_e$, respectively, for the two emitters. For the two-photon bath Hamiltonian, in contrast, we change from the basis states $|K\rangle$, in which the bath is characterized by effective interactions between two-photon bound states with center-of-mass wave numbers K and K',

$$\underline{H}_{\text{b}}^{\text{adia,1}} = \underline{\Delta}_{K,b} + \frac{g^2}{JN}\underline{G}_{K,K'}(n_1,n_2), \tag{4.39}$$

to a basis in which the bath Hamiltonian $\hat{H}_{\text{b}}^{\text{adia,1}}$ is diagonal. Performing the diagonalization, we find that the energy spectrum of the adiabatic bath Hamiltonian $\hat{H}_{\text{b}}^{\text{adia,1}}$ consists of a continuum, similar to the two-photon bound state band, and an "isolated state" whose energy is energetically separated from the bottom of the two-excitation continuum; this state lives in the band gap and corresponds to a bound state.

The isolated state $|\text{pol}\rangle$ is well reproduced by an ansatz with Lorentzian distributed

expansion coefficients d_K [60],

$$|\text{pol}\rangle = \sum_K d_K |K\rangle \tag{4.40}$$

and

$$d_K = \frac{(2L_{\text{eff}}^{-1}a)^{3/2}}{\sqrt{N}} \frac{1}{(2Ka)^2 + (L_{\text{eff}}^{-1}a)^2}, \tag{4.41}$$

where the normalization is chosen such that

$$a\int_{-\infty}^{\infty} |d_K|^2 dK = 1. \tag{4.42}$$

In writing this ansatz, it is assumed that $L_{\text{eff}}^{-1}a$ is much smaller than π so that the integration limits can be safely extended from $\pm\pi$ to $\pm\infty$. We refer to the isolated state as a polaron-like state as it represents a quasi-particle that is a superposition of states with different center-of-mass momenta. The wave number width of the expansion coefficients d_K is given by $(L_{\text{eff}})^{-1}$. We determine L_{eff} by minimizing the ground state energy of $\hat{H}_{\text{b}}^{\text{adia,1}}$. To make the calculations tractable analytically, we approximate the effective interactions $\underline{G}_{K,K'}(n_1,n_2)$ by a constant, namely their value at $K = K' = K^{(0)}$. We find

$$\frac{L_{\text{eff}}}{a} = \frac{2J^3}{g^2|G_{K^{(0)},K^{(0)}}(n_1,n_2)|\sqrt{U^2+16J^2}} \tag{4.43}$$

and

$$E_{\text{pol}} = -\delta - \frac{g^4}{8J^4}|G_{K^{(0)},K^{(0)}}(n_1,n_2)|^2\sqrt{U^2+16J^2}. \tag{4.44}$$

This variational result reproduces the numerically determined ground state energy of $\hat{H}_{\text{b}}^{\text{adia,1}}$ very well. In the condensed matter context, the Hamiltonian that supports the polaron-like state shows up when an impurity or defect in a one-dimensional lattice is associated with attractive all-to-all momentum space interactions. All-to-all interactions are currently being investigated by a number of groups due to their relevance in quantum gravity and spin glass physics [170, 171, 172].

As already alluded to in Sec. 4.2.4, the effective interactions $\underline{G}_{K,K'}(n_1,n_2)$ are essentially purely real for $K = K'$. Figures 4.8(c) and 4.8(d) show $\mathrm{Re}[G_{K^{(0)},K^{(0)}}(n_1,n_2)]$ as functions of δ/J and U/J for $x/a = 0$ and $x/a = 10$, respectively. It can be seen that $G_{K^{(0)},K^{(0)}}(n_1,n_2)$ depends extremely weakly on the separation x/a. Consequently, the energy E_{pol} of the photonic polaron is to a very good approximation independent of the emitter separation x/a.

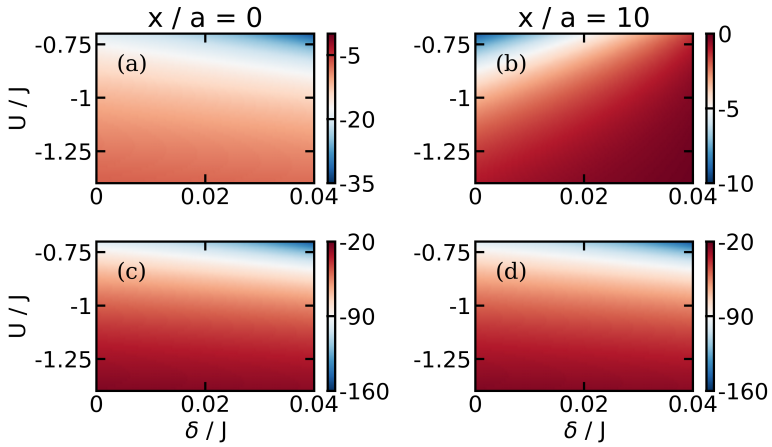

Figure 4.8: Contour plots of the effective dimensionless interaction $F_{K^{(0)},b}(n_1,n_2)$ between the states $|e,e,\mathrm{vac}\rangle$ and $\hat{P}^{\dagger}_{K^{(0)},b}|g,g,\mathrm{vac}\rangle$ and the effective dimensionless interaction $G_{K^{(0)},K^{(0)}}(n_1,n_2)$ between the states $|g,g,K^{(0)}\rangle$ and $|g,g,K^{(0)}\rangle$ as functions of δ/J and U/J; to obtain the actual interaction strengths, $F_{K^{(0)},b}(n_1,n_2)$ and $G_{K^{(0)},K^{(0)}}(n_1,n_2)$ need to be multiplied by $g^2/(N^{1/2}J)$ and $g^2/(NJ)$, respectively. (a) $\mathrm{Re}[F_{K^{(0)},b}(n_1,n_2)]$ for $x/a = 0$. (b) $\mathrm{Re}[F_{K^{(0)},b}(n_1,n_2)]$ for $x/a = 10$. (c) $\mathrm{Re}[G_{K^{(0)},K^{(0)}}(n_1,n_2)]$ for $x/a = 0$. (d) $\mathrm{Re}[G_{K^{(0)},K^{(0)}}(n_1,n_2)]$ for $x/a = 10$. The color schemes for $\mathrm{Re}[F_{K^{(0)},b}(n_1,n_2)]$ are different for the two separations. The color schemes for $\mathrm{Re}[G_{K^{(0)},K^{(0)}}(n_1,n_2)]$, in contrast, are the same for the two separations.

Next, we rewrite $\hat{H}^{\mathrm{adia,1}}$ in the product basis in which the emitter and bath Hamiltonians are diagonal. Transforming the system-bath coupling $g^2N^{-1/2}\vec{F}_{K,b}(n_1,n_2)/J$ to the new basis and restricting the Hilbert space to the states $|e,e,\mathrm{vac}\rangle$ and $|g,g,\mathrm{pol}\rangle$, we arrive at the

following matrix representation of the two-state Hamiltonian $\hat{H}^{\text{2-st.}}$:

$$\underline{H}^{\text{2-st.}} = \begin{pmatrix} 2\Delta_e & G_{\text{eff}}(n_1,n_2) \\ [G_{\text{eff}}(n_1,n_2)]^* & E_{\text{pol}} \end{pmatrix}. \tag{4.45}$$

Using our variational expression for $|g,g,\text{pol}\rangle$, the effective coupling $G_{\text{eff}}(n_1,n_2)$ between states $|e,e,\text{vac}\rangle$ and $|g,g,\text{pol}\rangle$ can be written as

$$G_{\text{eff}}(n_1,n_2) = \frac{g^3(U^2+16J^2)^{1/4}}{2J^{5/2}} \times F_{K^{(0)},b}(n_1,n_2)|G_{K^{(0)},K^{(0)}}(n_1,n_2)|^{1/2}. \tag{4.46}$$

Figures 4.8(a) and 4.8(b) show $\text{Re}[F_{K^{(0)},b}(n_1,n_2)]$ as functions of δ/J and U/J for $x/a=0$ and $x/a=10$, respectively. It can be seen that $\text{Re}[F_{K^{(0)},b}(n_1,n_2)]$ [Figs. 4.8(a)-4.8(b)] varies much more strongly with x/a than $\text{Re}[G_{K^{(0)},K^{(0)}}(n_1,n_2)]$ [Figs. 4.8(c)-4.8(d)]. We conclude that, in the regime where the two-state model $\hat{H}^{\text{2-st.}}$ provides a faithful description, the separation dependence of the hybridized energy eigen states of $\hat{H}$ (see the discussion surrounding Figs. 4.6 and 4.7) is due to the dependence of $G_{\text{eff}}(n_1,n_2)$ on $F_{K^{(0)},b}(n_1,n_2)$.

The eigen states $\Psi_\pm$ and eigen energies $E_\pm$ of $\hat{H}^{\text{2-st.}}$ read

$$\Psi_\pm = d_{\text{vac}}^{(\pm)}|e,e,\text{vac}\rangle + d_{\text{pol}}^{(\pm)}|g,g,\text{pol}\rangle \tag{4.47}$$

and

$$E_\pm = \left(\Delta_e + \frac{E_{\text{pol}}}{2}\right) \pm \sqrt{\left(\Delta_e - \frac{E_{\text{pol}}}{2}\right)^2 + |G_{\text{eff}}|^2}, \tag{4.48}$$

where the expansion coefficients $d_{\text{vac}}^{(\pm)}$ and $d_{\text{pol}}^{(\pm)}$ are given by

$$d_{\text{vac}}^{(\pm)} = N_\pm G_{\text{eff}} \tag{4.49}$$

and

$$d_{\text{pol}}^{(\pm)} = N_\pm \left(-\Delta_e + \frac{E_{\text{pol}}}{2} \pm \sqrt{\left(\Delta_e - \frac{E_{\text{pol}}}{2}\right)^2 + |G_{\text{eff}}|^2}\right), \tag{4.50}$$

respectively; in Eqs. (4.49)-(4.50), N_+ and N_- denote normalization constants. We refer to Ψ_+ and Ψ_- as symmetric hybridized state and anti-symmetric hybridized state, respectively.

Figure 4.9 compares the two eigen energies supported by $\hat{H}^{\text{2-st.}}$ (red solid lines) for $\delta/J = 0.0011$ and $x/a = 10$ with the two eigen energies of $\hat{H}$, whose eigen states have the largest overlap with the initial state $|e,e,\text{vac}\rangle$ (black circles), as a function of U/J. The two-state model reproduces the energy of the hybridized energy eigen states of the full Hamiltonian well. The state Ψ_- is bound for $|U/J|$ values smaller than 1.4 and unbound for $|U/J|$ values larger than 1.4. Since a strong onsite interaction (large $|U/J|$) corresponds to more localized two-photon bound states (in real space), the "reach" of the two-photon bound state for large $|U/J|$ is too small to induce a new bound state. As discussed in the next section, the two-state Hamiltonian $\hat{H}^{\text{2-st.}}$ describes several key characteristics of the dynamics predicted by the full Hamiltonian in the $|\delta/J| \to 0$ limit.

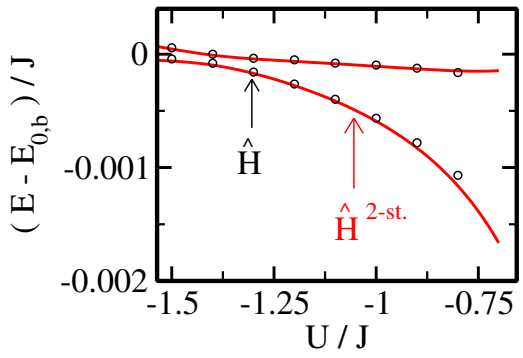

Figure 4.9: Energy of the hybridized states as a function of U/J for $g/J = 1/50$, $\delta/J = 0.0011$, and $x/a = 10$. The black circles and red lines are obtained using the full Hamiltonian $\hat{H}$ and the two-state Hamiltonian $\hat{H}^{\text{2-st.}}$, respectively. The agreement is very good for the parameter regime considered.

4.4 Dynamics

This section discusses the radiation dynamics for $U/J = -1$ for various detunings δ/J and separations x/a. Throughout, the initial state is taken to be the excited emitter state $|e,e,\text{vac}\rangle$. Figure 4.10 shows the decomposition of the state $|e,e,\text{vac}\rangle$ into the energy eigen states ϕ_E of $\hat{H}$ for $U/J = -1$ and two different separations, namely, $x/a = 0$ (top row) and $x/a = 10$ (bottom row). Two different detunings are considered: $\delta/J = 0.0431$ (left column) and $\delta/J = 0.0011$ (right column). As discussed in Sec. 4.2.5, the Markov approximation provides a good description of the radiation dynamics for $\delta/J = 0.0431$ but breaks down for $\delta/J = 0.0011$. For the larger detuning, the initial state is dominated by a few eigen states whose energy is close to those corresponding to $K^{(*)}$. The applicability of the Markov approximation relies on the fact that the overlap coefficients peak around one energy value and fall off quickly away from this energy. We emphasize that the overall behavior of the overlap coefficients for $x/a = 0$ [Fig. 4.10(a)] and $x/a = 10$ [Fig. 4.10(b)] is similar. Note, however, that the scale of the energy axis and the number of eigen states that contribute are significantly smaller for $x/a = 10$ than for $x/a = 0$.

As the detuning decreases to small positive values, where the two-emitter energy is very close to the bottom of the energy band, the decomposition of the initial state into the energy eigen states changes significantly. For $x/a = 0$, the initial state is dominated by a single state [red square in Fig. 4.10(c)] whose energy is separated from the energy continuum (round circles). Altogether, the states corresponding to the energy continuum contribute 34.5 %. For $x/a = 10$, in contrast, there are two energy eigen states that contribute appreciably [84.6 % and 12.0 %; see red squares in Fig. 4.10(d)]. The eigen states corresponding to the red squares in Figs. 4.10(c) and 4.10(d) are quite well described by the two-state model Hamiltonian $\hat{H}^{\text{2-st.}}$, Eq. (4.45).

Figure 4.11 shows the time evolution of the population $P_{ee}(t)$ of state $|e,e,\text{vac}\rangle$ for $U/J = -1$. For $\delta/J = 0.0431$ (left column), $P_{ee}(t)$ falls off roughly exponentially. The

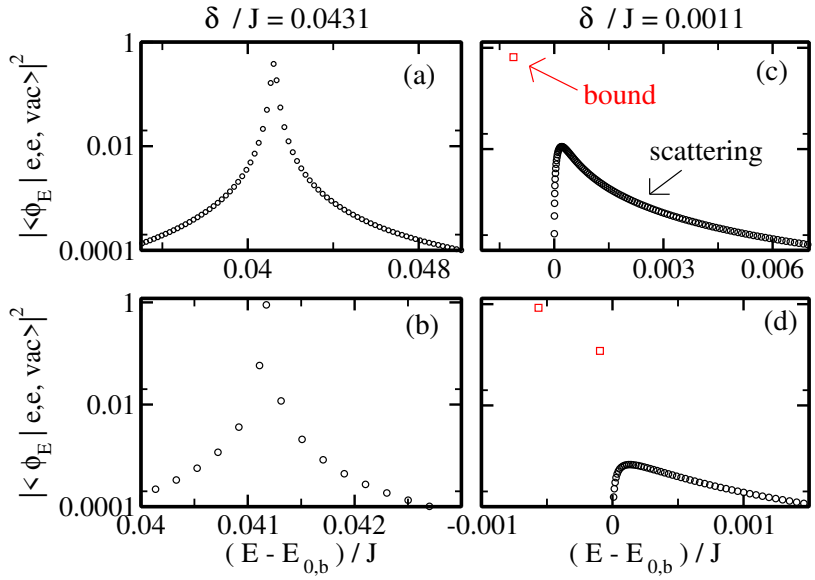

Figure 4.10: Projection of the initial state $|e,e,\mathrm{vac}\rangle$ onto the energy eigen states ϕ_E of $\hat{H}$ for $U/J=-1$ and $g/J=1/50$. The square of the absolute value of the overlap onto scattering states and bound states is shown by black circles and red squares, respectively, for (a) $\delta/J=0.0431$ and $x/a=0$, (b) $\delta/J=0.0431$ and $x/a=10$, (c) $\delta/J=0.0011$ and $x/a=0$, and (d) $\delta/J=0.0011$ and $x/a=10$.

decay is faster for $x/a=0$ [Fig. 4.11(a)] than for $x/a=5$ and $x/a=10$ [Figs. 4.11(b) and 4.11(c)]. For this large δ/J, the Markov approximation works well and the agreement between the results for $\hat{H}$ (solid lines), $\hat{H}^{\mathrm{adia},1}$ (dotted lines), and $\hat{H}^{\mathrm{adia},0}$ (dashed lines) is quite good. For $x/a=0$, 5, and 10, the population of the single-photon states (i.e., the sum of $\sum_{j=1,2}\sum_k |c_{jk}|^2$) is approximately equal to 1.8 %, 2.0 %, and 4.0 %, respectively. The comparatively large population of the single-photon states for $x/a=10$ signals that the adiabatic elimination deteriorates for large x/a. The inset of Fig. 4.11(c) shows that the radiation emitted by the first and second emitters are uncorrelated initially. We find that the oscillations displayed by the black solid line are well reproduced by the single-emitter dynamics, i.e., by treating the two emitters as independent quantities (effectively, this corresponds to setting $U=0$).

For small δ/J, the dynamics changes significantly. The middle and right most columns of Fig. 4.11 correspond to $\delta/J = 0.0011$ and $\delta/J = 0.0001$, respectively. For these two detunings, the population $P_{ee}(t)$ does not change exponentially but instead exhibits damped or essentially undamped oscillatory behaviors for $x/a = 0$, 5, and 10. For all six parameter combinations [Figs. 4.11(d)-4.11(i)], the adiabatic elimination Hamiltonian $\hat{H}^{\text{adia,1}}$ (red dotted lines), which accounts for the effective interactions $\underline{G}_{K,K'}(n_1,n_2)$, reproduces the key features of the dynamics of the full Hamiltonian $\hat{H}$ (black solid line)—such as the amplitude, frequency, and degree of damping—faithfully. The adiabatic elimination Hamiltonian $\hat{H}^{\text{adia,0}}$ (blue dashed lines), in contrast, provides a comparatively poor description of the oscillatory dynamics [Figs. 4.11(d)-4.11(i)]. The comparison shows that appearance of essentially undamped oscillations depends critically on the effective interactions $\underline{G}_{K,K'}(n_1,n_2)$; recall, these are not included in $\hat{H}^{\text{adia,0}}$. The inset of Fig. 4.11(i) illustrates, as for the larger detuning, that the elimination of the single-photon states from the Hilbert space does remove fast oscillations and fails to capture the initial decay of $P_{ee}(t)$ that is due to uncorrelated decay of single photons.

Figure 4.12 shows the populations $|c_{K,b}(t)|^2$ of the two-photon states $|g,g,K\rangle$ as functions of $Jt/\hbar$ and Ka/π for $\delta/J = 0.0431$ (top row) and $\delta/J = 0.0011$ (bottom row). The behavior for large and small detunings is distinct. For $\delta/J = 0.0431$, a few Ka/π values—centered around $K^{(*)}a/\pi$—get populated as time increases for $x/a = 0$ [Fig. 4.12(a)] and $x/a = 10$ [Fig. 4.12(c)]. The excitations, which exist initially in the form of matter, get transferred to the photons. Since the decay involves multiple states, the radiation emitted is incoherent. For $\delta/J = 0.0011$, the populations $|c_{K,b}(t)|^2$ with $K \approx 0$ oscillate in time for $x/a = 0$ [Fig. 4.12(b)] and $x/a = 10$ [Fig. 4.12(d)]. As expected, the oscillation frequencies are the same as those displayed in Figs. 4.11(d) and 4.11(f).

The undamped Rabi oscillations displayed in Fig. 4.11 are readily explained by the fact that the Hamiltonian $\hat{H}$ supports two bound states for sufficiently large x/a. The initial

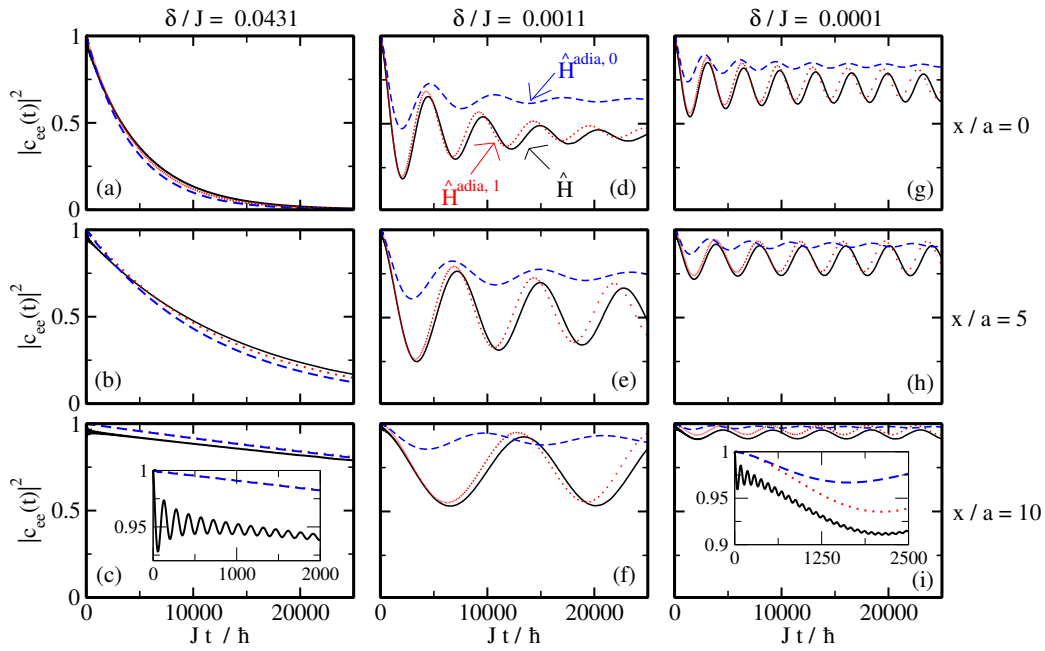

Figure 4.11: Radiation dynamics for the initial state $|e,e,\mathrm{vac}\rangle$, $U/J=-1$, and $g/J=1/50$. The lines show the population $P_{ee}(t)$ for various x/a and δ/J. The value of x/a increases from the top row to the bottom row ($x/a=0$, 5, and 10 for the first, second, and third row, respectively). The value of δ/J decreases from the left most to the right most column ($\delta/J=0.0431$, 0.0011, and 0.0001 for the first, second, and third column, respectively). In all panels, the solid, dotted, and dashed lines show $P_{ee}(t)$ obtained by propagating the initial state $|e,e,\mathrm{vac}\rangle$ under the Hamiltonian $\hat{H}$, $\hat{H}^{\mathrm{adia},1}$, and $\hat{H}^{\mathrm{adia},0}$, respectively. The data shown in panels (a)-(f) are also shown in Ref. [60].

state can, to a good approximation be written as a superposition of the symmetric and anti-symmetric hybridized energy eigen states Ψ_+ and Ψ_-. As a function of time, population is transferred between the two bound energy eigen states, with the angular oscillation frequency being equal to $(E_- - E_+)/\hbar$.

To explain the damping, we decompose the initial state $|e,e,\mathrm{vac}\rangle$ into the energy eigen states ϕ_E of $\hat{H}$. For this calculation, we divide the energy eigen states into two groups. The state ϕ_0 with energy E_0 (lowest energy eigen state) and the states $\{\phi_j\}$ with energy E_j

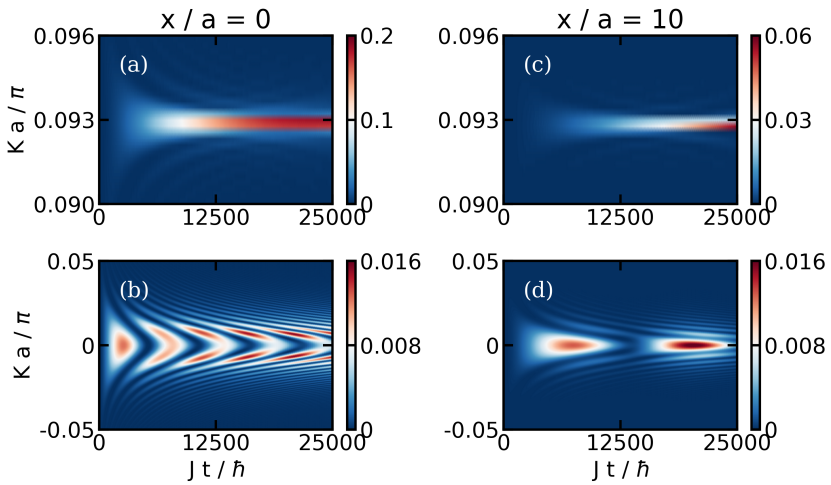

Figure 4.12: Contour plot of the populations $|c_{K,b}(t)|^2$ of the two-photon bound states $|g,g,K\rangle$ as functions of the dimensionless center-of-mass wave number Ka/π and the dimensionless time $Jt/\hbar$ for $U/J=-1$ and $g/J=1/50$. (a) $\delta/J=0.0431$ and $x/a=0$. (b) $\delta/J=0.0011$ and $x/a=0$. (c) $\delta/J=0.0431$ and $x/a=10$. (d) $\delta/J=0.0011$ and $x/a=10$. The color scheme and range of the vertical axis are adjusted in each panel for ease of viewing.

($j=1,2,\cdots$; all other states). The latter group of states includes the scattering states and the hybridized state Ψ_-, whose energy is either just below or immersed into the scattering continuum. Using this grouping, we find

$$|c_{ee}(t)|^2 \approx (P_0)^2 + 2P_0 \sum_{j>0} P_j \cos\left[\frac{(E_0-E_j)t}{\hbar}\right], \tag{4.51}$$

where the time-independent probabilities P_j are given by

$$P_j = |\langle e,e,\mathrm{vac}|\phi_j\rangle|^2 \tag{4.52}$$

(the P_j are positive). In writing Eq. (4.51), we dropped the term $C(t)$,

$$C(t) = \sum_{j>0,j'>0} P_j P_{j'} \cos\left[\frac{(E_j-E_{j'})t}{\hbar}\right], \tag{4.53}$$

on the right hand side; we find numerically that the term $C(t)$ contributes neglegibly to $|c_{ee}(t)|^2$. The damping of the Rabi oscillations is thus due to the energy spread of the energy states ϕ_j ($j > 0$) with non-vanishing P_j. We refer to this as dephasing.

If we replace the energies E_j with $j > 0$ in Eq. (4.51) by E_-, we find

$$|c_{ee}(t)|^2 \approx (P_0)^2 + 2P_0(1-P_0)\cos\left[\frac{(E_0 - E_-)t}{\hbar}\right]. \tag{4.54}$$

The fractional population [107], i.e., the large t limit of $|c_{ee}(t)|^2$, is to a very good approximation given by $(P_0)^2$. Equation (4.54) describes undamped Rabi oscillations, which reproduce the short-time amplitude and oscillation frequency very well (see Fig. 4.13). The damping, which is due—as already pointed out above—to the energy spread of the E_j with $j > 1$, is not captured by Eq. (4.54). Alternatively, the damping can be explained by using that the hybridized state Ψ_-, supported by $\hat{H}$ and $\hat{H}^{\text{adia},1}$, is for small x/a immersed in the scattering continuum. As such, its energy acquires an imaginary part, which provides a finite lifetime or damping coefficient.

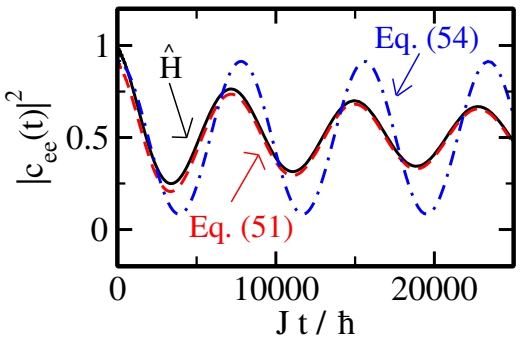

Figure 4.13: Population $P_{ee}(t) = |c_{ee}(t)|^2$ as a function of time for $U/J = -1$, $g/J = 1/50$, $\delta/J = 0.0011$, and $x/a = 5$. The black solid line shows $P_{ee}(t)$ obtained by propagating the initial state $|e,e,\text{vac}\rangle$ under the Hamiltonian $\hat{H}$. The red dashed and blue dash-dotted lines show $P_{ee}(t)$ obtained using Eqs. (4.51) and (4.54), respectively.

4.5 Conclusion

This paper discussed the dynamics of two emitters coupled to a wave guide with Kerr-like non-linearity. Our interest was in the regime where the two emitters are in resonance with the two-photon bound state supported by the one-dimensional wave guide. Even though the emitters are not interacting with each other, correlated dynamics is introduced through the coupling of the emitters to the wave guide. The induced correlations occur on length scales that are comparable to the size of the two-photon bound state. Somewhat surprisingly, a regime where the excitations are transferred back and forth between the emitter and photonic degrees of freedom is observed. The essentially undamped Rabi oscillations are due to the emergence two hybridized bound states whose energies lie in the band gap. This behavior is unique to the two-emitter system: the single-emitter system does not display an analogous behavior.

Throughout, we worked in the weak coupling regime; specifically, the figures all use a coupling strength of $g/J = 1/50$. In the Markovian regime [scenario (A); see Fig. 4.2(b)], the coupling constant enters as a multiplicative factor, i.e., the decay constant Γ_{bath} is directly proportional to $(g/J)^4$ [see Eq. (4.31)]. This regime had previously been investigated in Ref. [106]. For resonance wave vectors $K^{(*)}$ near the bottom of the band [scenarios (B) and (C); see Fig. 4.2(b)], the g-dependence is more intricate. Within the two-state Hamiltonian $\hat{H}^{\text{2-st.}}$, the coupling constant enters through Δ_e, E_{pol}, and $G_{\text{eff}}(n_1, n_2)$: Δ_e is directly proportional to $-(g/J)^2$, E_{pol} contains a term that is proportional to $-(g/J)^4$, and $G_{\text{eff}}(n_1, n_2)$ is directly proportional to $(g/J)^3$. Because of this non-trivial g-dependence, the energies of the hybridized eigen states and, correspondingly, the Rabi oscillation frequency vary notably with g/J. In addition, the regime where the two-state Hamiltonian $\hat{H}^{\text{2-st.}}$ provides a reliable description depends on g/J. For g/J values that are smaller than the value considered in this paper, the observation of Rabi oscillations requires smaller detuning δ/J. Conversely, a larger g/J allows for the observation of Rabi oscillations for larger

δ/J. It is an open question how large g/J can be before counter-rotating terms, which are not included in $\hat{H}$, play a non-negligible role. We are not aware of any previous work on cavity arrays with Kerr-like non-linearity coupled to two-level emitters that looked at parameter combinations corresponding to scenarios (B) and (C). As shown in this paper, these scenarios give rise to qualitatively new behaviors that are inaccessible in the absence of the non-linearity and in cavity array–single-emitter systems.

Our treatment neglects, as already pointed out in the last paragraph of Sec. 4.2.1, single-photon losses. If the single-photon loss rate is denoted by κ, the exponential decay for the initial state $|e, \text{vac}\rangle$ is characterized by Γ_1, where $\Gamma_1 = \kappa g^2/[4J^{1/2}(\hbar\omega_c - 2J - \hbar\omega_e)^{3/2}]$ [105]. For the dynamics to be dominated by correlated two-photon processes, we must thus require $\Gamma_1 \ll \Gamma_{\text{bath}}$ or, dropping all factors that are (roughly) of order 1, $\hbar\kappa/J \ll (g/J)^2$. Reference [106] argues that this regime can be reached with non-linear photonic lattices or superconducting qubits coupled to an array of microwave resonators. Recent experimental work on two transmon qubits coupled to a superconducting microwave photonic crystal, e.g., demonstrated tunable onsite and interbound state interactions [57].

The results presented open the door for several follow-up investigations. Continuing to work in the two-excitation sub-space, it would be interesting to consider an emitter array coupled to the non-linear wave guide. Intriguing hopping dynamics of the radiation might be observed when the radiation is initially localized in two of the emitters. In addition, it might be interesting to investigate the dependence of the dynamics on the initial state. For example, it might be interesting to compare the dynamics for initial states that can be written as a product states to that for entangled superposition states.

Acknowledgement: Support by the National Science Foundation through grant number PHY-1806259 is gratefully acknowledged. This work used the OU Supercomputing Center for Education and Research (OSCER) at the University of Oklahoma (OU).

Chapter 5

Photon-induced droplet-like bound states in one-dimensional qubit array

by J. Talukdar[1, 2] and D. Blume[1, 2]

[1]Homer L. Dodge Department of Physics and Astronomy, The University of Oklahoma,
440 W. Brooks Street, Norman, Oklahoma 73019, USA

[2]Center for Quantum Research and Technology, The University of Oklahoma,
440 W. Brooks Street, Norman, Oklahoma 73019, USA

Under review in Physical Review A (American Physical Society)

We consider an array of N_e non-interacting qubits or emitters that are coupled to a one-dimensional cavity array with tunneling energy J and non-linearity of strength U. The number of cavities is assumed to be larger than the number of qubits. Working in the two-excitation manifold, we focus on the bandgap regime where the energy of two excited qubits is off-resonant with the two-photon bound state band. A two-step adiabatic elimination of the photonic degrees of freedom gives rise to a one-dimensional spin Hamiltonian with effective interactions; specifically, the Hamiltonian features constrained single-qubit hopping and pair hopping interactions not only between nearest neighbors but also between next-to-nearest and next-to-next-to-nearest spins. For a regularly arranged qubit array, we identify parameter combinations for which the system supports novel droplet-like bound states whose characteristics depend critically on the pair hopping. The droplet-like states can be probed dynamically. The bound states identified in our work for off-resonance conditions are distinct from localized hybridized states that emerge for on-resonance conditions.

5.1 Introduction

Qubits or, more generally, few-level emitters coupled to a cavity array provide a platform with which to investigate fundamental aspects of matter-light interactions. Topics of interest include the generation of photon-mediated entanglement between non-interacting separated qubits [114, 14, 115, 116], of ultrastrong matter-light interactions [146, 147, 148, 149, 150, 151, 152], of broad matter-light hybrid bound states [153, 154, 160, 105, 97, 174, 175], and of effective photon-photon interactions [176, 177, 178, 179]. Photonic baths have been realized using nanophotonic wave guides [80, 81, 82, 84, 83, 88, 89, 90], superconducting resonators [86, 87, 111, 59], and plasmonic waveguides [85]. Qubit realizations include Rydberg atoms [180, 181], quantum dots [182], and transmon qubits [94, 95, 47, 96, 57].

It was recently shown that the addition of a Kerr-like non-linearity to the tight-binding Hamiltonian, which accounts for the tunnel-coupling of the single-mode cavities, leads to intriguing and qualitatively novel phenomena if the energy of two excited qubits is tuned to be in resonance with the two-photon bound state band that exists due to the Kerr-like non-linearity [106, 60, 61]. For two qubits initialized in their excited state, e.g., the non-trivial mode structure of the bath, i.e., the cavity array with non-linearity, was shown to support emission dynamics that ranges from exponential decay to fractional populations to Rabi oscillations [60, 61]. For many qubits, supercorrelated radiance was predicted [106]. This work instead investigates the off-resonant or band-gap regime [167] within the framework of Schrödinger quantum mechanics. To reduce the high-dimensional Hilbert space to a physically intuitive and numerically more tractable model, effective constrained single-qubit and pair hopping interactions are derived through a two-step procedure that adiabatically eliminates single- and two-photon processes. The resulting effective one-dimensional spin Hamiltonian, which lives in the two-excitation manifold (i.e., two flipped spins), is shown to capture the key features of the full Hamiltonian.

The effective constrained single- and two-qubit hopping interactions, which are derived

under the assumption that the coupling strength g between an emitter and a cavity is small compared to the tunneling energy J, are directly proportional to g^2 and g^4, respectively. Even though the scaling of the effective interactions with g suggests that the single-qubit hopping dominates over the two-qubit hopping, we identify a parameter regime where the latter, which depends on the non-linearity U, impacts the eigenstate characteristics appreciably. Specifically, the pair hopping interaction favors localization of excited qubits in or near the middle of the qubit array, giving rise to a new class of droplet-like bound states. These bound states are distinct from two-string bound states that exist, e.g., in the XXX spin Hamiltonian that is solvable via the Bethe ansatz [184, 185]. Unlike Hamiltonian that are tractable via the Bethe ansatz, our emergent one-dimensional spin model features non-negligible nearest-neighbor, next-to-nearest-neighbor, and next-to-next-to-nearest-neighbor interactions. It is shown that the radiation dynamics, if initiated from an initial state that contains two qubit excitations but no photons, depends strongly on how the two qubit excitations are distributed among all possible two-qubit excitation eigenkets. A fully symmetric initial state is shown to induce oscillatory dynamics between the droplet-like ground state and a scattering state. Dependence of the dynamics on the initial state is, of course, a well known phenomenon that has, e.g., been exploited in the study of phase transitions and critical points as well as in sensing applications.

The remainder of this article is organized as follows. Section 5.2 introduces the system Hamiltonian and the reduction of the Hilbert space to the qubit degrees of freedom. Section 5.3 shows that the effective qubit Hamiltonian supports a new class of liquid-like or droplet-like bound states. Section 5.4 illustrates that these droplet-like states can be probed dynamically. Last, a summary and outlook are provided in Sec. 5.5.

5.2 Derivation of Effective Qubit Hamiltonian

Section 5.2.1 introduces the total Hamiltonian $\hat{H}$ of the matter-light hybrid system. Focusing on the band gap regime of the photonic lattice, Sec. 5.2.2 derives the effective spin Hamiltonian $\hat{H}_{\text{spin}}$.

5.2.1 Total Hamiltonian $\hat{H}$

The total Hamiltonian $\hat{H}$ reads

$$\hat{H} = \hat{H}_{\text{qubit}} + \hat{H}_{\text{bath}} + \hat{H}_{\text{qubit-bath}}, \tag{5.1}$$

where $\hat{H}_{\text{qubit}}$ is the Hamiltonian of the uncoupled qubits, $\hat{H}_{\text{bath}}$ the bath Hamiltonian, and $\hat{H}_{\text{qubit-bath}}$ the qubit-bath coupling Hamiltonian. The qubit system consists of N_e qubits with a transition energy of $\hbar\omega_e$ between the ground state $|g\rangle_j$ and the excited state $|e\rangle_j$ of the jth qubit (see purple ovals and rectangular box in top-left corner in Fig. 5.1). We are interested in the regime where the qubits form a regularly arranged finite lattice (N_e finite and much greater than 1). The qubit Hamiltonian $\hat{H}_{\text{qubit}}$ is given by

$$\hat{H}_{\text{qubit}} = \frac{\hbar\omega_e}{2} \sum_{j=1}^{N_e} (\hat{\sigma}_j^z + \hat{I}_j), \tag{5.2}$$

where $\hat{\sigma}_j^z = |e\rangle_j \langle e| - |g\rangle_j \langle g|$ and $\hat{I}_j^z = |e\rangle_j \langle e| + |g\rangle_j \langle g|$.

The bath Hamiltonian $\hat{H}_{\text{bath}}$ is a one-dimensional tight-binding Hamiltonian with non-linearity U,

$$\hat{H}_{\text{bath}} = \hbar\omega_c \sum_{n=1}^{N} \hat{a}_n^\dagger \hat{a}_n - J \sum_{n=1}^{N} \left(\hat{a}_n^\dagger \hat{a}_{n+1} + \hat{a}_{n+1}^\dagger \hat{a}_n \right) + \frac{U}{2} \sum_{n=1}^{N} \hat{a}_n^\dagger \hat{a}_n^\dagger \hat{a}_n \hat{a}_n, \tag{5.3}$$

where $\hat{a}_n^\dagger$ and $\hat{a}_n$, respectively, create and destroy a photon at the nth cavity (blue box in Fig. 5.1). In our calculations, the number of cavities N is chosen such that the results are independent of N; we find that $N = 501$ is sufficiently large for the N_e considered. In Eq. (5.3), $\hbar\omega_c$ is the single-mode photon energy, J ($J > 0$) denotes the tunneling energy

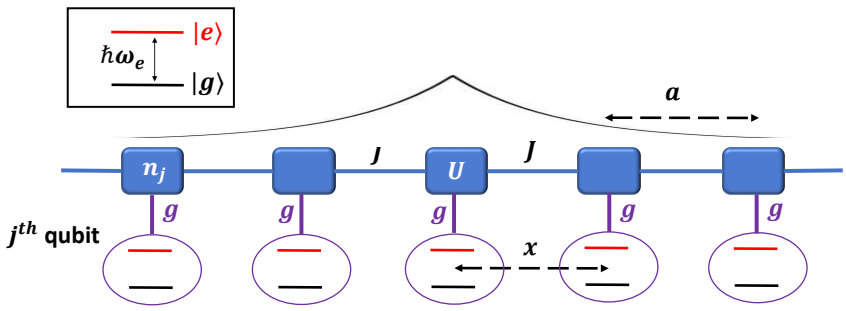

Figure 5.1: Schematic of the set up. The jth qubit is coupled with strength g to the n_jth cavity of a one-dimensional cavity array (blue boxes) with lattice spacing a. The cavities are tunnel-coupled to nearest neighbors with strength J (blue lines between two neighboring blue boxes). For more than one photonic excitation, there exists an onsite interaction U between photons. As a result of the onsite interaction, the cavity array (bath) supports two-photon bound states. One of these is shown by the black line above the cavity array. The distance between two neighboring qubits is denoted by x. In the schematic, x is equal to a; values of $x/a = 0$ and 2 are also discussed in this work. The top-left rectangular box illustrates a qubit, i.e., a two-level system with a transition energy $\hbar\omega_e$ between the ground state $|g\rangle$ and the excited state $|e\rangle$.

of the tunnel coupled cavities, and U is the non-linear onsite interaction. The Kerr-like non-linearity in Eq. (5.3) corresponds to effectively repulsively interacting photon pairs ($U > 0$) or effectively attractively interacting photon pairs ($U < 0$). In our work, we consider a negative U, which gives rise to two-photon bound states $\psi_{K,b}$ with center-of-mass wave vector K and energy $E_{K,b}$, in addition to the two-photon scattering continuum (blue and dark green regions in Fig. 5.2) [123, 124, 125, 126]. The black line in Fig. 5.1 shows a sketch of a two-photon bound state wave function $\psi_{K,b}$ that extends over several lattice sites. Accounting for all allowed center-of-mass wave vectors K, the two-photon bound states give rise to an energy band (green and dark green regions in Fig. 5.2). For large values of the onsite interaction strength $|U|$ ($|U|/J > 4$), the two-photon bound state band does not

overlap with the two-photon scattering continuum. For $|U|/J = 1$, as considered in this paper, the upper part of the two-photon bound state band overlaps with the lower part of the two-photon scattering continuum (the overlap region is shown in dark green in Fig. 5.2). The difference between the energy $2\hbar\omega_e$ of the two-qubit excited state and the $K = 0$ two-photon bound state energy $E_{0,b}$, which coincides with the bottom of the two-photon bound state band, defines the detuning δ,

$$\delta = 2\hbar\omega_e - E_{0,b}. \tag{5.4}$$

The band gap regime, which is the focus of the present work, is characterized by negative detunings δ.

The qubits are coupled to the photons through the system-bath or qubit-bath Hamiltonian $\hat{H}_{\text{qubit-bath}}$,

$$\hat{H}_{\text{qubit-bath}} = g \sum_{j=1}^{N_e} \left(\hat{a}_{n_j} \hat{\sigma}_j^+ + \hat{a}_{n_j}^\dagger \hat{\sigma}_j^- \right), \tag{5.5}$$

where $\hat{\sigma}_j^+$ is the raising operator ($\hat{\sigma}_j^+ = |e\rangle_j \langle g|$) and $\hat{\sigma}_j^-$ the lowering operator ($\hat{\sigma}_j^- = |g\rangle_j \langle e|$) of the jth qubit. The label n_j can take any value between 1 and N. In this work, the qubits are assumed to be arranged in a regular pattern with spacing x, where $x/a = n_j - n_{j-1}$. Related works considered regularly placed impurity qubits coupled to an atomic array [186, 187]. Our figures concentrate on $x/a = 1$. For reference, a larger qubit spacing $x/a = 2$ as well as the case where the qubits are all coupled to the same cavity ($x/a = 0$) are discussed in the text. Since the counter rotating terms are excluded in Eq. (5.5), our treatment is restricted to the weak coupling regime, i.e., $g \ll J$. The requirement that single- and two-photon processes are off-resonant [$|(\hbar\omega_c - 2J) - \hbar\omega_e| > g$ and $|\delta| > g$] can, for negative δ as considered in this work, be combined into one equation, namely

$$|U| > 4J\sqrt{\left(1 + \frac{g}{4J}\right)^2 - 1}. \tag{5.6}$$

For fixed U/J, Eq. (5.6) puts an upper limit on g/J. Conversely, for fixed g/J, Eq. (5.6) puts a lower limit on $|U|/J$.

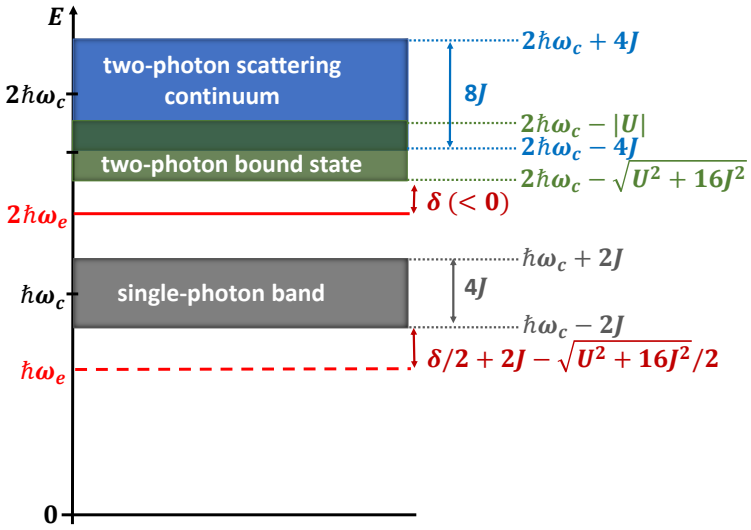

Figure 5.2: Schematic of the energy bands for the one- and two-excitation manifolds for fixed ω_c, ω_e, and U. This work focuses on the band gap regime, i.e., negative detunings δ. Adiabatic elimination of the gray single-photon and green two-photon bound state bands introduces the effective interactions W and Y (see Fig. 5.3 for an illustration of these interactions), respectively, between qubit groups. The two-photon scattering continuum is far off-resonant and does not play a role. Explicit expressions for the energy bands can be found, e.g., in Ref. [125].

The total Hamiltonian conserves the number of total excitations (sum of qubit and photonic excitations) [153, 154, 106, 160, 105]. As a consequence, the Hilbert spaces with 0, 1, 2, ... total excitations are decoupled. This work focuses on the two-excitation manifold.

5.2.2 Effective spin Hamiltonian $\hat{H}_{\text{spin}}$

As mentioned above, we focus on negative detunings such that the energy of two excited qubits is in resonance with the band gap. We find that the band gap physics in the two-excitation manifold is well described by the spin Hamiltonian $\hat{H}_{\text{spin}}$, which is derived by adiabatically eliminating the photon degrees of freedom in a two-step process (see

Appendix C for details). We emphasize that the approach taken here is distinct from the master equation approach pursued in Ref. [106]. The first step is, in spirit, identical to prior work [106, 60, 61]. Neglecting the two-photon scattering continuum and adiabatically eliminating the single-photon states, effective constrained single-qubit hopping interactions of strength W_{jl} (see $\hat{H}_{\text{single}}$ below), effective interactions between states with two and no qubit excitations [$F_{K,b}$ in Eq. (C.12)], and effective interactions between two two-photon bound states with wave vector K and K' [$G_{K,K'}$ in Eq. (C.13)] arise. While the latter two interactions were discussed in Refs. [106, 60, 61], the effective qubit hopping interaction was not. The reason is that Refs. [106, 60, 61] focused on $N_e = 2$ ($\hat{H}_{\text{single}}$ vanishes for $N_e = 2$). The hopping Hamiltonian $\hat{H}_{\text{single}}$ reads

$$\hat{H}_{\text{single}} = \frac{1}{2} \sum_{i,j,l=1}^{N_e} \left(W_{jl} \hat{\sigma}_i^+ \hat{\sigma}_j^+ \hat{\sigma}_i^- \hat{\sigma}_l^- + W_{il} \hat{\sigma}_i^+ \hat{\sigma}_j^+ \hat{\sigma}_l^- \hat{\sigma}_j^- \right). \tag{5.7}$$

Since the triple sum includes terms where two or three of the indices are equal, the order of the operators in Eq. (5.7) is important. As discussed in more detail below, $\hat{H}_{\text{single}}$ describes constrained single-qubit hopping or constrained flip-flop interactions. We find that the effective interactions $G_{K,K'}$ contribute negligibly to the band gap physics considered in this work; thus, they are set to zero.

Calculations that treat the full Hamiltonian $\hat{H}$ show that the photonic contribution to the eigenstates is smaller than 10% for the parameter combinations considered in this work. This motivates our second approximation, namely, the adiabatic elimination of the states $\hat{B}_K^\dagger |g, \cdots, g, \text{vac}\rangle$, i.e., basis kets that describe a photon pair with wave vector K, with the qubits in the ground state. Step two yields the effective spin Hamiltonian $\hat{H}_{\text{spin}}$ (see Appendix C for details),

$$\hat{H}_{\text{spin}} = \hat{H}_{\text{single}} + \hat{H}_{\text{pair}}, \tag{5.8}$$

where

$$\hat{H}_{\text{pair}} = \sum_{i=1}^{N_e-1} \sum_{j=i+1}^{N_e} \sum_{l=1}^{N_e-1} \sum_{h=l+1}^{N_e} Y_{ij,lh} \hat{\sigma}_i^+ \hat{\sigma}_j^+ \hat{\sigma}_l^- \hat{\sigma}_h^-. \tag{5.9}$$

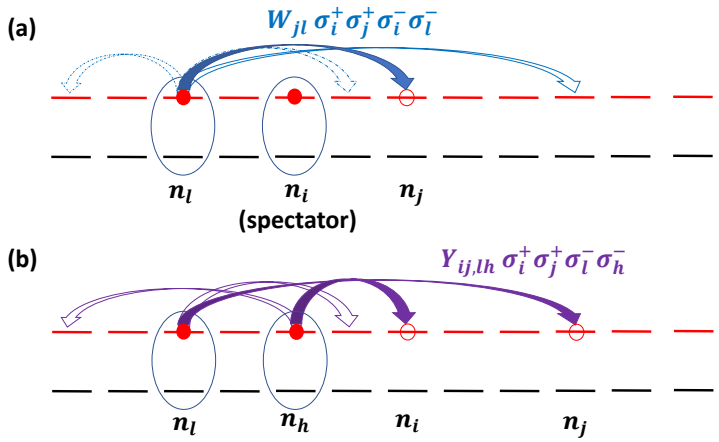

Figure 5.3: Schematic of constrained single-qubit hopping interaction W and pair hopping interaction Y entering into $\hat{H}_{\text{spin}}$. (a) The term $W_{jl}\hat{\sigma}_i^+\hat{\sigma}_j^+\hat{\sigma}_i^-\hat{\sigma}_l^-$ (here illustrated assuming $i \neq j \neq l$) describes the annihilation of an excitation at the lth qubit and the creation of an excitation at the jth qubit (solid blue arrow). This corresponds to the hopping of an excitation with strength W_{jl}, with the excitation at the ith qubit acting as a "spectator", i.e., the single-qubit hopping is only allowed if qubit i is excited. (b) The term $Y_{ij,lh}\hat{\sigma}_i^+\hat{\sigma}_j^+\hat{\sigma}_l^-\hat{\sigma}_h^-$ (here illustrated assuming $i \neq j \neq l \neq h$) describes the annihilation of excitations at qubits l and h, and the creation of excitations at qubits i and j (solid purple arrows). This corresponds to the hopping of a pair of excitations with strength $Y_{ij,lh}$. The open blue and open purple arrows show selected additional constrained hopping and pair hopping interactions, respectively.

The effective four-qubit (or two-qubit hopping) interactions $Y_{ij,lh}$ emerge from the interactions $F_{K,b}$ (see below). As might be expected naively, W_{jl} and $Y_{ij,lh}$ are directly proportional to g^2 and g^4, respectively, since they emerge as a consequence of the first and second adiabatic elimination steps, respectively. The effective spin Hamiltonian $\hat{H}_{\text{spin}}$ is independent of the photonic degrees of freedom. The characteristics of the cavity array and the geometric arrangement of the qubits (i.e., the value of x) enter through the interaction strengths W_{jl} and $Y_{ij,lh}$.

We now highlight selected properties of the single- and two-qubit hopping interactions.

Figure 5.3(a) illustrates the constrained single-qubit hopping interaction $W_{jl}\hat{\sigma}_i^+\hat{\sigma}_j^+\hat{\sigma}_i^-\hat{\sigma}_l^-$. The term "constrained" is used since the hopping of the excitation from qubit l to qubit j ($\hat{\sigma}_j^+\hat{\sigma}_l^-$ piece) depends on the number of excitations at qubit i ($\hat{\sigma}_i^+\hat{\sigma}_i^-$ piece; in this example, we assume $i \neq j$ and $i \neq l$). If qubit i is excited, hopping from qubit l to qubit j occurs with strength W_{jl}. If, in contrast, qubit i is not excited, hopping from qubit l to qubit j does not take place. We refer to the excited qubit i as a spectator. We emphasize that our treatment does not assume that the system is in the Markovian regime. After the first adiabatic elimination, basis kets with two excited qubits are coupled to each other via $\hat{H}_{\text{single}}$ if they contain a common excited qubit. The second adiabatic elimination leaves $\hat{H}_{\text{single}}$ unchanged. Thus, in the Hilbert space spanned by the $N_e(N_e-1)/2$ two-excitation qubit states, $\hat{H}_{\text{single}}$ couples each basis ket that contains two excited qubits to $2(N_e-2)$ other basis kets as well as to itself. While we refer to $W(0)$ as onsite hopping interaction, it is also known as "self interaction" or "self energy" (see, e.g., Ref. [106]).

The strength W_{jl},

$$W_{jl} = W(0)\exp\big(-|n_j - n_l|a/L_0\big), \tag{5.10}$$

of the constrained single-qubit hopping interaction falls off exponentially as a function of $|n_j - n_l|a$, i.e., the difference between the cavities n_j and n_l that the qubits j and l are coupled to. The onsite hopping energy $W(0)$ and length L_0 read

$$W(0) = -\frac{2J\left(\frac{g}{2J}\right)^2}{\sqrt{\left(\frac{\Delta}{2J}\right)^2 - 1}} \tag{5.11}$$

and

$$L_0 = -\frac{a}{\ln\left(\frac{\Delta}{2J} - \sqrt{\left(\frac{\Delta}{2J}\right)^2 - 1}\right)}, \tag{5.12}$$

respectively, where

$$\Delta = \hbar(\omega_c - \omega_e) = \frac{1}{2}\left(-\delta + 4J\sqrt{1 + \left(\frac{U}{16J}\right)^2}\right). \tag{5.13}$$

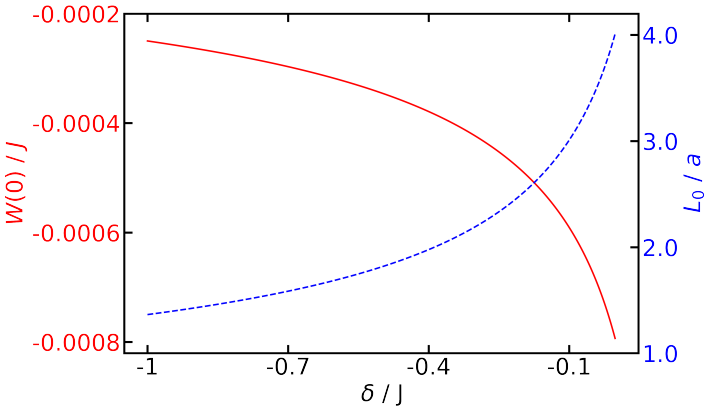

Figure 5.4: The red solid and blue dashed lines show the dimensionless on-site hopping energy $W(0)/J$ (left axis) and length L_0/a (right axis) as a function of the detuning δ/J for $g/J = 1/50$ and $U/J = -1$.

Figure 5.4 shows the onsite hopping energy $W(0)$ and length L_0 for fixed g/J and U/J as a function of the dimensionless detuning δ/J. It can be seen that $W(0)/J$ is negative and that the magnitude of $W(0)$ increases with decreasing $|\delta/J|$. Larger $|W(0)|$ (note, Fig. 5.4 shows $W(0)$ as opposed to $|W(0)|$) are accompanied by larger L_0. For the detuning considered in this work ($|\delta/J| \ll 1$), W_{jl} is—for $x/a = 1$—appreciable not only for nearest neighbor hopping but also for next-to-nearest and next-to-next-to-nearest neighbor hopping.

Next, we discuss the effective pair hopping interaction $Y_{ij,lh}$. Figure 5.3(b) illustrates $Y_{ij,lh}\hat{\sigma}_i^+\hat{\sigma}_j^+\hat{\sigma}_l^-\hat{\sigma}_h^-$, which annihilates excitations at the lth and hth qubit and creates excitations at the jth and ith qubit. The effective pair hopping interaction $Y_{ij,lh}$ is given by

$$Y_{ij,lh} = -\frac{g^4}{NJ^2}\sum_K \frac{F_{K,b}(n_i,n_j)F^*_{K,b}(n_l,n_h)}{\Delta_{K,b}}, \tag{5.14}$$

where $F_{K,b}$ is given in Eq. (C.12). As W_{jl}, $Y_{ij,lh}$ is negative. The pair hopping interaction $\hat{H}_{\text{pair}}$ couples each excited qubit pair to all other excited qubit pairs. Figure 5.5 shows the interaction $Y_{ij,lh}$ for $x/a = 1$ as functions of the pairs (i,j) and (l,h) for $N_e = 60$. Specifically, the indices that specify the states $\hat{\sigma}_i^+\hat{\sigma}_j^+|g,\cdots,g\rangle$ are organized based on the separation

between the excited qubits, i.e., $|j-i|$. In a qubit array with N_e qubits, there are N_e-1 basis states with a separation of $|j-i|=1$, N_e-2 basis states with a separation of $|j-i|=2$, and so on. The "lower left block" corresponds to $|j-i|=|h-l|=1$ [the pairs (i,j) and (l,h) both take the values $(1,2)$, $(2,3)$,$\cdots$, $(59,60)$]. The "upper right block" corresponds to $|j-i|=|h-l|=9$ [the pairs (i,j) and (l,h) both take the values $(1,10)$, $(2,11)$,$\cdots$, $(51,60)$]. Note that Fig. 5.5 only considers a subset of pairs, i.e., $|j-i|\leq 9$ and $|h-l|\leq 9$. Within each block, the interaction is most negative along the diagonal and falls off approximately Lorentzian as one moves away from the diagonal. Moreover, starting with the block in the lower left corner, the interactions on the diagonal are less negative as one moves to blocks characterized by larger separations.

A key characteristic of the interaction $Y_{ij,lh}$ is that it is—within each block—constant along the diagonal, along the off-diagonal, and so on. The fall-off of the interactions as one moves away from the diagonal within each block indicates that the $Y_{ij,lh}$ interaction depends on the actual locations of the involved qubits in the spin chain. This implies that it is energetically more favorable for two excitations to be located in the middle of the chain than at the edge of the chain since the pair can hop to the left and to the right when located at the center and only to one side when located at the edge. This location dependence is critical for the formation of the droplet-like states discussed in the next section.

5.3 Stationary Solutions

Since we are working in the regime where $g/J \ll 1$, it might be expected naively that the constrained single-qubit hopping term $\hat{H}_{\text{single}}$, which is directly proportional to g^2, dominates over the pair hopping term $\hat{H}_{\text{pair}}$, which is directly proportional to g^4. While this is, indeed, the case in an appreciable portion of the parameter space, we show that there exists a parameter window in which the pair hopping interaction qualitatively changes the system characteristics. It is noted that a fourth-order two-photon virtual process, which is

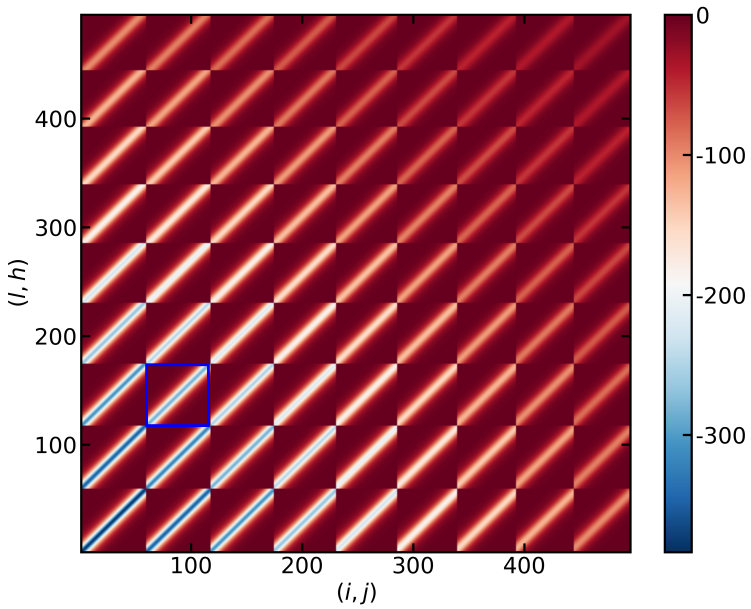

Figure 5.5: Contour plot of the effective dimensionless interaction $Y_{ij,lh}J^3/g^4$ for $U/J=-1$, $\delta/J=-1/50$, $N_e=60$, and $x/a=1$. The x- and y-axis are labeled by the index pairs (i,j) and (l,h); the plot includes all (i,j) and (l,h) pairs with $|j-i|\leq 9$ and $|h-l|\leq 9$. In each block, the separation (i.e., $j-i$ and $h-l$) between the two qubit excitations is fixed while the "center-of-mass coordinates" [i.e., $(i+j)/2$ and $(l+h)/2$] are changing. As an example, the blue rectangle corresponds to a block with $|j-i|=2$ and $|h-l|=3$. Values of (x, y) = (100, 150), e.g., correspond to $(i,j)=(41,43)$ and $(l,h)=(33,36)$.

proportional to g^4, was observed experimentally in transmon qubits coupled to a photonic crystal [57]. Specifically, this section shows that the Y-term has a "pinning effect" that leads to the emergence of liquid- or droplet-like bound states. Droplet states are self-bound and incompressible, and their excitation spectrum can be divided into compressional and surface modes [183]. We will show that the states referred to as droplet-like in this work are incompressible (their size is not solely set by the extent of the emitter array but by the entirety of system parameters). Moreover, the ground state is accompanied by a

sequence of excitations that resemble compressional modes. While our analysis is based on the approximate spin Hamiltonian $\hat{H}_{\text{spin}}$, we checked that this Hamiltonian captures the key features of the full system Hamiltonian $\hat{H}$ qualitatively and in many cases even quantitatively correctly. The main advantage of using $\hat{H}_{\text{spin}}$ comes from the fact that it allows for a transparent interpretation of the results, in addition to being an interesting model in its own right.

We start by setting $\hat{H}_{\text{pair}} = 0$. We find it useful to compare $\hat{H}_{\text{single}}$ to the unconstrained one-qubit hopping Hamiltonian $\hat{\tilde{H}}_{\text{single}}$, where $\hat{\tilde{H}}_{\text{single}} = 2\sum_{i,j=1}^{N_e} W_{ij}\hat{\sigma}_i^+\hat{\sigma}_j^-$. This Hamiltonian emerges (without the factor of 2) when one works in the single-excitation manifold and adiabatically eliminates the single-photon states [97, 174, 175]. $\hat{H}_{\text{single}}$ differs from $\hat{\tilde{H}}_{\text{single}}$ because of the presence of the "spectator", i.e., the constraint makes the Hamiltonian $\hat{H}_{\text{single}}$ considered in our work unique. To highlight the differences, red and blue circles in Fig. 5.6 show the eigenenergies of $\hat{H}_{\text{single}}$ and $\hat{\tilde{H}}_{\text{single}}$, respectively, for $N_e = 60$, $g/J = 1/50$, $U/J = -1$, $\delta/J = -1/50$, and $x/a = 1$. The constraint introduces an upshift of the eigenenergies for all eigenstates. The upshift is larger for the more negative eigenenergies (measured relative to the bottom $E_{0,b}$ of the two-photon bound state band) than the less negative eigenenergies. Interestingly, both $\hat{H}_{\text{single}}$ and $\hat{\tilde{H}}_{\text{single}}$ support step like pattern, with each plateau containing close to N_e eigenstates for the energetically lowest lying states. For the higher excited states, the steps are less pronounced. Reference [105] referred to the energy band formed by the qubit dominated states as a metaband. While we observe, similarly to Ref. [105], that the width of the band decreases with increasing x, it is important to point out that that work considered qubit-array physics in the single-excitation manifold on resonance (and not off-resonance as in our case) and for significantly stronger coupling strengths (g/J of order 1).

For comparison, the black circles in Fig. 5.6 show the eigenenergies for $\hat{H}_{\text{spin}}$. It can be seen that $\hat{H}_{\text{pair}}$ appreciably impacts the 10 or so energetically lowest lying states and

less so the higher-lying states. Importantly, the energies of the lowest few eigenstates of $\hat{H}_{\text{spin}}$ are pushed down due to the presence of the $\hat{H}_{\text{pair}}$ term. The downshift of the energies is associated with significant changes of the character of the eigenstates, i.e., a change from delocalized scattering states to localized bound states. We refer to this as "pinning" (see below for details). The energy spectrum shown in Fig. 5.6 is unique to a qubit spacing of $x/a = 1$. For larger spacings, but otherwise identical parameters, the hopping energies are smaller and the step-like pattern is washed out. Moreover, the most strongly bound states are less separated from the other states than for $x/a = 1$ (i.e., $\hat{H}_{\text{pair}}$ introduces a smaller downshift for the ground state for $x/a = 2$ than for $x/a = 1$). For $x = 0$, there exist three degenerate energy levels: for the same N_e, g/J, U/J, and δ/J as considered in Fig. 5.6, the $x/a = 0$ spectrum for $\hat{H}_{\text{spin}}$ contains a single state with energy $E - E_{0,b} = -0.2256J$, $N_e - 1$ states with energy $E - E_{0,b} = -0.0629J$, and $N_e(N_e - 3)/2$ states with energy $E - E_{0,b} = \delta = -0.02J$.

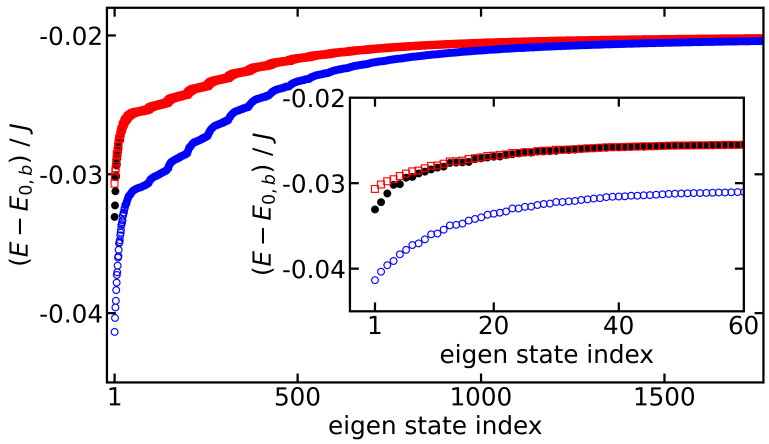

Figure 5.6: Eigenenergy, measured with respect to $E_{0,b}$, for $N_e = 60$, $g/J = 1/50$, $U/J = -1$, $\delta/J = -1/50$, and $x/a = 1$ as a function of the state index. The black filled circles, red open squares, and blue open circles show the energy for $\hat{H}_{\text{spin}}$, $\hat{H}_{\text{single}}$, and $\hat{\tilde{H}}_{\text{single}}$, respectively. Inset: Blow-up of the lower part of the energy spectrum.

To understand the influence of $\hat{H}_{\text{pair}}$ on the eigenspectrum, we use first-order non-degenerate perturbation theory. Treating $\hat{H}_{\text{pair}}$ as a perturbation, the first-order correction $E_n^{(1)}$ to the eigenenergy $E_n^{(0)}$ of the nth droplet-like eigenket $\left|\phi_n^{(0)}\right\rangle$ of $\hat{H}_{\text{single}}$ is given by

$$E_n^{(1)} = \left\langle \phi_n^{(0)} \right| \hat{H}_{\text{pair}} \left| \phi_n^{(0)} \right\rangle . \tag{5.15}$$

Figure 5.7(a) considers the six energetically lowest-lying droplet-like states ($n = 1-6$). These droplet-like states correspond to state numbers 1, 2, 3, 4, 7, and 10. Figure 5.7(a) shows that the perturbation energies (the open blue circles show $E_n^{(0)} + E_n^{(1)}$) lie below the zeroth-order energies $E_n^{(0)}$ (green open triangles), i.e., the stronger binding of $\hat{H}_{\text{spin}}$ compared to $\hat{H}_{\text{single}}$ due to $\hat{H}_{\text{pair}}$ is captured qualitatively in first-order perturbation theory. Higher-order corrections, which account for the mixing of the unperturbed states $\left|\phi_n^{(0)}\right\rangle$ play a larger role for the ground state ($n = 1$) than for the excited droplet-like states ($n = 2-6$). Figure 5.7(b) focuses on the energy of the lowest-lying droplet-like state and shows that energy as a function of the detuning. The detuning marked by an arrow is identical to the detuning used in Fig. 5.7(a). For large to moderate detunings, the results from the perturbation calculation (blue open circles) agree well with the exact diagonalization of $\hat{H}_{\text{spin}}$ (black solid circles). For relatively small detunings, however, deviations are visible. While the first-order perturbative energy improves upon the unperturbed energy, higher-order corrections play an increasingly more important role.

To characterize the eigenstates $|\phi_E\rangle$ of $\hat{H}_{\text{spin}}$, we expand them in terms of the basis kets $\sigma_i^+ \sigma_j^+ |g, \cdots, g\rangle$,

$$|\phi_E\rangle = \sum_{i=1}^{N_e-1} \sum_{j=i+1}^{N_e} c_{i,j}^{(E)} \sigma_i^+ \sigma_j^+ |g, \cdots, g\rangle , \tag{5.16}$$

and analyze the expansion coefficients $c_{i,j}^{(E)}$ as well as the pair correlation function $P_{\text{pair}}(\alpha)$, which measures the likelihood that the two excitations are located at qubits that are separated by α. The corresponding operator is given by

$$\hat{P}_{\text{pair}}(\alpha) = \sum_{i=1}^{N_e-\alpha} \hat{\sigma}_i^+ \hat{\sigma}_{i+\alpha}^+ |g, \cdots, g\rangle \langle g, \cdots, g| \hat{\sigma}_i^- \hat{\sigma}_{i+\alpha}^- , \tag{5.17}$$

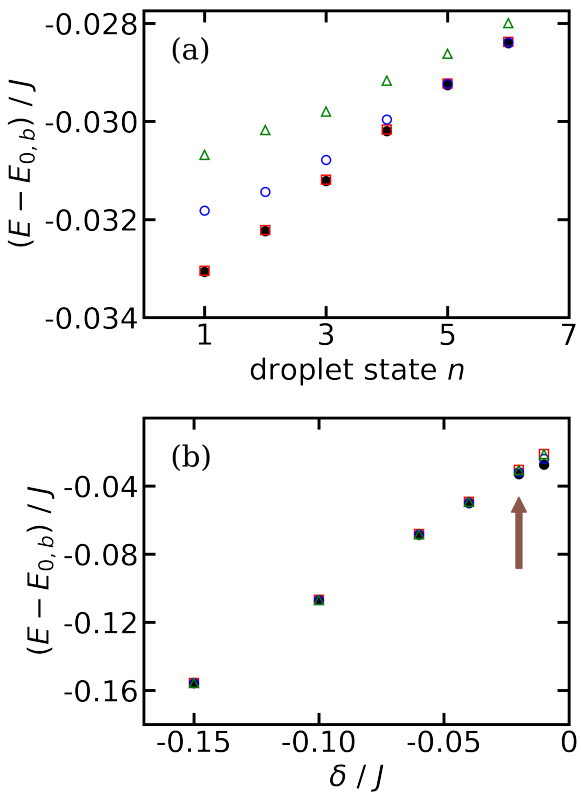

Figure 5.7: Energy of droplet-like states, measured with respect to $E_{0,b}$, for $N_e = 60$, $g/J = 1/50$, $U/J = -1$, and $x/a = 1$ as a function of (a) the excitation number n for $\delta/J = -1/50$ and (b) the detuning δ/J for $n = 1$. The black filled circles, green open triangles, red open squares, and blue open circles show the energies for $\hat{H}_{\text{spin}}$, $\hat{H}_{\text{single}}$, the variational wavefunction given in Eqs. (5.18)-(5.20), and for the perturbative calculation ($\hat{H}_{\text{pair}}$ is treated in first-order perturbation theory), respectively. In (a), the red and black symbols are nearly indistinguishable. In (b), all four calculations yield, on the scale shown, nearly indistinguishable energies except when $|\delta/J|$ is extremely small. The arrow in (b) marks the detuning used in (a).

where α takes the values $1, 2, \cdots, N_e - 1$. For example, if $\alpha = 1$, the excitations are located at neighboring spins. In terms of the expansion coefficients, the pair correlation function for

the eigenstate $|\phi_E\rangle$ is given by $P_{\rm pair}(\alpha) = \sum_{i=1}^{N_e-\alpha} |c_{i,i+\alpha}^{(E)}|^2$.

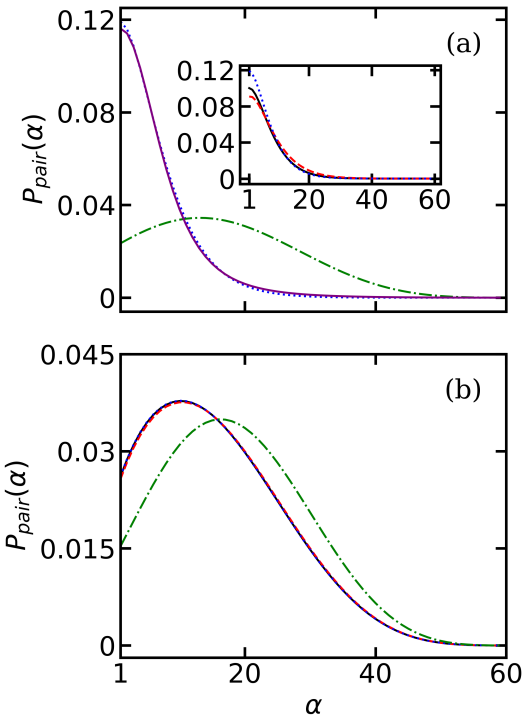

Figure 5.8: Pair correlation function $P_{\rm pair}(\alpha)$ for the ground state as a function of the separation α between two excited qubits for $N_e = 60$, $g/J = 1/50$, $U/J = -1$, $x/a = 1$, and (a) $\delta/J = -1/50$ and (b) $\delta/J = -3/20$. The black solid, blue dotted, and red dashed lines are for $\hat{H}_{\rm full}$, $\hat{H}_{\rm spin}$, and $\hat{H}_{\rm single}$, respectively. The inset in (a) replots the blue dotted line and additionally shows the variational results by green open circles.

Figures 5.8(a) and 5.8(b) show $P_{\rm pair}(\alpha)$ for the ground state for $N_e = 60$, $g/J = 1/50$, $U/J = -1$, and $x/a = 1$ for two different detunings, namely $\delta/J = -1/50$ and $-3/20$. The blue dotted lines are obtained using $\hat{H}_{\rm spin}$. The full Hamiltonian $\hat{H}_{\rm full}$ (black solid lines) yields results that are quite similar to those for $\hat{H}_{\rm spin}$, thus providing evidence that $\hat{H}_{\rm spin}$ yields faithful results. For small $|\delta/J|$ [Fig. 5.8(a)], the pair correlation function peaks at $\alpha = 1$ and is essentially zero for $\alpha \gg 1$. This indicates that the two excited qubits want to stay together. The fall-off of $P_{\rm pair}(\alpha)$ suggests that the ground state corresponds to a bound

state. This interpretation is confirmed by calculations for larger arrays (larger N_e) with otherwise identical parameters. We find that $P_{\text{pair}}(\alpha)$ for the ground state remains essentially unchanged when N_e is increased, i.e., the size of the ground state is independent of N_e, thereby justifying the classification as a self-bound state. For larger $|\delta/J|$ [Fig. 5.8(b)], in contrast, the pair correlation function peaks at $\alpha \approx 10$ for $\hat{H}_{\text{full}}$ and $\hat{H}_{\text{spin}}$. This indicates that the two excited qubits have a tendency to spread out over the entire array. This interpretation is supported by the fact that the fall-off of the pair correlation function moves to larger α for larger N_e but otherwise identical parameters. Correspondingly, we classify the ground state considered in Fig. 5.8(b) as unbound. The inclusion of $\hat{H}_{\text{pair}}$ in the effective spin Hamiltonian $\hat{H}_{\text{spin}}$ (blue dotted line) is crucial. A comparison of the blue dotted line [$P_{\text{pair}}(\alpha)$ for $\hat{H}_{\text{spin}}$] and red dashed line [$P_{\text{pair}}(\alpha)$ for $\hat{H}_{\text{single}}$] reveals that $\hat{H}_{\text{pair}}$ has a pinning effect: it enhances, as already alluded to in Sec. 5.2.2, the probability to find excitations located at qubits that are close to each other. The effect is very prominent in Fig. 5.8(a), where the red line is much broader than the blue line. If $\hat{H}_{\text{pair}}$ is neglected and N_e is increased, the red line in Fig. 5.8 does not maintain its size, as is the case for $\hat{H}_{\text{spin}}$, but increases. This unequivocally shows that $\hat{H}_{\text{pair}}$ is responsible for the emergence of self-bound states.

Figure 5.9 shows the real part of the coefficients $c_{i,j}^{(n)}$ for the four energetically lowest lying droplet-like bound states ($n = 1-4$) for $N_e = 60$, $g/J = 1/50$, $U/J = -1$, $\delta/J = -1/50$, and $x/a = 1$; the imaginary part is equal to zero. The droplet-like states shown in Fig. 5.9 correspond to the state numbers 1, 2, 3, and 4. Figure 5.9 employs relative and center-of-mass coordinates r and R, respectively, of the two excited qubits, $r = |j-i|$ and $R = (i+j)/2$. The white area characterized by $r \geq 2R$ for $R < N_e/2$ and $r \geq 2(N_e - R)$ for $R \geq N_e/2$ is unphysical as there is a constraint of $i < j$ on the eigencoefficients due to the bosonic character or, equivalently, the exchange symmetry of the excitations. The small white dots, which exist in the physical $i < j$ portions in Fig. 5.9, result from the transformation from the (i, j) spin indices to the (R, r) coordinates. In Figs. 5.9(a)-5.9(d),

the magnitude of the coefficients $c_{i,j}^{(n)}$ decreases with increasing r for fixed R. Along the R coordinate, the number of nodes increases from zero for the ground state [$n = 1$ in Fig. 5.9(a)] to three for the third excited droplet-like state [$n = 4$ in Fig. 5.9(d)]. The nodes are to a very good approximation parametrized by $R_{\text{node}} \approx$ constant, i.e., they are, on the scale of Fig. 5.9, independent of r.

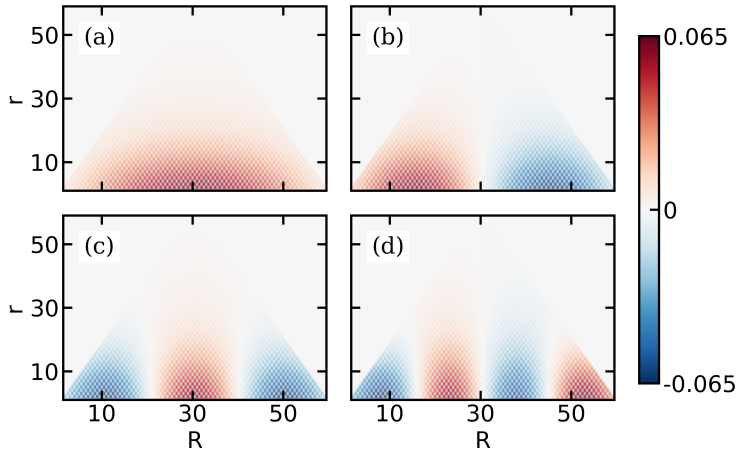

Figure 5.9: Contour plots of the expansion coefficients $c_{ij}^{(n)}$ as functions of R and r for $N_e = 60$, $g/J = 1/50$, $U/J = -1$, $\delta/J = -1/50$, and $x/a = 1$. The coefficients are obtained by diagonalizing the effective Hamiltonian $\hat{H}_{\text{spin}}$. (a), (b), (c), and (d) are for n=1 (droplet-like ground state), 2 (droplet-like first excited state), 3 (droplet-like second excited state), and 4 (droplet-like third excited state), respectively.

In what follows, we use a variational ansatz to understand the length scale that governs the droplet-like states and the number of droplet-like states that are supported by a qubit array of size N_e. Since Fig. 5.9 suggests that the expansion coefficients of the nth droplet-like eigenstate decouple when plotted as functions of the relative coordinate r and the center-of-mass coordinate R, we introduce the product ansatz

$$c_{r,R}^{(n)} = Q^{(n)}(R)q(r). \tag{5.18}$$

Here, the function $Q^{(n)}(R)$,

$$Q^{(n)}(R) = \sqrt{\frac{2}{N_e}} \sin\left(\frac{n\pi}{N_e} R\right), \tag{5.19}$$

corresponds to the nth particle in the box wave function and the function $q(r)$,

$$q(r) = 2\sqrt{\frac{L_r^3}{\pi a^3}} \left[\frac{1}{(r-1)^2 + (\frac{L_r}{a})^2}\right], \tag{5.20}$$

to an n-independent Lorentzian with characteristic length L_r. The length L_r is treated as a variational parameter. By construction, the variational states with different n are orthogonal.

Figure 5.7(a) compares the variational energies (red open squares) of the six droplet-like states that are supported by the qubit array for $N_e = 60$, $g/J = 1/50$, $U/J = -1$, $\delta/J = -1/50$, and $x/a = 1$ with those obtained by diagonalizing $\hat{H}_{\text{spin}}$ (black solid circles). We see that the variational energies agree extremely well with the exact eigenenergies of $\hat{H}_{\text{spin}}$. In Fig. 5.7(b), the energy of the ground droplet-like state is shown as a function of δ/J for the same N_e, g/J, U/J, and x/a as used in Fig. 5.7(a). For large to moderate, in magnitude, detunings, the energies from the variational calculation (red open squares) agree well with the exact eigenenergies of $\hat{H}_{\text{spin}}$ (black solid circles). For small detunings, small deviations are visible. The variational calculation not only predicts the eigenenergy accurately but also the corresponding eigenstates. As an example, the green open circles in the inset of Fig. 5.8(a) show the pair correlation function obtained by the variational treatment; it agrees well with the results obtained for $\hat{H}_{\text{spin}}$ (blue dotted line). The number of droplet-like states supported by the qubit array is approximately equal to aN_e/L_r. Intuitively, this can be understood as follows. The system develops additional nodes along the R direction till the spacing between the nodes is comparable to the size of the droplet-like state along the r direction. For $g/J = 1/50$, $U/J = -1$, $\delta/J = -1/50$, and $x/a = 1$, the variational ground state energy is minimized for $L_r \approx 10a$. The qubit array with $N_e = 60$ supports six droplet-like states, in agreement with the estimate $aN_e/L_r \approx 6$. As the qubit array spacing x is changed from a to $2a$, the number of droplet-like bound states decreases

from six to four. For $x = 3a$, droplet-like bound states are no longer supported. Similar results are found for other parameter combinations. We note that $\hat{H}_{\text{spin}}$ also supports more highly excited modes, which have nodes along the r-coordinate. The variational treatment of these energetically higher-lying droplet-like states is beyond the scope of this work.

5.4 Dynamics

This section discusses the dynamics for negative δ (band-gap regime) for two different initial states in the two-excitation manifold, namely the partially symmetric state $|\text{PS}\rangle$,

$$|\text{PS}\rangle = \frac{1}{\sqrt{N_e - 1}} \sum_{i=1}^{N_e-1} \sigma_i^+ \sigma_{i+1}^+ |g, \cdots, g\rangle \,, \tag{5.21}$$

and the fully symmetric state $|\text{FS}\rangle$,

$$|\text{FS}\rangle = \frac{\sqrt{2}}{\sqrt{N_e(N_e-1)}} \sum_{i=1}^{N_e-1} \sum_{j=i+1}^{N_e} \sigma_i^+ \sigma_j^+ |g, \cdots, g\rangle \,. \tag{5.22}$$

The fully symmetric state is a superposition of all basis kets (all basis kets contribute with an expansion coefficient $\frac{\sqrt{2}}{\sqrt{N_e(N_e-1)}}$). The partially symmetric state, in contrast, only considers basis kets for which the excited qubits are nearest neighbors.

Figures 5.10(a) and 5.10(b) show the decomposition of the states $|\text{PS}\rangle$ and $|\text{FS}\rangle$, respectively, into the energy eigenstates $|\phi_E\rangle$ of $\hat{H}_{\text{spin}}$ for $N_e = 60$, $g/J = 1/50$, $U/J = -1$, $\delta/J = -1/50$, and $x/a = 1$. The state $|\text{PS}\rangle$ has finite overlap with a large number of eigenstates from all over the eigenspectrum. The ground state contributes about 10% and the other states 3% or less. For the state $|\text{FS}\rangle$ [Fig. 5.10(b)], in contrast, there are two energy eigenstates that dominate and together contribute 89% [52.6%, red square in Fig. 5.10(b), and 36.4%, blue triangle in Fig. 5.10(b)]. The lowest eigenstate, which contributes 52.6%, has droplet-like character while the excited eigenstate, which contributes 36.4%, has scattering characteristics. Since the fully symmetric initial state is dominated by two eigenstates, the dynamics is expected to feature Rabi-like two-state oscillation dynamics. The dynamics

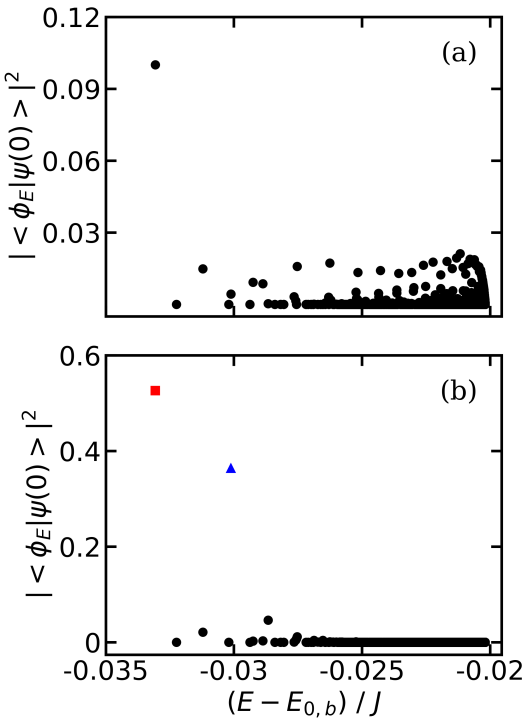

Figure 5.10: Square of the absolute value of the projection of the initial state $|\psi(0)\rangle$ onto the energy eigenstates $|\phi_E\rangle$ of $\hat{H}_{\rm spin}$ as a function of the eigenenergy E, measured relative to the bottom $E_{0,b}$ of the two-photon bound state band, for $N_e = 60$, $g/J = 1/50$, $U/J = -1$, $\delta/J = -1/50$, and $x/a = 1$. (a) The initial state is $|\psi(0)\rangle = |\mathrm{PS}\rangle$. (b) The initial state is $|\psi(0)\rangle = |\mathrm{FS}\rangle$. The red square and blue triangle correspond to the two largest values of $|\langle\phi_E|\mathrm{FS}\rangle|^2$.

for the partially symmetric state, in contrast, is expected to display features of dephasing, at least over certain time scales, due to the superposition of many energy eigenstates.

Figure 5.11 shows the time dependence of the probability that two excitations belong to nearest neighbor qubits, i.e., qubits that are separated by $\alpha = 1$ (black solid line), to qubits that are separated by $\alpha = 6$ (red dashed line), and to qubits that are separated by $\alpha = 21$ (blue dotted line). These observables are for the same parameters as those used in Fig. 5.10. The time evolution of $P_{\rm pair}(\alpha,t)$ for the initial states $|\mathrm{PS}\rangle$ [Fig. 5.11(a)] and $|\mathrm{FS}\rangle$

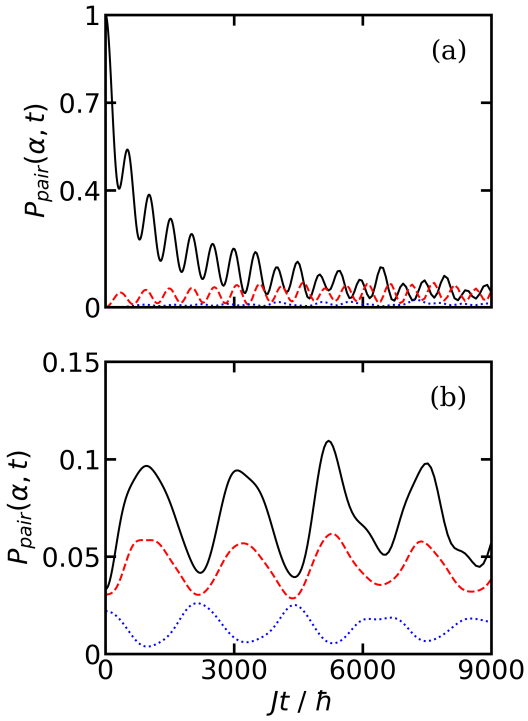

Figure 5.11: Pair correlation function $P_{\text{pair}}(\alpha,t)$ for $\hat{H}_{\text{spin}}$ as a function of time for three different separations α for $N_e = 60$, $g/J = 1/50$, $U/J = -1$, $\delta/J = -1/50$, and $x/a = 1$. The solid black, red dashed, and blue dotted lines show $P_{\text{pair}}(\alpha,t)$ for $\alpha = 1$, 6, and 21, respectively. The initial state $|\psi(0)\rangle$ is equal to (a) $|\text{PS}\rangle$ and (b) $|\text{FS}\rangle$.

[Fig. 5.11(b)] is—as already anticipated based on the initial state decomposition—distinct. In Fig. 5.11(a), $P_{\text{pair}}(\alpha,t)$ for $\alpha = 1$ decays with damped oscillations. The damping or decay are attributed to the fact that a large number of eigenstates contribute to the initial state with comparable weight, giving rise to dephasing. In Fig. 5.11(b), $P_{\text{pair}}(\alpha,t)$ oscillates with nearly undamped amplitude for all α considered. The slight "distortions" of the oscillations are caused by dephasing effects of the eigenstates that contribute to the fully symmetric initial state with a small weight, i.e., less than 5%. The oscillation period of $t \approx 2000\hbar/J$ corresponds to an energy of $0.0031J$. This energy agrees with the difference in energies of the two eigenstates that have the largest overlap with the initial state $|\text{FS}\rangle$ [red square and

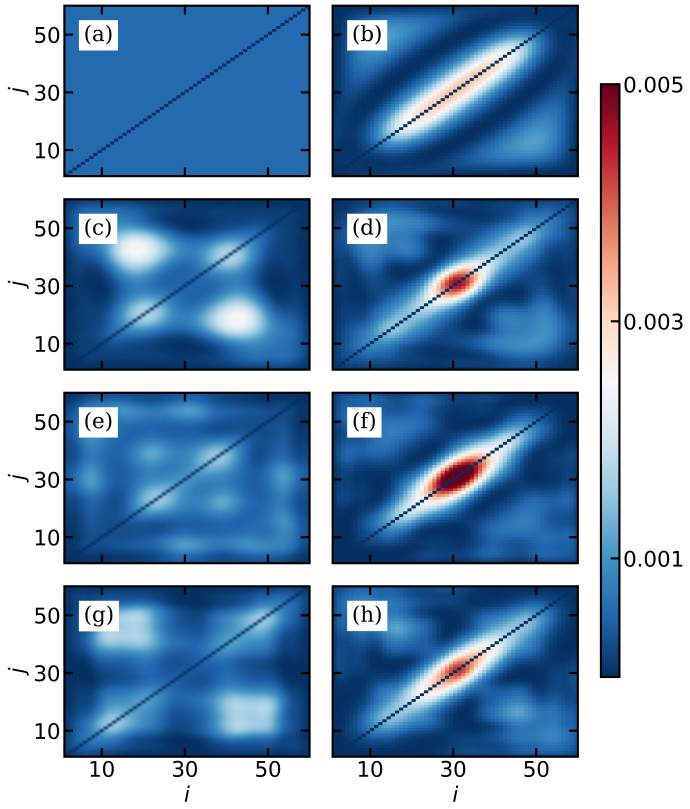

Figure 5.12: Snapshots of $P_{\rm corr}(i,j,t)$ for $\hat{H}_{\rm spin}$ for $N_e = 60$, $g/J = 1/50$, $U/J = -1$, $\delta/J = -1/50$, and $x/a = 1$ as functions of i and j for the initial state $|\psi(0)\rangle = |{\rm FS}\rangle$. (a)-(h) correspond to $Jt/\hbar = 0$, 960, 2220, 3080, 4440, 5220, 6540, and 7500, respectively. As discussed in the main text in the context of Fig. 5.9, the coefficients $c_{i,j}^{(n)}$ are only defined for $i < j$; to plot $P_{\rm corr}(i,j,t)$, we artificially set $c_{i,j}^{(n)} = c_{j,i}^{(n)}$ for $i > j$ and $c_{i,j}^{(n)} = 0$ for $i = j$ for ease of readibility.

blue triangle in Fig. 5.10(b)].

Figure 5.12 shows the spin-spin correlation function $P_{\rm corr}(i,j,t)$,

$$P_{\rm corr}(i,j,t) = \langle\psi(t)|\,\hat{\sigma}_i^+\hat{\sigma}_j^+\,|g,\cdots,g\rangle \times \langle g,\cdots,g|\,\hat{\sigma}_i^-\hat{\sigma}_j^-\,|\psi(t)\rangle \tag{5.23}$$

at eight different times ranging from zero in Fig. 5.12(a) to $Jt/\hbar = 7500$ in Fig. 5.12(h) for $N_e = 60$, $g/J = 1/50$, $U/J = -1$, $\delta/J = -1/50$, and $x/a = 1$. The initial state is $|{\rm FS}\rangle$.

The plots in the left column are for $Jt/\hbar = 0$, 2220, 4440, and 6540. Comparison with Fig. 5.11(b) shows that $P_{\text{pair}}(\alpha = 1, t)$ takes on a local minimum at these times. The plots in the right column of Fig. 5.12, in contrast, are such that $P_{\text{pair}}(\alpha = 1, t)$ takes on a local maximum. We can see that $P_{\text{corr}}(i, j, t)$ is mostly concentrated around the middle of the diagonal in the right column while it is much more spread out in the left column. The observation that the spin-spin correlations alternate between being more localized and being more spread out can be readily explained by the fact that the initial state $|\text{FS}\rangle$ is dominated by contributions from the ground droplet-like state and a delocalized scattering state [red square and blue triangle Fig. 5.10(b)]. This suggests that the droplet-like ground state can be probed by initializing the qubit array in the fully symmetric state $|\text{FS}\rangle$.

The calculations presented consider the ideal case scenario, where the excited state qubit has an infinite lifetime, the photon loss from the cavities is ignored, and imperfections—such as, e.g., a finite spread ΔJ of the tunneling energies J and a finite spread $\Delta\omega_c$ of the cavity frequencies ω_c that exist to a varying degree in experiment—are neglected. To observe the oscillations displayed in Fig. 5.11(b), the time scales associated with spontaneous qubit decay, photon losses, and "dephasing" due to the spread of system parameters must be larger than about $10^4\hbar/J$. In the following discussion, we assume that the excited state lifetime of the qubit is longer than the time scale for photon losses.

A finite "bare" photon lifetime of $\hbar\kappa^{-1}$ leads to a characteristic decay time $(\Gamma_c)^{-1}$ that scales, for $|\delta_0| \ll 2J$, as $\Gamma_c = p_{\text{ph}}\kappa/\hbar$, where $p_{\text{ph}} \approx g^2 J^{-1/2}\delta_0^{-3/2}/4$ and δ_0 denotes the detuning in the single-excitation manifold, $\delta_0 = (\hbar\omega_c - 2J) - \hbar\omega_e$ [106, 105]. Physically, the multiplicative factor p_{ph} can be understood as arising from the admixture of the photonic degrees of freedom to the hybridized bound state in the single-excitation manifold. Rewriting δ_0 in terms of the detuning δ in the two-excitation manifold, we find

$$p_{\text{ph}} = \frac{g^2}{4\sqrt{J}}\left[\frac{1}{2}\left(-\delta + \sqrt{U^2 + 16J^2}\right) - 2J\right]^{-3/2}. \tag{5.24}$$

For $\delta/J = -1/50$ and $-3/20$, as used in this paper, p_{ph} is equal to 5×10^{-3} and 2×10^{-3},

respectively. To observe multiple oscillations, $(\Gamma_c)^{-1}$ must be much larger than $10^4\hbar/J$; the equal sign holds for $\kappa/J = 2\times10^{-2}$ and 5×10^{-2}, respectively. Superconducting circuit experiments have realized an eight cavity system with $U/h = -255$ MHz, $J/h = 5-20$ MHz, and $\kappa/h = 5$ kHz [59]. This translates to $\kappa/J = 2.5\times10^{-4}$ to 10^{-3}, i.e., experiments are already operating in a regime where the photon lifetime is sufficiently long to observe the predicted phenomena. For fixed spreads ΔJ and $\Delta\omega_c$, one may attempt to increase δ such that the spreads become, if measured as a multiple of the detuning, smaller. Since a larger δ corresponds to a smaller photon contribution $p_{\rm ph}$ and hence a longer time scale for the photon losses, there is some room to optimize the parameters for a specific experimental set-up. While challenging, we conclude that the theory predictions put forward in this paper can be tested in state-of-the-art experiments.

5.5 Conclusion

This paper discussed the time-independent and time-dependent behaviors of a qubit array coupled to a non-linear photonic waveguide. Our interest was in the regime where the two-qubit transition energy lies in the band gap below the two-photon bound state band that is supported by the one-dimensional waveguide. We focused our attention on the two-excitation manifold. Even though the qubits are not interacting with each other, effective interactions—mediated by the waveguide—are introduced between qubits as a result of a two-step adiabatic elimination process. The resulting effective spin Hamiltonian, which was shown to accurately reproduce the key characteristics of the full Hamiltonian, features constrained single-qubit hopping and pair hopping interactions. The emergence of the latter critically depends on the presence of the Kerr-like non-linearity U. The effective spin Hamiltonian was shown to support a new class of droplet-like bound states that arise due to the pair hopping interaction. These droplet-like states extend over many qubit lattice sites and can be probed dynamically. For the fully symmetric initial state, the populations

were found to oscillate back and forth between a droplet-like bound state and a delocalized scattering state. While most of our discussion focused on $N_e = 60$, $g/J = 1/50$, $U/J = -1$, and $\delta/J = -1/50$, we emphasize that the characteristics discussed in this paper are also observed for other parameter combinations.

For fixed g/J, δ/J, N_e, and x/a, we find that the number of droplet-like states supported by the qubit array decreases as U/J becomes more negative. As $|U|/J$ increases, the two-photon bound state becomes more localized and hence the overall strength of the pair hopping interaction becomes less negative. Whether or not droplet-like bound states exist also depends on the qubit array spacing x. If the separation between two neighboring qubits is increased, the number of droplet-like states supported by the array decreases.

The giant droplet-like bound states discovered in this work provide an intriguing example of utilizing structured baths to engineer effective spin-spin interactions that support quantum states with non-trivial correlations. The droplet-like states considered in this paper, which emerge in the two-excitation sub-space, are distinct from the two-excitation scattering states considered in Ref. [174] in the absence of the non-linearity U. They are also distinct from hydrid qubit-photon states that emerge in the single-excitation manifold [106]. Possible extensions may focus on topological wave guides [15, 188], higher-dimensional baths, superlattice-type arrangements of the qubits, qubits with multiple transition frequencies [189], multi-level emitters, qubits with multiple point contacts [190], and higher-excitation manifolds [191]. In all these scenarios, it will be interesting to explore the interplay between constrained single-qubit and pair hopping interactions.

5.6 Acknowledgement

Support by the National Science Foundation through grant number PHY-2110158 is gratefully acknowledged. This work used the OU Supercomputing Center for Education and Research (OSCER) at the University of Oklahoma (OU).

Chapter 6

Conclusions and outlook

This thesis studied the physics of a collection of emitters coupled to a structured photonic environment with Kerr-like non-linearity that features center-of-mass momentum dependent two-photon bound states. We analyzed the dynamic and static properties of the emitter-photon coupled system in the two-excitation manifold. One of the main objectives of the thesis was to develop both analytical and numerical tools to study the impact of a non-linear structured bath in the two-excitation manifold.

We began our theoretical investigation with two quantum emitters and employed a complete quantum mechanical framework to study the radiative behaviors in the two-excitation manifold. Our focus was on understanding the role of the two-photon bound state band, a non-trivial feature of the photonic environment made possible by the Kerr-like non-linearity [60, 61]. We identified a regime where the radiation dynamics display almost perfect oscillatory behavior. We developed an analytical two-state model to explain the emergence of this non-Markovian dynamics. Although our primary focus was on the emitter properties influenced by the environment characteristics, we also studied the properties of the photonic bath in the presence of the emitters. This detour led to the discovery that the emitters enable all-to-all momentum space interactions, facilitating the formation of a photonic polaron-like state in the structured bath. This results in the creation of emitter-photon hybridized symmetric and anti-symmetric states that lie energetically below the radiative interacting continuum when the two emitters are separated by several cavity sites, indicating the emergence of long-range interactions in the system. The exchange of population between the symmetric and anti-symmetric emitter-photon hybridized states leads to the unique phenomenon of undamped Rabi oscillations, which is not observed in an emitter-photon coupled system [105, 192, 193] where the photonic environment lacks onsite

photon-photon interaction. Therefore, our system offers a platform that enables the creation of correlated states in the structured photonic bath via coupling to quantum emitters.

We generalized our study to the case with multiple emitters or qubits that form a regularly arranged one-dimensional array. We worked in the band gap regime where the two-emitter energy lies below the two-photon bound state band. Single-photon as well as two-photon bound states are adiabatically eliminated. The effective spin Hamiltonian that arises from the adiabatic eliminations has two types of interactions. One is the constrained single qubit hopping interaction, which is proportional to g^2. The other is the interaction between pairs of excited qubits, which is proportional to g^4. One notable aspect of our system is its behavior in the regime of weak emitter-photon coupling, where $g/J \ll 1$. Surprisingly, we discovered a parameter regime where the interaction term proportional to g^4 prevails over the term proportional to g^2. This unexpected phenomenon contradicts our intuitive expectation that the effects of the g^2 term would dominate over g^4 in the weak coupling limit. This reversal in the hierarchy of scales leads to the emergence of a series of bound states in the array of emitters in the two-excitation manifold. The novel droplet-like bound states that emerge are distinct from the emitter-photon hybridized states that are generally discussed in the context of emitters coupled to a structured photonic bath [167, 105, 57, 60, 61]. The droplet-like states span several sites in the emitter array and exhibit collective behavior. Although these unique bound states have numerous states in their spectrum, they exhibit similar size. These states can be distinguished in terms of the number of nodes present in the wave function along the center-of-mass coordinate in the abstract excitation space. The abstract excitation space is determined by the positions of the excited emitters in the emitter array. Therefore, each pair of positions corresponds to a distinct configuration of the emitter array in the two-excitation manifold. Furthermore, we demonstrate that the droplet-like states can be probed by initializing the emitter array in a state where all basis states with two excited emitters contribute equally. Our findings highlight the potential of utilizing emitter-photon

coupled systems to generate effective spin-spin interactions and explore correlated quantum many-body systems.

The research results presented in this thesis lay the foundation for future studies on how the system evolves with variables such as an in-resonance emitter array, different types of emitters, different excitation manifolds, and variations in the strength of the emitter-photon coupling. This thesis considered the off-resonant case of an emitter array coupled to the structured photonic bath with Kerr-like non-linearity in the two-excitation manifold. An emitter array where the two-emitter transition energy is in resonance with the two-photon bound state band has not been explored previously. We have some interesting preliminary results, which show the impact of the Kerr-like non-linearity on the radiative dynamics of an emitter array. We analyze the time evolution of three distinct initial states $|\Psi(0)\rangle$ in our study. These states are given by

$$|\Psi(0)\rangle = |eeg\cdots g, \text{vac}\rangle, \tag{6.1}$$

$$|\Psi(0)\rangle = \frac{1}{\sqrt{N_e-1}} \sum_{j=1}^{N_e-1} \hat{\sigma}_j^+ \hat{\sigma}_{j+1}^+ |g\cdots g, \text{vac}\rangle, \tag{6.2}$$

and

$$|\Psi(0)\rangle = \frac{1}{\sqrt{N_e(N_e-1)/2}} \sum_{i=1}^{N_e-1} \sum_{j=i+1}^{N_e} \hat{\sigma}_i^+ \hat{\sigma}_j^+ |g\cdots g, \text{vac}\rangle. \tag{6.3}$$

The states given in Eqs. (6.1)-(6.3) correspond to a collection of emitters in a ground state with two excited emitters located on one end of the one-dimensional array, the superposition of two adjacent excited emitters in the array, and the symmetric superposition of basis states with two excited emitters separated by a variable number of ground-state emitters in the array, respectively. It is crucial to mention that in contrast to the research work explained in Chapter 5, we can not eliminate the two-photon bound states adiabatically in this situation. This is due to the resonance condition, which causes a significant variation in the contribution of two-photon bound states over time. To simplify the analysis, we utilize

the Born-Markov approximation and derive a set of coupled differential equations based on the emitter degrees of freedom. However, we must exercise caution when applying the Born-Markov approximation to the emitter array, as the number of emitters plays a significant role in determining the effective coupling strength g_{eff} between the emitters and photons. Although we operate in the weak coupling regime ($g/J \ll 1$), the number N_e of emitters introduces an approximate scaling factor of $\sqrt{N_e}$ to the emitter-photon coupling strength, i.e., $g_{\text{eff}} \approx \sqrt{N_e}g$. As a result, as the number of emitters increases, the effective emitter-photon coupling strength also increases by a factor of $\sqrt{N_e}$. Therefore, we need to carefully select a combination of g and N_e to ensure that the effective emitter-photon coupling remains within the weak coupling regime ($g_{\text{eff}}/J \ll 1$), thereby validating the applicability of the Born-Markov approximation. We solve the set of differential equations obtained as a result of the Born-Markov approximation to investigate the behavior of the system over time. The effective Hamiltonian that arises from these equations is non-Hermitian in nature. Using the non-Hermitian Hamiltonian in the emitter degrees of freedom, we can generate a quantum master equation.

Another intriguing extension of the emitter array in the resonance case could involve examining the radiative characteristics when all the emitters are in the excited state. Because of the complexity of the Hilbert space, utilizing a quantum master equation framework might be the most efficient approach for analyzing such a system. Working within the weak emitter-photon coupling regime, the system could be initialized in a Greenberger-Horne-Zeilinger (GHZ) state with multiple emitters ($N_e \gg 1$), i.e., $|\Psi(0)\rangle = \frac{1}{\sqrt{N_e}}\left[|ee\cdots e\rangle + |gg\cdots g\rangle\right]$ [194]. The GHZ state is characterized by a high degree of entanglement, making the investigation of the time dependence of system-bath entanglement in this scenario particularly interesting [195].

Exploring a group of three- or four-level emitters coupled to the structured photonic environment could be a compelling avenue for future research. This would enlarge the size

of the Hilbert space associated with the emitter degrees of freedom. Additionally, multiple transition energies would be present due to the emitters having multiple levels. Consequently, incorporating an internal detuning, such as the disparity between two transition energies in the case of a three-level emitter, into the system Hamiltonian would enhance the tunability of the problem. Within the bandgap regime, this system could serve as a quantum simulation platform of systems with a spin larger than $S = 1/2$.

Moreover, it would be compelling to investigate the emitter-photon coupled system in the three-excitation manifold, which is a logical extension of this study. The focus would primarily be on the three-photon bound states that are supported by the structured photonic environment. This scenario involves two types of three-photon bound states [200], one of which is deeply bound, while the other two are weakly bound, particularly in the presence of stronger photon-photon onsite interaction. This problem would be intriguing from the viewpoint of the validity of the adiabatic elimination since we would need to consider the contribution from the scattering continuum of two-photon bound states and single photons.

Another potential area of study is the investigation of the system in the regime of strong coupling between emitters and photons, where the counter-rotating terms in the emitter-photon interaction Hamiltonian cannot be disregarded. This research would pose its own set of challenges since many excitation manifolds would be coupled. It would be intriguing to investigate the relationship between the emitter-photon coupling strength and the minimum total number of excitations needed to accurately describe the coupled system of emitters and photons.

Appendix A

Single-emitter dynamics

Section 4.4 uses the dynamics of a single emitter coupled to cavity n as a reference. This appendix summarizes the single-emitter results. Note that the results are independent of n since the emitter position does not matter.

We expand the time-dependent wave packet as [173, 107]

$$\begin{aligned} |\psi(t)\rangle &= \exp(-\imath\omega_e t)\times \\ &\quad \left[d_e(t)|e,\mathrm{vac}\rangle + \sum_k d_k(t)\hat{a}_k^\dagger|g,\mathrm{vac}\rangle \right], \end{aligned} \tag{A.1}$$

where $d_e(t)$ and $d_k(t)$ are expansion coefficients. Starting at time $t=0$ in the state $|e,\mathrm{vac}\rangle$ [i.e., setting $d_e(0)=1$ and $d_k(0)=0$] and following the steps of Ref. [107], one finds

$$\dot{d}_e(t) = -\int_0^t d_e(t-t')\mathscr{M}(t')dt', \tag{A.2}$$

where

$$\mathscr{M}(t') = \frac{g^2}{\hbar^2 N}\sum_k \exp\left(-\frac{\imath\Delta_k t'}{\hbar}\right). \tag{A.3}$$

The integral in Eq. (A.2) can be evaluated analytically [173].

In what follows, we review results obtained within the Markov approximation [107, 173]. The presence of the bath memory function $\mathscr{M}(t')$ in Eq. (A.2) indicates that the dynamics is, in general, non-Markovian: the evolution of the coefficient $d_e(t)$ depends on the past, i.e., the system's state at earlier times. If the bath memory time τ_{bath} is short, i.e., if

$$\left|\frac{\dot{d}_e(t)}{d_e(t)}\tau_{\mathrm{bath}}\right| \ll 1, \tag{A.4}$$

the Markov approximation

$$\int_0^t \mathscr{M}(t')d_e(t-t')dt' \approx d_e(t)\int_0^t \mathscr{M}(t')dt' \tag{A.5}$$

should be reliable. Using

$$\mathrm{Re}\left[\lim_{t\to\infty}\int_0^t \exp\left(-\frac{\imath\Delta_k t'}{\hbar}\right)dt'\right] = \pi\hbar\delta(\Delta_k) \tag{A.6}$$

and dropping the imaginary part, which introduces a negligible energy shift Δ_{single}, Eq. (A.2) can be rewritten as

$$\dot{d}_e(t) = -\Gamma_{\text{single}} d_e(t) \tag{A.7}$$

or

$$d_e(t) = \exp\left(-\Gamma_{\text{single}} t\right), \tag{A.8}$$

where

$$\Gamma_{\text{single}} = \frac{\pi g^2}{\hbar N}\sum_k \delta(\Delta_k). \tag{A.9}$$

Equation (A.7) describes the effect of the bath on the expansion coefficient of the state $|e,\text{vac}\rangle$. The emitter-bath coupling induces an exponential decay of the population, with a decay rate $2\Gamma_{\text{single}}$, and an energy shift Δ_{single} in the energy of the state $|e,\text{vac}\rangle$.

To find an explicit expression for Γ_{single}, we replace the sum over k by an integral,

$$\sum_k(\cdots) = \frac{Na}{2\pi}\int_{-\pi/a}^{\pi/a}(\cdots)dk, \tag{A.10}$$

and perform a change of variable,

$$dk = \frac{\partial k}{\partial E_k}dE_k = \left(\frac{\partial E_k}{\partial k}\right)^{-1} dE_k. \tag{A.11}$$

Defining the density of states $\rho_{\text{single}}(k)$ through

$$\rho_{\text{single}}(k) = J\left(\frac{\partial E_k}{\partial k}\right)^{-1} \tag{A.12}$$

and using Eqs. (A.10)-(A.12) in Eq. (A.9), we find

$$\Gamma_{\text{single}} = \frac{g^2 a}{\hbar J}\int_{\hbar\omega_c-2J}^{\hbar\omega_c+2J}\delta(E_k-\hbar\omega_e)\rho_{\text{single}}(k)dE_k. \tag{A.13}$$

Evaluating the integral yields Eq. (4.35) from the main text.

Appendix B

Details on adiabatic elimination

Equations (4.16)-(4.19) of the main text are equivalent to the time-dependent Schrödinger equation within the two-excitation subspace. After adiabatic elimination, the equations reduce to

$$\imath\hbar\dot{c}_{ee}(t) = 2\Delta_e c_{ee}(t) + \frac{g^2}{J\sqrt{N}}\sum_K F_{K,b}(n_1,n_2)c_{K,b}(t) + \frac{g^2}{J\sqrt{N}}\sum_K\sum_q F_{K,q}(n_1,n_2)c_{K,q}(t), \tag{B.1}$$

$$\imath\hbar\dot{c}_{K,b}(t) = \Delta_{K,b}c_{K,b}(t) + \frac{g^2}{J\sqrt{N}}F^*_{K,b}(n_1,n_2)c_{ee}(t) + \frac{g^2}{JN}\sum_{K',K} G_{K,K'}(n_1,n_2)c_{K',b}(t) + \frac{g^2}{JN}\sum_{K'}\sum_q H_{K,K',q}(n_1,n_2)c_{K',q}(t), \tag{B.2}$$

and

$$\imath\hbar\dot{c}_{K,q}(t) = \Delta_{K,q}c_{K,q}(t) + \frac{g^2}{J\sqrt{N}}F^*_{K,q}(n_1,n_2)c_{ee}(t) + \frac{g^2}{JN}\sum_{K',K}\sum_{q',q}[H_{K',K,q'}(n_1,n_2)]^* c_{K',b}(t) + \frac{g^2}{JN}\sum_{K',K}\sum_{q',q} J_{K,K',q,q'}(n_1,n_2)c_{K',q'}(t), \tag{B.3}$$

where

$$F_{K,b}(n_1,n_2) = -\sum_k\sum_{\alpha=1,2}\frac{J}{N\Delta_k}\exp\big(-\imath k a n_{\beta(\alpha)}\big)[M_b(k,n_\alpha,K)]^*, \tag{B.4}$$

$$F_{K,q}(n_1,n_2) = -\sum_k\sum_{\alpha=1,2}\frac{J}{N\Delta_k}\exp\big(-\imath k a n_{\beta(\alpha)}\big)[M_q(k,n_\alpha,K)]^*, \tag{B.5}$$

$$G_{K,K'}(n_1,n_2) = -\sum_k\sum_{\alpha=1,2}\frac{J}{N\Delta_k}[M_b(k,n_\alpha,K)]^* M_b(k,n_\alpha,K'), \tag{B.6}$$

$$H_{K,K',q}(n_1,n_2) = -\sum_k \sum_{\alpha=1,2} \frac{J}{N\Delta_k} [M_b(k,n_\alpha,K)]^* M_q(k,n_\alpha,K'), \tag{B.7}$$

$$J_{K,K',q,q'}(n_1,n_2) = -\sum_k \sum_{\alpha=1,2} \frac{J}{N\Delta_k} [M_q(k,n_\alpha,K)]^* M_{q'}(k,n_\alpha,K'), \tag{B.8}$$

and Δ_e is given in Eq. (4.33) of the main text. The quantity $2\Delta_e$ can be interpreted as an effective Stark shift [106] that is introduced by the single-photon states. Before the adiabatic elimination, energies are measured relative to the energy $2\hbar\omega_e$ of the initial state. After the adiabatic elimination, the state with two emitter excitations is "detuned with respect to itself". The Stark shift was set to zero in Ref. [106]. This approximation is justified when the resonance wave vector lies in the middle of the band. Near the bottom of the band, however, the quantity $2\Delta_e$ introduces a non-perturbative correction [60].

The quantity $G_{K,K'}(n_1,n_2)$ describes effective off-diagonal couplings between two-photon bound states with center-of-mass wave numbers K and K'. Before the adiabatic elimination, the right hand side of the equation for $\dot{c}_{K,b}(t)$ does not depend on $c_{K',b}(t)$ for $K' \neq K$. After the adiabatic elimination, the right hand side of the equation for $\dot{c}_{K,b}(t)$ depends on $c_{K',b}(t)$ for $K' \neq K$.

The equations above simplify significantly if the contributions from the scattering states are dropped. The result is given in Eqs. (4.26)-(4.29) of the main text. The next step is to go to a rotating frame. Rewriting the coupled equations in terms of $\tilde{c}_{ee}(t)$ and $\tilde{c}_{K,b}(t)$, where

$$\tilde{c}_{ee}(t) = \exp\left(2\imath\Delta_e t/\hbar\right) c_{ee}(t) \tag{B.9}$$

and

$$\tilde{c}_{K,b}(t) = \exp\left(\imath\Delta_{K,b} t/\hbar\right) c_{K,b}(t), \tag{B.10}$$

the diagonal terms vanish:

$$\imath\hbar\dot{\tilde{c}}_{ee}(t) = \frac{g^2}{J\sqrt{N}} \sum_K F_{K,b}(n_1,n_2) \exp\left(-\frac{\imath\tilde{\Delta}_{K,b} t}{\hbar}\right) \tilde{c}_{K,b}(t) \tag{B.11}$$

and

$$\imath\hbar\dot{\tilde{c}}_{K,b}(t) = \frac{g^2}{J\sqrt{N}}[F_{K,b}(n_1,n_2)]^* \exp\left(\frac{\imath\tilde{\Delta}_{K,b}t}{\hbar}\right)\tilde{c}_{ee}(t) \tag{B.12}$$

with

$$\tilde{\Delta}_{K,b} = \Delta_{K,b} - 2\Delta_e. \tag{B.13}$$

We now specialize to the initial state $|e,e,\text{vac}\rangle$. Integrating Eq. (B.12) and using the result in Eq. (B.11), we obtain an equation for the coefficient $\tilde{c}_{ee}(t)$ that is independent of $\tilde{c}_{K,b}(t)$:

$$\dot{\tilde{c}}_{ee}(t) = -\int_0^t \mathscr{M}(t',n_1,n_2)\tilde{c}_{ee}(t-t')dt', \tag{B.14}$$

where the bath memory function $\mathscr{M}(t',n_1,n_2)$ reads

$$\mathscr{M}(t',n_1,n_2) = \frac{g^4}{\hbar^2 J^2 N}\sum_K |F_{K,b}(n_1,n_2)|^2 \exp\left(-\frac{\imath\tilde{\Delta}_{K,b}t'}{\hbar}\right). \tag{B.15}$$

Following the same steps as in Appendix A and defining the density of states $\rho(K)$ through

$$\rho(K) = J\left(\frac{\partial\Delta_{K,b}}{\partial K}\right)^{-1}, \tag{B.16}$$

we find Eq. (4.31) of the main text.

Appendix C

Derivation of $\hat{H}_{\text{spin}}$

Starting with the full Hamiltonian $\hat{H}$, this appendix derives the effective spin Hamiltonian $\hat{H}_{\text{spin}}$. The adiabatic elimination procedure discussed in this appendix is illustrated in Fig. C.1.

Time-dependent wave packet: Throughout, we assume that the two-photon scattering states can be neglected. This is justified since we are working in a regime where the two-qubit transition energy is far detuned from the two-photon scattering continuum. Under this approximation, the wavepacket $|\psi(t)\rangle$ in the two-excitation manifold can be written as [106, 60, 61]

$$|\psi(t)\rangle = \exp(-2\imath\omega_e t)\Big[\sum_{i=1}^{N_e-1}\sum_{j=i+1}^{N_e} d_{ij}(t)\sigma_i^+\sigma_j^+|g,\cdots,g,\text{vac}\rangle + \sum_{i=1}^{N_e}\sum_k c_{ik}(t)\sigma_i^+\hat{a}_k^\dagger|g,\cdots,g,\text{vac}\rangle + \sum_K c_{K,b}(t)\hat{B}_K^\dagger|g,\cdots,g,\text{vac}\rangle\Big], \tag{C.1}$$

where $d_{ij}(t)$, $c_{ik}(t)$, and $c_{K,b}(t)$ denote expansion coefficients. $\hat{B}_K^\dagger$ is the creation operator for a two-photon bound state with momentum K. Inserting Eq. (C.1) into the time-dependent Schrödinger equation, we obtain a set of coupled differential equations

$$\imath\hbar\dot{d}_{ij}(t) = \frac{g}{\sqrt{N}}\sum_k\left[\exp(\imath kan_i)c_{jk}(t) + \exp\big(\imath kan_j\big)c_{ik}(t)\right], \tag{C.2}$$

$$\imath\hbar\dot{c}_{ik}(t) = \Delta_k c_{ik}(t) + \frac{g}{\sqrt{N}}\sum_{j=1,j\neq i}^{N_e}\exp\big(-\imath kan_j\big)d_{\tilde{i}\tilde{j}}(t) + \frac{g}{N}\sum_K M_b(k,n_i,K)c_{K,b}(t), \tag{C.3}$$

and

$$\imath\hbar\dot{c}_{K,b}(t) = \Delta_{K,b}c_{K,b}(t) + \frac{g}{N}\sum_{i=1}^{N_e}\sum_k[M_b(k,n_i,K)]^* c_{ik}(t), \tag{C.4}$$

where $\tilde{i} = \min(i,j)$ and $\tilde{j} = \max(i,j)$. The energy detunings Δ_k and $\Delta_{K,b}$ are given by

$$\Delta_k = E_k - \hbar\omega_e \tag{C.5}$$

and

$$\Delta_{K,b} = E_{K,b} - 2\hbar\omega_e, \tag{C.6}$$

where E_k denotes the energy of a single photon with wave vector k. The matrix elements $M_b(k,n,K)$ are defined as [60, 61]

$$M_b(k,n,K) = \sqrt{2} \times \sum_m \exp\left[\imath m\left(k - \frac{K}{2}\right)a + \imath n(K-k)a\right]\psi_{K,b}(m), \tag{C.7}$$

where $\psi_{K,b}(m) = \langle ma|\psi_{K,b}\rangle$ is the two-photon bound state wave function (ma denotes the relative distance between the two photons). Stationary and time-dependent solutions to the Schrödinger equation for $\hat{H}_{\text{full}}$ are obtained through exact diagonalization, excluding the basis kets that span the two-photon scattering continuum. To characterize the distribution of the excited qubits, we monitor the pair correlation function $P_{\text{pair}}(\alpha,t)$,

$$P_{\text{pair}}(\alpha,t) = \langle\psi(t)| \sum_{i=1}^{N_e-\alpha} \hat{\sigma}_i^+ \hat{\sigma}_{i+\alpha}^+ |g,\cdots,g,\text{vac}\rangle \times \langle g,\cdots,g,\text{vac}| \hat{\sigma}_i^- \hat{\sigma}_{i+\alpha}^- |\psi(t)\rangle, \tag{C.8}$$

as well as the spin-spin correlation function $P_{\text{corr}}(i,j,t)$,

$$P_{\text{corr}}(i,j,t) = \langle\psi(t)| \hat{\sigma}_i^+ \hat{\sigma}_j^+ |g,\cdots,g,\text{vac}\rangle \times \langle g,\cdots,g,\text{vac}| \hat{\sigma}_i^- \hat{\sigma}_j^- |\psi(t)\rangle. \tag{C.9}$$

In what follows, we introduce several approximations that eliminate the photonic degrees of freedom from the problem and, in turn, introduce effective interactions between groups of qubits.

Adiabatic elimination of the single-photon states: Assuming that the changes of $c_{ik}(t)$ with time can be neglected, i.e., $\dot{c}_{ik}(t) = 0$ in Eq. (C.3), the single-photon states $\hat{\sigma}_j^+ |g,\cdots,g,k\rangle$ can be adiabatically eliminated. This approximation breaks down when g is too large or

the single-qubit transition energy is too close to the single-photon band. The resulting differential equations read

$$\imath\hbar\dot{d}_{ij}(t) = \sum_{l=1,l\neq j}^{N_e} W_{il} d_{\tilde{l}\tilde{j}}(t) + \sum_{l=1,l\neq i}^{N_e} W_{lj} d_{\tilde{i}\tilde{l}'}(t) + \frac{g^2}{\sqrt{N}J} \sum_K F_{K,b}(n_i,n_j) c_{K,b}(t) \tag{C.10}$$

and

$$\imath\hbar\dot{c}_{K,b}(t) = \Delta_{K,b} c_{K,b}(t) + \frac{g^2}{\sqrt{N}J} \sum_{i=1}^{N_e} \sum_{j=i+1}^{N_e} F^*_{K,b}(n_i,n_j) d_{ij}(t) + \frac{g^2}{NJ} \sum_{K'} G_{KK'}(\vec{n}) c_{K',b}(t), \tag{C.11}$$

where $\tilde{l} = \min(l,j)$, $\tilde{j} = \max(l,j)$, $\tilde{i} = \min(l,i)$, $\tilde{l}' = \max(l,i)$, and $\vec{n} = (n_1, n_2, \cdots, n_{N_e})$. It can be seen that the adiabatic elimination of the single-photon states introduces three effective interactions, namely $F_{K,b}$, $G_{KK'}$, and W_{jl}. The effective interaction $F_{K,b}(n_i,n_j)$ between the states $\hat{\sigma}_i^+ \hat{\sigma}_j^+ |g,\cdots,g,\text{vac}\rangle$ and $\hat{B}_K^\dagger |g,\cdots,g,\text{vac}\rangle$ is given by [106, 60, 61]

$$\begin{aligned} F_{K,b}(n_i,n_j) = \\ -\sum_k \frac{J}{N\Delta_k} \Big(\exp(-\imath k a n_i) [M_b(k,n_j,K)]^* + \\ \exp\big(-\imath k a n_j\big) [M_b(k,n_i,K)]^* \Big). \end{aligned} \tag{C.12}$$

The effective interaction $G_{KK'}(\vec{n})$ between the states $\hat{B}_K^\dagger |g,\cdots,g,\text{vac}\rangle$ and $\hat{B}_{K'}^\dagger |g,\cdots,g,\text{vac}\rangle$ is given by [106, 60, 61]

$$\begin{aligned} G_{KK'}(\vec{n}) = -\sum_{j=1}^{N_e} \sum_k \frac{J}{N\Delta_k} [M_b(k,n_j,K)]^* \times \\ M_b(k,n_j,K'). \end{aligned} \tag{C.13}$$

The interactions $F_{K,b}$ and $G_{KK'}$ have been discussed extensively in the context of the two-qubit system ($\hat{H}$ with $N_e = 2$) [106, 60, 61]. The effective interaction W_{jl}, in contrast, does not exist for $N_e = 2$; it critically depends on having more than two qubits coupled to the cavity array. The functional form of W_{jl} is given in Eq. (5.10) of the main text.

Equations (C.10)–(C.11) correspond to the effective Hamiltonian $\hat{H}_{\text{adia},0}$,

$$\hat{H}_{\text{adia},0} = \hat{H}_{\text{single}} + \frac{g^2}{J\sqrt{N}} \sum_{i=1}^{N_e} \sum_{j=i+1}^{N_e} \sum_{K} \left[F_{K,b}(n_i,n_j) \hat{\sigma}_i^+ \hat{\sigma}_j^+ \hat{B}_K + F^*_{K,b}(n_i,n_j) \hat{\sigma}_i^- \hat{\sigma}_j^- \hat{B}_K^\dagger \right] + \sum_K \Delta_K \hat{B}_K^\dagger \hat{B}_K + \frac{g^2}{NJ} \sum_K \sum_{K'} G_{KK'}(\vec{n}) \hat{B}_K^\dagger \hat{B}_{K'}, \tag{C.14}$$

where $\hat{H}_{\text{single}}$ is given in Eq. (5.7) of the main text. For $N_e = 2$, Refs. [60, 61] found that the effective interaction $G_{KK'}$ plays a non-negligible role only when the transition energy $2\hbar\omega_e$ of two qubits is in or nearly in resonance with the bottom of the two-photon bound state band. Since $G_{KK'}$ plays, in general, a negligible role away from the bottom of the band, it is useful to define the effective Hamiltonian $\hat{H}_{\text{adia},1}$ by setting $G_{KK'}$ in $\hat{H}_{\text{adia},0}$ to zero. The effective Hamiltonians $\hat{H}_{\text{adia},0}$ and $\hat{H}_{\text{adia},1}$ live in the $\left(\frac{N_e(N_e-1)}{2}+N\right)$–dimensional Hilbert space that is spanned by the states $\hat{\sigma}_i^+ \hat{\sigma}_j^+ |g,\cdots,g,\text{vac}\rangle$ and $\hat{B}_K^\dagger |g,\cdots,g,\text{vac}\rangle$ with wave vector K.

Adiabatic elimination of the two-photon bound states: For the band gap physics considered in this paper, the energy $2\hbar\omega_e$ of two excited qubits is not in resonance with the two-photon bound state band. Consequently, we adiabatically eliminate the two-photon bound states, i.e., we set the left hand side of Eq. (C.11) to zero. Using this to eliminate $c_{K,b}(t)$ from Eq. (C.10), the resulting set of coupled equations reads

$$\imath\hbar \dot{d}_{ij}(t) = \sum_{l=1,l\neq j}^{N_e} W_{il} d_{\tilde{l}\tilde{j}}(t) + \sum_{l=1,l\neq i}^{N_e} W_{lj} d_{\tilde{i}\tilde{l}'}(t) + \sum_{l=1}^{N_e-1} \sum_{h=l+1}^{N_e} Y_{ij,lh} d_{lh}(t). \tag{C.15}$$

Equation (C.15) corresponds to the effective spin Hamiltonian $\hat{H}_{\text{spin}}$ given in Eq. (5.8) of the main text, which lives in the $N_e(N_e-1)/2$–dimensional Hilbert spanned by the qubit states $\hat{\sigma}_i^+ \hat{\sigma}_j^+ |g,\cdots,g\rangle$.

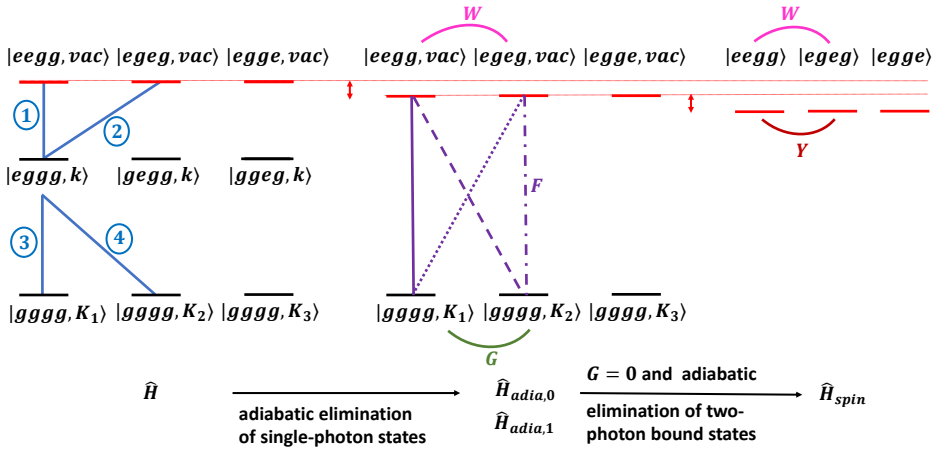

Figure C.1: Approximations made to obtain the effective spin Hamiltonian $\hat{H}_{\text{spin}}$ (right column) from the total Hamiltonian $\hat{H}$ (left column). The schematic considers $N_e = 4$ as an example and shows only a subset of the basis kets. The red and black horizontal lines show a subset of basis kets. The blue, pink, purple, green, and dark red lines represent interactions. As a result of the adiabatic elimination of the single-photon states $|eggg, k\rangle$, the interactions 1 and 2 give rise to the interaction W between the states $|eegg, \text{vac}\rangle$ and $|egeg, \text{vac}\rangle$ (solid pink line), the interactions 1 and 3 give rise to the interaction F between the states $|eegg, \text{vac}\rangle$ and $|gggg, K_1\rangle$ (solid purple line), the interactions 2 and 3 give rise to the interaction F between the states $|egeg, \text{vac}\rangle$ and $|gggg, K_1\rangle$ (dotted purple line), the interactions 1 and 4 give rise to the interaction F between the states $|eegg, \text{vac}\rangle$ and $|gggg, K_2\rangle$ (dashed purple line), the interactions 2 and 4 give rise to the interaction F between the states $|egeg, \text{vac}\rangle$ and $|gggg, K_2\rangle$ (dash-dotted purple line), and the interactions 3 and 4 give rise to the interaction G between the states $|gggg, K_1\rangle$ and $|gggg, K_2\rangle$ (green line). As a result of setting G to zero and adiabatically eliminating the two-photon bound states $|gggg, K\rangle$, the interactions F (e.g., solid and dotted lines, and dashed and dash-dotted lines) give rise to the interaction Y between the states $|eegg\rangle$ and $|egeg\rangle$ (solid dark red line). The down shifts of the red basis states in the middle and right columns represent the Stark shifts that are due to the adiabatic eliminations.

Appendix D

Technical details: Numerical calculations

This chapter focuses on the technical details of the numerical calculations of our work. The context of our work is in a structured photonic environment where the position and momentum are discrete. The dynamical behavior of our system is explained by the time-dependent Schrödinger equation. In our study, this equation is represented as a linear differential equation with time as the variable. Various techniques, such as direct integration and spectral methods, can be used to solve it [164, 173]. We utilize a numerical diagonalization method to investigate the time-dependent as well as the time-independent characteristics of the coupled emitter-photon system. The GNU Scientific Library (GSL) subroutine for complex hermitian matrices is essential in carrying out the diagonalization [164, 196]. Specifically, we used the subroutine "gsl_eigen_hermv()" since the Hamiltonian matrices we disgonalized are complex hermitian matrices. Although calling the subroutine is relatively straightforward, it is crucial to elaborate on how we derive the Hamiltonian and the size of the associated Hilbert space.

D.1 Size of the Hilbert space

Our study focuses on analyzing a system that consists of an array of N cavities coupled to N_e emitters in the two-excitation manifold. To achieve this, we span the Hilbert space using emitter states and eigenstates of the bath Hamiltonian, i.e., we use the momentum space eigenstates of the Bose-Hubbard model for photons. There are $N_e(N_e-1)/2$ emitter basis states in this manifold. There are N momentum values available to each photon in the first Brillouin zone because of the N cavities present in the structured photonic environment. Due to the Kerr-like non-linearity, there are N two-photon bound states with distinct center-of-mass momenta in the two-excitation manifold.

A two-photon scattering state can be characterized by the center-of-mass momentum K and the relative momentum k; $|K,k\rangle$, where $K = k_1 + k_2$ and $k = \frac{1}{2}(k_1 - k_2)$. Alternatively, we could use $|k_1, k_2\rangle$. As an example, we consider a photon-photon scattering state with a center-of-mass momentum of $K = 0$. Since the photon-photon scattering states are not bound, each of the two photons can have a momentum between $-\pi/a$ and π/a, as long as the center-of-mass momentum K is zero. Therefore, each of the photons can have positive (negative) and negative (positive) values of equal magnitude. To illustrate this, the following states $|k_1 = 0, k_2 = 0\rangle$, $\left|k_1 = \frac{-1}{2a}, k_2 = \frac{1}{2a}\right\rangle$, $\left|k_1 = \frac{1}{2a}, k_2 = \frac{-1}{2a}\right\rangle$, $\left|k_1 = \frac{1}{a}, k_2 = \frac{-1}{a}\right\rangle$, and $\left|k_1 = \frac{-1}{a}, k_2 = \frac{1}{a}\right\rangle$, correspond to $\left|K = 0, k = \frac{-1}{2a}\right\rangle$, $\left|K = 0, k = \frac{1}{2a}\right\rangle$, $\left|K = 0, k = \frac{1}{a}\right\rangle$, and $\left|K = 0, k = \frac{-1}{a}\right\rangle$, respectively. Therefore, it is evident that for a center-of-mass momentum $K = 0$, there exist, in general, various values for the relative momentum k. Consequently, the fixed K scattering continuum has a "width". It is worth mentioning that the "width", and hence the density of states for two photons varies with the center-of-mass momentum K. Since each of center-of-mass momentum K and relative momentum k can take N values, there are N^2 states in the photon-photon scattering continuum.

We also need to include single-photon processes that involve one of the emitters in an excited state and a single-photon that takes one of the N possible single-particle momenta. Thus, we have $N_e N$ states that describe the single-photon processes for N_e emitters. Thus, the number of basis states that span the full Hilbert space of the emitter-photon coupled system is $\left[N_e(N_e-1)/2 + N + N^2 + N_e N\right]$. The Hamiltonian expressed in that basis has a size of $\left[N_e(N_e-1)/2 + N + N^2 + N_e N\right]^2$. Figure D.1 illustrates the memory required to store the Hamiltonian matrix as a function of N. In Fig. D.1(a), we see that at least 30 GB memory is required to study a two-emitter system coupled to an array with $N = 201$ cavities. Due to the memory limitations of our local computer, which is restricted to 64 GB, we were unable to store the full Hamiltonian matrix of the emitter-photon coupled system when N exceeds 201 for the simplest case with two emitters, i.e., $N_e = 2$. The memory demand is

driven by the N^4 scaling with the number of cavities.

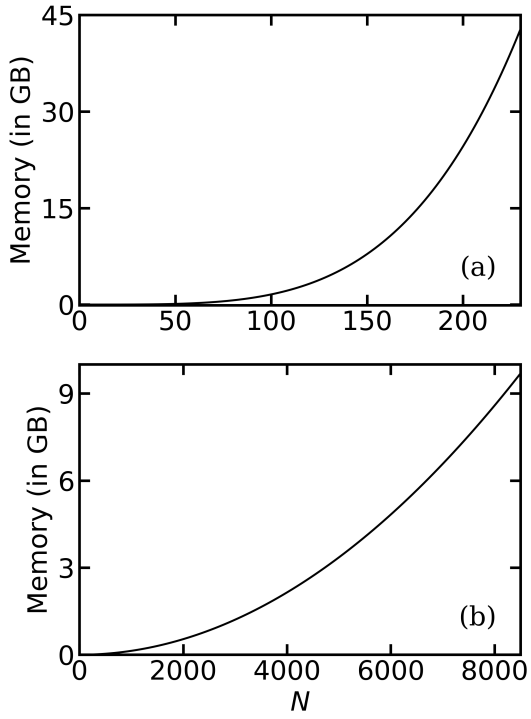

Figure D.1: Memory required to store a Hamiltonian with matrix elements treated as complex double precision variables as a function of the size of the cavity array N for two emitters, i.e., $N_e = 2$. The unit used for the memory is Giga Bytes (GB). (a) The Hamiltonian is the full Hamiltonian. (b) The Hamiltonian is obtained excluding the two-photon scattering states.

To make the problem computationally tractable, it is essential to decrease the memory required. This can be achieved by thoroughly analyzing the parameter space of the emitter-photon system and reducing the size of the Hilbert space. This requires several approximations, such as neglecting two-photon scattering states, which reduces the dimension of the Hilbert space to $(N_e(N_e-1)/2+N_eN+N)$. The reduction of the Hilbert space has implications because the basis states of the reduced space do not cover the entire Hilbert space where the full Hamiltonian of the emitter-photon coupled system lives in. Neverthe-

less, we operate in parameter regimes where the influence of the two-photon scattering states is negligible when compared to the contributions of other basis states in the full Hilbert space. The reduced Hilbert space allows for a numerical calculation with less memory; thus, a much larger cavity array can be considered. According to Fig. D.1(b), when the two-photon scattering states are excluded from the Hilbert space, less than 10 GB memory can describe a two-emitter system with $N = 8001$ cavities.

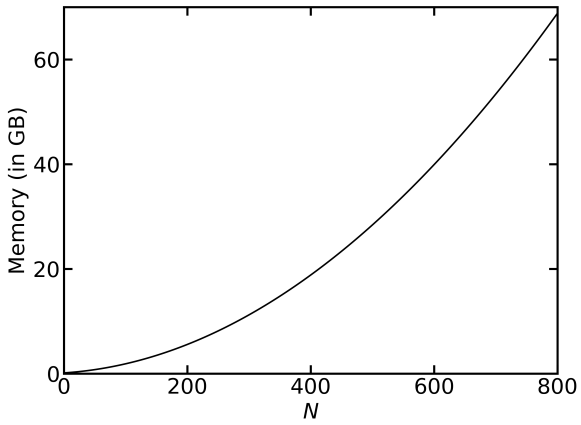

Figure D.2: Memory required to store a Hamiltonian with matrix elements treated as complex double precision variables for an emitter array with $N_e = 80$ emitters as a function of the size of the cavity array N. The Hamiltonian considered is obtained by excluding the two-photon scattering states. The unit used for the memory is Giga Bytes (GB).

When dealing with a large number of emitters ($N_e \gg 1$), the Hilbert space where two-photon scattering states are omitted is used as a benchmark for other calculations. Figure D.2 demonstrates the memory requirement in that Hilbert space for $N_e = 80$ as a function of the number of cavities N. We found that at least 35 GB of memory is needed to store the Hamiltonian for $N_e = 80$ emitters and $N = 501$ cavities. Thus, the presence of multiple emitters in the system makes the problem more expensive computationally even when a reduced Hilbert space is considered.

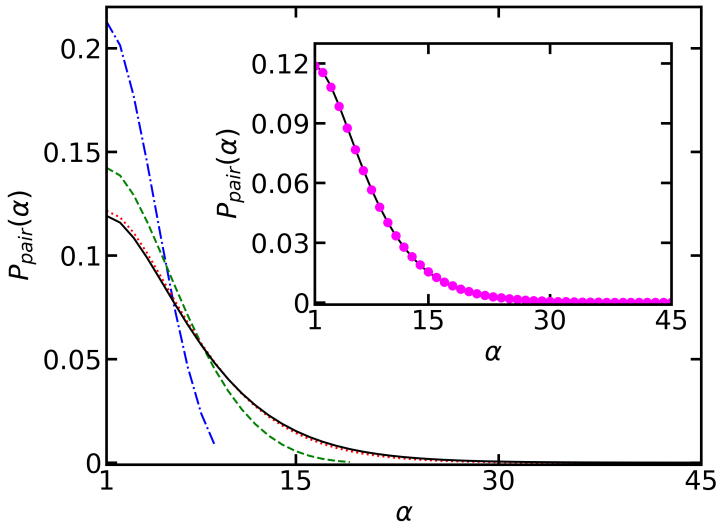

Figure D.3: Pair correlation function $P_{\text{pair}}(\alpha)$ for the ground state of $\hat{H}_{\text{spin}}$ (given in Eq. (5.8)) as a function of the separation α between two excited qubits for $g/J = 0.02$, $U/J = -1$, $x/a = 1$, and $\delta/J = -0.02$. The blue dash-dotted, green dashed, red dotted, and black solid lines are for $N_e = 10$, $N_e = 20$, $N_e = 40$, and $N_e = 60$, respectively. The inset replots the black solid line and additionally shows the results for $N_e = 80$ by magenta solid circles.

Our calculations are performed with careful consideration of the parameters involved, so that the reduced Hilbert space still captures the physics. To accurately characterize the emitter-photon coupled system, it is essential to analyze observables such as population, energy, emission rate, etc. for various number of emitters or cavities. For example, the behavior of the emitter array in the band gap regime described in Chapter 5 is heavily influenced by the number of emitters. Even though the droplet-like bound states in this regime are localized, they span multiple sites in the emitter array. Figure D.3 shows the pair correlation function $P_{\text{pair}}(\alpha)$ for the ground state of $\hat{H}_{\text{spin}}$ for $g/J = 0.02$, $U/J = -1$, $\delta/J = -0.02$, and $x/a = 1$ for four different lengths N_e of the emitter array, namely $N_e = 10$, $N_e = 20$, $N_e = 40$, and $N_e = 60$. The pair correlation function shows that the maximum values and tails for $N_e = 10$ and $N_e = 20$ differ from each other significantly, even though the

maximum occurs at $\alpha = 1$ for both cases. For $N_e = 10$, the tail of the function does not go to zero, indicating that the ground state occupies all the available space in the emitter array. When the number of emitters is increased to $N_e = 20$, the pair correlation function exhibits a noticeable difference compared to the case with $N_e = 10$ emitters. The tail of the function goes to zero at the edge of the emitter array, indicating that the ground state barely fits inside the emitter array. This deviation is very small for larger emitter arrays with $N_e = 40$ and $N_e = 60$. The inset in Fig. D.3 shows that $P_{\text{pair}}(\alpha)$ for the ground state remains essentially unchanged when N_e is increased from 60 (black solid line) to 80 (magenta solid circle). Therefore, to differentiate the self-bound states from other eigenstates of the emitter-photon system, the number of emitters in the array must be greater than 40, i.e., $N_e > 40$. If the number of emitters is less than 40, these states will occupy all the available space in the array, making it difficult to distinguish them from other eigenstates. Therefore, in order to fully understand the physics of the coupled emitter array and cavity array system, it is crucial to use a large enough emitter array. This requires close attention to the memory demands (shown in Fig. D.2) of the calculations.

Drawing from our understanding of the coupling strength between emitters and photons, as well as the energy detuning, we simplified the problem by neglecting states involving photon-photon scattering and performing an adiabatic elimination of single-photon states. Our focus was primarily in the regime of weak emitter-photon coupling ($g/J \ll 1$) and negative single emitter-photon detuning ($\delta_1/J < 0$) such that $|\delta_1/| > g$. These conditions ensured the validity of the aforementioned approximations. The adiabatic elimination of single-photon states enabled us to uncover new effective interactions and streamline the computational aspect by reducing the size of the Hilbert space. However, these approximations impose constraints on the range of acceptable parameters. To explore beyond these limitations, it becomes necessary to drop some of these approximations, leading to a substantial increase in the size of the Hilbert space. For instance, if we wish to consider a

relatively stronger emitter-photon coupling strength ($g/J \approx 1$), the adiabatic elimination approach becomes invalid. Additionally, two-photon scattering states will have non-negligible contribution in such scenarios. Furthermore, the implementation of rotating wave approximations during the derivation of the emitter-photon coupling Hamiltonian becomes infeasible, thereby preventing us from strictly working within the two-excitation manifold, as other excitation manifolds will also contribute.

D.2 Exact diagonalization to evaluate time-dependence

Now that we understand the size of the Hilbert space, let us discuss how we use exact diagonalization to study both time-dependent and time-independent properties of our system. When examining the time evolution of a system prepared in an initial state $|\psi(t=t_0)\rangle$ under a Hamiltonian $\hat{H}(t)$, three possibilities arise. Firstly, if the Hamiltonian is time-independent, denoted by $\hat{H}(t)=\hat{H}$, the state of the system at a later time t can be obtained using

$$|\psi(t)\rangle = \exp\left(-\frac{\imath}{\hbar}\hat{H}(t-t_0)\right)|\psi(t_0)\rangle\,. \tag{D.1}$$

Secondly, if the Hamiltonian is time dependent, but satisfies the condition $[\hat{H}(t),\hat{H}(t')]=0$, meaning that the Hamiltonians at different times commute, the evolved state $|\psi(t)\rangle$ can be determined from

$$|\psi(t)\rangle = \exp\left[-\frac{\imath}{\hbar}\int_{t_0}^{t}\hat{H}(t')dt'\right]. \tag{D.2}$$

Lastly, if the Hamiltonian is time dependent, but does not satisfy the condition $[\hat{H}(t),\hat{H}(t')]=0$, indicating that the Hamiltonians at different times do not commute, the state of the system at time t can be obtained using the Dyson series [161]:

$$|\psi(t)\rangle = \left[\mathbb{1}+\sum_{n=1}^{\infty}\left\{\left(\frac{-\imath}{\hbar}\right)^n\int_{t_0}^{t}dt_1\int_{t_0}^{t_1}dt_2\cdots\int_{t_0}^{t_{n-1}}dt_n\hat{H}(t_1)\hat{H}(t_2)\cdots\hat{H}(t_n)\right\}\right]|\psi(t_0)\rangle\,, \tag{D.3}$$

where $t\geq t_1\geq t_2\cdots\geq t_n\geq t_0$ that highlights the associated time-ordering.

In our work, the Hamiltonian of the emitter-photon coupled system is time-independent. Thus, given an initial state, we can determine the state at a later time using Eq. (D.1). We use eigenvalues and eigenvectors of the Hamiltonian to calculate the time-dependent state of the system. We use exact diagonalization for that purpose. Exact diagonalization involves diagonalizing the full Hamiltonian, denoted by $\hat{H}$, which provides the eigenvalues and eigenvectors that span the entire Hilbert space that $\hat{H}$ lives in. The eigenstate $\left|\eta_j\right\rangle$ with eigenenergy E_j is obtained by acting the Hamiltonian on it, as in

$$\hat{H}\left|\eta_j\right\rangle = E_j\left|\eta_j\right\rangle, \tag{D.4}$$

where eigen index j goes from 1 to size of the Hilbert space. To investigate the time-dependent properties, we consider an initial state with two excited emitters or a superposition of such states, without any photonic components. If $|\psi(0)\rangle$ is the initial state at time $t = 0$, then we calculate the time-dependent state of the system by rewriting Eq. (D.1) as

$$|\psi(t)\rangle = \exp\left(-\imath\hat{H}t/\hbar\right)|\psi(0)\rangle. \tag{D.5}$$

Since the initial state is not an eigenstate of the Hamiltonian, we calculate the overlap between the initial state $|\psi(0)\rangle$ and the eigenstates $\left|\eta_j\right\rangle$ of the Hamiltonian, i.e., $\left\langle\eta_j\middle|\psi(0)\right\rangle$. Since the kets $\left|\eta_j\right\rangle$ form a complete set, using the completeness relation $\sum_j \left|\eta_j\right\rangle\left\langle\eta_j\right| = \mathbb{1}$, we can rewrite Eq. (D.5) as

$$|\psi(t)\rangle = \sum_j \left\langle\eta_j\middle|\psi(0)\right\rangle \exp\left(-\imath E_j t/\hbar\right)\left|\eta_j\right\rangle. \tag{D.6}$$

Thus, finding the overlap $\left\langle\eta_j\middle|\psi(0)\right\rangle$ is crucial when studying time-dependent properties [161].

As discussed in Sec. D.1, storing the Hamiltonian matrix in the full Hilbert space is computationally expensive. To overcome this limitation, we employ a reduced Hilbert space description, which decreases the memory requirements. Since this approach is build upon approximations, it introduces errors compared to the exact diagonalization. For instance,

when neglecting the two-photon scattering states, the eigenstates $\left|\eta'_j\right\rangle$ of the Hamiltonian that live in the reduced Hilbert space do not form a complete set. However, since the contribution of the two-photon scattering states is negligible, we find that $\sum_j \left|\eta'_j\right\rangle \left\langle\eta'_j\right| \approx \mathbb{1}$, where j ranges from 1 to the size of the full Hilbert space minus the number of two-photon scattering states. Based on this observation, we renormalize the set of states $\left|\eta'_j\right\rangle$ so that $\sum_j \left|\eta'_j\right\rangle \left\langle\eta'_j\right| = \mathbb{1}$. Physically, this assumption implies that during the time evolution of the emitter-photon coupled system, no population flows into or out of the two-photon scattering states. As a result, this renormalization assumption leads to shifts in the energy eigenvalues of the Hamiltonian in the reduced Hilbert space. In the reduced Hilbert space, Eq. (D.5) takes the form:

$$|\psi(t)\rangle \approx \sum_j \left[\left\langle\eta'_j\middle|\psi(0)\right\rangle \exp\left(-\imath E'_j t/\hbar\right)\right] \left|\eta'_j\right\rangle, \tag{D.7}$$

where the E'_j represent the shifted energy eigenvalues. Consequently, we observe slight discrepancies between the energy eigenvalues of the full Hamiltonian (obtained using exact diagonalization) and those obtained by matrix diagonalization of the Hamiltonian in the Hilbert space where the two-photon scattering states are excluded. This discrepancy also impacts the system dynamics due to the superposition of states described by Eq. (D.7).

The matrix diagonalization method has a significant advantage over approaches like fourth-order Runge-Kutta [164, 197] in that it does not produce numerical errors. Runge-Kutta and other differential equation solvers tend to accumulate numerical errors over time [164, 197], which depend on the time step used in the evolution process. There are limitations to using the matrix diagonalization method for numerical analysis of physical systems. If the Hamiltonian includes time-dependent elements, the process becomes computationally expensive because the Hamiltonian matrix must be diagonalized at each time step. In our scenario, all Hamiltonians are independent of time, so we are not limited by this constraint.

The number of cavities N determines the convergence of several interaction terms,

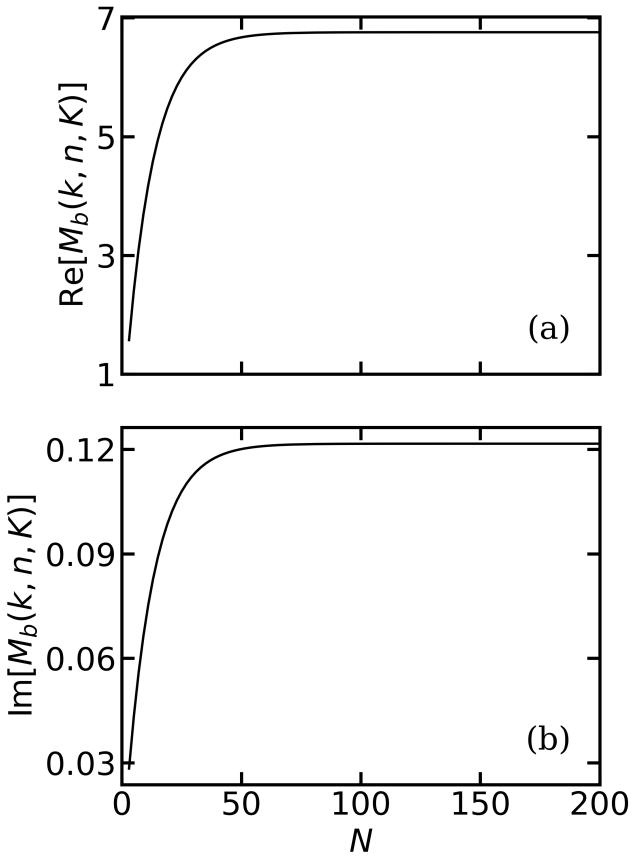

Figure D.4: Coupling matrix element $M_b(k,n,K)$ between a single-photon state with momentum k and a two-photon bound state with center-of-mass momentum K as a function of the size of the cavity array N. (a) $\mathrm{Re}[M_b(k,n,K)]$ for $n=2$, $U/J=-0.7$, $ka=0.01$, and $Ka=0.001$. (a) $\mathrm{Im}[M_b(k,n,K)]$ for $n=2$, $U/J=-0.7$, $ka=0.01$, and $Ka=0.001$.

including $F_{K,b}(n_i,n_j)$ between an excited pair of emitters and a two-photon bound state with center-of-mass momentum K, $G_{K,K'}$ between two two-photon bound states with momentum K and K', respectively, and $M_b(k,n_i,K)$ between a single photon with momentum k and a two-photon bound state with center-of-mass momentum K. The convergence of interaction terms is analyzed by checking their behavior with respect to the number of cavities N. Figure D.4 shows the impact of the cavity array size N on the coupling matrix $M_b(k,n,K)$

for $n = 2$, $U/J = -0.7$, $ka = 0.01$, and $Ka = 0.001$. In Fig. D.4(a), we can see that the real part of $M_b(k,n,K)$, i.e., Re$[M_b(k,n,K)]$, is essentially constant for $N \gtrsim 200$. This suggests that the real part converges around $N \approx 200$ for the specified parameters, with an accuracy of approximately 10^{-15}. Likewise, based on the findings in Fig. D.4(b), we determined that in order to achieve an accuracy of approximately 10^{-15} for the imaginary part of $M_b(k,n,K)$, i.e., Im$[M_b(k,n,K)]$, a minimum of $N = 200$ cavities is required. To guarantee accurate results for the interaction terms in the emitter-photon coupled system, it is essential to carefully monitor the convergence of $M_b(k,n,K)$, which appears explicitly in all effective interactions.

The length of the coupled cavity array, determined by the number of cavities, also impacts boundary effects such as reflections and interferences that must be considered. Absorbing boundary conditions can be used to eliminate these effects [198, 199]. However, based on our current understanding, implementing absorbing boundary conditions requires expressing the basis states associated with the photonic bath in real space representation. In this representation, it becomes exceedingly difficult to distinguish between the two-photon bound states and the two-photon scattering states, as we can easily do in momentum space representation. Consequently, implementing absorbing boundary conditions using the current numerical setup proves to be challenging.

To understand the boundary related issues, we calculate the time scale for the emergence of boundary effects by computing the group velocity of single-photon and two-photon bound states. Our objective is to determine the minimal size of the cavity array that captures the physics of the system under study. For example, the phenomenon of population revival is a dynamic non-Markovian effect caused by boundary effects [58, 187]. This effect occurs at a certain time, which is determined by the size of the cavity array and the group velocity of the resonant photonic modes. The group velocity $v_{K,b}$ of a two-photon bound state with

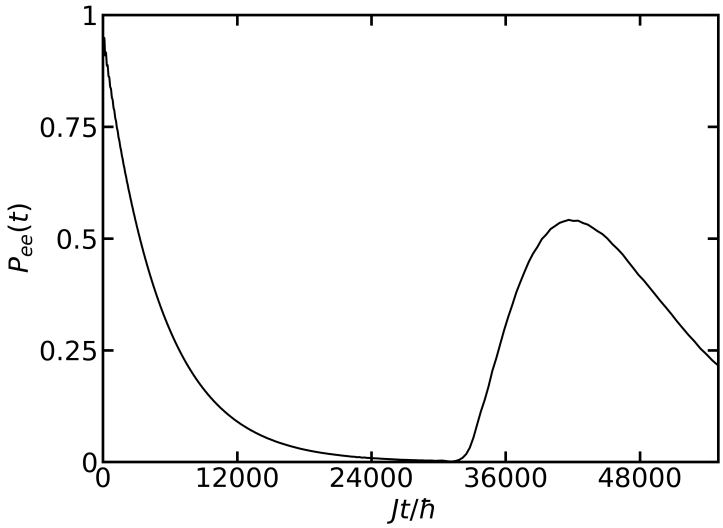

Figure D.5: The population $P_{ee}(t)$ of the state $|ee,\text{vac}\rangle$ as a function of time for $g/J = 0.02$, $U/J = -1.0$, $\delta/J = 0.0431$, $x/a = 0$, and $N = 9001$.

center-of-mass momentum K can be calculated using [61, 106]

$$v_{K,b} = \frac{1}{\hbar}\frac{4Ja\sin(Ka)}{\sqrt{(U/J)^2 + 16\cos^2(Ka/2)}}. \tag{D.8}$$

The resonance center-of-mass momentum K_0 which is given by

$$K_0 = \frac{2}{a}\arccos\left[\frac{1}{16}\left\{\left(\sqrt{(U/J)^2+16} - \delta/J\right)^2 - 4(U/J)^2\right\}\right], \tag{D.9}$$

is the most relevant momentum for calculating the group velocity $v_{K,b}$.

The time taken by the two-photon bound state to travel around the cavity array under periodic boundary conditions is determined by $t_b = \frac{Na}{v_{K_0,b}}$, where N is the number of cavities in the array. For $U/J = -1$ and $\delta/J = 0.0431$, Eq. (D.9) yields $K_0 a = 0.2984$. This implies that it takes approximately $t_b \approx 30100\hbar/J$ for the bound state to complete a revolution around the array of $N = 9001$ cavities. Figure D.5 shows the time-dependent population $P_{ee}(t)$ of the state $|ee,\text{vac}\rangle$ for $g/J = 0.02$, $U/J = -1$, $\delta/J = 0.0431$, $x/a = 0$, and $N = 9001$. We observe that $P_{ee}(t)$ decays exponentially to zero at time $t \approx 27000\hbar/J$. We can see that

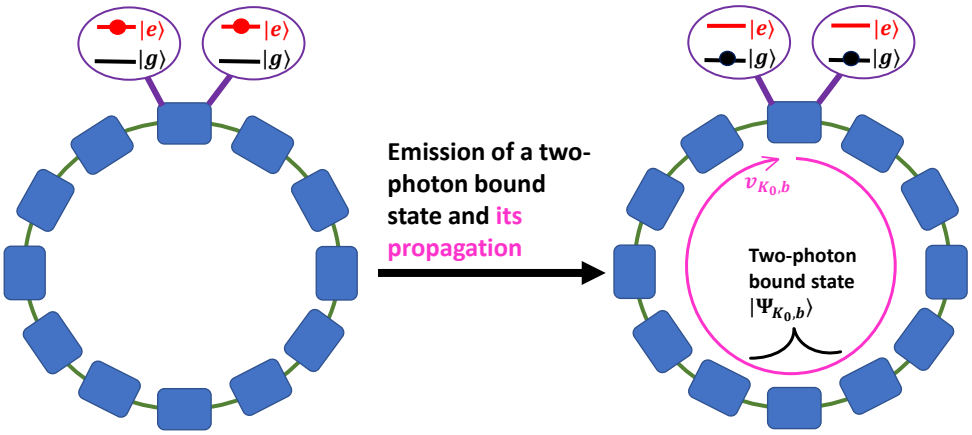

Figure D.6: Schematic of two emitters coupled to the same site of an array of cavities under periodic boundary condition. The blue boxes represent cavities in the array. In the left figure, the emitters are in excited states denoted by solid red filled circles inside the purple oval, and there are no two-photon bound states present in the cavity array. On the right, the diagram shows the emission of the resonant two-photon bound state $\left|\Psi_{K_0,b}\right\rangle$ into the cavity array, with the emitters in their ground states shown by the solid black filled circles inside the purple oval. The resonant two-photon bound state travels with the group velocity $v_{K_0,b}$ from the site of emission (where both emitters are coupled to the same site) and returns to the same site, as indicated by the circular solid magenta arrow.

after the entire population in the emitter degrees of freedom has decayed into the photonic degrees of freedom, there is a reappearance at $t \approx 30000\hbar/J$ of the population $P_{ee}(t)$. This population revival is consistent with the time scale t_b associated with the resonance two-photon bound state group velocity, and can be attributed to the periodic boundary condition of the cavity array. Figure D.6 illustrates this scenario schematically. Since the two-photon bound state takes the time t_b to complete one round around the cavity array and reach the emitters, it is absorbed to some extent by the emitters again after that time interval. This results in the revival of the population $P_{ee}(t)$.

Appendix E

Technical details: Analytical calculations

This chapter is dedicated to discussing the technical aspects of our analytical calculations. In the preceding chapter of this thesis, we focused on the numerical aspects of our work, including the techniques we used and their limitations. This chapter complements the previous one by delving into the analytical calculations we employed, establishing important connections between pen-and-paper and computer-based calculations. Firstly, we discuss the calculation of contour integrals associated with effective interactions that result from the adiabatic elimination of single-photon and two-photon bound state processes. Our approach involves turning certain lattice sums in momentum space to contour integrals [201]. After that, we move on to the calculation of the energy of two-photon bound state using the Lippmann-Schwinger equation [161, 200]. The expression obtained for the energy of the two-photon bound state is critical as it is the main characteristic of the structured photonic environment in our work. We explain these computations and discuss the challenges associated with them.

E.1 Evaluation of lattice sums: Contour integral

The strength W_{ij} of the hopping of excitations in the emitter array, which emerges from the adiabatic elimination of the single-photon states [97, 175, 63], has been previously discussed in Chapter 1 and Chapter 5. The expression for W_{ij}, which represents the strength of excitation hopping between the sites i and j in the emitter array, is provided as follows:

$$W_{ij} = -\frac{g^2}{N}\sum_k \left[\frac{\exp\left(\imath ka(n_i - n_j)\right)}{2J - \delta_1 - 2J\cos\left(ka\right)}\right]. \tag{E.1}$$

We know that in the cavity array, k-space is discretized. In the large N limit, the spacing between two nearest k values, i.e., $\frac{2\pi}{Na}$ is infinitesimally small. Thus, we can turn the k-sum in

the above equation into an integral over the first Brillouin zone using $\frac{1}{N}\sum_k \rightarrow \frac{1}{2\pi/a}\int_{-\pi/a}^{\pi/a} dk$. Therefore, Eq. (E.1) can be rewritten as

$$W_{ij} = -\frac{g^2}{2\pi/a}\int_{-\pi/a}^{\pi/a} dk \left[\frac{\exp\left(\imath ka(n_i - n_j)\right)}{2J - \delta_1 - 2J\cos\left(ka\right)}\right]. \tag{E.2}$$

If $(n_i - n_j) \geq 0$, we can define a new variable $z = \exp(\imath ka)$ straightaway and using the relation $dk = \frac{dz}{\imath z a}$, we rewrite Eq. (E.2) as

$$W_{ij} = -\frac{g^2}{2\pi\imath}\int_{C_1} \frac{dz}{z}\left[\frac{z^{n_i - n_j}}{2J - \delta_1 - J(z + 1/z)}\right], \tag{E.3}$$

where C_1 is a contour of unit radius in the complex plane with the origin at its center. To deal with the case where $(n_i - n_j) < 0$, we need to perform some additional variable transformations to convert Eq. (E.2) in to a contour integral. It begins by rewriting Eq. (E.2) as follows:

$$W_{ij} = -\frac{g^2}{2\pi/a}\int_{-\pi/a}^{\pi/a} dk \left[\frac{\exp\left(-\imath ka(n_j - n_i)\right)}{2J - \delta_1 - 2J\cos\left(ka\right)}\right]. \tag{E.4}$$

Performing a variable transformation $k \rightarrow -k$ in Eq. (E.4), we can obtain a new equation that reads

$$W_{ij} = -\frac{g^2}{2\pi/a}\int_{-\pi/a}^{\pi/a} dk \left[\frac{\exp\left(\imath ka(n_j - n_i)\right)}{2J - \delta_1 - 2J\cos\left(ka\right)}\right], \tag{E.5}$$

which can be used for the case where $(n_i - n_j) < 0$. As explained previously for the $(n_i - n_j) \geq 0$ case, the expression given in Eq. (E.5) can similarly be transformed into a contour integral using the variable $z = \exp(\imath ka)$ as follows:

$$W_{ij} = -\frac{g^2}{2\pi\imath}\int_{C_1} \frac{dz}{z}\left[\frac{z^{n_j - n_i}}{2J - \delta_1 - J(z + 1/z)}\right]. \tag{E.6}$$

We combine Eqs. (E.3) and (E.6), and obtain the following general form, applicable to all $n_i - n_j$:

$$W_{ij} = \frac{g^2}{2\pi\imath}\int_{C_1} dz \left[\frac{z^{|n_i - n_j|}}{Jz^2 + (\delta_1 - 2J)z + J}\right]. \tag{E.7}$$

To solve Eq. (E.7), we must determine the poles of the integrand, which can be found by solving the quadratic equation

$$Jz^2 + (\delta_1 - 2J)z + J = 0. \tag{E.8}$$

By solving Eq. (E.8) for z, we find that

$$z_{\pm} = \left(1 - \frac{\delta_1}{2J}\right) \pm \sqrt{\left(1 - \frac{\delta_1}{2J}\right)^2 - 1}. \tag{E.9}$$

In terms of the roots $z_{\pm}$, we can rewrite Eq. (E.7) as

$$W_{ij} = \frac{g^2}{2\pi\imath} \int_{C_1} dz \left[\frac{z^{|n_i - n_j|}}{J(z - z_+)(z - z_-)} \right]. \tag{E.10}$$

As δ_1/J is a real negative number, the pole z_- is the only one that is inside the contour C_1 and, therefore, it is the only pole that is relevant for the integral in Eq. (E.10). Thus, using the residue theorem, we can write

$$W_{ij} = \frac{g^2}{2\pi\imath} \left[2\pi\imath \lim_{z \to z_-} \left\{ (z - z_-) \frac{z^{|n_i - n_j|}}{J(z - z_+)(z - z_-)} \right\} \right] \tag{E.11}$$

Further simplifications to the above equation leads to

$$W_{ij} = \frac{g^2}{J} \frac{z_-^{|n_i - n_j|}}{z_- - z_+}. \tag{E.12}$$

Substituting the expression for $z_{\pm}$ from Eq. (E.9) into Eq. (E.12), we obtain

$$W_{ij} = -\frac{g^2}{2J} \frac{\left[\left(1 - \frac{\delta_1}{2J}\right) - \sqrt{\left(1 - \frac{\delta_1}{2J}\right)^2 - 1} \right]^{|n_i - n_j|}}{\sqrt{\left(1 - \frac{\delta_1}{2J}\right)^2 - 1}}. \tag{E.13}$$

In Chapter 5, we demonstrate that when we adiabatically eliminate the two-photon bound states, it results in pair-pair interactions between two excited pairs of emitters, characterized by the strength $Y_{ij,lh}$. The expression for $Y_{ij,lh}$ is given as

$$Y_{ij,lh} = -\frac{g^4}{NJ^2} \sum_K \frac{F_{K,b}(n_i, n_j) F^*_{K,b}(n_l, n_h)}{\Delta_{K,b}}, \tag{E.14}$$

where the expression for $F_{K,b}(n_i, n_j)$ can be found in Eq. (B.4) and $\Delta_{K,b}$ is given by

$$\Delta_{K,b} = -\delta + \sqrt{U^2 + 16J^2} - \sqrt{U^2 + 16J^2 \cos^2(Ka/2)}. \tag{E.15}$$

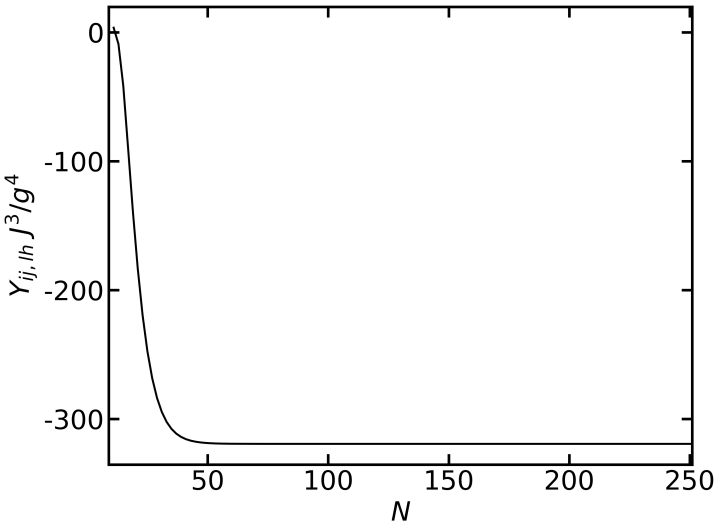

Figure E.1: The solid line shows the scaled dimensionless effective interaction $\frac{Y_{ij,lh}J^3}{g^4}$ between the emitter states $\hat{\sigma}_i^+\hat{\sigma}_j^+|gg\cdots g\rangle$ and $\hat{\sigma}_l^+\hat{\sigma}_h^+|gg\cdots g\rangle$ as a function of the size of the cavity array N for $N_e = 10$, $U/J = -0.7$, $\delta/J = -0.02$, $x/a = 1$, $(i,j) = (1,4)$, and $(l,h) = (1,8)$.

We were unable to find an analytical expression for $F_{K,b}(n_i,n_j)$ due to the complexity of the terms involved and the multiple sums over both position and momentum coordinates. Furthermore, attempts to rewrite the sum in Eq. (E.14) as a complex integral were unsuccessful because the associated poles, branch points, and branch cuts could not be found. Thus, we calculated the sum in Eq. (E.14) numerically. As discussed in Chapter 5, $Y_{ij,lh}$ is responsible for the emergence of droplet-like bound states in the emitter array. The calculation of the summation in Eq. (E.14) depends on the number of cavities N in the cavity array. Figure E.1 illustrates the dependence of the scaled effective interaction $\frac{Y_{ij,lh}J^3}{g^4}$ on the cavity array size. For example, we found that in order to achieve an accuracy of 10^{-15} when computing $\frac{Y_{ij,lh}J^3}{g^4}$ for $N_e = 10$, $U/J = -0.7$, $\delta/J = -0.02$, $x/a = 1$, $(i,j) = (1,4)$, and $(l,h) = (1,8)$, a minimum of 201 cavities is required.

E.2 Two-photon bound state energy and wavefunction

This section discusses the derivation of the two-photon bound state energies and wave functions. An integral equation is solved to obtain the bound state energy spectrum and the corresponding wave functions [200, 202, 203]. The Hamiltonian for the structured photonic environment can be divided into two parts as

$$\hat{H}_{\text{photon}} = \hat{H}_0 + \hat{V}, \tag{E.16}$$

where $\hat{H}_0$ is the non-interacting part and $\hat{V}$ is the interaction part of the Hamiltonian. From Eq. (2.26), the non-interacting and interacting parts of the Hamiltonian for the photonic environment can be identified as [125]

$$\hat{H}_0 = \hbar\omega_c \sum_{n=1}^{N} \hat{a}_n^\dagger \hat{a}_n - J \sum_{n=1}^{N} \left(\hat{a}_n^\dagger \hat{a}_{n+1} + \hat{a}_{n+1}^\dagger \hat{a}_n \right) \tag{E.17}$$

and

$$\hat{V} = \frac{U}{2} \sum_{n=1}^{N} \hat{a}_n^\dagger \hat{a}_n^\dagger \hat{a}_n \hat{a}_n. \tag{E.18}$$

The reason why Eq. (E.17) is referred to as non-interacting is that it contains terms involving the motion of individual photons that can be expressed as a sum when there are multiple photons. In contrast, Eq. (E.18) cannot be broken down into contributions from single photons, and therefore, it is considered the interacting part.

The Bose-Hubbard Hamiltonian for a single photon, denoted by $\hat{H}_0^{(1)}$, can be written in the position space representation as [125]

$$\hat{H}_0^{(1)} = \hbar\omega_c \sum_{r=0}^{(N-1)a} |r\rangle \langle r| - J \sum_{r=0}^{(N-1)a} \left(|r\rangle \langle r+a| + |r+a\rangle \langle r| \right). \tag{E.19}$$

In the above equation, $|r\rangle$ represents the state where a single photon is present at site r in the cavity array, N is the number of cavities, and a is the array spacing in the cavity array. The first term in the equation corresponds to the energy of a photon at site r (single-mode energy contribution), and the second term represents the tunnelling of photons between sites r and

$r+a$ (nearest neighbour hopping contribution). The state $|r\rangle$ can be expressed in terms of the Fock space representation as $|r\rangle = \hat{a}_r^\dagger |\text{vac}\rangle$, where $\hat{a}_r^\dagger$ represents the creation operator of a photon at site r. In the case of two photons, we can express the non-interacting part $\hat{H}_0$ in terms of the two-photon position-space representation by a direct generalization of Eq. (E.19) [125]. This leads to

$$\begin{aligned}\hat{H}_0 = \hbar\omega_c \sum_{r_1=0}^{(N-1)a} |r_1\rangle\langle r_1| - J \sum_{r_1=0}^{(N-1)a} \left(|r_1\rangle\langle r_1+a| + |r_1+a\rangle\langle r_1|\right) \\ +\hbar\omega_c \sum_{r_2=0}^{(N-1)a} |r_2\rangle\langle r_2| - J \sum_{r_2=0}^{(N-1)a} \left(|r_2\rangle\langle r_2+a| + |r_2+a\rangle\langle r_2|\right),\end{aligned} \tag{E.20}$$

where $|r_1\rangle$ and $|r_2\rangle$ denote the state of two photons individually in the position space representation. The labels r_1 and r_2 are used to represent two separate photons because they hop independently in the cavity array. The interacting part, denoted by $\hat{V}$, can be written in the position space as

$$\hat{V} = U \sum_{r=0}^{(N-1)a} |r,r\rangle\langle r,r|. \tag{E.21}$$

As the onsite interaction represented by $\hat{V}$ requires the presence of at least two photons, it is non-zero only when two photons are present at the same site in the cavity array. In Eq. (E.21), the two-photon state $|r,r\rangle$ corresponds to the presence of two photons at site r in the cavity array. It is expressed in position space representation, which is equivalent to the Fock space representation $\frac{1}{\sqrt{2}}\hat{a}_r^\dagger\hat{a}_r^\dagger|\text{vac}\rangle$. The factor $\frac{1}{\sqrt{2}}$ is introduced for normalization purposes as $\hat{a}^\dagger\hat{a}^\dagger|\text{vac}\rangle = \sqrt{2}|2\rangle$.

Before discussing the properties of two-photon bound states, we will discuss two non-interacting photons as a starting point. For two non-interacting photons with momenta k_1 and k_2, the total energy E_{1+1} is

$$E_{1+1}(k_1,k_2) = E_1(k_1) + E_1(k_2). \tag{E.22}$$

Inserting the single-photon energy, Eq. (2.30), into Eq. (E.22), we find

$$E_{1+1}(k_1,k_2) = 2\hbar\omega_c - 2J\left[\cos(k_1a) + \cos(k_2a)\right]. \tag{E.23}$$

Rewriting k_1 and k_2 in terms of the center-of-mass momentum K and the relative momentum k,

$$k_1 = \frac{K}{2} + k \tag{E.24}$$

and

$$k_2 = \frac{K}{2} - k, \tag{E.25}$$

Eq. (E.23) can be rewritten as

$$E_{1+1}(K,k) = 2\hbar\omega_c - 4J\cos(Ka/2)\cos(ka). \tag{E.26}$$

Since the momenta are limited to the first Brillouin zone, k_1, k_2, k and K lie between $-\pi/a$ and π/a. This is why, for a given value of the total momentum K, the total energy of two non-interacting photons is bounded from below and above by $E_{1+1}^{min} = 2\hbar\omega_c - 4J\cos(Ka/2)$ and $E_{1+1}^{max} = 2\hbar\omega_c + 4J\cos(Ka/2)$, respectively. This also determines the two-photon scattering thresholds when the onsite interaction U is present, i.e., the energy of two scattered photons is bounded above and below by E_{1+1}^{max} and E_{1+1}^{min}, respectively.

The structured photonic environment supports two-photon bound states that lie outside the two-photon scattering continuum. To determine the energy and corresponding wave function of a two-photon bound state with center-of-mass momentum K, we solve an integral equation that is based on the Lippmann-Schwinger equation [161, 200, 202, 203]:

$$\left|\Psi_{K,b}\right\rangle = \frac{1}{E_{K,b} - \hat{H}_0}\hat{V}\left|\Psi_{K,b}\right\rangle, \tag{E.27}$$

where $\left|\Psi_{K,b}\right\rangle$ describes the two-photon bound state and $E_{K,b}$ is its energy. Equation (E.27) can be rewritten in terms of the two-photon wave function $\Psi_{K,b}(r_1,r_2)$,

$$\Psi_{K,b}(r_1,r_2) = \langle r_1,r_2| \frac{1}{E_{K,b} - \hat{H}_0}\hat{V}\left|\Psi_{K,b}\right\rangle. \tag{E.28}$$

Since the center-of-mass momentum K of two photons is a good quantum number, the "motions" in the center-of-mass coordinate R and the relative coordinate ρ separate,

$$\Psi_{K,b}(r_1,r_2) = \exp(\imath KR)\psi_{K,b}(\rho), \tag{E.29}$$

where

$$R = \frac{r_1 + r_2}{2} \tag{E.30}$$

and

$$\rho = r_1 - r_2. \tag{E.31}$$

The expression on the right hand side of Eq. (E.28) is determined with the help of Eqs. (E.20) and (E.21), the completeness relations in real space and momentum space,

$$\sum_{r_1}\sum_{r_2} |r_1, r_2\rangle \langle r_1, r_2| = \sum_{k_1}\sum_{k_2} |k_1, k_2\rangle \langle k_1, k_2| = \mathbb{1}, \tag{E.32}$$

and Eq. (E.29). Using the closure relation $\sum_{k_1}\sum_{k_2} |k_1, k_2\rangle \langle k_1, k_2| = \mathbb{1}$ in momentum space, the right hand side of Eq. (E.28) can be expanded as

$$\Psi_{K,b}(r_1, r_2) = \sum_{k_1}\sum_{k_2} \langle r_1, r_2|k_1, k_2\rangle \langle k_1, k_2| \frac{1}{E_{K,b} - \hat{H}_0} \hat{V} \left|\Psi_{K,b}\right\rangle. \tag{E.33}$$

As $|k_1, k_2\rangle$ is an eigenstate of the non-interacting Hamiltonian $\hat{H}_0$, i.e.,

$$\hat{H}_0 |k_1, k_2\rangle = E_{1+1}(k_1, k_2) |k_1, k_2\rangle, \tag{E.34}$$

Eq. (E.33) simplifies to

$$\Psi_{K,b}(r_1, r_2) = \sum_{k_1}\sum_{k_2} \langle r_1, r_2|k_1, k_2\rangle \frac{1}{E_{K,b} - E_{1+1}(k_1, k_2)} \langle k_1, k_2| \hat{V} \left|\Psi_{K,b}\right\rangle. \tag{E.35}$$

As $\sum_{r_1'}\sum_{r_2'} |r_1', r_2'\rangle \langle r_1', r_2'| = \mathbb{1}$, Eq. (E.35) can be expanded as

$$\Psi_{K,b}(r_1, r_2) = \sum_{r_1'}\sum_{r_2'}\sum_{k_1}\sum_{k_2} \Big[\langle r_1, r_2|k_1, k_2\rangle \frac{1}{E_{K,b} - E_{1+1}(k_1, k_2)} \langle k_1, k_2| \hat{V} \left|r_1', r_2'\right\rangle \times \left\langle r_1', r_2'\middle|\Psi_{K,b}\right\rangle \Big]. \tag{E.36}$$

Further simplification of Eq. (E.36) leads to

$$\Psi_{K,b}(r_1, r_2) = \sum_{r_1'}\sum_{r_2'}\sum_{k_1}\sum_{k_2} \Big[\langle r_1, r_2|k_1, k_2\rangle \frac{1}{E_{K,b} - E_{1+1}(k_1, k_2)} \left\langle k_1, k_2\middle|r_1', r_2'\right\rangle \times V(r_1', r_2')\Psi_{K,b}(r_1', r_2') \Big]. \tag{E.37}$$

Since $\langle r_1, r_2 | k_1, k_2 \rangle = \frac{1}{N} \exp\left[\imath \left(k_1 r_1 + k_2 r_2\right)\right]$ and $\langle k_1, k_2 | r_1', r_2' \rangle = \frac{1}{N} \exp\left[-\imath \left(k_1 r_1' + k_2 r_2'\right)\right]$, we get

$$\Psi_{K,b}(r_1, r_2) = \sum_{r_1'} \sum_{r_2'} \sum_{k_1} \sum_{k_2} \left[\left\{ \frac{1}{N} \exp\left[\imath \left(k_1 r_1 + k_2 r_2\right)\right] \right\} \frac{1}{E_{K,b} - E_{1+1}(k_1, k_2)} \right.$$
$$\left. \left\{ \frac{1}{N} \exp\left[-\imath \left(k_1 r_1' + k_2 r_2'\right)\right] \right\} V(r_1', r_2') \Psi_{K,b}(r_1', r_2') \right]. \quad \text{(E.38)}$$

We now show that $V(r_1', r_2') \Psi_{K,b}(r_1', r_2')$ can be transformed such that it is a function of the center of mass and relative coordinates k, K, r, and R. From Eq. (E.21), we get

$$V \Psi_{K,b} = U \delta_{r_1', r_2'} \Psi_{K,b}(r_1', r_2'). \quad \text{(E.39)}$$

Using Eq. (E.29), we obtain

$$V \Psi_{K,b} = U \delta_{\rho',0} \psi_{K',b}(\rho') \exp\left(\imath K' R'\right). \quad \text{(E.40)}$$

Making the variable transformations $(r_1, r_2) \to (R, \rho)$, $(r_1', r_2') \to (R', \rho')$, $(k_1, k_2) \to (K, k)$, and $(k_1', k_2') \to (K', k')$, we find from Eq. (E.38)

$$\Psi_{K,b}(r_1, r_2) = \sum_{R'} \sum_{\rho'} \sum_{K} \sum_{k} \left[\left\{ \frac{1}{N} \exp\left[\imath \left(KR + k\rho\right)\right] \right\} \frac{1}{E_{K,b} - E_{1+1}(K, k)} \times \right.$$
$$\left. \left\{ \frac{1}{N} \exp\left[-\imath \left(KR' + k\rho'\right)\right] \right\} \left\{ U \delta_{\rho',0} \psi_{K',b}(\rho') \exp\left(\imath K' R'\right) \right\} \right]. \quad \text{(E.41)}$$

As $\frac{1}{N} \sum_{R'} \exp\left[\imath R' \left(K' - K\right)\right] = \delta_{K,K'}$, we get

$$\Psi_{K,b}(r_1, r_2) = \sum_{k} \sum_{\rho'} \left[\left\{ \frac{1}{N} \exp\left[\imath \left(K' R + k\rho\right)\right] \right\} \frac{1}{E_{K,b} - E_{1+1}(K', k)} \times \right.$$
$$\left. \left\{ \exp\left[-\imath \left(k\rho'\right)\right] \right\} \left\{ U \delta_{\rho',0} \psi_{K',b}(\rho') \right\} \right]. \quad \text{(E.42)}$$

Rearranging the terms in Eq. (E.42) leads to

$$\Psi_{K,b}(r_1, r_2) = \exp\left(\imath K' R\right) \frac{1}{N} \sum_{k} \left[\frac{\exp\left(\imath k \rho\right)}{E_{K,b} - E_{1+1}(K', k)} \times \right.$$
$$\left. \sum_{\rho'} \left\{ \exp\left(-\imath k \rho'\right) \left(U \delta_{\rho',0} \psi_{K',b}(\rho') \right) \right\} \right]. \quad \text{(E.43)}$$

Further simplification of Eq. (E.43) and the use of $\frac{1}{N}\sum_k \rightarrow \frac{1}{2\pi/a}\int_{-\pi/a}^{\pi/a} dk$ leads to

$$\Psi_{K,b}(r_1,r_2) = \exp\left(\imath K'R\right)\int_{-\frac{\pi}{a}}^{\frac{\pi}{a}} \frac{dk}{2\pi/a}\frac{\cos(k\rho)+\imath\sin(k\rho)}{E_{K,b}-E_{1+1}(K',k)}\left[U\psi_{K',b}(0)\right]. \tag{E.44}$$

From Eq. (E.26), it follows that $E_{1+1}(K',k) = E_{1+1}(K',-k) =$, i.e., $E_{1+1}(K',k)$ is an even function of k. Since $\sin(k\rho)$ is an odd function of k, Eq. (E.44) simplifies to

$$\Psi_{K,b}(r_1,r_2) = \exp\left(\imath K'R\right)U\psi_{K',b}(0)\int_{-\frac{\pi}{a}}^{\frac{\pi}{a}} \frac{dk}{2\pi/a}\frac{\cos(k\rho)}{E_{K,b}-E_{1+1}(K',k)}. \tag{E.45}$$

Rearranging the terms in Eq. (E.45), we get

$$\exp\left(-\imath K'R\right)\Psi_b(r_1,r_2) = U\psi_{K',b}(0)\int_{-\frac{\pi}{a}}^{\frac{\pi}{a}} \frac{dk}{2\pi/a}\frac{\cos(k\rho)}{E_{K,b}-E_{1+1}(K',k)}. \tag{E.46}$$

Since K' is just a parameter in Eq. (E.46), we replace K' with K and using Eq.(E.29), we obtain

$$\psi_{K,b}(\rho) = U\psi_{K,b}(0)\int_{-\frac{\pi}{a}}^{\frac{\pi}{a}} \frac{dk}{2\pi/a}\frac{\cos(k\rho)}{E_{K,b}-E_{1+1}(K,k)}. \tag{E.47}$$

Using Eq. (E.26), we get

$$\psi_{K,b}(\rho) = U\psi_{K,b}(0)\int_{-\frac{\pi}{a}}^{\frac{\pi}{a}} \frac{dk}{2\pi/a}\frac{\cos(k\rho)}{E_{K,b}-2\hbar\omega_c+4J\cos(\frac{Ka}{2})\cos(ka)}. \tag{E.48}$$

Evaluating Eq. (E.48) for $\rho = 0$, we get the equation

$$\psi_{K,b}(0) = U\psi_{K,b}(0)\int_{-\frac{\pi}{a}}^{\frac{\pi}{a}} \frac{dk}{2\pi/a}\left\{\frac{1}{E_{K,b}-2\hbar\omega_c+4J\cos(\frac{Ka}{2})\cos(ka)}\right\}. \tag{E.49}$$

We rewrite Eq. (E.49) as

$$\psi_{K,b}(0)\left[1-U\int_{-\frac{\pi}{a}}^{\frac{\pi}{a}} \frac{dk}{2\pi/a}\left\{\frac{1}{E_{K,b}-2\hbar\omega_c+4J\cos(\frac{Ka}{2})\cos(ka)}\right\}\right] = 0. \tag{E.50}$$

Since $\psi_{K,b}(0) \neq 0$, we make further simplification to Eq. (E.50) and obtain

$$\frac{1}{U} = \int_{-\frac{\pi}{a}}^{\frac{\pi}{a}} \frac{dk}{2\pi/a}\left\{\frac{1}{E_{K,b}-2\hbar\omega_c+4J\cos(\frac{Ka}{2})\cos(ka)}\right\}. \tag{E.51}$$

To determine the bound state energies, we solve the equation (E.51). The calculation involves the sign of the onsite interaction parameter U, which is explicitly considered in the next

steps. Using a method similar to the one discussed earlier, we evaluate the contour integral on the right-hand side of Eq. (E.51). For negative values of U, the bound state energy $E_{K,b}$ is found to be:

$$E_{K,b} = 2\hbar\omega_c - \sqrt{U^2 + 16J^2\cos^2(Ka/2)}. \tag{E.52}$$

The binding energy E_{binding} of a two-photon bound state with a center-of-mass momentum K can be determined by calculating the absolute difference between the energy of the two-photon bound state $E_{K,b}$ and the bottom energy of the two-photon scattering continuum, given by $E_{1+1}(K,0)$. This can be expressed as:

$$E_{\text{binding}} = |E_{K,b} - E_{1+1}(K,0)|. \tag{E.53}$$

By using Eq. (E.52) and Eq. (E.26), we can simplify equation (E.53) as:

$$E_{\text{binding}} = |4J\cos(Ka/2) - -\sqrt{U^2 + 16J^2\cos^2(Ka/2)}|. \tag{E.54}$$

In order to obtain the wavefunction for the two-photon bound state, we can modify Eq. (E.48) as follows:

$$\psi_{K,b}(\rho) = U\psi_{K,b}(0)\int_{-\frac{\pi}{a}}^{\frac{\pi}{a}} \frac{dk}{2\pi/a}\left[\frac{\{\exp(\imath ka)\}^{\rho/a}}{E_{K,b} - 2\hbar\omega_c + 4J\cos(\frac{Ka}{2})\cos(ka)}\right] \tag{E.55}$$

by exploiting the evenness of the denominator in Eq. (E.48) with respect to the variable k. The integral in Eq. (E.55) can be evaluated using a method similar to the one used in the previous section. The wavefunction is normalized using $|C|^2\sum_\rho |\psi_{K,b}(\rho)|^2 = 1$, where C is the normalization constant. This summation is a geometric series and we find the normalization constant to be $C = \frac{\sqrt{|\frac{U}{4J\cos(Ka/2)}|}}{\left(\left(\frac{U}{4J\cos(Ka/2)}\right)^2+1\right)^{1/4}}$. Thus, the normalized two-photon bound state wave function can be expressed as:

$$\psi_{K,b}(\rho) = \frac{\sqrt{|\frac{U}{4J\cos(Ka/2)}|}}{\left(\left(\frac{U}{4J\cos(Ka/2)}\right)^2+1\right)^{1/4}}\left[\sqrt{\left(\frac{U}{4J\cos(Ka/2)}\right)^2+1} - |\frac{U}{4J\cos(Ka/2)}|\right]^{|\rho|/a} \tag{E.56}$$

It is crucial to point out the significance of Eq. (E.56) in this thesis. In order to compute the term $M_b(k, n_i, K)$ as given in Eq. (4.25), it is necessary to first determine the expression for the two-photon bound state wavefunction. This quantity, in turn, is required for all the effective interactions of the system comprising the emitter and photon.

E.3 Two-photon scattering state wavefunction

In this section, we study the scattering state wavefunction for two photons. In order to do so, we calculate the scattering phase-shift caused by the onsite interaction U in the structured photonic environment. The expression for the scattering state wavefunction appears in the interaction terms given in Eq. (4.24) [61]. Just like how we handled the wavefunction for two-photon bound states, we also split the scattering state wavefunction into center-of-mass and relative degrees of freedom. This allows us to express the scattering state wavefunction as:

$$\Psi^{sc}_{K,k}(r_1, r_2) = \exp(\imath K R)\, \psi_{K,k}(\rho). \tag{E.57}$$

where the additional degree of freedom k corresponds to the relative momentum k between the two photons and it is given by $k = \frac{1}{2}(k_1 - k_2)$. To determine an expression for $\psi_{K,k}(\rho)$, we consider the relative eigenstates $\phi_{K,k}(\rho)$ of two non-interacting photons, $\phi_{K,k}(\rho) = \cos(k\rho)$. The interaction $\hat{V}$ introduces a phase shift with respect to the relative wave function of two non-interacting photons. Since the two photons interact via onsite interaction, an ansatz can be made for the form of $\psi_{K,k}(\rho)$, given by [125]

$$\psi_{K,k}(\rho) = C\left[\cos(k\rho) + \theta(K,k)\sin(k|\rho|)\right], \tag{E.58}$$

where $\theta(K,k)$ is the scattering phase shift and C is a normalization constant. To determine the phase shift $\theta(K,k)$, using position space representation, we solve the time-independent Schrödinger equation

$$(\hat{H}_0 + \hat{V})\, \psi^{sc}_{K,k}(r_1, r_2) = E_{1+1}(K,k)\, \psi^{sc}_{K,k}(r_1, r_2). \tag{E.59}$$

Substituting the expression for $\hat{H}_0$ and $\hat{V}$ from Eq. (E.20) and Eq. (E.21), respectively, we get

$$-2J\cos(Ka/2)\left[\psi_{K,k}(\rho-a)+\psi_{K,k}(\rho+a)\right]+U\delta_{\rho,0}\psi_{K,k}(\rho)= \\ \left[-4J\cos(Ka/2)\cos(ka)\right]\psi_{K,k}(\rho). \tag{E.60}$$

Plugging $\rho = 0$ to Eq. (E.60), we get

$$-2J\cos(Ka/2)\left[\psi_{K,k}(-a)+\psi_{K,k}(a)\right]+U\psi_{K,k}(0)=-4J\cos(Ka/2)\cos(ka)\psi_{K,k}(0) \tag{E.61}$$

From Eq. (E.58), we can find that

$$\psi_{K,k}(0)=C \tag{E.62}$$

and

$$\psi_{K,k}(a)=C\left[\cos(ka)+\theta(K,k)\sin(ka)\right]. \tag{E.63}$$

Since $\psi_{K,k}(a)=\psi_{K,k}(-a)$, substituting the expressions for $\psi_{K,k}(0)$ and $\psi_{K,k}(a)$ in Eq. (E.61), we obtain

$$-4J\cos(Ka/2)\left[\cos(ka)+\theta(K,k)\sin(ka)\right]+U=-4J\cos(Ka/2)\cos(ka). \tag{E.64}$$

Further simplification of Eq. (E.64) leads to

$$\theta(K,k)=\frac{U}{4J\cos(Ka/2)\sin(ka)}. \tag{E.65}$$

Plugging the expression for $\theta(K,k)$ into Eq. (E.58), we obtain the two-photon scattering state wavefunction up to the normalization constant C:

$$\psi_{K,k}(\rho)=C\cos(k\rho)+C\left[\frac{U}{4J\cos(Ka/2)\sin(ka)}\right]\sin(k|\rho|). \tag{E.66}$$

Since our Hamiltonian only contains contact interaction and nearest neighbouring interactions, the scattering state wavefunction given in Eq. (E.66) is valid for all ρ. To determine the normalization constant C in Eq. (E.66), we use box normalization for a cavity array

consisting of N sites. In the discretized real space of the cavity array, we can numerically compute C by using the following equation:

$$C = \frac{1}{\sqrt{\sum_{\rho} |\psi_{K,k}(\rho)|^2}}. \tag{E.67}$$

Since the scattering states occupy the entire available space in a cavity array, the value of C depends on N, the number of cavities present in the array. That is why we call this approach a numerical box normalization calculation.

References

[1] S. Deffner and S. Campbell, Quantum Thermodynamics: An introduction to the thermodynamics of quantum information, Morgan Claypool Publishers (2019).

[2] J. Gemmer, M. Michel, and G. Mahler, Quantum thermodynamics: Emergence of thermodynamic behavior within composite quantum systems, Vol. 784, Springer (2009).

[3] H. Breuer and F. Petruccione, The Theory of Open Quantum Systems, Oxford University Press, New York (2002).

[4] C. Gardiner and P. Zoller, Quantum noise: a handbook of Markovian and non-Markovian quantum stochastic methods with applications to quantum optics, Springer Science Business Media (2004).

[5] V. V. Kornyak, Subsystems of a closed quantum system in finite quantum mechanics, Journal of Mathematical Sciences, 261(5), 717-729 (2022).

[6] C. P. Koch, Controlling open quantum systems: tools, achievements, and limitations, Journal of Physics: Condensed Matter, 28(21), 213001 (2016).

[7] I. Rotter and J. P. Bird, A review of progress in the physics of open quantum systems: theory and experiment, Reports on Progress in Physics, 78(11), 114001 (2015).

[8] I. de Vega and D. Alonso, Dynamics of non-Markovian open quantum systems, Rev. Mod. Phys. 89, 015001 (2017).

[9] H.-P. Breuer, E.-M. Laine, J. Piilo, and B. Vacchini, Colloquium: Non-Markovian dynamics in open quantum systems, Rev. Mod. Phys. 88, 021002 (2016).

[10] S. Hilt and E. Lutz, System-bath entanglement in quantum thermodynamics, Phys. Rev. A 79, 010101(R) (2009).

[11] P. Haughian, M. Esposito, and T. L. Schmidt, Quantum thermodynamics of the resonant-level model with driven system-bath coupling, Phys. Rev. B 97, 085435 (2018).

[12] J. Anders, M. Esposito, Focus on quantum thermodynamics, New J. Phys, 19(1), 010201 (2017).

[13] M. Perarnau-Llobet, H. Wilming, A. Riera, R. Gallego, and J. Eisert, Strong Coupling Corrections in Quantum Thermodynamics, Phys. Rev. Lett. 120, 120602 (2018).

[14] H. Pichler, T. Ramos, A. J. Daley, and P. Zoller, Quantum optics of chiral spin networks, Phys. Rev. A 91, 042116 (2015).

[15] M. Bello, G. Platero, J. I. Cirac, and A. González-Tudela, Unconventional quantum optics in topological waveguide QED, Sci. Adv. 5, eaaw0297 (2019).

[16] L. M. Sieberer, M. Buchhold, and S. Diehl, Keldysh field theory for driven open quantum systems, Reports on Progress in Physics, 79(9), 096001 (2016).

[17] V. Semin, I. Sinayskiy, and F. Petruccione, Initial correlation in a system of a spin coupled to a spin bath through an intermediate spin, Phys. Rev. A 86, 062114 (2012).

[18] R. Nandkishore and S. Gopalakrishnan, Many body localized systems weakly coupled to baths, Annalen der Physik, 529(7), 1600181, (2017).

[19] D. Patanè, A. Silva, L. Amico, R. Fazio, and G. E. Santoro, Adiabatic Dynamics in Open Quantum Critical Many-Body Systems, Phys. Rev. Lett. 101, 175701 (2008).

[20] R. Nandkishore, S. Gopalakrishnan, and D. A. Huse, Spectral features of a many-body-localized system weakly coupled to a bath, Phys. Rev. B 90, 064203 (2014).

[21] T. Ramos, B. Vermersch, P. Hauke, H. Pichler, and P. Zoller, Non-Markovian dynamics in chiral quantum networks with spins and photons, Phys. Rev. A 93, 062104 (2016).

[22] M. S. Sarandy and D. A. Lidar, Adiabatic Quantum Computation in Open Systems, Phys. Rev. Lett. 95, 250503 (2005).

[23] T. Albash and D. A. Lidar, Decoherence in adiabatic quantum computation, Phys. Rev. A 91, 062320 (2015).

[24] D. Rossini, T. Calarco, V. Giovannetti, S. Montangero, and R. Fazio, Decoherence induced by interacting quantum spin baths, Phys. Rev. A 75, 032333 (2007).

[25] A. Montina and F. T. Arecchi, Quantum Decoherence Reduction by Increasing the Thermal Bath Temperature, Phys. Rev. Lett. 100, 120401 (2008).

[26] O. V. Prezhdo and P. J. Rossky, Relationship between Quantum Decoherence Times and Solvation Dynamics in Condensed Phase Chemical Systems, Phys. Rev. Lett. 81, 5294 (1998).

[27] H. Dong, S. Yang, X. F. Liu, and C. P. Sun, Quantum thermalization with couplings, Phys. Rev. A 76, 044104 (2007).

[28] G. D. Palma, A. Serafini, V. Giovannetti, and M. Cramer, Necessity of Eigenstate Thermalization, Phys. Rev. Lett. 115, 220401 (2015).

[29] M. Žnidarič, T. Prosen, G. Benenti, G. Casati, and D. Rossini, Thermalization and ergodicity in one-dimensional many-body open quantum systems, Phys. Rev. E 81, 051135 (2010).

[30] K. Khodjasteh and L. Viola, Dynamically Error-Corrected Gates for Universal Quantum Computation, Phys. Rev. Lett. 102, 080501 (2009).

[31] S. Lieu, R. Belyansky, J. T. Young, R. Lundgren, V. V. Albert, and A. V. Gorshkov, Symmetry Breaking and Error Correction in Open Quantum Systems, Phys. Rev. Lett. 125, 240405 (2020).

[32] S. Choi, Y. Bao, X.-L. Qi, and E. Altman, Quantum Error Correction in Scrambling Dynamics and Measurement-Induced Phase Transition, Phys. Rev. Lett. 125, 030505 (2020).

[33] Q. Xu, G. Zheng, Y.-X. Wang, P. Zoller, A. A. Clerk, and L. Jiang, Autonomous quantum error correction and fault-tolerant quantum computation with squeezed cat qubits, arXiv:2210.13406 (2022).

[34] S. J. Beale, J. J. Wallman, M. Gutiérrez, K. R. Brown, and R. Laflamme, Quantum Error Correction Decoheres Noise, Phys. Rev. Lett. 121, 190501 (2018).

[35] W. Dür, M. Skotiniotis, F. Fröwis, and B. Kraus, Improved Quantum Metrology Using Quantum Error Correction, Phys. Rev. Lett. 112, 080801 (2014).

[36] Alex W. Chin, Susana F. Huelga, and Martin B. Plenio, Quantum Metrology in Non-Markovian Environments, Phys. Rev. Lett. 109, 233601 (2012).

[37] W.-T. He, H.-Y. Guang, Z.-Y. Li, R.-Q. Deng, N.-N. Zhang, J.-X. Zhao, F.-G. Deng, and Q. Ai, Quantum metrology with one auxiliary particle in a correlated bath and its quantum simulation, Phys. Rev. A 104, 062429 (2021).

[38] G. Clos and H.-P. Breuer, Quantification of memory effects in the spin-boson model, Phys. Rev. A 86, 012115 (2012).

[39] D. P. DiVincenzo and D. Loss, Rigorous Born approximation and beyond for the spin-boson model, Phys. Rev. B 71, 035318 (2005).

[40] A. P. Orioli, A. Safavi-Naini, M. L. Wall, and A. M. Rey, Nonequilibrium dynamics of spin-boson models from phase-space methods, Phys. Rev. A 96, 033607 (2017).

[41] A. Safavi-Naini, R. J. Lewis-Swan, J. G. Bohnet, M. Gärttner, K. A. Gilmore, J. E. Jordan, J. Cohn, J. K. Freericks, A. M. Rey, and J. J. Bollinger, Verification of a Many-Ion Simulator of the Dicke Model Through Slow Quenches across a Phase Transition, Phys. Rev. Lett. 121, 040503 (2018).

[42] X.-Y. Lü, Y. Wu, J. R. Johansson, H. Jing, J. Zhang, and F. Nori, Squeezed Optomechanics with Phase-Matched Amplification and Dissipation, Phys. Rev. Lett. 114, 093602 (2015).

[43] Y.-D. Wang and A. A. Clerk, Reservoir-Engineered Entanglement in Optomechanical Systems, Phys. Rev. Lett. 110, 253601 (2013).

[44] R. H. Dicke, Coherence in Spontaneous Radiation Processes, Phys. Rev. 93, 99 (1954).

[45] M. O. Scully and A. A. Svidzinsky, The super of superradiance, Science, 325(5947), (2009).

[46] S. J. Masson and A. Asenjo-Garcia, Universality of Dicke superradiance in arrays of quantum emitters, Nature Communications, 13(1), 2285 (2022).

[47] J. A. Mlynek, A. A. Abdumalikov, C. Eichler, and A. Wallraff, Observation of Dicke superradiance for two artificial atoms in a cavity with high decay rate, Nat. Commun. 5, 5186 (2014).

[48] Y. Chen, Z. Yu, and H. Zhai, Superradiance of Degenerate Fermi Gases in a Cavity, Phys. Rev. Lett. 112, 143004 (2014).

[49] M. O. Scully, Single Photon Subradiance: Quantum Control of Spontaneous Emission and Ultrafast Readout, Phys. Rev. Lett. 115, 243602 (2015).

[50] Y.-X. Zhang and K. Mølmer, Theory of Subradiant States of a One-Dimensional Two-Level Atom Chain, Phys. Rev. Lett. 122, 203605 (2019).

[51] Y.-X. Zhang and K. Mølmer, Subradiant Emission from Regular Atomic Arrays: Universal Scaling of Decay Rates from the Generalized Bloch Theorem, Phys. Rev. Lett. 125, 253601 (2020).

[52] P. Roushan, C. Neill, J. Tangpanitanon, V. M. Bastidas, A. Megrant, R. Barends, Y. Chen, Z. Chen, B. Chiaro, A. Dunsworth, A. Fowler, B. Foxen, M. Giustina, E. Jeffrey, J. Kelly, E. Lucero, J. Mutus, M. Neeley, C. Quintana, D. Sank, A. Vainsencher, J. Wenner, T. White, H. Neven, D. G. Angelakis, and J. Martinis, Spectroscopic signatures of localization with interacting photons in superconducting qubits, Science 358, 1175 (2017).

[53] M. Fitzpatrick, N. M. Sundaresan, A. C. Y. Li, J. Koch, and A. A. Houck, Observation of a dissipative phase transition in a one-dimensional circuit QED lattice, Phys. Rev. X 7, 011016 (2017).

[54] D. C. McKay, R. Naik, P. Reinhold, L. S. Bishop, and D. I. Schuster, High-Contrast Qubit Interactions Using Multimode Cavity QED , Phys. Rev. Lett. 114, 080501 (2015).

[55] M. Scigliuzzo, G. Calajo, F. Ciccarello, D. P. Lozano, A. Bengtsson, P. Scarlino, A. Wallraff, D. Chang, P. Delsing, and S. Gasparinetti, Controlling Atom-Photon Bound States in an Array of Josephson-Junction Resonators, Phys. Rev. X 12, 031036 (2022).

[56] S. Hacohen-Gourgy, V. V. Ramasesh, C. D. Grandi, I. Siddiqi, and S. M. Girvin, Cooling and Autonomous Feedback in a Bose-Hubbard Chain with Attractive Interactions, Phys. Rev. Lett. 115, 240501 (2015).

[57] N. M. Sundaresan, R. Lundgren, G. Zhu, A. V. Gorshkov, and A. A. Houck, Interacting Qubit-Photon Bound States with Superconducting Circuits, Phys. Rev. X 9, 011021 (2019).

[58] V. S. Ferreira, J. Banker, A. Sipahigil, M. H. Matheny, A. J. Keller, E. Kim, M. Mirhosseini, and O. Painter, Collapse and Revival of an Artificial Atom Coupled to a Structured Photonic Reservoir, Phys. Rev. X 11, 041043 (2021).

[59] R. Ma, B. Saxberg, C. Owens, N. Leung, Y. Lu, J. Simon, and D. I. Schuster, A dissipatively stabilized Mott insulator of photons, Nature 566, 51–57 (2019).

[60] J. Talukdar and D. Blume, Undamped Rabi oscillations due to polaron-emitter hybrid states in a nonlinear photonic waveguide coupled to emitters, Phys. Rev. A 106, 013722 (2022).

[61] J. Talukdar and D. Blume, Two emitters coupled to a bath with Kerr-like nonlinearity: Exponential decay, fractional populations, and Rabi oscillations, Phys. Rev. A 105, 063501 (2022).

[62] L. Amico, R. Fazio, A. Osterloh, and V. Vedral, Entanglement in many-body systems, Rev. Mod. Phys. 80, 517 (2008).

[63] J. Talukdar and D. Blume, Photon-induced droplet-like bound states in one-dimensional qubit array, under review in Phys. Rev. A.

[64] I. M. Georgescu, S. Ashhab, and F. Nori, Quantum simulation, Rev. Mod. Phys. 86, 153 (2014).

[65] F. Schäfer, T. Fukuhara, S. Sugawa, Y. Takasu, and Y. Takahashi, Tools for quantum simulation with ultracold atoms in optical lattices, Nature Reviews Physics, 2(8), (2020).

[66] A. Browaeys, and T. Lahaye, Many-body physics with individually controlled Rydberg atoms, Nature Physics, 16(2), 132-142 (2020).

[67] H. Bernien, S. Schwartz, A. Keesling, H. Levine, A. Omran, H. Pichler, S. Choi, M. D. Lukin, Probing many-body dynamics on a 51-atom quantum simulator, Nature 551, 7682 (2017).

[68] R. Blatt and C. F. Roos, Quantum simulations with trapped ions. Nature Physics, 8(4), 277-284, (2012).

[69] C. Cohen-Tannoudji, J. Dupont-Roc, and G. Grynberg, Atom-photon interactions: basic processes and applications, John Wiley and Sons (1998).

[70] S. Haroche and J.-M. Raimond, Exploring the quantum: atoms, cavities, and photons, Oxford University Press (2006).

[71] E. T. Jaynes and F. W. Cummings, Comparison of Quantum and Semiclassical Radiation Theories with Application to the Beam Maser, Proceedings of the IEEE 51, 89–109 (1963).

[72] P. Lambropoulos and D. Petrosyan, Fundamentals of Quantum Optics and Quantum Information, Springer, New York (2007).

[73] A. Blais, A. L. Grimsmo, S. M. Girvin, and A. Wallraff, Circuit quantum electrodynamics, Rev. Mod. Phys. 93, 025005 (2021).

[74] I. I. Rabi, On the Process of Space Quantization, Phys. Rev. 49, 324 (1936).

[75] I. I. Rabi, Space Quantization in a Gyrating Magnetic Field, Phys. Rev. 51, 652 (1937).

[76] Q. Xie, H. Zhong, M. T. Batchelor, and C. Lee, The quantum Rabi model: solution and dynamics, Journal of Physics A: Mathematical and Theoretical, 50(11), 113001 (2017).

[77] A. Metelmann and A. A. Clerk, Nonreciprocal Photon Transmission and Amplification via Reservoir Engineering, Phys. Rev. X 5, 021025 (2015).

[78] A. Tomadin, S. Diehl, M. D. Lukin, P. Rabl, and P. Zoller, Reservoir engineering and dynamical phase transitions in optomechanical arrays, Phys. Rev. A 86, 033821 (2012).

[79] A. Blais, R.S. Huang, A. Wallraff, S. Girvin, and R. J. Schoelkopf, Cavity quantum electrodynamics for superconducting electrical circuits: an architecture for quantum computation, Phy. Rev. A 69, 062320 (2004).

[80] D. Roy, C. M. Wilson, and O. Firstenberg, Colloquium: Strongly interacting photons in one-dimensional continuum, Rev. Mod. Phys. 89, 021001 (2017).

[81] E. Shahmoon, P. Grišins, H. P. Stimming, I. Mazets, and G. Kurizki, Highly nonlocal optical nonlinearities in atoms trapped near a waveguide, Optica 3, 725-733 (2016).

[82] F. Lombardo, F. Ciccarello, and G. M. Palma, Photon localization versus population trapping in a coupled-cavity array, Phys. Rev. A 89, 053826 (2014).

[83] P. Longo, P. Schmitteckert, and K. Busch, Few-Photon Transport in Low-Dimensional Systems: Interaction-Induced Radiation Trapping, Phys. Rev. Lett. 104, 023602 (2010).

[84] H. Zheng, D. J. Gauthier, and H. U. Baranger, Waveguide QED: Many-body bound-state effects in coherent and Fock-state scattering from a two-level system, Phys. Rev. A 82, 063816 (2010).

[85] D. Chang, A. S. Sørensen, E. Demler, and M. D. Lukin, A single-photon transistor using nanoscale surface plasmons, Nat. Phys. 3, 807–812 (2007).

[86] L. Zhou, Z. R. Gong, Y.-X. Liu, C. P. Sun, and F. Nori, Controllable Scattering of a Single Photon inside a One-Dimensional Resonator Waveguide, Phys. Rev. Lett. 101, 100501 (2008).

[87] J.-T. Shen and S. Fan, Coherent Single Photon Transport in a One-Dimensional Waveguide Coupled with Superconducting Quantum Bits, Phys. Rev. Lett. 95, 213001 (2005).

[88] D. Reitz, C. Sayrin, R. Mitsch, P. Schneeweiss, and A. Rauschenbeutel, Coherence Properties of Nanofiber-Trapped Cesium Atoms, Phys. Rev. Lett. 110, 243603 (2013).

[89] R. Yalla, M. Sadgrove, K. P. Nayak, and K. Hakuta, Cavity Quantum Electrodynamics on a Nanofiber Using a Composite Photonic Crystal Cavity, Phys. Rev. Lett. 113, 143601 (2014).

[90] J. D. Hood, A. Goban, A. Asenjo-Garcia, M. Lu, S.-P. Yu, D. E. Chang, and H. J. Kimble, Atom-atom interactions around the band edge of a photonic crystal waveguide, Proc. Natl. Acad. Sci. U.S.A. 113, 10507 (2016).

[91] P. Lodahl, S. Mahmoodian, and S. Stobbe, Interfacing single photons and single quantum dots with photonic nanostructures, Rev. Mod. Phys. 87, 347 (2015).

[92] P. E. Barclay, K.-M. Fu, C. Santori, and R. G. Beausoleil, Hybrid photonic crystal cavity and waveguide for coupling to diamond NV-centers, Opt. Express 17, 9588-9601 (2009).

[93] B. J. M. Hausmann, B. J. Shields, Q. Quan, Y. Chu, N. P. de Leon, R. Evans, M. J. Burek, A. S. Zibrov, M. Markham, D. J. Twitchen, H. Park, M. D. Lukin, and M. Loncăr, Coupling of NV Centers to Photonic Crystal Nanobeams in Diamond, Nano Lett. 13 (12), 5791-5796 (2013).

[94] O. Astafiev, A. M. Zagoskin, A. A. Abdumalikov, Yu. A. Pashkin, T. Yamamoto, K. Inomata, Y. Nakamura, and J. S. Tsai, Resonance fluorescence of a single artificial atom, Science 327, 840 (2010).

[95] I.-C. Hoi, C. M. Wilson, G. Johansson, T. Palomaki, B. Peropadre, and P. Delsing, Demonstration of a Single-Photon Router in the Microwave Regime, Phys. Rev. Lett. 107, 073601 (2011).

[96] M. Mirhosseini, E. Kim, X. Zhang, A. Sipahigil, P. B. Dieterle, A. J. Keller, A. Asenjo-Garcia, D. E. Chang, and O. Painter, Cavity quantum electrodynamics with atom-like mirrors, Nature (London) 569, 692 (2019).

[97] J. Douglas, H. Habibian, C.-L. Hung, A. V. Gorshkov, H. J. Kimble, and D. E. Chang, Quantum many-body models with cold atoms coupled to photonic crystals, Nature Photon. 9, 326–331 (2015).

[98] A. Gonzalez-Tudela, D. Martin-Cano, E. Moreno, L. Martin-Moreno, C. Tejedor, and F. J. Garcia-Vidal, Entanglement of Two Qubits Mediated by One-Dimensional Plasmonic Waveguides, Phys. Rev. Lett. 106, 020501 (2011).

[99] K. Stannigel, P. Rabl, and P. Zoller, Driven-dissipative preparation of entangled states in cascaded quantum-optical networks, New J. Phys. 14, 063014 (2012).

[100] H. Zheng and H. U. Baranger, Persistent Quantum Beats and Long-Distance Entanglement from Waveguide- Mediated Interactions, Phys. Rev. Lett. 110, 113601 (2013).

[101] E. Shahmoon and G. Kurizki, Nonradiative interaction and entanglement between distant atoms, Phys. Rev. A 87, 033831 (2013).

[102] P. Facchi, M. S. Kim, S. Pascazio, F. V. Pepe, D. Pomarico, and T. Tufarelli, Bound states and entanglement generation in waveguide quantum electrodynamics, Phys. Rev. A 94, 043839 (2016).

[103] N. V. Corzo, J. Raskop, A. Chandra, A. S. Sheremet, B. Gouraud, and J. Laurat, Waveguide-coupled single collective excitation of atomic arrays, Nature 566, 359–362 (2019).

[104] A. S. Prasad, J. Hinney, S. Mahmoodian, K. Hammerer, S. Rind, P. Schneeweiss, A. S. Sørensen, J. Volz, and A. Rauschenbeutel, Correlating photons using the collective nonlinear response of atoms weakly coupled to an optical mode, Nat. Photonics 14, 719–722 (2020).

[105] G. Calajó, F. Ciccarello, D. Chang, and P. Rabl, Atom-field dressed states in slow-light waveguide QED, Phys. Rev. A 93, 033833 (2016).

[106] Z. Wang, T. Jaako, P. Kirton, and P. Rabl, Supercorrelated Radiance in Nonlinear Photonic Waveguides, Phys. Rev. Lett. 124, 213601 (2020).

[107] S. John and T. Quang, Spontaneous emission near the edge of a photonic band gap, Phys. Rev. A 50, 1764 (1994).

[108] A. G. Kofman, G. Kurizki, and B. Sherman, Spontaneous and Induced Atomic Decay in Photonic Band Structures, J. Mod. Opt. 41, 353 (1994).

[109] A. González-Tudela and J. I. Cirac, Quantum Emitters in Two-Dimensional Structured Reservoirs in the Non-perturbative Regime, Phys. Rev. Lett. 119, 143602 (2017).

[110] O. A. Iversen and T. Pohl, Strongly Correlated States of Light and Repulsive Photons in Chiral Chains of Three-Level Quantum Emitters, Phys. Rev. Lett. 126, 083605 (2021).

[111] I. Carusotto, A. A. Houck, A. J. Kollár, P. Roushan, D. I. Schuster, and J. Simon, Photonic materials in circuit quantum electrodynamics, Nat. Phys. 16, 268–279 (2020).

[112] F. W. Cummings, Spontaneous emission from a single two-level atom in the presence of N initially unexcited identical atoms, Phys. Rev. A 33, 1683 (1986).

[113] A. S. Sheremet, M. I. Petrov, I. V. Iorsh, A. V. Poshakinskiy, and A. N. Poddubny, Waveguide quantum electrodynamics: collective radiance and photon-photon correlations, Rev. Mod. Phys. 95, 015002 (2023).

[114] K. Sinha, P. Meystre, E. A. Goldschmidt, F. K. Fatemi, S. L. Rolston, and P. Solano, Non-Markovian Collective Emission from Macroscopically Separated Emitters, Phys. Rev. Lett. 124, 043603 (2020).

[115] H. R. Haakh, S. Faez, and V. Sandoghdar, Polaritonic normal-mode splitting and light localization in a one-dimensional nanoguide, Phys. Rev. A 94, 053840 (2016).

[116] A. V. Poshakinskiy, J. Zhong, and A. N. Poddubny, Quantum Chaos Driven by Long-Range Waveguide-Mediated Interactions, Phys. Rev. Lett. 126, 203602 (2021).

[117] A. N. Poddubny, Quasiflat band enabling subradiant two-photon bound states, Phys. Rev. A 101, 043845 (2020).

[118] A. Goban, C.-L. Hung, J. D. Hood, S.-P. Yu, J. A. Muniz, O. Painter, and H. J. Kimble, Superradiance for Atoms Trapped along a Photonic Crystal Waveguide, Phys. Rev. Lett. 115, 063601 (2015).

[119] A. Albrecht, L. Henriet, A. Asenjo-Garcia, P. B. Dieterle, O. Painter, and D. E. Chang, Subradiant states of quantum bits coupled to a one-dimensional waveguide, New J. Phys. 21, 025003 (2019).

[120] J. Zhong, N. A. Olekhno, Y. Ke, A. V. Poshakinskiy, C. Lee, Y. S. Kivshar, and A. N. Poddubny, Photon-Mediated Localization in Two-Level Qubit Arrays, Phys. Rev. Lett. 124, 093604 (2020).

[121] Y.-X. Zhang, C. Yu, and K. Mølmer, Subradiant bound dimer excited states of emitter chains coupled to a one-dimensional waveguide, Phys. Rev. Res. 2, 013173 (2020).

[122] We note that Ref. [106] presents a benchmark plot (Fig. 4 of the Supplemental Material) that was obtained by accounting for the scattering continuum. In addition, Ref. [106] noted that the contributions from the scattering states were confirmed to be small for the parameter combinations considered. Our calculations support these statements.

[123] R. Piil and K. Mølmer, Tunneling couplings in discrete lattices, single-particle band structure, and eigenstates of interacting atom pairs, Phys. Rev. A 76, 023607 (2007).

[124] N. Nygaard, R. Piil, and K. Mølmer, Two-channel Feshbach physics in a structured continuum, Phys. Rev. A 78, 023617 (2008).

[125] M. Valiente and D. Petrosyan, Two-particle states in the Hubbard model, J. Phys. B: At. Mol. Opt. Phys. 41, 161002 (2008).

[126] D. Petrosyan, B. Schmidt, J. R. Anglin, and M. Fleischhauer, Quantum liquid of repulsively bound pairs of particles in a lattice, Phys. Rev. A 76, 033606 (2007).

[127] The matrix element $M_b(k,n,K)$ used in our work is by a factor of N larger than that defined in Eq. (25) of the Supplemental Material of Ref. [106]. The definition employed by us (see also Ref. [61]) makes the value of $M_b(k,n,K)$ for a given ka and Ka independent of the number of lattice sites N.

[128] S. Mahmoodian, G. Calajó, D. E. Chang, K. Hammerer, and A. S. Sørensen, Dynamics of Many-Body Photon Bound States in Chiral Waveguide QED, Phys. Rev. X 10, 031011 (2020).

[129] S.-S. Wen, Y.-G. Huang, X.-Y. Wang, J. Liu, Y. Li, X.-E Quan, H. Yang, J.-Z. Peng, K. Deng, and H.-P. Zhao, Bound state and non-Markovian dynamics of a quantum emitter around a surface plasmonic nanostructure, Opt. Express 28, 6469-6489 (2020).

[130] D. Lonigro, P. Facchi, A. D. Greentree, S. Pascazio, F. V. Pepe, and D. Pomarico, Photon-emitter dressed states in a closed waveguide, Phys. Rev. A 104, 053702 (2021).

[131] M. Stewart, J. Kwon, A. Lanuza, and D. Schneble, Dynamics of matter-wave quantum emitters in a structured vacuum, Phys. Rev. Res. 2, 043307 (2020).

[132] A. Javadi, I. Söllner, M. Arcari, S. L. Hansen, L. Midolo, S. Mahmoodian, G. Kiršanskė, T. Pregnolato, E. H. Lee, J. D. Song, S. Stobbe, and P. Lodahl, Single-photon non-linear optics with a quantum dot in a waveguide, Nat. Commun. 6, 8655 (2015).

[133] G. Guarnieri, M. Kolář, and R. Filip, Steady-State Coherences by Composite System-Bath Interactions, Phys. Rev. Lett. 121, 070401 (2018).

[134] M. Schlosshauer, Decoherence, the measurement problem, and interpretations of quantum mechanics, Rev. Mod. Phys. 76, 1267 (2005).

[135] M. Schlosshauer, Decoherence and the Quantum-to-Classical Transition (Springer, Berlin/Heidelberg, 2007).

[136] J. T. Barreiro, M. Müller, P. Schindler, D. Nigg, T. Monz, M. Chwalla, M. Hennrich, C. F. Roos, P. Zoller, and R. Blatt, An open-system quantum simulator with trapped ions, Nature 470, 486–491 (2011).

[137] S. Diehl, E. Rico, M. A. Baranov, and P. Zoller, Topology by dissipation in atomic quantum wires, Nat. Phys. 7, 971–977 (2011).

[138] Y. Yanay and A. A. Clerk, Reservoir engineering with localized dissipation: Dynamics and prethermalization, Phys. Rev. Res. 2, 023177 (2020).

[139] Z.-P. Cian, G. Zhu, S.-K. Chu, A. Seif, W. DeGottardi, L. Jiang, and M. Hafezi, Photon Pair Condensation by Engineered Dissipation, Phys. Rev. Lett. 123, 063602 (2019).

[140] T. Botzung, S. Diehl, and M. Müller, Engineered dissipation induced entanglement transition in quantum spin chains: From logarithmic growth to area law, Phys. Rev. B 104, 184422 (2021).

[141] P. Zapletal, A. Nunnenkamp, and M. Brunelli, Stabilization of Multimode Schrödinger Cat States Via Normal-Mode Dissipation Engineering, PRX Quantum 3, 010301 (2022).

[142] A. Tomadin, S. Diehl, and P. Zoller, Nonequilibrium phase diagram of a driven and dissipative many-body system, Phys. Rev. A 83, 013611 (2011).

[143] C. E. Bardyn, M. A. Baranov, C. V. Kraus, E. Rico, A. Imamoglu, P. Zoller, and S. Diehl, Topology by dissipation, New J. Phys. 15, 085001 (2013).

[144] M. Lemeshko and H. Weimer, Dissipative binding of atoms by non-conservative forces, Nat. Commun. 4, 2230 (2013).

[145] H. Weimer, A. Kshetrimayum, and R. Orús, Simulation methods for open quantum many-body systems, Rev. Mod. Phys. 93, 015008 (2021).

[146] L. Henriet, Z. Ristivojevic, P. P. Orth, and K. L. Hur, Quantum dynamics of the driven and dissipative Rabi model, Phys. Rev. A 90, 023820 (2014).

[147] F. A. Wolf, M. Kollar, and D. Braak, Exact real-time dynamics of the quantum Rabi model, Phys. Rev. A 85, 053817 (2012).

[148] M.-J. Hwang, R. Puebla, and M. B. Plenio, Quantum Phase Transition and Universal Dynamics in the Rabi Model, Phys. Rev. Lett. 115, 180404 (2015).

[149] F. Altintas and R. Eryigit, Dissipative dynamics of quantum correlations in the strong-coupling regime, Phys. Rev. A 87, 022124 (2013).

[150] S. Mahmoodian, Chiral Light-Matter Interaction beyond the Rotating-Wave Approximation, Phys. Rev. Lett. 123, 133603 (2019).

[151] A. F. Kockum, A. Miranowicz, S. D. Liberato, S. Savasta, and F. Nori, Ultrastrong coupling between light and matter, Nat. Rev. Phys. 1, 19–40 (2019).

[152] P. Forn-Díaz, L. Lamata, E. Rico, J. Kono, and E. Solano, Ultrastrong coupling regimes of light-matter interaction, Rev. Mod. Phys. 91, 025005 (2019).

[153] E. Sánchez-Burillo, D. Zueco, L. Martín-Moreno, and J. J. García-Ripoll, Dynamical signatures of bound states in waveguide QED, Phys. Rev. A 96, 023831 (2017).

[154] G. Díaz-Camacho, D. Porras, and J. J. García-Ripoll, Photon-mediated qubit interactions in one-dimensional discrete and continuous models, Phys. Rev. A 91, 063828 (2015).

[155] G. Díaz-Camacho, A. Bermudez, and J. J. García-Ripoll, Dynamical polaron Ansatz: A theoretical tool for the ultrastrong-coupling regime of circuit QED, Phys. Rev. A 93, 043843 (2016).

[156] D. L. Hurst and P. Kok, Analytic few-photon scattering in waveguide QED, Phys. Rev. A 97, 043850 (2018).

[157] K. Piasotski and M. Pletyukhov, Diagrammatic approach to scattering of multiphoton states in waveguide QED, Phys. Rev. A 104, 023709 (2021).

[158] F. Dinc, Diagrammatic approach for analytical non-Markovian time evolution: Fermi's two-atom problem and causality in waveguide quantum electrodynamics, Phys. Rev. A 102, 013727 (2020).

[159] Note that our definition of the detuning δ differs from that employed in Ref. [106].

[160] T. Shi, Y.-H. Wu, A. González-Tudela, and J. I. Cirac, Bound States in Boson Impurity Models, Phys. Rev. X 6, 021027 (2016).

[161] J. J. Sakurai and J. Napolitano, Modern Quantum Mechanics, Cambridge University Press (2017).

[162] O. Firstenberg, T. Peyronel, Q.-Y. Liang, A. V. Gorshkov, M. D. Lukin, V. Vuletić, Attractive photons in a quantum nonlinear medium, Nature 502, 71–75 (2013).

[163] K. Winkler, G. Thalhammer, F. Lang, R. Grimm, J. H. Denschlag, A. J. Daley, A. Kantian, H. P. Büchler, and P. Zoller, Repulsively bound atom pairs in an optical lattice, Nature 441, 853–856 (2006).

[164] W. H. Press, B. P. Flannery, S. A. Teukolsky, and W. T. Vetterling, Numerical Recipes in C, 1986.

[165] P. Bykov, Sov. J. Quantum Electron. 4, 7 (1975).

[166] D. E. Chang, J. S. Douglas, A. González-Tudela, C.-L. Hung, and H. J. Kimble, Colloquium: Quantum matter built from nanoscopic lattices of atoms and photons, Rev. Mod. Phys. 90, 031002 (2018).

[167] S. John and J. Wang, Quantum electrodynamics near a photonic band gap: Photon bound states and dressed atoms, Phys. Rev. Lett. 64, 2418 (1990).

[168] L. Qiao and C.-P. Sun, Atom-photon bound states and non-Markovian cooperative dynamics in coupled-resonator waveguides, Phys. Rev. A 100, 063806 (2019).

[169] H. J. Carmichael, Statistical Methods in Quantum Optics 2: Non-Classical Fields, Springer, Dordrecht/Boston (2008).

[170] A. Periwal, E. S. Cooper, P. Kunkel, J. F. Wienand, E. J. Davis, and M. Schleier-Smith, Programmable interactions and emergent geometry in an array of atom clouds, Nature 600, 630–635 (2021).

[171] F. A. An, E. J. Meier, J. Ang'ong'a, and B. Gadway, Correlated Dynamics in a Synthetic Lattice of Momentum States, Phys. Rev. Lett. 120, 040407 (2018).

[172] M. A. Perlin, D. Barberena, M. Mamaev, B. Sundar, R. J. Lewis-Swan, and A. M. Rey, Engineering infinite-range SU(n) interactions with spin-orbit-coupled fermions in an optical lattice, Phys. Rev. A 105, 023326 (2022).

[173] A. González-Tudela and J. I. Cirac, Markovian and non-Markovian dynamics of quantum emitters coupled to two-dimensional structured reservoirs, Phys. Rev. A 96, 043811 (2017).

[174] T. Shi, Y-H Wu, A. González-Tudela, and J. I. Cirac, Effective many-body Hamiltonians of qubit-photon bound states, New J. Phys. 20, 105005 (2018).

[175] Y. Chougale, J. Talukdar, T. Ramos, and R. Nath, Dynamics of Rydberg excitations and quantum correlations in an atomic array coupled to a photonic crystal waveguide, Phys. Rev. A 102, 022816 (2020).

[176] A. Morvan et al., Formation of robust bound states of interacting microwave photons, Nature 612, 240–245 (2022).

[177] A. V. Gorshkov, J. Otterbach, M. Fleischhauer, T. Pohl, and M. D. Lukin, Photon-Photon Interactions via Rydberg Blockade, Phys. Rev. Lett. 107, 133602 (2011).

[178] H. L. Jeannic, A. Tiranov, J. Carolan, T. Ramos, Y. Wang, M. H. Appel, S. Scholz, A. D. Wieck, A. Ludwig, N. Rotenberg, L. Midolo, J. J. García-Ripoll, A. S. Sørensen, and P. Lodahl, Dynamical photon–photon interaction mediated by a quantum emitter, Nat. Phys. 18, 1191–1195 (2022).

[179] L. Zhang, V. Walther, K. Mølmer, and T. Pohl, Photon- photon interactions in Rydberg-atom arrays, Quantum 6, 674 (2022).

[180] M. Saffman, T. G. Walker, and K. Mølmer, Quantum information with Rydberg atoms, Rev. Mod. Phys. 82, 2313 (2010).

[181] H. Levine, A. Keesling, A. Omran, H. Bernien, S. Schwartz, A. S. Zibrov, M. Endres, M. Greiner, V. Vuletić, and M. D. Lukin, High-Fidelity Control and Entanglement of Rydberg-Atom Qubits, Phys. Rev. Lett. 121, 123603 (2018).

[182] P. Lodahl, S. Mahmoodian, and S. Stobbe, Interfacing single photons and single quantum dots with photonic nanostructures, Rev. Mod. Phys. 87, 347 (2015).

[183] M. Casas and S. Striscasasngari, Elementary Excitations of ^{4}He Clusters, J. Low Phys. Temp. **79**, 135 (1990).

[184] J. Mölter, T. Barthel, U. Schollwöck, and V. Alba, Bound states and entanglement in the excited states of quantum spin chains, J. Stat. Mech., P10029 (2014).

[185] Z. Wang, J. Wu, W. Yang, A. K. Bera, D. Kamenskyi, A. T. M. N. Islam, S. Xu, J. M. Law, B. Lake, C. Wu, and A. Loidl, Experimental observation of bethe strings, Nature 554, 219-223 (2018).

[186] S. J. Masson and A. Asenjo-Garcia, Atomic-waveguide quantum electrodynamics, Phys. Rev. Res. 2, 043213 (2020).

[187] D. Castells-Graells, D. Malz, C. C. Rusconi, and J. I. Cirac, Atomic waveguide QED with atomic dimers, Phys. Rev. A 104, 063707 (2021).

[188] E. Kim, X. Zhang, V. S. Ferreira, J. Banker, J. K. Iverson, A. Sipahigil, M. Bello, A. González-Tudela, M. Mirhosseini, and O. Painter, Quantum Electrodynamics in a Topological Waveguide, Phys. Rev. X 11, 011015 (2021).

[189] L. Qiao and J. Gong, Coherent Control of Collective Spontaneous Emission through Self-Interference, Phys. Rev. Lett. 129, 093602 (2022).

[190] O. A. Iversen and T. Pohl, Self-ordering of individual photons in waveguide QED and Rydberg-atom arrays, Phys. Rev. Res. 4, 023002 (2022).

[191] O. Rubies-Bigorda, S. Ostermann, and S. F. Yelin, Generating multi-excitation subradiant states in incoherently excited atomic arrays, Phys. Rev. A 107, L051701 (2023).

[192] H. Z. Shen, Shuang Xu, H. T. Cui, and X. X. Yi, Non-Markovian dynamics of a system of two-level atoms coupled to a structured environment, Phys. Rev. A 99, 032101 (2019).

[193] L. Qiao and C.-P. Sun, Universal trapping law induced by an atomic cloud in single-photon cooperative dynamics, Phys. Rev. A 101, 063831 (2020).

[194] D. Bouwmeester, J.-W. Pan, M. Daniell, H. Weinfurter, and A. Zeilinger, Observation of Three-Photon Greenberger-Horne-Zeilinger Entanglement, Phys. Rev. Lett. 82, 1345 (1999).

[195] B. Bellomo, R. L. Franco, S. Maniscalco, and G. Compagno, Entanglement trapping in structured environments, Phys. Rev. A 78, 060302(R) (2008).

[196] https://www.gnu.org/software/gsl/doc/html/eigen.html

[197] J. C. Butcher, Numerical methods for ordinary differential equations, John Wiley and Sons (2016).

[198] M. Elbracht and M. Potthoff, Accessing long timescales in the relaxation dynamics of spins coupled to a conduction-electron system using absorbing boundary conditions, Phys. Rev. B 102, 115434 (2020).

[199] S. Selsto and S. Kvaal, Absorbing boundary conditions for dynamical many-body quantum systems, J. Phys. B: At. Mol. Opt. Phys., 43, 065004 (2010).

[200] M. Valiente, D. Petrosyan, and A. Saenz, Three-body bound states in a lattice, Phys. Rev. A 81, 011601 (R) (2010).

[201] D. Zwillinger, The Handbook of Integration, CRC Press (1992).

[202] Y. Nishida, Y. Kato, and C. D. Batista, Efimov effect in quantum magnets, Nat. Phys., 9(2), 93-97 (2013).

[203] Y. Kato, S.-S. Zhang, Y. Nishida, and C. D. Batista, Magnetic field induced tunability of spin Hamiltonians: Resonances and Efimov states in $Yb_2Ti_2O_7$, Phys. Rev. Res. 2, 033024 (2020).